CONTROLLED DOPING OF ORGANIC SEMICONDUCTORS AND 2D MATERIALS WITH MOLECULAR REDUCTANTS AND OXIDANTS

A Thesis
Presented to
The Academic Faculty

by

Siyuan Zhang

In Partial Fulfillment
of the Requirements for the Degree
Doctor of Philosophy in the
School of Chemistry and Biochemistry

Georgia Institute of Technology

August 2016

CONTROLLED DOPING OF ORGANIC SEMICONDUCTORS AND 2D MATERIALS WITH MOLECULAR REDUCTANTS AND OXIDANTS

Approved by:

Dr. Seth R. Marder, Advisor
School of Chemistry and Biochemistry
Georgia Institute of Technology

Dr. David M. Collard
School of Chemistry and Biochemistry
Georgia Institute of Technology

Dr. John Reynolds
School of Chemistry and Biochemistry
Georgia Institute of Technology

Dr. Zhigang Jiang
School of Physics
Georgia Institute of Technology

Dr. Jean-Luc Brédas
Solar and Photovoltaics Engineering Research Center, Physical Science and Engineering Division
King Abdullah University of Science and Technology

Date Approved: May 23, 2016

To my parents and my future.

ACKNOWLEDGEMENTS

My deepest gratitude is to my advisor, Dr. Seth Marder, for supporting me during the past four and half years. I have been very fortunate to have an advisor who gave me not only the guidance to conduct research and critical thinking, but also the freedom to explore on my own. He has been supportive throughout my whole Ph.D., and I hope that I could be able to command an audience as well as he can someday. I am also very grateful to Dr. Steve Barlow for his scientific advice and knowledge. He is always available to provide many insightful discussions and suggestions. I am also thankful to Dr. Tim Parker for helping with instruments in the lab and useful suggestions for this dissertation. I would also like to thank the members of my Ph.D. committee: Dr. John Reynolds, Dr. Jean-Luc Brédas, Dr. David Collard, and Dr. Zhigang Jiang, for their helpful suggestions and career advice.

I feel grateful that I met many good mentors, who were very open with their knowledge and experience, especially Dr. Swagat Mohapatra and Dr. Sergio Paniagua in Marder group, who showed me how to do air-sensitive synthesis and surface characterization; Dr. José Baltazar and Dr. Hossein Sojoudi, who trained me on cleanroom photolithography, and graphene growth and transfer techniques; and Marcel Said, for showing me how to fabricate organic solar cells. I would like to acknowledge and thank my surface modification subgroup members Dr. Anthony Giordano, Dr. O'Neil Smith, Rebecca Hill, Hyekyung Kim, and Federico Pulvirenti for their support and helpful discussions, and thanks to my mentees, Catherine Robinson, Kodzo Deku

and Kelsey Rainey, who were always enthusiastic about learning science. I am also indebted to the rest of the Marder Group, from whom I have received much help during my graduate studies. Particularly, I would like to acknowledge Dr. Raghunath R. Dasari, Dr. Yadong Zhang, Dr. Junxiang Zhang, Fadi Jradi, Dr..Kostiantyn Ziabrev, Dr. Iryna Davydenko, Janos Simon, Matthew Copper, Carolyn Buckley, and Xiaochu Ba. I also appreciate Dr. Denise Bale and Walaa Compton for their support to guarantee the whole group functions in a well-organized manner.

Outside of the Marder group, I would like thank Dr. John Reynolds, Dr. Samuel Graham, and Dr. Elsa Reichmanis, for their guidance and allowing me to use their lab resources for various studies; especially big thanks to Dr. Jean-Luc Brédas and the members of his group, Dr. Chad Risko, Dr. Hong Li and Junghyun Noh for helping with complex calculations to complement experimental results. I also want to acknowledge collaborators from other departments, including Meng-Yen Tsai and Dr. Alexey Tarasov from Materials Science and Engineering, Dr. Boyi Fu and Dr. Gang Wang at Chemical Engineering, Dr. Hyungchul Kim at Mechanical Engineering, Yuxuan Jiang at Physics Department, as well as Walter Henderson and Todd Walter who have helped me maintain the Kratos XPS for the past two years. I thank the Center for Organic Photonics and Electronics (COPE) for the fellowship awarded.

I am also grateful to have the opportunity to work with groups outside the GT campus: Dr. Ben Naab from Dr. Zhenan Bao's group at Stanford University; You-Chia Chang from Dr. Theodore B. Norris at University of Michigan; several group members

in Dr. Amassian's group at King Abdullah University of Science and Technology in Saudi Arbia. All of these experiences have made me a more capable and well-rounded scientist.

Most importantly, none of this would have been possible without the love and patience of my family. I am forever grateful that my parents raised me up to be who I am, being adventurous, optimistic, having an open-mind, and never giving up easily; I am thankful that wherever I go, I always meet good people, who are supportive and helpful, and become lifelong good friends; and I appreciate that there is always a new opportunity waiting for me right around the corner.

I owe a huge debt of gratitude to all the people who have made this dissertation possible. I will cherish and benefit from my graduate experience for the rest of my life.

TABLE OF CONTENTS

LIST OF TABLES

Page

LIST OF FIGURES

Page

LIST OF SYMBOLS AND ABBREVIATIONS

E	energy
E_c	conduction band minimum
E_f	Fermi level
E_v	valence band maximum
k_B	Boltzman's constant
T	temperature
Φ	work function
ε_r	relative permittivity of the dielectric
$\Delta E'_{hole}$	hole injection energy barrier
AFM	atomic force microscopy
BHJ	bulk heterojunction
CA	contact angle
CB	conduction band
CNT	carbon nanotube
COPE	Center for Organic Photonics and Electronics
Cp	cyclopentadiene
Cp*	pentamethylcyclopentadiene
CV	cyclic voltammetry
CVD	chemical vapor deposition

DFT	density functional theory
DOS	density of state
DSC	detergent/solvent-cleaned
EA	electron affinity
ETL	electron transport layer
ESR	electron transport layer
F-D	Fermi-Dirac statistics
FET	field-effect transistor
GFET	graphene field-effect transistor
HTL	hole transport layer
HOMO	highest occupied molecular orbital
IMFP	inelastic mean free path
IE	ionization energy
ITO	indium tin oxide
LUMO	lowest unoccupied molecular orbital
M-B	Maxwell-Boltzmann statistics
NMR	nuclear magnetic resonance spectroscopy
OFET	organic field effect transistor
OLED	organic light emitting dipole
OPV	organic photovoltaic
PA	phosphonic acid

PCBM	phenyl-C_{61}-butyric acid methyl ester
SAM	self-assembled monolayer
SEE	secondary electron edge
SGL	single layer graphene
SWNTS	single-wall nanotubes
TIPSp	6,13-bis(triisopropylsilylethynyl)pentacene
TCE	transparent conducting electrode
TGA	thermogravimetric analysis
TMDCs	transition metal dichalcogenide
UPS	ultraviolet photoelectron spectroscopy
VB	valence band
VBM	valence band maximum
WF	work function
XPS	X-ray photoelectron spectroscopy

SUMMARY

Flexible electronics is a rapidly developing research field. This dissertation focuses on understanding the chemistry involved in doping and surface modification processes on a variety of materials with different applications in flexible electronics. Particular attention is given to the modification of organic semiconductors and 2D materials, including graphene and transition metal dichalcogenides (TMDCs), through the use of redox-active organic and metal-organic dopants.

In this dissertation, new air-stable dimeric n-dopants are synthesized and studied in detail with respect to the kinetics of both their redox reaction in solution with and their doping in the solid-state of various organic semiconductor acceptors. Detailed mechanistic studies are necessary to recognize the strengths and limitations of existing dimers to inform future dopant design. The newly synthesized n-dopants together with other redox-active n- and p-dopants are then used to surface modify mono- and multi-layer graphene, which shows a large decrease in the sheet resistance and tunable work function over a range of 2 eV. A subset of these molecules is applied to MoS_2 and WSe_2 to realize controllable n- and p-doping, respectively, to improve their electrical properties. Other experimental techniques, especially UPS and XPS, are coupled with the electrical measurements to give information about work function shifts, surface coverage, charge transfer efficiency, and etc. Finally, organic diodes, solar cells, and field-effect transistors with doped graphene electrodes were fabricated, where the work function engineering of graphene electrodes via doping proved to be important in reducing the carrier-injection barriers.

CHAPTER 1 Introduction

The purpose of this chapter is to introduce the basics of doping in flexible electronics. A brief introduction to flexible electronics will be described first. After a discussion of the importance of doping and interface modification in these flexible electronics, various approaches for doping and modification reported in the literature will be discussed, together with their advantages and disadvantages. Then, a brief literature review of the applications of dopants and modifiers in flexible electronics will be provided. In the end, experimental techniques that can be used to characterize the doping effects and the overview of this dissertation will be introduced.

1.1 Flexible electronics

Flexible electronics has a long history. Back to the 1960s, flexible solar cell arrays were fabricated from a single crystal silicon wafer with a thickness down to ca. 100 μm on top of a plastic substrate.[1,2] It has been driven more and more as a research interest by future promise in energy conversion, environmental monitoring, displays and human-machine interactivity, and healthcare.[3] The development of flexible electronics requires breakthroughs in materials that are not only flexible but also have the desirable electrical insulating, semiconducting, or metallic properties. Recent advances on thin-film materials and device fabrication techniques fuel the further development of this field.[4-7]

The candidate materials used for flexible electronics applications include silicon (in amorphous, nanocrystalline, or polycrystalline form), II–VI compound

semiconductors, organic semiconductors, and new emerging two-dimensional (2D) materials such as graphene and transition metal dichalcogenides (TMDCs). Diodes and transistors are among the most commonly used thin-film devices for digital and analog circuits, and the mobility is an important figure of merit for these devices, which illustrates how quickly a charge carrier (electron or hole) can move within the materials upon electric field. Figure 1.1 compares the charge mobility of these candidate materials and their flexibility with the data summarized from the literatures.[8-25] Inorganic semiconductors, such as III-V compound semiconductors and silicon, have high mobility (about 100 $cm^2 V^{-1} s^{-1}$) but low strain limit, and the crack at low strain will be detrimental to their electrical properties.[14,15,18] Even though they can be flexible when their thicknesses are down to several hundred microns, this will bring up other questions, such as cost and scalability issues.[11,22] For the content of this dissertation, the discussion will be focusing on organic semiconductors, 2D materials, and carbon nanotubes (CNTs), all of which have much higher flexibility.

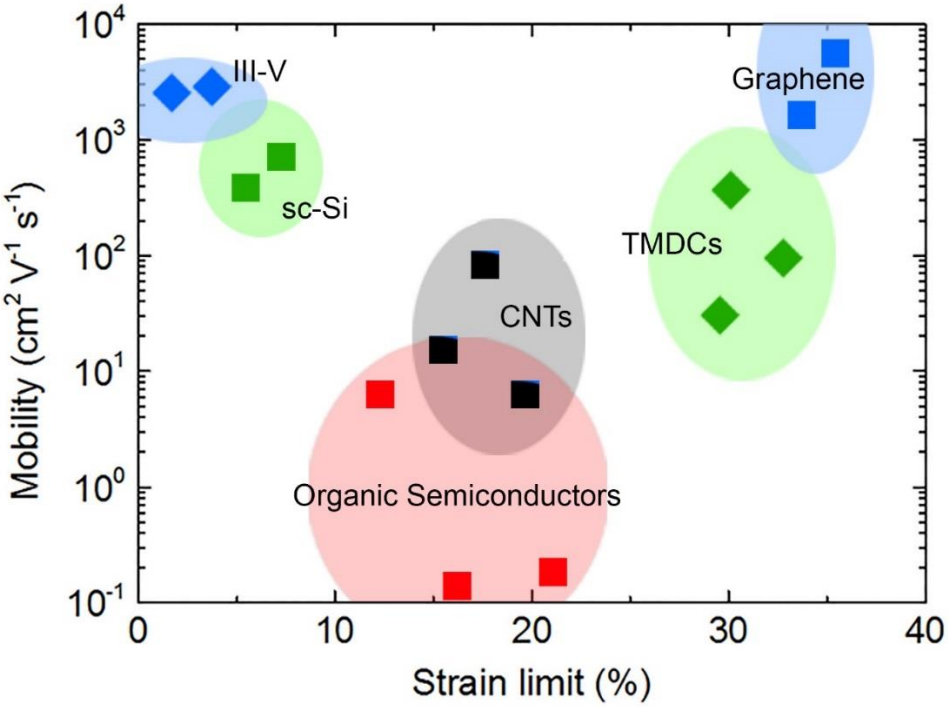

Figure 1.1 Mobility and strain comparison of candidate materials for flexible electronics. Data taken from literatures.[8-25]

Thin films of organic semiconductors (small molecules and polymer) have been explored for flexible electronics applications.[7,26-29] They are light-weight, can be synthetically modified, and allow low-temperature processing. As the examples shown in Figure 1.2 for representative π-conjugated polymers, they were initially studied as conductive and semiconductive materials, followed by research on integrating these materials into organic electronic devices such as field-effect transistors (OFET), electrochromic displays, light emitting diodes (OLED), sensors, and organic photovoltaic (OPV) devices. Single-crystal OFETs have relative higher device performance than organic thin-film transistors, and the reported benchmark values of carrier mobility (20–40 $cm^2\ V^{-1}\ s^{-1}$) are one order of magnitude higher than those of polycrystalline organic semiconductors.[30-33] There are several demonstrations of organic thin-film materials fabricated on flexible plastic substrates, for the transistor,[34-

[36] reflective liquid crystal display (LCDs),[37-39] OLED displays[26,40,41] and electrophoretic displays.[42]

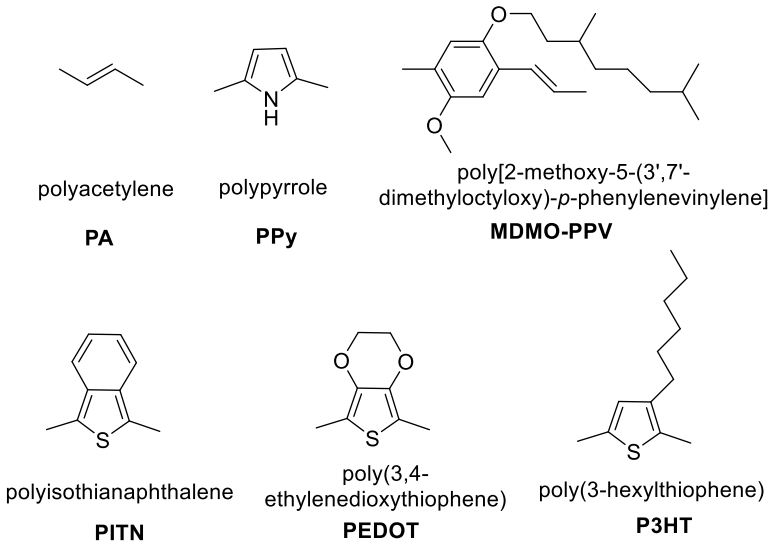

Figure 1.2 Chemical structures of representative π-conjugated polymers: PA, PPy, MDMO-PPV, PITN, PEDOT, and P3HT.

More recently, two-dimensional (2D) materials have been the focus of interest for conventional semiconductor technology and flexible electronic applications. 2D materials are atomically or few-atom thin, layered crystalline solids with intra-layer covalent bonding and inter-layer van der Waals bonding, enabling exfoliation into two-dimensional layers of single unit cell thickness.[6] They are the thinnest unsupported crystalline solids, possess no dangling surface bonds and exhibit superior intra-layer transport of fundamental excitations, such as charge, heat, spin and light.[6,43-45] Graphene as the first 2D crystal received widespread attention and exhibits excellent optoelectronic and mechanical properties;[46] but, it lacks a bandgap that limits its use as a semiconductor. Even though band gaps can be engineered in graphene using various methods, decrease of mobilities are observed in many cases.[47-49] In contrast, several 2D TMDCs possess sizable bandgaps around 1–2 eV, with promising applications in new

FET and optoelectronic devices.[6,50] Although TMDCs have been studied for decades, recent advances in nanoscale materials characterization and device fabrication have opened up new opportunities for 2D materials in nanoelectronics and optoelectronics. The expanding family of 2D materials, currently includes 2D crystal graphene,[45,51] TMDCs,[43,50,52] diatomic hexagonal boron nitride (h-BN),[24,53] and new emerging monoatomic buckled crystals termed Xenes, which include silicene,[54,55] germanene,[56] and phosphorene.[57,58] These atomic sheets afford unmatched combinations of both desirable device physical properties in a variety of material categories (including semiconductors, insulators, transparent conductors and transducers) and mechanical properties that are commonly accessible on soft polymer substrates.

Carbon nanotubes (CNTs) are suitable candidates for flexible electronic applications, they can be either transferred or directly solution-processed on flexible substrates. They can be either metallic or semi-conducting, depending on the "twist" of the tube (detailed discussion will be presented in Chapter 3). Moreover, they are light-weight, flexible, and chemically inert under many conditions. Their tunable intrinsic carrier mobility, conductivity, and mechanical flexibility allow them to be used as both the channel material in FETs and as transparent electrodes.[5] Single-wall carbon nanotubes (SWNTs), for example, have enabled flexible transparent OFETs with mobilities comparable to that of a-Si:H TFTs.[59,60]

Except diodes and transistors, other possible market products for the flexible electronics can be categorized into the following five groups: (1) lighting, such as LED and OLED; (2) photovoltaics, such as organic solar cells, organic tandem solar cells,

dye-sensitized cells, and the new emerging perovskite cells; (3) displays, such as liquid crystal displays, OLED, and e-papers; (4) integrated smart systems, including sensors, actuators, electronic textiles, and sport fitness/healthcare devices; and (5) electronics and components, such as batteries, antennas, and interconnects.[61] For the contents of the dissertation, doping and surface modification studies for organic semiconductors and 2D materials with their applications in field-effect transistors and organic solar cells will be discussed, and their operating principle will be mentioned in the corresponding chapters.

1.2 Doping and interface modification fundamentals

The fundamental properties of thin-film materials and the quality of device interfaces give rise to inherent device performance limitations. The breakthrough in classical silicon technology came when the conduction type was no longer determined by impurities but could be controlled by doping. Doping of inorganic semiconductors have been extensively investigated and are well understood.[62,63] Until now, most of the new emerging materials with possible applications in flexible electronics, such as organic semiconductors and 2D materials, are usually prepared in the pristine form, despite the need for tuning their electrical properties to realize certain functions. The following section will discuss the basic concepts of doping and interface modification.

1.2.1 Electronic band structure

In isolated atoms, the electron wavefunctions (i.e. orbitals in the one-electron approximation) lead to a series of discrete energy levels. In molecules, the atomic orbitals combine to form molecular orbitals. In solids, the combination of atomic

orbitals can lead to the formation of electronic bands, with lower occupied (or upper unoccupied) band reflected to the valence (or conduction) band. An energy gap, the band gap, appears between the valence and conduction bands in the case of semiconductors and insulators.[64]

The probability of a certain energy level being filled with an electron is governed by the Fermi–Dirac (F-D) distribution. The F-D distribution function can be expressed by:

Equation 1.1 $$f_0(E, T) = \frac{1}{1+e^{(E-E_f)/k_B T}}$$

where k_B is Boltzmann's constant; T, the absolute temperature; and E_f , the Fermi energy or chemical potential, and often referred to as the Fermi level. The location of the Fermi level is closely related to many electronic properties (including the optical, electrical, and magnetic properties). Figure 1.3 shows the F-D distribution function versus energy E at three different temperatures. At absolute zero (T = 0 K), $f_0(E) = 1$ for $E < E_f$, and $f_0(E) = 0$ for $E > E_f$, which means that the probability of finding an electron on a level with energy smaller than the Fermi energy is equal to unity, and there is zero probability of finding an electron with energy greater than the Fermi energy. At T > 0 K, $f_0(E) = 0.5$ at $E = E_f$; some of the quantum levels below E_f become partially empty, while some of the quantum level above E_f become partially filled.[65]

The valence and conduction bands are more relevant for the electronics and optoelectronics properties.[66] Whether or not there are electrons in the conduction band is crucial to the conduction process: in insulators, the electrons in the valence band are separated by a large gap from the conduction band; in metals (conductors), the valence band and the conduction band overlap at the Fermi energy and there is no bandgap, as

shown in Figure 1.3(a); in semiconductors, there is a bandgap but, at finite finite temperature, some of the valence can bridge this gap and participate in electrical conduction upon thermal or other excitations (Figure 1.3(b)).

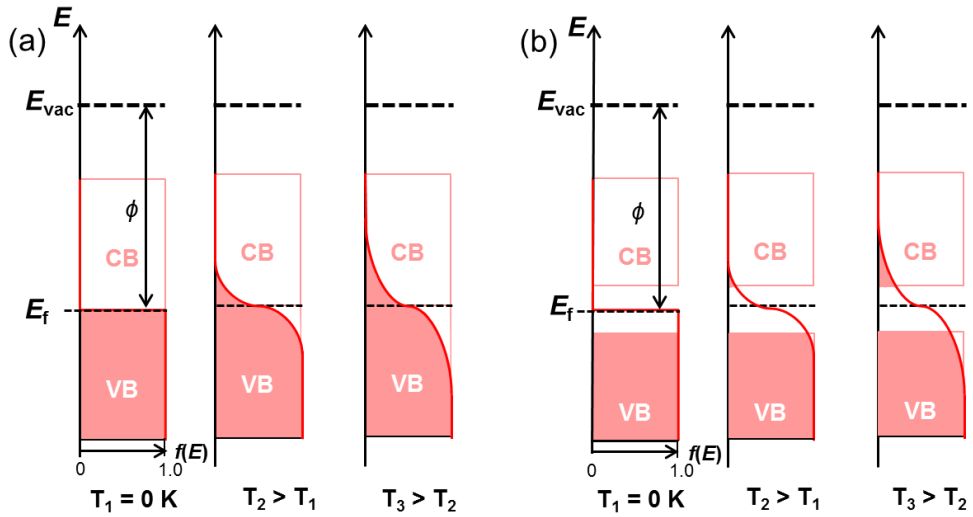

Figure 1.3 Fermi-Dirac distribution function $f_0(E)$ at various temperature for (a) a metal and (b) a semiconductor.

1.2.2 Effects of doping on charge transport of semiconductors

Doping can be used to control the Fermi-level position of the semiconductor, which is related to the number of free charge carries created in the semiconductor. As described earlier, the semiconductors are defined as insulators with small band gaps. Figure 1.4 shows the band diagram of the semiconductor. Different levels, including conduction band minimum (E_c), valence band maximum (E_c), Fermi level (E_f) are also shown. At finite temperature, some electrons are excited from the lower valence band to the conduction band, so there are holes in the valence band and the electrons in the conduction one, which can contribute to the charge transport. Such semiconductor is called intrinsic. Doping is the process of introducing charge carriers with the impurity atoms or molecules, which leads to a shift of the Fermi level. Figure 1.4(b-c) shows the Fermi level position changes for the n-doped and p-doped semiconductors. As the extra

charge carriers are added into the conduction band or valence band, the Fermi level shifts based on the density of states and carrier concentrations, and it can serve as a reference for the doping levels.

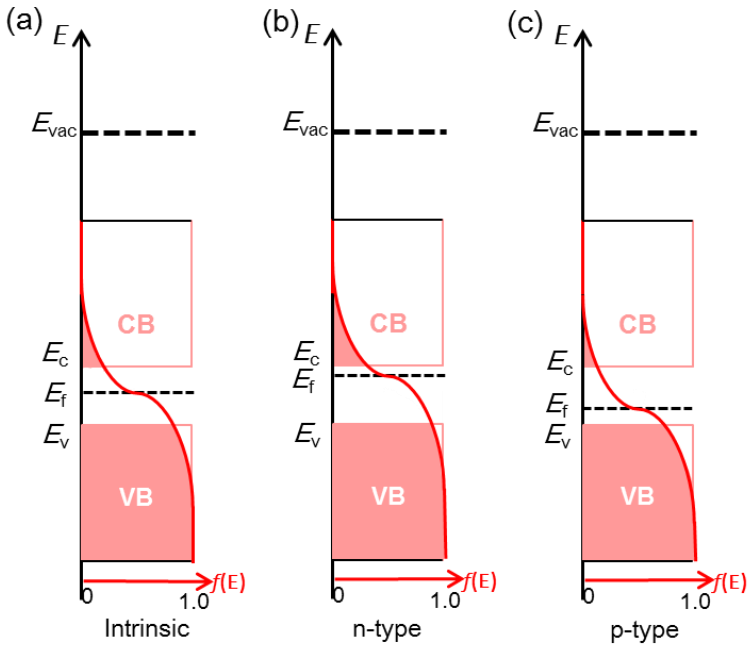

Figure 1.4 Schematic band diagram and Fermi-Dirac distribution for (a) intrinsic, (b) n-type, and (c) p-type semiconductors at thermal equilibrium.

Doping inorganic semiconductors by controllably introducing impurity atoms is the basis of the functionality in today's inorganic electronic devices. In inorganic semiconductors, doping can dramatically increase their conductivity with low doping ratios, typically in the range of 10^{-6}–10^{-3}. In inorganic semiconductors, the overall low dopant concentrations are critical to retaining high charge-carrier mobilities, because dopant atoms inevitably act as scattering centers in these inorganic semiconductors. In the inorganic semiconductor doping process, the hydrogen model could be used to explain most observations: the host and dopants have the same or very similar electronic shells (*e.g.* phosphorus in silicon, or boron in silicon), the release of an electron bound

in a Bohr state around the charged ion core. In inorganic semiconductors, the Ohmic losses are low, because of the high conductivity of the transport layers. However, in organics, the low carrier mobility increases Ohmic losses, thus, higher the fields are needed to drive the currents. The basic doping principle in organic semiconductors are similar to the inorganic ones, but with few differences: (1) the transport in organic semiconductors generally takes place by hopping in a distribution of more or less localized states; (2) the effective mass in organics is much higher, thus, large Coulomb interaction exists between charge carriers; (3) the host organics and the molecular dopants normally have quite different structures, which will raise the questions of how they arrange microscopically. Unlike inorganic semiconductors, the understanding of the doping process of the organic semiconductor is still rudimentary, further experimental and theoretical studies of the doping process are needed.

In organic semiconductors, the hopping rate is controlled by the energy difference between the occupied states and the effective transport level. The presence of impurities and defects in organic semiconductors lead to the formation of trap states lying deeper in the gap than the effective transport states, which will hinder the charge transport and leads to low charge mobility. Upon doping, these deep traps are filled and the energy distribution of occupied states are raised, thus increasing charge carrier density in an energetically disordered hopping system will strongly increase the mobility.[67] As shown in Figure 1.5, upon n-doping, the trap states can be passivated at low doping concentration, and this in principle should improve the effective charge mobility.

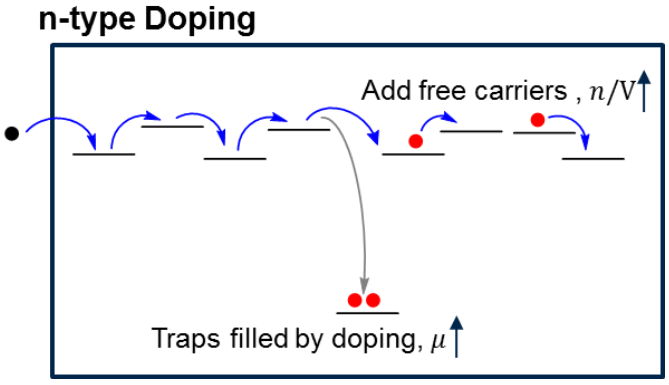

Figure 1.5 General diagram to depict the trap-filling, and increase of free charge carriers upon n-doping.

1.2.3 Effects of doping at interfaces

Device function in most electronic devices involves the flow of charges from electrodes into the organic semiconducting layer, or vice versa. The alignment of material energy levels of semiconductors with respect to the Fermi level of contacts is of utmost importance for charge-carrier injection efficiency, and consequently device efficiency.[68] Work function matching of the electrode and active layers allows for better energy-level alignment in organic optoelectronic devices, thereby decreasing the energetic barriers for carrier injection, as explained below.[69]

To realize the full potential of materials in devices, interfaces between organic thin films and electrodes, dielectrics, or other organic films is important, as they may limit charge injection and overall transport through the devices. The mechanisms that determine the electronic properties of these interfaces, *i.e.*, the relative position of molecular levels and charge carrier transport states, is an important research topic for developing reliable device processing conditions.[68,70,71] When we predict charge injection barriers at an electrode-semiconductor interface, it is generally assumed that the hole-injection barrier is the difference between the ionization energy (IE) of the

organic material and the work function of the metal (Φ_M), while electron-injection barrier is the difference between the Φ_M and electron affinity of organic film.[72] This prediction is based on rule of vacuum alignment, which is also known as Schottky-Mott limit [Figure 1.6(a)]. Researchers soon realized that the vacuum levels rarely align, and the real situation is far more complicated than this. The interface shift between the vacuum level of two materials, or interface dipole barrier, is the reason for break-down of the vacuum level-alignment rule [Figure 1.6(b)].[69] The intrinsic interface dipole between unmodified metal and semiconductors, is caused by the electron redistribution between metal Fermi level and interface gap states to equalize E_F in the two materials. Upon n-doping, as shown in Figure 1.6(c), the E_F of the semiconductor is shifted towards the empty states (E_{LUMO}), which leads to a decrease of the electron-injection barrier ($\Delta E_{electron}$) when the electrode and semiconductor are brought in contact [Figure 1.6(d)]. Same principle can be applied to the p-doping side for the hole-injection barrier (ΔE_{hole}). Hence, interfacial doping in semiconductors can promote more efficient charge injection through interfaces in devices. Doping can largely reduce the charge injection barrier, and the application of doping techniques in devices has led to improved *J-V* characteristics and improved device performance.[73-75]

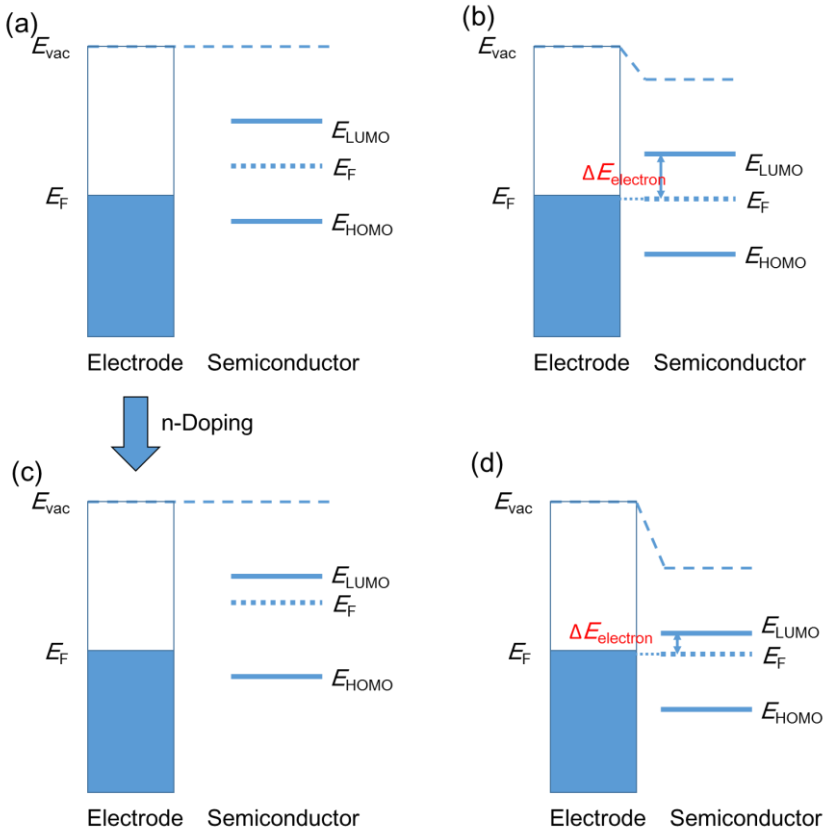

Figure 1.6 Schematic energy level diagrams for electrode and semiconductor (electron-transport material) before (a, c) and after (b, d) in contact when the Fermi levels align, and effects of n-doping on the electron injection barrier ($\Delta E_{electron}$).

1.3 The state of art for dopants and modifiers

Depending on the intrinsic properties of the host material and the desired device applications, different modification methods, such as bulk doping, surface doping (or modification) or a combination of both have been used. For the content of this dissertation, dopants only refer to the atoms or molecules which undergo complete charge transfer and form corresponding charged ions. Molecules, which only induce partial charge transfer and shift the vacuum levels to induce work-function change, will be referred as modifiers.

Bulk doping incorporates hetero-ions or -molecules directly into bulk hosts, which directly induces extra charge carriers into the materials and thus may tune the

Fermi level, and increases bulk conductivity and mobility. In bulk doping, relatively low doping level is mostly required, because the counterparts of the hetero-ions or –molecules can also interact with the charge carries to serve as scatting centers, and they may also disrupt the crystal structure of the host materials. For inorganic semiconductor doping, it was found that the optimal doping concentration decreases with increasing particle size. Surface doping (or modification), on the other hand, is depositing dopants (or modifiers) on the surface of the hosts. Surface-doped molecules create an internal electric field to drive charge carriers to quickly drift to the surface. For the surface doping and modification, when the modifier and host substrate are brought into contact with each other, the surface molecules interact, giving rise to attractive forces that may be physical, chemical, or electrostatic, corresponding to adsorption, covalent bonding, or van der Waals forces, respectively. For surface doping where only charge transfer occurrs without forming a new covalent bond, the doped counter ions, and the substrates are bonded electrostatically. The surface doping normally will not disrupt the structure of the host materials, and it can be used to improve interfacial charge carrier transfer. Physisorption generally occurs in a solid/fluid or a solid/gas system through interactions such as van der Waals forces, weak coordinate bonds, or hydrogen bonds. Chemisorption involves a chemical reaction between the surface and the adsorbate, and new chemical bonds are formed. The typical binding energy of physisorption is much smaller than that of chemisorption. Thus, when the attachment happens through physisorption, the molecules may be easily removed via heat, solvents, or sonication, while the modification formed through the chemisorption is normally irreversible.

1.3.1 Dopants: oxidants and reductants

The general doping process can be described as in Figure 1.7, where electron donor or acceptors are added to the materials generating additional charge carriers. n-Dopants are materials with relative low ionization energy, so they can donate electrons to the lowest unoccupied molecular orbitals (LUMOs); while high electron affinity is required for the p-dopants, so they can extract electrons from the highest occupied molecular orbitals (HOMOs).

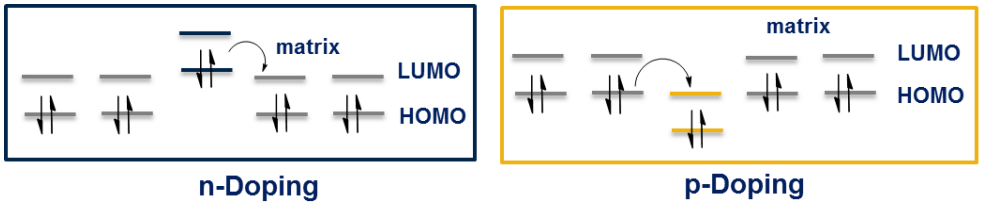

Figure 1.7 Scheme of doping process for molecular n- and p-doping, where the dopant acts as a donor or acceptor.

The following sections will summarize different types of dopants and modifiers based on their doping mechanism and binding types.

1.3.1.1 n-Dopants

Suitable molecular n-dopants are scarce, mainly because a low value of ionization energy is required for effective electron transfer to most organic electronic materials, which makes it challenge to design a dopant which has both strong reducing strength and reasonable air stability.[77]

An ideal n-dopant should have the following features: (1) the ability to dope a wide variety of electron-transport materials; (2) simple electron transfer into the host materials with no side reactions or minimizing formation of side-products; (3) formation of stable doping product that does not migrate, and do not act as deep

electrostatic traps for charge carriers; (5) easy processing; and (6) reasonable stability for handling in air. Different doping strength is required at different situations: for ETMs used in OLEDs, which have EA as low as ca. 2 eV,[78] strong dopants with high reducing power are required, but for the purpose of trap-filling, relatively weak dopants with better air stability can fulfill the role. ETMs used in OLEDs with low EA (ca. 2 eV) are still beyond the doping ability of the dopants that have developed to date.[78] Thus, the design of new n-dopants in which air-stable precursors can be converted to more powerful molecular n-dopants during or subsequent to deposition of the active layers of a device would be extremely useful.

1.3.1.1.1 One-electron reductants as n-dopants

Alkali and alkaline earth metals, *e.g.* lithium, sodium, and potassium, have been widely used as the n-dopants for various applications. For example, the first reported lithium metal doped OLED devices showed ~10 times higher luminance and increased current efficacy than the undoped one;[79] polymer films of poly(p-phenylene) upon exposure with potassium exhibited more than 10 order of magnitude higher conductivity than the un-modified film;[80] potassium was also used to dope graphene, where significant work function decrease and higher conductivities were observed.[81] However, the drawbacks of electrical doping using alkali metal are also obvious; their highly reactive nature, as well as the high diffusivity of the corresponding ions, have limited their applications.[82] It has been demonstrated that lithium cation can diffuse up to 80 nm into the organic materials, and can lead to formation of electrostatic traps for charge carriers.[83]

Thus, larger ions are desired that may be less prone to diffusion and less likely to interact with carriers acting as electrostatic traps, although this may also lead to more disruption of host structure. Molecular dopants with low ionization energy were identified and used for electronic applications. As shown in Figure 1.8, the common feature of these molecular n-dopants is the low ionization energy. Cobalt bis(cyclopentadienyl) ($CoCp_2$) has an ionization potential of only 4 eV. It can shift the Fermi level of a tris(thieno)hexaazatriphenylene derivative (EA = 3 eV) by more than 0.5 eV toward the electron transport level, and increase the conductivity of the investigated films by about three orders of magnitude.[84] The reducing strength of $CoCp_2$ can be increased by introducing methyl groups on the Cp ring to give decamethylcobaltocene ($CoCp^*_2$), which has a lower ionization energy of 3.3 eV (E_{ox}= –1.94 V vs. $FeCp_2^{+/0}$).[85,86] Using metal complexes appears to be a good approach for n-doping in general. $Ru(terpy)_2$ was reported as an n-dopant with an oxidation potential similar to $CoCp^*_2$; their donating characters were strong enough to dope materials used in OSCs and OFETs, but was found not sufficient to dope electron transporting materials used in OLED applications (EA can be as low as ca. 2 eV).[87,88] Dopants with lower IEs were investigated, and the dimetal complexes of tungsten with the anion of 1,3,4,6,7,8-hexahydro-2*H*-pyrimido[1,2-a]pyrimidine (hpp), $W_2(hpp)_4$, were synthesized with estimated ionization energy as low as 2.7 eV (E_{ox}= – 2.37 V vs. $FeCp_2^{+/0}$). A strong shift in Fermi level toward the electron transport level was observed with the conductivity reaching 4 S cm^{-1} for C_{60}.[89]

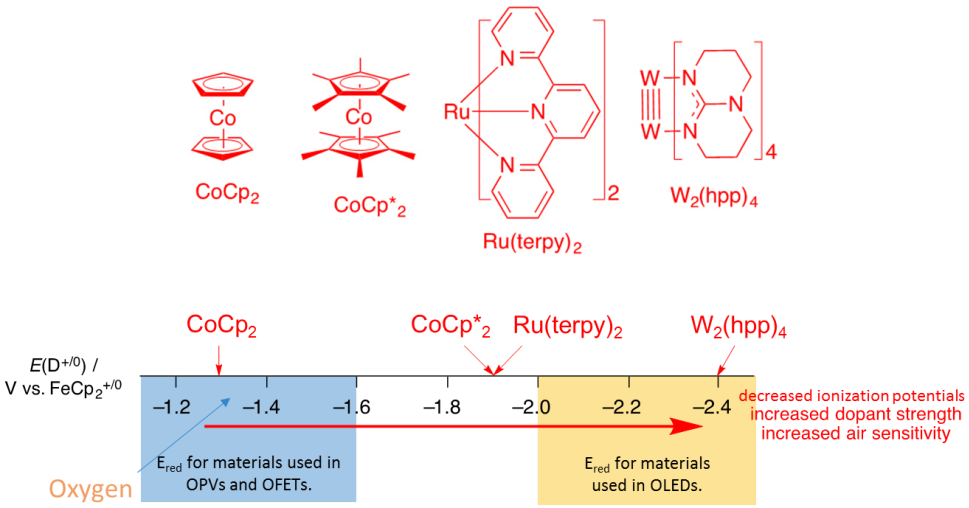

Figure 1.8 The chemical structures of some complexes used for direct n-doping and their oxidation potentials. This figure was modified from the literature.[90]

However, one general drawback of this approach is the increasing instability of the dopants to oxygen and water for lower IE values, making their synthesis and handling very difficult.

1.3.1.1.2 Air-stable n-dopants

For reductants that do not have an oxidation potential lower than the reduction potential of oxygen, the high-energy reductant may be 'stored' in a precursor form to possibly provide air stability. The lower energy precursor can then, in principle, be triggered to release the high energy intermediate upon exposure to an external stimulus.[91-93] Figure 1.9 shows some examples of the air-stable precursor molecular n-dopants. Cationic organic salts, such as $PyB^{+}Cl^{-}$ and DMBI-I can be deposited through the vacuum deposition, which leads to the formation of the reducing species upon heating.[92,94] It was reported that the conductivity of doped C_{60} films reaches 5 S cm^{-1}, which is 10^{8} times the conductivity of the undoped sample.[95] However, the doping mechanisms of these salt dopants are not well understood, and the doping effects

attributed to the formation of hydride-reduced or neutral radicals during the deposition of the dopants, without direct evidence.

Neutral hydride donor molecules, such as leucocrystal violet (LCV) and 2,3-dihydro-1*H*-benzimidazoles (DMBI-H), have also been reported as n-dopants. They were used to dope C_{60} and its derivatives, where high conductivities were achieved.[96,97] They were incorporated in order to improve the performance of various electron-transport materials in OPVs, OFETs, thermoelectrics, perovskite solar cells, graphene and CNTs.[98-102] The doping mechanism of DMBI-H derivatives in organic semiconductors, especially fullerene derivatives, was studied, which showed a hydride transfer was involved in the doping process.[103]

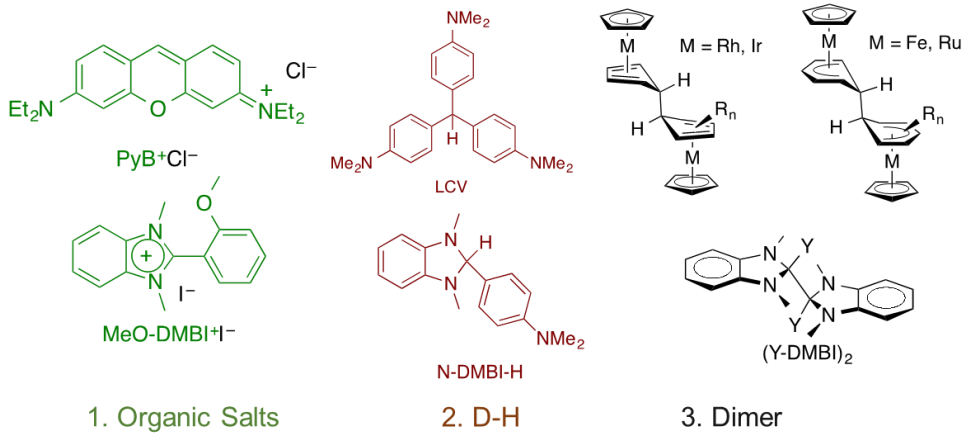

Figure 1.9 Chemical structures for the air-stable n-dopants.

Easier synthesis and handling of these air-stable precursors makes them attractive candidates as n-dopants for various applications such as trap-filling. However, both cases will lead to the formation of side products, which may disrupt the conjugation of host materials and degrade device performance. Moreover, role of H transfer means the doping strength cannot be determined only with the redox potential, but need to know the H-accepting ability of the host material as well.

The third class of air-stable n-dopants is dimers of high energy intermediates, such as neutral organometallic complexes or benzimidazoline radicals, where stable cations would be formed upon splitting and electron transfer to the acceptor, without any side-reaction or by-products.[104-106] In contrast to previously reported "air-stable precursor" molecular n-dopants, side reaction and side products of the doping process are likely to be minimized, and ETMs with much lower EA have been successfully doped. There are various examples of nineteen-electron transition metal sandwich compounds that tend to dimerize and achieve the eighteen-electron configuration, such as rhodocenes,[107-109] iridocenes[110] and some mixed cyclopentadienyl/ arene sandwich compounds of iron[111,112] and ruthenium.[113,114] These dimers normally have reasonable air-stability, but typically are not as stable as the D-H or salt species. For example, the oxidation potentials for the rhodocene dimer is about –0.7 V versus ferrocene, and the oxidation potential of the monomer is –1.85 V.[115] Its doping strength depends on the dissociation energy of the dimer and the oxidation potential of monomer. These dimer dopants have been used in organic semiconductor devices and 2D material-based electronics, where strong doping effects were demonstrated.[116-119] Chapter 2 will describe a similar strategy involving dimers of highly reducing organic radicals.

1.3.1.2 p-Dopants

Strong oxidizing halogens, *e.g.*, iodine or bromine, have been used as the p-dopants for various organic semiconductors,[120-122] graphene[123,124] and carbon nanotubes[125]. However, their small size leads to a large tendency for diffusion, and they cannot provide a thermally stable doped layer. I_2 doping of polymer is often reversible because its volatile nature. Moreover, halogens might react with some semiconductors,

where halogenation rather than electron transfer happens.

Acidic liquids, such as chlorosulfonic acid,[126] HNO_3, H_2SO_4,[127] or $SOCl_2$,[128] have also been used to modify CNT and 2D materials, where p-doping effects were observed. However, most of them suffer from thermal and chemical stability problems. They will also introduce mobile ions into the network, which can easily diffuse and disrupt the device performance. Similar problems were observed for transition metal chlorides, such as $FeCl_3$[129] and $AuCl_3$.[130]

Transition metal oxide (TMO), such as vanadium pent-oxide (V_2O_5), tungsten tri-oxide (WO_3), and molybdenum tri-oxide (MoO_3) especially, have been used for wide band gap organic semiconductor doping. With EA around 6.7 eV determined by IPES, MoO_x can induce a rapid shift of the Fermi level towards the HOMO states and a steep increase in conductivity when doping 4,4'-bis(N-carbazolyl)-1,1'-biphenyl (CBP).[131] MoO_x, has also been used to p-dope CNT,[132,133] graphene,[134] and TMDCs.[133,135] However, TMOs are only vacuum processable, and have mostly been used as hole-transport layer in OLEDs[136-138] and OPVs,[139] or buffer layers for semi-transparent devices.[140,141]

Molecular p-dopants, as shown in Figure 1.10, on the other hand, could solve the diffusion problem and form relatively more stable ions. Tetracyanoquinodimethane (TCNQ) and its derivative tetrafluorotetracyanoquinodimethane (F_4TCNQ) have been the most widely used p-dopants so far. With EA at 4.2 eV and 5.1 eV[142] (reduction potential -0.25 V and 0.16 V versus Fc^+/Fc[143]), TCNQ and F_4TCNQ proved to be effective dopants for various organic semiconductors,[76,144-147] graphene,[148,149] CNTs, and metal oxides.[150,151] The doping behaviors of TCNQ based p-dopants have been studied extensively. The absorption of the CN-stretching mode of F_4TCNQ depends on its charging state, thus, the efficiency of charge transfer between the dopants and the

host materials can be determined.

Molybdenum tris-[1,2-bis(trifluoromethyl)ethane-1,2-dithiolene] [$Mo(tfd)_3$] and its more soluble derivative molybdenum tris-[1-(methoxycarbonyl)-2 -(trifluoromethyl)ethane-1,2-dithiolene ($Mo(tfd\text{-}CO_2Me)_3$ have higher electron affinity at 5.6 eV and 5.0 eV, respectively, have been reportedly used as p-dopants for organic semiconductors[152-154] and graphene.[119] Even though $Mo(tfd\text{-}CO_2Me)_3$ is a weaker oxidant than $Mo(tfd)_3$, its better solubility allows more choices of processing methods.

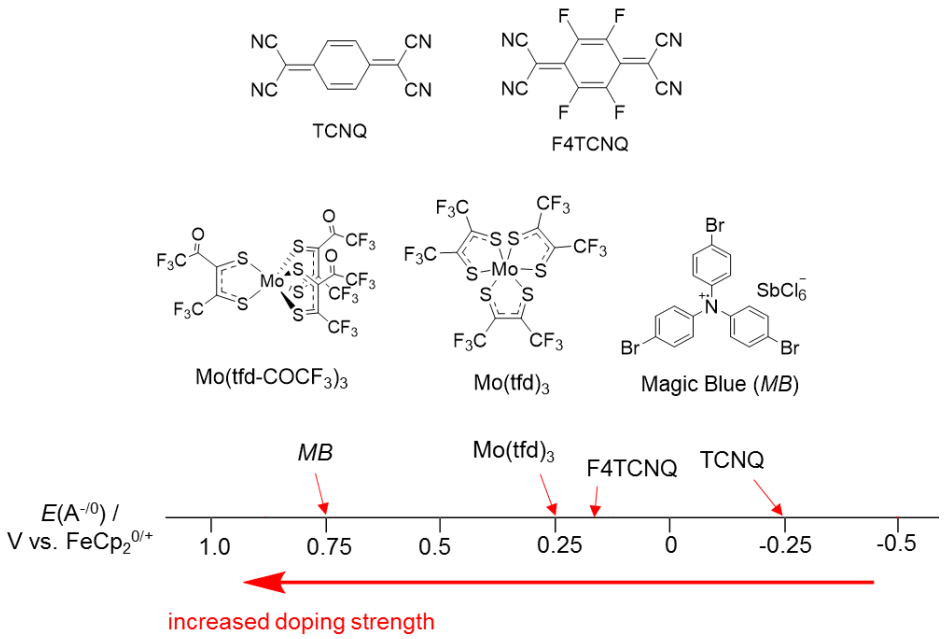

Figure 1.10 The chemical structures of some complexes used for p-doping and their reduction potentials.

Recently, the Marder group reported using the triarylaminium radical cation salt as p-dopant for 2D materials doping studies. Tris(4-bromophenyl) ammoniumyl hexachloroantimonate, which is colloquially known as *Magic Blue* because of its intense royal blue color, is a strong one-electron oxidant used widely in organic chemistry. Our recent work showed that it can be used as strong p-dopant for metal oxide,[155] graphene,[156] and MoS_2,[157] where the work function shifts as large as ca. 1 eV were observed.

1.3.2 Molecular mono- and few-layer modifiers

Interface modification with molecular mono- or multi-layers, and the deposition of ultrathin layers of atoms and compounds (sub-monolayer, monolayer and few-layer coverage) has been extensively researched.[158-160] In many applications, monolayer are preferred, because of their closely packed and well-aligned structures. A self-assembled layers (SAM) relies on a strong specific interaction between adsorbate and the substrate to drive the spontaneous formation of a monolayer film.[161] In flexible electronics, they are widely used to alter the wettability and to tune the work function of surfaces, such as gold, ITO, and ZnO. They can be formed spontaneously on the surface by being immersed in a dilute (ca. 1 mM) solution of the adsorbate for an interval varying from a few minutes to several days, depending on the system. SAMs typically consist of an anchor group, spacer, and functional end group as the tail. Each component of the SAM layer can be synthetically modified for the desired property, making it an attractive approach towards manipulating surfaces.

Other than the self-assembly molecules which are normally chemisorbed on the surface, an ultrathin layer of polymer or polymer precursors has also been widely used to modify the surface through the physisorption. Polymers containing aliphatic amine groups, such as polyethylenimine ethoxylated (PEIE) and branched polyethylenimine (PEI), have been used to lower the work function of various substrates, including metal oxides, metals, conducting polymers, and graphene,[162] with WFs decrease as large as 1 eV. More efficient electron injection (or extraction) was observed with improved device performance in FETs,[162] OLEDs,[163] OPVs,[164] and perovskite solar cells.[165] They also exhibit good thermal stability up to 190 °C, making them compatible with the processing of printed electronic devices on plastic substrates (typically at temperatures below 200 °C).

1.4 Application of dopants and modifiers in flexible electronics

1.4.1 Applications in organic electronics

Research on organic semiconductor thin films, such as organic light-emitting diode (OLEDs) and organic solar cells (OSCs), has been accelerated due to their potential for low cost and large area flexible devices. Key properties of these devices are charge transport through the thin films either from the contacts to the active layer or the reversed manner. Thus, the effective charge transport in the active layer and efficient charge injection are important.

In OLEDs, the doped charge transport layers undergo significant development. It has been shown that, regardless of the detailed configuration of the OLED devices, the doped transport layers can lead to superior power efficiency. For example, Xia *et al.* showed that the turn-on voltage of a simple bilayer structure can be reduced ca. 20 V through p-doping.[166] Given that, the organic molecules used in OLEDs are typically wide-gap materials, doping the same matrix with p- and n-doping would be challenging, since it requires one of the dopants to possess either a very high EA (p-dopant) or low IE (n-dopant). Thus, in many cases, heterojunctions are used where the relatively easily doped materials for p- and n-region can be chosen separately. Harada *et al.* reported the use of a homojunction p-i-n OLED with proper choice of dopants.[167] Moreover, it has been shown that ITO can be used as both anode and cathode in OLED when n-doped electron-injection layer is used,[168] which makes it possible to replace the relatively low work function electrode materials to solve the air-stability issues.

For solar cell applications, it has been found that low levels of p-doping applied

to the active layer of bulk-heterojunction polymer/PCBM system can increase the power conversion efficiency (PCE), mostly due to the increase in the short-circuit current.[169,170] Moreover, doping at the electron-collecting electrode of OPVs can increase the efficiency of electron collection. Schulze *et al.* showed that higher efficiency heterojunction solar cells can be achieved when embedded between a p-doped HTL on the anode side and aluminum on the cathode side, which is mainly caused by the higher field factor and open-circuit voltage.[171,172]

1.4.2 Applications in 2D materials

Graphene, a two-dimensional, one-atom-thick layer of sp^2-hybridized carbon, is a promising candidate for flexible transparent electrodes. As mentioned earlier, ITO is the dominant material used in transparent conductive films. However, ITO is brittle, degrades over time (particularly in touchscreens), and thus is not ideal for the use in flexible electronics applications. Graphene, on the hand, has remarkable conductivity. Moreover, its high transparency (97% percent for a single sheet of graphene), flexibility, low weight, and cheap raw material makes it very appealing to use as a transparent electrode.[173] Stable doping of graphene is needed to further reduce its sheet resistance, especially for larger area CVD-grown samples. In Chapter 3, doping of mono- and multi-layer graphene using various redox-active, solution-processible dopants is shown to decrease its sheet resistance and adjust its work function while maintaining transparency. Graphene is a zero-band-gap material, so doping is highly desired for inducing a gap in graphene for transistor applications. In bilayer graphene, the band structure is sensitive to the symmetry of the two layers. If the individual layers in bilayer

graphene are rendered inequivalent, then a gap opens.[174,175] It has been shown that the band structure near the Dirac point of bilayer graphene can be tuned by doping, where p-doped bilayer graphene can have a band gap as large as 0.43 eV.[176] A detailed literature review of graphene doping studies will be given in Chapter 3.

Unlike graphene, TMDCs offer a wide range of band gaps intrinsically, which makes these materials very attractive for a variety of device applications. Controlled doping can provide a powerful tool for modifying their electrical and optical properties, and for improving device performance. Alternatively, self-assembled monolayers or sub-monolayer can be applied to effectively dope overlying or underlying TMDCs layers. While chemical doping has been extensively used to modify graphene,[119,177] little has been done so far to apply these methods to TMDCs. In pioneering work, MoS_2 and WSe_2 flakes were n-doped using potassium,[178] but this method suffers from high reactivity of the dopant and diffusivity of the resulting ions. Recent studies have shown that the molecular air-sensitive reductant benzyl viologen[179] can also be used for surface n-doping of MoS_2. Cesium carbonate[180] and polyethyleneimine (PEI),[181] which are less obviously reductants, have also been reported to n-dope TMDCs. In Chapter 4, solution-processed n- and p-Doping of TMDCs with redox-active metal-organic species will be discussed.

1.5 Selected techniques commonly used for doping and surface modification studies

Chemical doping and surface modification of semiconductors, metals, metal oxide and 2D materials can be characterized by various techniques, such as

photoemission spectroscopy (PES), ultraviolet/visible spectroscopy, atomic-force microscopy (AFM), electrical transport measurement, transmission electron microscopy (TEM), scanning electron microscopy (SEM), contact angle measurements (CA), cyclic voltammetry measurements (CV), and so on. The binding mode between the modifier and the substrates may be elucidated by infrared spectroscopy, along with Raman. A brief introduction of some of these techniques is presented below, and throughout the remainder of this thesis.

1.5.1 Photoelectron spectroscopy

Core and valence-level photoelectron spectroscopy have widely used to study semiconductor heterojunctions and interfaces. Useful information such as the composition and electronic state of the surface region of a sample can be provided. Photoemission spectra measure the kinetic energies of electrons emitted from the sample, and are displayed in the binding energy relative to the Fermi edge of the sample. In general, the photoionization process to produce state *i* of the positive ion (M) can be described by the following expression:

Equation 1.2 $$I_i = h\nu + K_i$$

where I is the ionization energy.

Photoemission is commonly assumed to occur in a three-step process: 1) the incoming photons are absorbed by the electrons; 2) the electrons ejected by photons travel to the sample surface, during which process the majority of the generated electrons suffer inelastic collisions, and lose some of their kinetic energy; 3) the electrons are ejected into the vacuum, and their kinetic energies are measured by the

detector. In both XPS and UPS, the free electrons generated by the photoelectric effect have certain kinetic energy, depending on the exciting photon energy, *hv*, the work function of the sample, Φ_s, the binding energy, E_b, of the excited electron, and inelastic scattering processes in the sample. The photoemission spectra consist of two principal components: primary electrons, referring to electrons which do not suffer inelastic collisions; and secondary electrons, which represent those electrons that lose varying amounts of energy. In the photoemission spectra, primary electrons result in distinct spectral features and peaks which mirror the density of state (DOS) of the sample.

XPS with energy (*hv)* higher than 1000 eV (Al-Kα and Mg-Kα are commonly used source lines, with the energy of 1253.6 eV and 1486.6 eV, respectively) can reach core level. In XPS, the X-rays can penetrate a few microns into the sample, but only the signal from the top layers (ca. 10 nm) can be detected. These are collected by the spectrometer detector, which separates the electrons as a function of their kinetic energies. These kinetic energies, in turn, relate back to the orbital energies from which they originated. The intensities of the peaks allow one to determine the relative atomic concentrations near the interface. Given that the chemical environment changes the core orbital energies slightly, information on the functionalities present can be also be extracted. Detection limits as low as 0.1% atom concentrations can be achieved.[182]

UPS with lower photon energy, whose ionization sources are Ne I (16.6 eV), Ne II (26.8 eV) and He I (21.2 eV), He II (40.8 eV) can only ionize the valence states typically. In general, the boundary of the binding energy between the core levels and valence band states can be found around 10-15 eV, levels with higher BE mostly

represent the core level states, while levels with lower BE contains information about the valence orbitals.

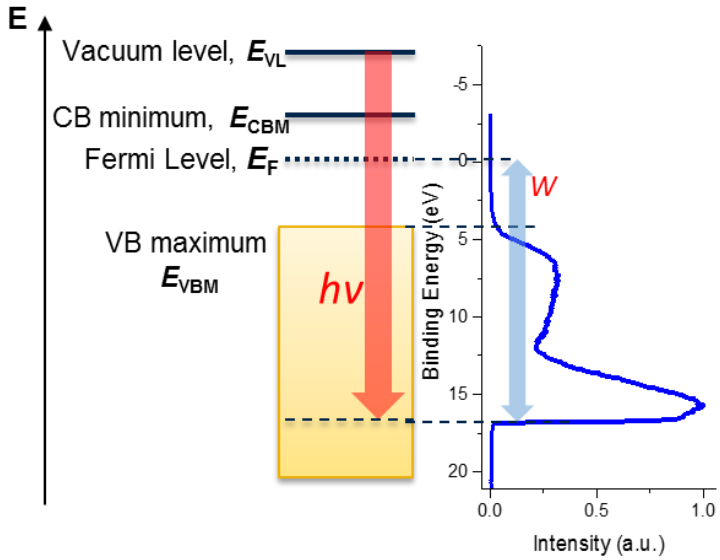

Figure 1.11 Schematic of photoemission spectroscopy process on semiconducting sample, with energy levels aligned with the UPS spectrum.

UPS can be used to determine the work function, which can be calculated by subtracting the width of the range for the emitted electron (W) (from the onset of the secondary electrons up to the Fermi edge) from the energy of the incident UV light, *hv*, as shown in Figure 1.11. The equation can be expressed as following:

Equation 1.3 $$\varphi_m = h\nu - W$$

The UPS spectra for a metal sample is straightforward, since there is DOS down to the Fermi level, and less straightforward in the case of organic molecules, or molecular film adsorbed on metal. There are several reasons: 1) charge transfer may exist at the interface, especially for the system of a strong acceptor molecule with a low work function substrate or a strong donor molecule with a high work function substrate, thus, interface dipole will be formed; 2) polarization of the electron cloud attracted by

the image charge formed in the metal may cause the redistribution of the electron cloud; 3) interfacial chemical reaction may exist. For example, for the UPS measurements of different thickness of pentacene on Hf, there is interfacial dipole at the interface between pentacene and Hf cause the vacuum level shifts.

1.5.2 Electrical transport measurement

In many device applications, the ultimate goal of doping and surface modification is to improve the electrical performance, such as charge-carrier mobility and/or conductivity. Doping in principle will passivate trap states at low doping concentration, thus improve the effective charge mobility. To determine charge carrier mobility in semiconductors, a number of methods have been employed, including field-effect transistors (FET), space-charge-limited-current (SCLC), time-of-flight (TOF) and charge extraction by linearly increasing voltage (CELIV).[183-186] It should be noted that carrier densities under which these techniques are carried out can be very different. For the content of this dissertation, FET, SCLC, and four-point probe method have been used to characterize the modified thin films of organic semiconductor, graphene, TMDCs, CNTs and silver nanowires. A very brief introduction is provided here, and the detailed calculation methods will be discussed in the corresponding chapters.

FET measures the film mobility parallel to the substrate plane, while SCLC and TOF characterize the mobility perpendicular to the substrate plane. FET uses an electric field to control the electrical conductivity of the channel in a semiconductor material. The applied gate voltage attracts or repels charge carriers to or from the interface between the semiconductor and dielectric layer, and between the source and drain

terminals. The density of these induced charge carriers can affect the conductivity of the film.[187] TOF is widely used to estimate the mobility of dielectric layers and organic semiconductors, in which the excess charges are generated by application of the laser or voltage pulse.[183,188] However, it normally requires several micron thick films, and it is often difficult to replicate the morphology of such thin films in devices, which are usually ~10 nm thick. As a consequence, the charge carrier mobility measured using TOF method with several microns thick films could be different than the actual mobility encountered with nanometer thick thin films used in a device. SCLC, on the other hand, does not require thicker films and involves a relatively simple experimental setup. The mobility in the SCLC regime is determined from the electrical characterization of a diode produced by sandwiching an organic layer of interest between two metal electrodes. The choice of electrodes is made in such a way that only quasi-unipolar (only positive or negative) charge carriers are injected into the active layer. The value of charge carrier mobility can be evaluated by the fitting of current density-voltage (*J-V*) curves in the SCLC region.[189,190]

The Van der Pauw technique is widely used in the semiconductor industry to determine the resistivity due to its convenience.[191,192] It can be used to determine the sheet carrier density and mobility of the majority carrier, by using the Hall-effect measurement. From this the charge density and doping level can be found. Other common methods of measuring thin film resistivity are by using either the two- or four-point probe method, with probes aligned linearly or in a square pattern which contacts the surface of the test material. Although the two-point probe method is capable of

calculating the surface resistivity, the four-point probe method is superior due to the use of two additional probes, which do not carry any current, are used to measure the voltage potential of the material surface.[193-195]

1.5.3 Cyclic voltammetry

Cyclic voltammetry (CV) is a commonly used technique to measure the oxidation and the reduction potentials of organic semiconductors and dopants, and from which the ionization energy and the electron affinity can be estimated. These potentials can give preliminary information about the dopant strength and the electrical doping process. n-Doping will occur if the reduction potential of the host materials is higher than the oxidation potential of the dopant in an electrolyte solution, assuming it is a simple one-electron redox process. Similarly, for p-doping, the oxidation potential of the host materials will need to be lower than the reduction potential of the dopant.

As shown in Figure 1.12, the setup of CV measurements consists of three-electrode electrochemical cell and a potentiostat. The potential across the cell is ramped linearly with time until a redox process of a given species in solution is observed as a change in current; then the potential ramp is reverted to observe the reversible redox reaction. The peak potentials are always referenced to a standard, typically ferrocene, which has a well-defined redox process. CV may also be used to analyze quality and thickness of monolayers using the same setup, where the surface-modified electrode serves as the working electrode. The properties of the working electrode effect the shape of the curve, peak potential separations and the currents registered. Compared with different monolayers and against the bare (unmodified) electrode, the charge transfer

rates through the monolayers can be determined.

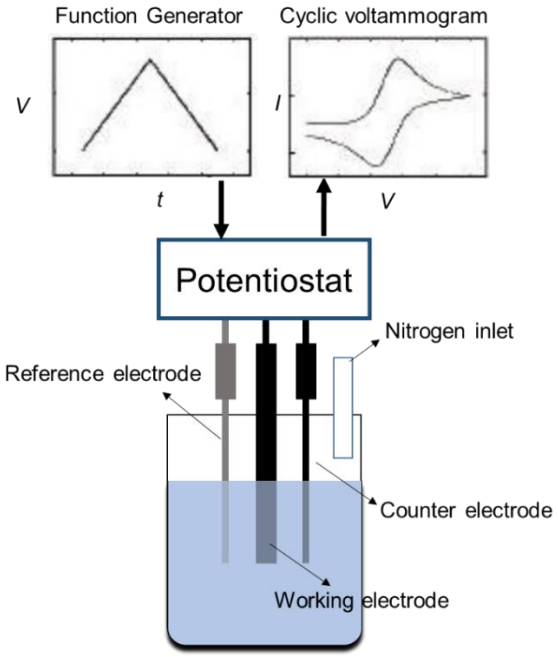

Figure 1.12 Example of an electrochemical cell. Desired potential is applied through working electrode, counter electrode balances the charges by passing the current required and reference electrode is used to measure and control the potential of working electrode. Modified from Paniagua-Barrantes with the permission.[196]

1.5.4 UV/vis/ NIR absorption spectroscopy

UV/vis/ NIR absorption spectroscopy can be a powerful tool to characterize the doping process. Absorption in the visible or near-infrared region is an important parameter for organic materials used in OPVs and OLEDs. For organic semiconductors, the radical cations (after p-doping) or anions (n-doping), also known as polarons, formed after doping are generally distinguishable features that may be separated from those of neutral species. By monitoring a featured peak using vis/NIR absorption spectroscopy, useful information such as doping ability and doping reaction rate can be extracted. For example, 6,13-bis(triisopropylsilylethynyl) pentacene (TIPSp) will form a featured peak at ~745 nm for the anion, and at 805 nm for the di-anion, which is well separated from the neutral peak at 635 nm. More detailed characterization by using the

UV/vis/ NIR absorption spectroscopy will be discussed in Chapter 2.

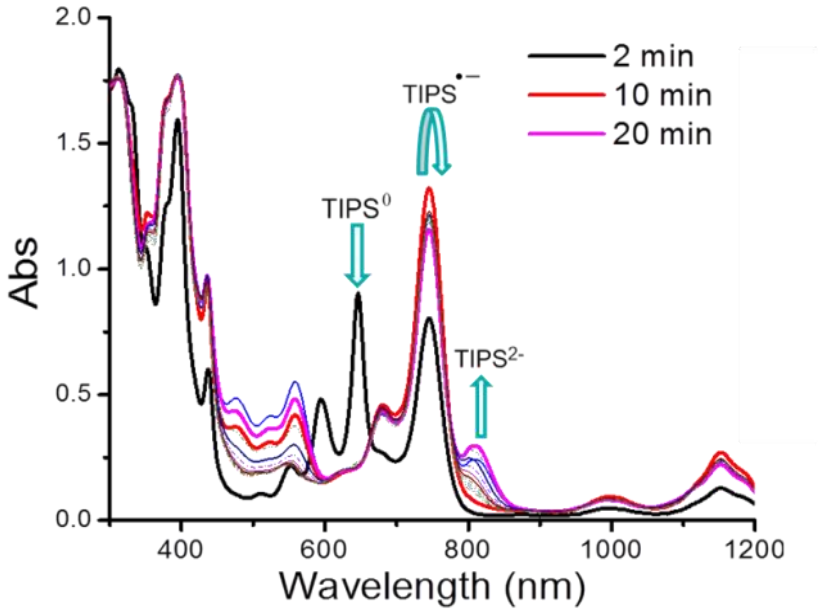

Figure 1.13 Vis/NIR absorption spectra of neutral TIPSp and its radical anion generated with n-dopant.

1.6 Thesis overview

The introduction and background information discussed previously in this chapter served to introduce the studies presented in this thesis. The work presented in this dissertation is focusing on design, synthesis, characterization of redox-active dopants in the applications of organic semiconductors, and 2D material based electronics. While all chapters are closely related to doping studies relevant to flexible electronics, each one is focusing on different aspects.

Chapter 2 focuses on the design and synthesis of new air-stable, solution- and vacuum-processible benzimidazolium dimers. $(DMBI)_2$ with different functional groups were synthesized. The doping studies were conducted on various organic semiconductors, and studied by XPS, UPS, ESR, PDS, and kinetics measurements.

These dimers exhibited a strong doping effect in a more diverse array of materials. It is shown that the choice of the substituents in these dimers has a significant influence on the kinetics of their reaction with acceptors.

Chapters 3 and 4 discuss the solution-processed n- and p-doping of large-area 2D materials with redox-active species. Chapter 3 shows that by applying molecular reductants and oxidants as the dopants, the work function of CVD graphene can be tuned from ca. 3 to 5 eV, and the sheet resistance of monolayer graphene can be reduced by more than 90 %. Doping studies of TMDCs, including molybdenum disulfide (MoS_2) and tungsten diselenide (WSe_2), are discussed in Chapter 4; these materials were characterized by electrical measurements, UPS, XPS, and Raman spectroscopy. The doping effects can be controlled through the choice of dopant, treatment time, and the concentration of dopant in solution.

In Chapter 5, doped graphene is applied as the electrode in organic field-effect transistors, diodes, and solar cells devices is presented, and the performance is comparable to, or even better than, that of similar devices with metal or metal-oxide electrodes. Work-function engineering of graphene electrode via doping was proven to be important in reducing the carrier injection barriers.

Chapter 6 summarizes the findings reported throughout the dissertation, their significance and broader impact. It concludes by putting forth a perspective on the field of doping and surface modification of flexible electronics and some of the challenges that need to be met.

1.7 References

(1) Crabb, R. L.; Treble, F. C. *Nature* **1967**, *213*, 1223.

(2) Ray, K. A. *IEEE Trans. Aerosp. Electron. Syst.* **1967**, *1*, 107.

(3) Wong, W. S.; Salleo, A. *Flexible electronics: materials and applications*; Springer Science & Business Media, 2009; Vol. 11.

(4) Rogers, J. A.; Someya, T.; Huang, Y. *Science* **2010**, *327*, 1603.

(5) Park, S.; Vosguerichian, M.; Bao, Z. *Nanoscale* **2013**, *5*, 1727.

(6) Akinwande, D.; Petrone, N.; Hone, J. *Nat. Commun.* **2014**, *5*.

(7) Etxebarria, I.; Ajuria, J.; Pacios, R. *Org. Electron.* **2015**, *19*, 34.

(8) Chang, H.-Y.; Yang, S.; Lee, J.; Tao, L.; Hwang, W.-S.; Jena, D.; Lu, N.; Akinwande, D. *ACS Nano* **2013**, *7*, 5446.

(9) Zhou, H.; Seo, J.-H.; Paskiewicz, D. M.; Zhu, Y.; Celler, G. K.; Voyles, P. M.; Zhou, W.; Lagally, M. G.; Ma, Z. *Sci. Rep.* **2013**, *3*, 1291.

(10) Snow, E. S.; Campbell, P. M.; Ancona, M. G.; Novak, J. P. *Appl. Phys. Lett.* **2005**, *86*, 033105.

(11) Defrance, N.; Lecourt, F.; Douvry, Y.; Lesecq, M.; Hoel, V.; Etangs-Levallois, A. L. D.; Cordier, Y.; Ebongue, A.; Jaeger, J. C. D. *IEEE Trans. Electron Devices* **2013**, *60*, 1054.

(12) Zhai, Y.; Mathew, L.; Rao, R.; Xu, D.; Banerjee, S. K. *Nano Lett.* **2012**, *12*, 5609.

(13) Kim, H.-S.; Won, S. M.; Ha, Y.-G.; Ahn, J.-H.; Facchetti, A.; Marks, T. J.; Rogers, J. A. *Appl. Phys. Lett.* **2009**, *95*, 183504.

(14) Li, Y. V.; Ramirez, J. I.; Sun, K. G.; Jackson, T. N. *IEEE Electron Device Lett.* **2013**, *34*, 891.

(15) Wei, C. Y.; Kuo, S. H.; Hung, Y. M.; Huang, W. C.; Adriyanto, F.; Wang, Y. H. *IEEE Electron Device Lett.* **2011**, *32*, 90.

(16) Sun, D.-m.; Timmermans, M. Y.; Tian, Y.; Nasibulin, A. G.; Kauppinen, E. I.; Kishimoto, S.; Mizutani, T.; Ohno, Y. *Nat. Nano.* **2011**, *6*, 156.

(17) Bao, W.; Cai, X.; Kim, D.; Sridhara, K.; Fuhrer, M. S. *Appl. Phys. Lett.* **2013**, *102*, 042104.

(18) Yoon, C.; Cho, G.; Kim, S. *IEEE Trans. Electron Devices* **2011**, *58*, 1096.

(19) Wang, C.; Chien, J.-C.; Fang, H.; Takei, K.; Nah, J.; Plis, E.; Krishna, S.; Niknejad, A. M.; Javey, A. *Nano Lett.* **2012**, *12*, 4140.

(20) Song, H. S.; Li, S. L.; Gao, L.; Xu, Y.; Ueno, K.; Tang, J.; Cheng, Y. B.; Tsukagoshi, K. *Nanoscale* **2013**, *5*, 9666.

(21) Petrone, N.; Meric, I.; Hone, J.; Shepard, K. L. *Nano Lett.* **2013**, *13*, 121.

(22) Nathan, A.; Ahnood, A.; Cole, M. T.; Lee, S.; Suzuki, Y.; Hiralal, P.; Bonaccorso, F.; Hasan, T.; Garcia-Gancedo, L.; Dyadyusha, A.; Haque, S.; Andrew, P.; Hofmann, S.; Moultrie, J.; Chu, D.; Flewitt, A. J.; Ferrari, A. C.; Kelly, M. J.; Robertson, J.; Amaratunga, G. A. J.; Milne, W. I. *Proc. IEEE* **2012**, *100*, 1486.

(23) Lee, J.; Ha, T.-J.; Li, H.; Parrish, K. N.; Holt, M.; Dodabalapur, A.; Ruoff, R. S.; Akinwande, D. *ACS Nano* **2013**, *7*, 7744.

(24) Watanabe, K.; Taniguchi, T.; Kanda, H. *Nat. Mater.* **2004**, *3*, 404.

(25) Lee, G.-H.; Yu, Y.-J.; Cui, X.; Petrone, N.; Lee, C.-H.; Choi, M. S.; Lee, D.-Y.; Lee, C.; Yoo, W. J.; Watanabe, K.; Taniguchi, T.; Nuckolls, C.; Kim, P.; Hone, J. *ACS Nano* **2013**, *7*, 7931.

(26) Liu, J.; Zhang, H.; Dong, H.; Meng, L.; Jiang, L.; Jiang, L.; Wang, Y.; Yu, J.; Sun, Y.; Hu, W. *Nat. Comm.* **2015**, *6*.

(27) Sekitani, T.; Zschieschang, U.; Klauk, H.; Someya, T. *Nat. Mater.* **2010**, *9*, 1015.

(28) Someya, T.; Kato, Y.; Sekitani, T.; Iba, S.; Noguchi, Y.; Murase, Y.; Kawaguchi, H.; Sakurai, T. *Proc. Natl. Acad. Sci. USA* **2005**, *102*, 12321.

(29) Gelinck, G. H.; Huitema, H. E. A.; van Veenendaal, E.; Cantatore, E.; Schrijnemakers, L.; van der Putten, J. B.; Geuns, T. C.; Beenhakkers, M.; Giesbers, J. B.; Huisman, B.-H. *Nat. Mater.* **2004**, *3*, 106.

(30) Menard, E.; Podzorov, V.; Hur, S. H.; Gaur, A.; Gershenson, M. E.; Rogers, J. A. *Adv. Mater.* **2004**, *16*, 2097.

(31) Takeya, J.; Yamagishi, M.; Tominari, Y.; Hirahara, R.; Nakazawa, Y.;

Nishikawa, T.; Kawase, T.; Shimoda, T.; Ogawa, S. *Appl. Phys. Lett.* **2007**, *90*, 102120.

(32) Sundar, V. C.; Zaumseil, J.; Podzorov, V.; Menard, E.; Willett, R. L.; Someya, T.; Gershenson, M. E.; Rogers, J. A. *Science* **2004**, *303*, 1644.

(33) Briseno, A. L.; Mannsfeld, S. C. B.; Ling, M. M.; Liu, S.; Tseng, R. J.; Reese, C.; Roberts, M. E.; Yang, Y.; Wudl, F.; Bao, Z. *Nature* **2006**, *444*, 913.

(34) Park, S. K.; Kim, Y. H.; Han, J. I.; Moon, D. G.; Kim, W. K. *IEEE Trans. Electron Devices* **2002**, *49*, 2008.

(35) Berggren, M.; Nilsson, D.; Robinson, N. D. *Nat. Mater.* **2007**, *6*, 3.

(36) Eder, F.; Klauk, H.; Halik, M.; Zschieschang, U.; Schmid, G.; Dehm, C. *Appl. Phys. Lett.* **2004**, *84*, 2673.

(37) Mach, P.; Rodriguez, S.; Nortrup, R.; Wiltzius, P.; Rogers, J. A. *Appl. Phys. Lett.* **2001**, *78*, 3592.

(38) Sheraw, C.; Zhou, L.; Huang, J.; Gundlach, D.; Jackson, T.; Kane, M.; Hill, I.; Hammond, M.; Campi, J.; Greening, B. *Appl. Phys. Lett.* **2002**, *80*, 1088.

(39) Liau, W.-L.; Lee, T.-H.; Chen, J.-T.; Hsu, C.-S. *J. Mater. Chem. C* **2016**, *4*, 2284.

(40) Shibata, M.; Sakai, Y.; Yokoyama, D. *J. Mater. Chem. C* **2015**, *3*, 11178.

(41) Kawamura, Y.; Goushi, K.; Brooks, J.; Brown, J. J.; Sasabe, H.; Adachi, C. *Appl. Phys. Lett.* **2005**, *86*, 71104.

(42) Rogers, J. A.; Bao, Z.; Baldwin, K.; Dodabalapur, A.; Crone, B.; Raju, V.; Kuck, V.; Katz, H.; Amundson, K.; Ewing, J. *Proc. Nat. Acad. Sci. USA* **2001**, *98*, 4835.

(43) Wang, Q. H.; Kalantar-Zadeh, K.; Kis, A.; Coleman, J. N.; Strano, M. S. *Nat. Nanotechnol.* **2012**, *7*, 699.

(44) Meric, I.; Dean, C. R.; Petrone, N.; Lei, W.; Hone, J.; Kim, P.; Shepard, K. L. *Proc. IEEE* **2013**, *101*, 1609.

(45) Schwierz, F. *Proc. IEEE* **2013**, *101*, 1567.

(46) Novoselov, K. S.; Geim, A. K.; Morozov, S. V.; Jiang, D.; Zhang, Y.; Dubonos, S. V.; Grigorieva, I. V.; Firsov, A. A. *Science* **2004**, *306*, 666.

(47) Ming-Wei, L.; Cheng, L.; Yiyang, Z.; Hyeun Joong, Y.; Mark Ming-Cheng, C.; Luis, A. A.; Nicholas, K.; Noppi, W.; Zhixian, Z. *Nanotechnology* **2011**, *22*, 265201.

(48) Li, X.; Wang, X.; Zhang, L.; Lee, S.; Dai, H. *Science* **2008**, *319*, 1229.

(49) Han, M. Y.; Özyilmaz, B.; Zhang, Y.; Kim, P. *Phys. Rev. Lett.* **2007**, *98*, 206805.

(50) Das, S.; Chen, H.-Y.; Penumatcha, A. V.; Appenzeller, J. *Nano Lett.* **2013**, *13*, 100.

(51) Geim, A. K.; Novoselov, K. S. *Nat. Mater.* **2007**, *6*, 183.

(52) Fang, H.; Chuang, S.; Chang, T. C.; Takei, K.; Takahashi, T.; Javey, A. *Nano Lett.* **2012**, *12*, 3788.

(53) Song, L.; Ci, L.; Lu, H.; Sorokin, P. B.; Jin, C.; Ni, J.; Kvashnin, A. G.; Kvashnin, D. G.; Lou, J.; Yakobson, B. I.; Ajayan, P. M. *Nano Lett.* **2010**, *10*, 3209.

(54) Vogt, P.; De Padova, P.; Quaresima, C.; Avila, J.; Frantzeskakis, E.; Asensio, M. C.; Resta, A.; Ealet, B.; Le Lay, G. *Phys. Rev. Lett.* **2012**, *108*, 155501.

(55) Li, X.; Mullen, J. T.; Jin, Z.; Borysenko, K. M.; Buongiorno Nardelli, M.; Kim, K. W. *Phys. Rev. B* **2013**, *87*, 115418.

(56) Butler, S. Z.; Hollen, S. M.; Cao, L.; Cui, Y.; Gupta, J. A.; Gutiérrez, H. R.; Heinz, T. F.; Hong, S. S.; Huang, J.; Ismach, A. F.; Johnston-Halperin, E.; Kuno, M.; Plashnitsa, V. V.; Robinson, R. D.; Ruoff, R. S.; Salahuddin, S.; Shan, J.; Shi, L.; Spencer, M. G.; Terrones, M.; Windl, W.; Goldberger, J. E. *ACS Nano* **2013**, *7*, 2898.

(57) Li, L.; Yu, Y.; Ye, G. J.; Ge, Q.; Ou, X.; Wu, H.; Feng, D.; Chen, X. H.; Zhang, Y. *Nat. Nano.* **2014**, *9*, 372.

(58) Wei, Q.; Peng, X. *Appl. Phys. Lett.* **2014**, *104*, 251915.

(59) Takenobu, T.; Takahashi, T.; Kanbara, T.; Tsukagoshi, K.; Aoyagi, Y.; Iwasa, Y. *Appl. Phys. Lett.* **2006**, *88*, 033511.

(60) Artukovic, E.; Kaempgen, M.; Hecht, D.; Roth, S.; Grüner, G. *Nano Lett.* **2005**, *5*, 757.

(61) Suganuma, K. *Introduction to printed electronics*; Springer Science & Business Media, 2014; Vol. 74.

(62) Waldrop, J. R.; Grant, R. W. *Physical Review Letters* **1979**, *43*, 1686.

(63) Horn, K. *Appl. Phys. A*, *51*, 289.

(64) Kittel, C. *Introduction to solid state physics*; Wiley, 2005.

(65) Li, S. S. *Semiconductor physical electronics*; Springer Science & Business Media, 2012.

(66) Hummel, R. E. *Electronic properties of materials*; Springer Science & Business Media, 2011.

(67) Arkhipov, V. I.; Heremans, P.; Emelianova, E. V.; Adriaenssens, G. J.; Bässler, H. *Appl. Phys. Lett.* **2003**, *82*, 3245.

(68) Braun, S.; Salaneck, W. R.; Fahlman, M. *Adv. Mater.* **2009**, *21*, 1450.

(69) Cahen, D.; Kahn, A.; Umbach, E. *Materials Today* **2005**, 32.

(70) Braun, S.; Osikowicz, W.; Wang, Y.; Salaneck, W. R. *Org. Electron.* **2007**, *8*, 14.

(71) Koch, N. *Chem. Phys. Chem.* **2007**, *8*, 1438.

(72) Hwang, J.; Wan, A.; Kahn, A. *Mater. Sci. Eng., R* **2009**, *64*, 1.

(73) Randon, J.; Blanc, P.; Paterson, R. *J. Membr. Sci.* **1995**, *98*, 119.

(74) Paniagua, S. A.; Hotchkiss, P. J.; Jones, S. C.; Marder, S. R.; Mudalige, A.; Marrikar, F. S.; Pemberton, J. E.; Armstrong, N. R. *J. Phys. Chem. C* **2008**, *112*, 7809.

(75) Hotchkiss, P. J.; Jones, S. C.; Paniagua, S. A.; Sharma, A.; Kippelen, B.; Armstrong, N. R.; Marder, S. R. *Acc. Chem. Res.* **2011**, *45*, 337.

(76) Lüssem, B.; Riede, M.; Leo, K. *Phys. Status Solidi (a)* **2013**, *210*, 9.

(77) Lüssem, B.; Riede, M.; Leo, K. *Phys Status Solidi* **2013**, *210*.

(78) Kahn, A.; Koch, N.; Gao, W. *J. Polym. Sci.* **2003**, *B41*, 2529.

(79) Kido, J.; Matsumoto, T. *Appl. Phys. Lett.* **1998**, *73*, 2866.

(80) Ivory, D.; Miller, G.; Sowa, J.; Shacklette, L.; Chance, R.; Baughman, R. *J. Chem. Phys.* **1979**, *71*, 1506.

(81) Bianchi, M.; Rienks, E.; Lizzit, S.; Baraldi, A.; Balog, R.; Hornekær, L.;

Hofmann, P. *Phys. Rev. B* **2010**, *81*, 041403.

(82) Helfrich, W.; Schneider, W. *Phys Rev Lett* **1965**, *14*.

(83) Parthasarathy, G.; Shen, C.; Kahn, A.; Forrest, S. *J. Appl. Phys.* **2001**, *89*, 4986.

(84) Chan, C. K.; Amy, F.; Zhang, Q.; Barlow, S.; Marder, S.; Kahn, A. *Chem. Phys. Lett.* **2006**, *431*, 67.

(85) Chan, C. K.; Zhao, W.; Barlow, S.; Marder, S.; Kahn, A. *Org. Electron.* **2008**, *9*, 575.

(86) Chan, C. K.; Kahn, A. *Appl. Phys. A* **2009**, *95*, 7.

(87) Harada, K.; Riede, M.; Leo, K.; Hild, O. R.; Elliott, C. M. *Phys. Rev. B* **2008**, *77*, 195212.

(88) Zhang, Y.; de Boer, B.; Blom, P. W. *Phys. Rev. B* **2010**, *81*, 085201.

(89) Menke, T.; Ray, D.; Meiss, J.; Leo, K.; Riede, M. *Appl. Phys. Lett.* **2012**, *100*, 093304.

(90) Barlow, S. In *MRS Conference* 2015.

(91) Chan, C. K.; Kim, E. G.; Brédas, J. L.; Kahn, A. *Adv Funct Mater* **2006**, *16*.

(92) Fenghong, L.; Ansgar, W.; Martin, P.; Karl, L.; Xianjie, L. *J. Phys. Chem. B* **2004**, *108*.

(93) Werner, A. G.; Li, F.; Harada, K.; Pfeiffer, M.; Fritz, T.; Leo, K. *Appl Phys Lett* **2003**, *82*.

(94) Peng, W.; Joon Hak, O.; Guifang, D.; Zhenan, B. *J Am Chem Soc* **2010**, *132*.

(95) Wei, P.; Menke, T.; Naab, B. D.; Leo, K.; Riede, M.; Bao, Z. *J. Am. Chem. Soc.* **2012**, *134*, 3999.

(96) Li, F.; Werner, A.; Pfeiffer, M.; Leo, K.; Liu, X. *J. Phys. Chem. B* **2004**, *108*.

(97) Peng, W.; Joon Hak, O.; Guifang, D.; Zhenan, B. *J. Am. Chem. Soc.* **2010**, *132*.

(98) Schlitz, R. A.; Brunetti, F. G.; Glaudell, A. M.; Miller, P. L.; Brady, M. A.; Takacs, C. J.; Hawker, C. J.; Chabinyc, M. L. *Adv. Mater.* **2014**, *26*, 2825.

(99) Naab, B. D.; Himmelberger, S.; Diao, Y.; Vandewal, K.; Wei, P.; Lussem, B.; Salleo, A.; Bao, Z. *Adv. Mater.* **2013**, *25*, 4663.

(100) Oh, J. H.; Wei, P.; Bao, Z. *Appl. Phys. Lett.* **2010**, *97*, 243305.

(101) Wei, P.; Liu, N.; Lee, H. R.; Adijanto, E.; Ci, L.; Naab, B. D.; Zhong, J. Q.; Park, J.; Chen, W.; Cui, Y. *Nano lett.* **2013**, *13*, 1890.

(102) Lu, M.; Nicolai, H. T.; Wetzelaer, G.-J. A.; Blom, P. W. *Appl. Phys. Lett.* **2011**, *99*, 173302.

(103) Naab, B.; Guo, S.; Olthof, S.; Evans, E.; Wei, P.; Millhauser, G.; Kahn, A.; Barlow, S.; Marder, S.; Bao, Z. *J. Am. Chem. Soc.* **2013**, *135*, 15018.

(104) Guo, S.; Mohapatra, S.; Romanov, A.; Timofeeva, T.; Hardcastle, K.; Yesudas, K.; Risko, C.; Brédas, J.-L.; Marder, S.; Barlow, S. *Chem Eur J* **2012**, *18*, 14760.

(105) Guo, S.; Kim, S.; Mohapatra, S.; Qi, Y.; Sajoto, T.; Kahn, A.; Marder, S.; Barlow, S. *Adv Mater* **2012**, *24*, 699.

(106) Naab, B. D.; Guo, S.; Olthof, S.; Evans, E. G. B.; Wei, P.; Millhauser, G. L.; Kahn, A.; Barlow, S.; Marder, S. R.; Bao, Z. *J Am Chem Soc* **2013**, *135*, 15018.

(107) Fischer, E. O.; Wawersik, H. *J. Org. Chem.* **1966**, *5*, 559.

(108) El Murr, N.; Sheats, J. E.; Geiger Jr, W. E.; Holloway, J. D. *Inorg. Chem.* **1979**, *18*, 1443.

(109) Gusev, O. V.; Denisovich, L. I.; Peterleitner, M. G.; Rubezhov, A. Z.; Ustynyuk, N. A.; Maitlis, P. M. *J. Organomet. Chem.* **1993**, *452*, 219.

(110) Gusev, O. V.; Peterleitner, M. G.; Ievlev, M. A.; Kal'sin, A. M.; Petrovskii, P. V.; Denisovich, L. I.; Ustynyuk, N. A. *J. Organomet. Chem.* **1997**, *531*, 95.

(111) Nesmeyanov, A.; Vol'Kenau, N.; Petrakova, V. *J. Organomet. Chem.* **1977**, *136*, 363.

(112) Hamon, J. R.; Astruc, D.; Michaud, P. *J. Am. Chem. Soc.* **1981**, *103*, 758.

(113) Gusev, O. V.; Ievlev, M. A.; Peterleitner, M. G.; Peregudova, S. M.; Denisovich, L. I.; Petrovskii, P. V.; Ustynyuk, N. A. *J. Organomet. Chem.* **1997**, *534*, 57.

(114) Gusev, O. V.; Ievlev, M. A.; Tat'yana, A. P.; Peterleitner, M. G.; Petrovskii, P. V.; Oprunenko, Y. F.; Ustynyuk, N. A. *J. Organomet. Chem.* **1998**, *551*, 93.

(115) Guo, S.; Mohapatra, S.; Romanov, A.; Timofeeva, T.; Hardcastle, K.; Yesudas, K.; Risko, C.; Brédas, J.-L.; Marder, S.; Barlow, S. *Chem. Eur. J.* **2012**, *18*, 14760.

(116) Qi, Y.; Mohapatra, S. K.; Bok Kim, S.; Barlow, S.; Marder, S. R.; Kahn, A. *Appl. Phys. Lett.* **2012**, *100*, 083305.

(117) Higgins, A.; Mohapatra, S. K.; Barlow, S.; Marder, S. R.; Kahn, A. *Appl. Phys. Lett.* **2015**, *106*, 163301.

(118) Singh, S.; Mohapatra, S. K.; Sharma, A.; Fuentes-Hernandez, C.; Barlow, S.; Marder, S. R.; Kippelen, B. *Appl. Phys. Lett.* **2013**, *102*, 153303.

(119) Paniagua, S. A.; Baltazar, J.; Sojoudi, H.; Mohapatra, S. K.; Zhang, S.; Henderson, C. L.; Graham, S.; Barlow, S.; Marder, S. R. *Mater. Horiz.* **2014**, *1*, 111.

(120) Chiang, C. K.; Fincher Jr, C.; Park, Y. W.; Heeger, A. J.; Shirakawa, H.; Louis, E. J.; Gau, S. C.; MacDiarmid, A. G. *Phys. Rev. Lett.* **1977**, *39*, 1098.

(121) Schön, J.; Kloc, C.; Bucher, E.; Batlogg, B. *Nature* **2000**, *403*, 408.

(122) Pfeiffer, M.; Leo, K.; Zhou, X.; Huang, J.; Hofmann, M.; Werner, A.; Blochwitz-Nimoth, J. *Org. Electron.* **2003**, *4*, 89.

(123) Poh, H. L.; Šimek, P.; Sofer, Z.; Pumera, M. *Chem. Eur. J.* **2013**, *19*, 2655.

(124) Tongay, S.; Hwang, J.; Tanner, D.; Pal, H.; Maslov, D.; Hebard, A. *Phys. Rev. B* **2010**, *81*, 115428.

(125) Jhi, S.-H.; Louie, S. G.; Cohen, M. L. *Solid State Commun.* **2002**, *123*, 495.

(126) David, S. H.; Amy, M. H.; Roland, L.; Liangbing, H.; Bryon, M.; Chad, C.; Steven, R. *Nanotechnology* **2011**, *22*, 075201.

(127) Tenent, R. C.; Barnes, T. M.; Bergeson, J. D.; Ferguson, A. J.; To, B.; Gedvilas, L. M.; Heben, M. J.; Blackburn, J. L. *Adv. Mater.* **2009**, *21*, 3210.

(128) Dettlaff-Weglikowska, U.; Skákalová, V.; Graupner, R.; Jhang, S. H.; Kim, B. H.; Lee, H. J.; Ley, L.; Park, Y. W.; Berber, S.; Tománek, D.; Roth, S. *J. Am. Chem. Soc.* **2005**, *127*, 5125.

(129) De Blauwe, K.; Kramberger, C.; Plank, W.; Kataura, H.; Pichler, T. *Phys. Status Solidi* **2009**, *246*, 2732.

(130) Kim, S. M.; Kim, K. K.; Jo, Y. W.; Park, M. H.; Chae, S. J.; Duong, D. L.; Yang, C. W.; Kong, J.; Lee, Y. H. *ACS Nano* **2011**, *5*, 1236.

(131) Kröger, M.; Hamwi, S.; Meyer, J.; Riedl, T.; Kowalsky, W.; Kahn, A. *Org. Electron.* **2009**, *10*, 932.

(132) Hellstrom, S. L.; Vosgueritchian, M.; Stoltenberg, R. M.; Irfan, I.; Hammock, M.; Wang, Y. B.; Jia, C.; Guo, X.; Gao, Y.; Bao, Z. *Nano Lett.* **2012**, *12*, 3574.

(133) Esconjauregui, S.; D'Arsié, L.; Guo, Y.; Yang, J.; Sugime, H.; Caneva, S.; Cepek, C.; Robertson, J. *ACS Nano* **2015**, *9*, 10422.

(134) Xie, L.; Wang, X.; Mao, H.; Wang, R.; Ding, M.; Wang, Y.; Özyilmaz, B.; Loh, K. P.; Wee, A. T.; Chen, W. *Appl. Phys. Lett.* **2011**, *99*, 012112.

(135) Choi, M. S.; Qu, D.; Lee, D.; Liu, X.; Watanabe, K.; Taniguchi, T.; Yoo, W. J. *ACS Nano* **2014**, *8*, 9332.

(136) Jiang, W.; Jianhua, H.; Yanxiang, C.; Zhiyuan, X.; Lixiang, W. *Semicond. Sci. Technol.* **2007**, *22*, 824.

(137) Li, J.; Yahiro, M.; Ishida, K.; Yamada, H.; Matsushige, K. *Synth. Met.* **2005**, *151*, 141.

(138) Xiuling, Z.; Jiaxin, S.; Xiaoming, Y.; Man, W.; Hoi-Sing, K. *Jpn. J. Appl. Phys.* **2007**, *46*, 1033.

(139) Chen, L.-M.; Hong, Z.; Li, G.; Yang, Y. *Adv. Mater.* **2009**, *21*, 1434.

(140) Chih-Wei, C.; Sheng-Han, L.; Chieh-Wei, C.; Shrotriya, V.; Yang, Y. *Appl. Phys. Lett.* **2005**, *87*, 193508.

(141) Meyer, J.; Hamwi, S.; Kröger, M.; Kowalsky, W.; Riedl, T.; Kahn, A. *Adv. Mater.* **2012**, *24*, 5408.

(142) Kanai, K.; Akaike, K.; Koyasu, K.; Sakai, K.; Nishi, T.; Kamizuru, Y.; Nishi, T.; Ouchi, Y.; Seki, K. *Appl. Phys. A* **2009**, *95*, 309.

(143) Kivala, M.; Boudon, C.; Gisselbrecht, J.-P.; Enko, B.; Seiler, P.; Müller, I. B.; Langer, N.; Jarowski, P. D.; Gescheidt, G.; Diederich, F. *Chem. Eur. J.* **2009**, *15*,

4111.

(144) Blochwitz, J.; Fritz, T.; Pfeiffer, M.; Leo, K.; Alloway, D.; Lee, P.; Armstrong, N. *Org. Electron.* **2001**, *2*, 97.

(145) Nollau, A.; Pfeiffer, M.; Fritz, T.; Leo, K. *J. Appl. Phys.* **2000**, *87*, 4340.

(146) Maennig, B.; Pfeiffer, M.; Nollau, A.; Zhou, X.; Leo, K.; Simon, P. *Phys. Rev. B* **2001**, *64*, 195208.

(147) Gao, Z. Q.; Mi, B. X.; Xu, G. Z.; Wan, Y. Q.; Gong, M. L.; Cheah, K. W.; Chen, C. H. *Chem. Commun.* **2008**, 117.

(148) Walter, A. L.; Jeon, K.-J.; Bostwick, A.; Speck, F.; Ostler, M.; Seyller, T.; Moreschini, L.; Kim, Y. S.; Chang, Y. J.; Horn, K. *Appl. Phys. Lett.* **2011**, *98*, 184102.

(149) Loh, K. P.; Bao, Q.; Ang, P. K.; Yang, J. *J. Mater. Chem.* **2010**, *20*, 2277.

(150) Hosaka, H.; Kawashima, N.; Meguro, K. *Bull. Chem. Soc. Jpn.* **1972**, *45*, 3371.

(151) Hosaka, H.; Fujiwara, T.; Meguro, K. *Bull. Chem. Soc. Jpn.* **1971**, *44*, 2616.

(152) Qi, Y.; Sajoto, T.; Barlow, S.; Kim, E.-G.; Brédas, J.-L.; Marder, S. R.; Kahn, A. *J. Am. Chem. Soc.* **2009**, *131*, 12530.

(153) Qi, Y.; Sajoto, T.; Kröger, M.; Kandabarow, A. M.; Park, W.; Barlow, S.; Kim, E.-G.; Wielunski, L.; Feldman, L. C.; Bartynski, R. A.; Brédas, J.-L.; Marder, S. R.; Kahn, A. *Chem. Mater.* **2010**, *22*, 524.

(154) Dai, A.; Zhou, Y.; Shu, A. L.; Mohapatra, S. K.; Wang, H.; Fuentes-Hernandez, C.; Zhang, Y.; Barlow, S.; Loo, Y.-L.; Marder, S. R.; Kippelen, B.; Kahn, A. *Adv. Funct. Mater.* **2014**, *24*, 2197.

(155) Giordano, A. J. *Ph.D. Thesis, Georgia Institute of Technology* **2014**.

(156) Chang, Y.-C.; Liu, C.-H.; Liu, C.-H.; Zhang, S.; Marder, S. R.; Narimanov, E. E.; Zhong, Z.; Norris, T. B. *Nat. Commun.* **2016**, *7*.

(157) Tarasov, A.; Zhang, S.; Tsai, M.-Y.; Campbell, P. M.; Graham, S.; Barlow, S.; Marder, S. R.; Vogel, E. M. *Adv. Mater.* **2015**, *27*, 1175.

(158) Wink, T.; J. van Zuilen, S.; Bult, A.; P. van Bennekom, W. *Analyst* **1997**,

122, 43R.

(159) Frank, S. *J. Phys. Condens. Matter* **2004**, *16*, R881.

(160) Jadhav, S. A. *Cent. Eur. J. Chem.* **2011**, *9*, 369.

(161) Zisman, W. A. In *Contact Angle, Wettability, and Adhesion* 1964; Vol. 43, p 1.

(162) Zhou, Y.; Fuentes-Hernandez, C.; Shim, J.; Meyer, J.; Giordano, A. J.; Li, H.; Winget, P.; Papadopoulos, T.; Cheun, H.; Kim, J.; Fenoll, M.; Dindar, A.; Haske, W.; Najafabadi, E.; Khan, T. M.; Sojoudi, H.; Barlow, S.; Graham, S.; Brédas, J.-L.; Marder, S. R.; Kahn, A.; Kippelen, B. *Science* **2012**, *336*, 327.

(163) Höfle, S.; Schienle, A.; Bruns, M.; Lemmer, U.; Colsmann, A. *Adv. Mater.* **2014**, *26*, 2750.

(164) Kyaw, A. K. K.; Wang, D. H.; Gupta, V.; Zhang, J.; Chand, S.; Bazan, G. C.; Heeger, A. J. *Adv. Mater.* **2013**, *25*, 2397.

(165) Zhou, H.; Chen, Q.; Li, G.; Luo, S.; Song, T.-b.; Duan, H.-S.; Hong, Z.; You, J.; Liu, Y.; Yang, Y. *Science* **2014**, *345*, 542.

(166) Zhou, X.; Blochwitz, J.; Pfeiffer, M.; Nollau, A.; Fritz, T.; Leo, K. *Adv. Funct. Mater.* **2001**, *11*, 310.

(167) Harada, K.; Werner, A.; Pfeiffer, M.; Bloom, C.; Elliott, C.; Leo, K. *Phys. Rev. Lett.* **2005**, *94*, 036601.

(168) Pfeiffer, M.; Forrest, S. R.; Zhou, X.; Leo, K. *Org. Electron.* **2003**, *4*, 21.

(169) Yuan, Z.; Huiqiong, Z.; Jason, S.; Lei, Y.; Alexander, M.; Alan, J. H.; Guillermo, C. B.; Thuc-Quyen, N. *Adv. Mater.* **2013**, *25*.

(170) Veysel Tunc, A.; De Sio, A.; Riedel, D.; Deschler, F.; Da Como, E.; Parisi, J.; von Hauff, E. *Org. Electron.* **2012**, *13*, 290.

(171) Schulze, K.; Uhrich, C.; Schüppel, R.; Leo, K.; Pfeiffer, M.; Brier, E.; Reinold, E.; Baeuerle, P. *Adv. Mater.* **2006**, *18*, 2872.

(172) Schulze, K.; Uhrich, C.; Schüppel, R.; Leo, K.; Pfeiffer, M.; Brier, E.; Reinold, E.; Bäuerle, P. In *Photonics Europe*; International Society for Optics and Photonics: 2006, p 61920C.

(173) Jo, G.; Choe, M.; Lee, S.; Park, W.; Kahng, Y. H.; Lee, T. *Nanotechnology* **2012**, *23*, 112001.

(174) Ohta, T.; Bostwick, A.; Seyller, T.; Horn, K.; Rotenberg, E. *Science* **2006**, *313*, 951.

(175) Castro, E. V.; Novoselov, K.; Morozov, S.; Peres, N.; Dos Santos, J. L.; Nilsson, J.; Guinea, F.; Geim, A.; Neto, A. C. *Phys. Rev. Lett.* **2007**, *99*, 216802.

(176) Denis, P. A. *Chem. Phys. Lett.* **2010**, *492*, 251.

(177) Maiti, U. N.; Lee, W. J.; Lee, J. M.; Oh, Y.; Kim, J. Y.; Kim, J. E.; Shim, J.; Han, T. H.; Kim, S. O. *Adv. Mater.* **2014**, *26*, 40.

(178) Fang, H.; Tosun, M.; Seol, G.; Chang, T. C.; Takei, K.; Guo, J.; Javey, A. *Nano Lett* **2013**, *13*, 1991.

(179) Kiriya, D.; Tosun, M.; Zhao, P.; Kang, J. S.; Javey, A. *J. Am. Chem. Soc.* **2014**, *136*, 7853.

(180) Lin, J. D.; Han, C.; Wang, F.; Wang, R.; Xiang, D.; Qin, S.; Zhang, X.-A.; Wang, L.; Zhang, H.; Wee, A. T. S.; Chen, W. *ACS Nano* **2014**, *8*, 5323.

(181) Du, Y.; Liu, H.; Neal, A. T.; Si, M.; Ye, P. D. *IEEE Electron Device Lett.* **2013**, *34*, 1328.

(182) Brune, D.; Hellborg, R.; Whitlow, H. J.; Hunderi, O. *Surface characterization: a user's sourcebook*; John Wiley & Sons, 2008.

(183) Haber, K. S.; Albrecht, A. C. *J. Phys. Chem.* **1984**, *88*, 6025.

(184) Horowitz, G.; Hajlaoui, R.; Fichou, D.; El Kassmi, A. *J. Appl. Phys.* **1999**, *85*, 3202.

(185) Spear, W. E. *J. Non-Cryst. Solids* **1969**, *1*, 197.

(186) Juška, G.; Genevičius, K.; Sliaužys, G.; Pivrikas, A.; Scharber, M.; Österbacka, R. *J. Appl. Phys.* **2007**, *101*, 114505.

(187) Kepler, R. *Phys. Rev.* **1960**, *119*, 1226.

(188) Lee, B. H.; Lopez-Hilfiker, F. D.; Mohr, C.; Kurtén, T.; Worsnop, D. R.; Thornton, J. A. *Environ. Sci. Technol.* **2014**, *48*, 6309.

(189) Rose, A. *Phys. Rev.* **1955**, *97*, 1538.

(190) Murgatroyd, P. *J. Phys. D: Appl. Phys.* **1970**, *3*, 151.

(191) Bartels, A.; Peiner, E.; Schlachetzki, A. *Rev. Sci. Instrum.* **1995**, *66*, 4271.

(192) Sun, Y.; Shi, J.; Meng, Q. *Semicond. Sci. Technol.* **1996**, *11*, 805.

(193) Sze, S. M.; Ng, K. K. *Physics of semiconductor devices*; John wiley & sons, 2006.

(194) Schroder, D. K. *Semiconductor material and device characterization*; John Wiley & Sons, 2006.

(195) Runyan, W. R.; Shaffner, T. J. *Semiconductor measurements and instrumentation*; McGraw Hill Professional, 1998.

(196) Paniagua-Barrantes, S. *Ph.D. Thesis, Georgia Institute of Technology* **2013**.

CHAPTER 2 Synthesis and Characterization of Solution- and Vacuum- Processable Benzimidazole-based Dimer Dopants

2.1 Air-stable n-type dopants

Dopants are divided into the n-type or p-type category based on their ability to donate or accept an electron respectively. For an n-dopant, a low ionization energy is usually required for effective electron transfer to a wide variety of acceptors, especially those typically used in organic semiconductors, for which EAs range from ca. 2 eV to 4 eV (for OLED and OFET, respectively).[1,2] Thus, it is quite challenging to design a dopant has both strong reductant strength and reasonable air stability.[3] Early work on the n-doping of organic semiconductors focused mainly on the alkali and alkaline earth metals, but their highly reactive nature, as well as the high diffusivity of the corresponding ions, have limited their applications.[4,5] For reductants having oxidation potentials lower than the reduction potential of oxygen, the high energy reductant must be 'stored' in a precursor if air stability is to be maintained, where the low reactivity precursor can be triggered to release a more highly reactive material upon exposure to an external stimulus.[6,7] As shown in Figure 2.1, examples of these air-stable precursor molecular n-dopants include: 1) cationic organic salts, such as crystal violet (CV), tetrabutylammonium salts (F^-, Br^-, I^-, OH^-, or AcO^- as the counter anions) and benzimidazolium iodide salts (DMBI-I);[7-9] 2) neutral hydride donor molecules, including leucocrystal violet (LCV) and 2,3-dihydro-1H-benzimidazole (DMBI-H), with strongly donating groups neighboring, for which the stable cation could form after losing a hydrogen atom and an electron;[7,10] and 3) dimers of highly reducing neutral

radicals. Dopants based on dimers of various 19-electron sandwich compounds, and organic radicals including those obtained by reduction of imidazolium and pyridinium species, have been reported in the patent literature. [11,12,13,14]

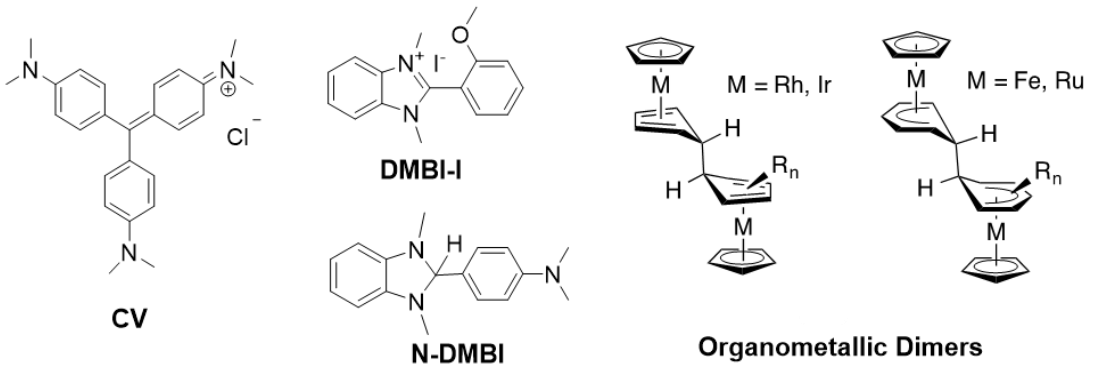

Figure 2.1 Strategies for air-stable n-type dopants.

However, the detailed mechanism studies showed that the first two cases will lead to the formation of side products, which may disrupt the conjugation of host materials and degrade the device performance. As described in Figure 2.2, cationic salt dopants (D^+X^-), such as CV and DMBI-I, will release unidentified reactive intermediates during the high-temperature thermal deposition process; in tetrabutylammonium salts doping process, fluoride or hydroxide acts as the nucleophile followed by electron transfer to another fullerene molecule.[15] The doping reaction between the neutral hydride dopants (D-H) and the acceptor is necessarily accompanied by hydride or hydrogen atom transfer.[8,10] Thus, even though n-doping using these salts and neutral hydride donor molecules has the advantages of using inexpensive materials that could be air-stable, the formation of side products during the doping process will typically be undesirable, and thus leaves room for improved dopants. For example, the reaction of D_2 and A can, in principle, proceed to form only D^+ and $A^{\bullet-}$ without side product (Figure 2.2).[12,16] The Marder group investigated several dimers of nineteen-

electron sandwich complexes as n-dopants.[11,16,17] They are moderately air-stable, and applicable to both vacuum and solution processing.

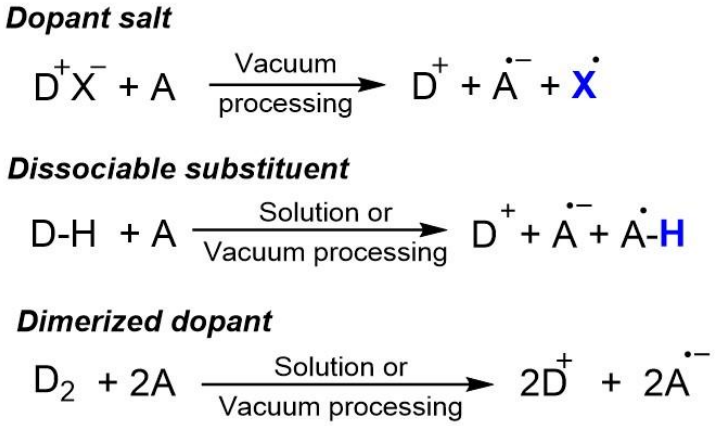

Figure 2.2 Doping behaviors of the air-stable n-type dopants.

This chapter describes the design, synthesis and characterization of DMBI based dimers with 2-metallocenyl substituents, which were formed from the neutral benzimidazoline-radicals. DMBI dimer with 2-alkyl substituent was synthesized by Dr. Ben Naab at Stanford University, and some results were also included here for comparison. All new DMBI dimers are moderately air-stable in the solid state, and can dope a variety of organic semiconductors, including fullerenes derivatives, perylene diimides, and bis(triisopropylsilyl)pentacene to form the corresponding radical anions and monomeric benzimidazolium cations. The doping behavior and mechanisms of these dimers and analogous monomeric hydrobenzoimidazole molecules (2-Y-DMBI-H) have been studied systematically in organic semiconductors, and will be discussed in this chapter. They have also been used to dope 2D materials, including graphene and MoS_2, which will be discussed in Chapter 3 and 4, respectively. The $(2\text{-Y-DMBI})_2$ dimers prove to be effective dopants for a variety of vapor- and solution-processed materials.[18]

2.2 Synthesis and characterization of benzimidazole-based monomer and dimer dopants

2.2.1 Design and synthesis

The synthetic route to the DMBI-based dopants is presented in Figure 2.3, and detailed procedures are provided in the Experimental Section (on Page 84). Benzimidazole-based monomers (DMBI-H) were synthesized from *N*,*N*'-dimethyl-*o*-phenylenediamine and metallocene (or alkyl) aldehyde, following the procedures from the literature.[19] Then, the hydride in Y-DMBI-H species was abstracted by triphenylmethyl hexafluorophosphate, forming Y-DMBI$^+$ cation. The cations can also be synthesized from acyl chloride and phenylenediamine as an alternative route. DMBI dimers were obtained through reduction of salts of the corresponding Y-DMBI$^+$ cations in THF using either 1 wt% Na-Hg or 25 wt% Na-K as the reducing reagent for 2 hours at room temperature. The Na-K reductions are faster, higher yielding, and can avoid the use of large quantities of mercury, but careful handling is required due to the highly pyrophoric nature of Na-K. As shown in Figure 2.3, the corresponding amides were obtained as side products when the Y-DMBI$^+$ salt is poorly soluble in THF: reduction of the poorly soluble PF_6^- or BPh_4^- salts of 2-Fc-DMBI$^+$ and 2-Rc-DMBI$^+$ affords amide to dimer ratios as large as 1:1, whereas the more soluble 2-Cyc-DMBI$^+$PF6$^-$ gives a ratio of ca. 1:10. No detectable side-products were formed on the reduction of the highly soluble tetrakis(3,5- bis(trifluoromethyl)phenyl)borate salts of 2-Fc-DMBI$^+$ and 2-Rc-DMBI$^+$. Detailed synthesis schemes for DMBI salts are provided in the Experimental Section on page 84.

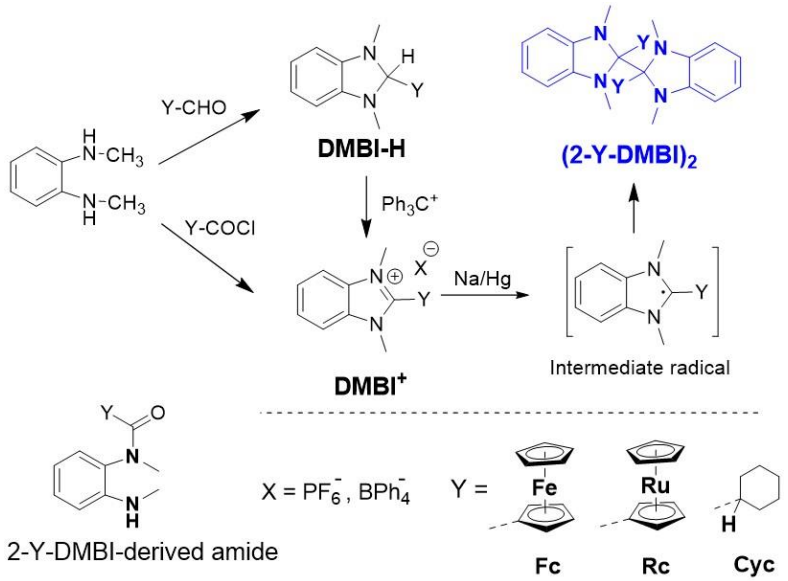

Figure 2.3 Synthetic route for benzimidazole-based dimer and monomer dopants.

2.2.2 Characterization of the DMBI dimeric dopants

2.2.2.1 Stability test

The three $(DMBI)_2$ compounds are reasonably stable in air as solids relative to other highly reducing compounds such as decamethylcobaltocene or $W_2(hpp)_4$, but decompose in solution on exposure to air. As the evidence, elemental analysis of the dimers after one week of storage in the air provided no evidence for decomposition, but ^1H NMR taken after the dimers were stored for 3 months in ambient conditions indicated ~5 mol% conversion to a decomposition product. Deoxygenated solutions of dimers show no decomposition, but all of the dimers decompose in non-deoxygenated solvents. As shown in Figure 2.4, in benzene-d_6 the decomposition of $(2\text{-Fc-DMBI})_2$ starts after 30 min, which is somewhat more rapidly than that of rhodocene and RuCp*(arene) dimers.[11] In contrast to organometallic dimers, such as $(RhCpCp^*)_2$ shown in Figure 2.1, which give the corresponding 18-electron cationic sandwich compounds, the DMBI dimers are quantitatively converted to the same amide species that are encountered as side-products in their syntheses (shown in Figure 2.3). The

moderate air-stability of the (Y-DMBI)$_2$ solids can be beneficial for weighing and handling compounds in the air; however, it is important to recognize that the air sensitivity of an n-doped thin film is more dependent on the host material EA than the dopant properties.

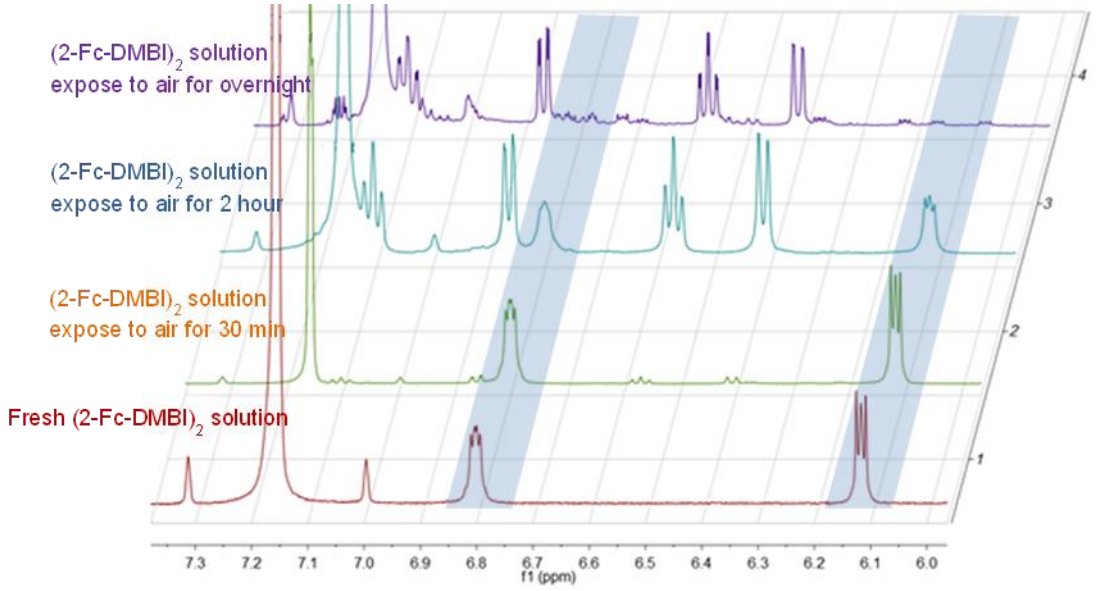

Figure 2.4 ^{1}H NMR spectra of (2-Fc-DMBI)$_2$ in C_6D_6 before and after exposure to air.

2.2.2.2 NMR spectroscopy of DMBI-based dopants

In the 400 MHz ^{1}H NMR spectra of all three dimers in benzene-d_6, the resonance assigned to the *N*-methyl group is broad at room temperature, but sharpens at high temperature, as shown in Figure 2.5. This observation is presumably due to restricted rotation around the central DMBI–DMBI bond or the DMBI–Y bond. As shown in the conformer found in the crystal structure of (2-Fc-DMBI)$_2$ (Figure 2.6 on Page 56), the two DMBI moieties are equivalent, but within each DMBI the two NMe groups are inequivalent. At room temperature, the rate of interconversion of two such conformers through rotation about the Fc–DMBI bond were relatively slow due to steric hindrance, thus, the peak for the *N*-methyl group is broad. Elevated temperature will

accelerate this rotation, and the two *N*-methyl groups become equivalent.

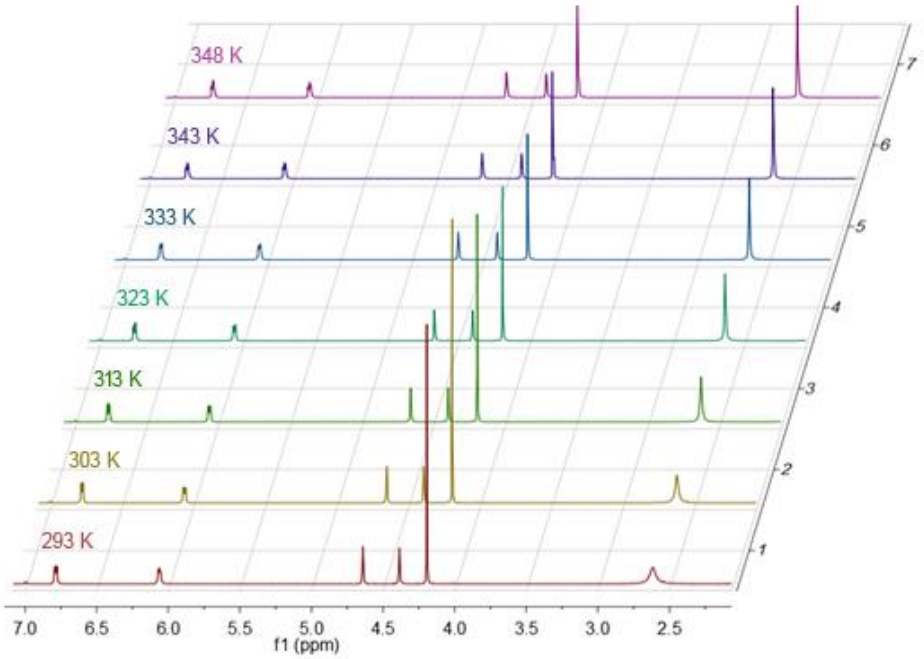

Figure 2.5 ^{1}H NMR for (2-Fc-DMBI)$_2$ in C_6D_6 at different temperatures.

2.2.2.3 X-ray crystal structure

The crystal structures for the dimers were determined by Dr. Evgheni V. Jucov in the group of Dr. Tatiana Timofeeva at New Mexico Highlands University. The crystals for (2-Fc-DMBI)$_2$ and (2-Cyc-DMBI)$_2$ were grown from benzene and heptane, respectively. The crystal structures determined by X-ray crystallography are shown in Figure 2.6, where the thermal ellipsoids are shown at the 50% probability level. The single-crystal X-ray structure confirmed their dimeric nature. The unit cell of (2-Fc-DMBI)$_2$ contains two crystallographically inequivalent molecules but are very similar geometrically. Each of the molecules is centrosymmetric (point group C_i) located on a crystallographic inversion center, with a perfectly staggered conformation around the central C—C bond. This is often found for hexa-substituted C—C fragments. The torsion angle in Fc–C–C–Fc is precisely 180° and the two DMBI units are parallel to

one another. The asymmetric unit of (2-Cyc-DMBI)$_2$ contains one molecule with approximate C_2 symmetry. The conformation about the central C—C bond significantly deviates from the perfectly staggered geometries. The Cyc—C—C—Cyc torsion angle is 140° and the angle between the planes of the two DMBI units is 20.3°.

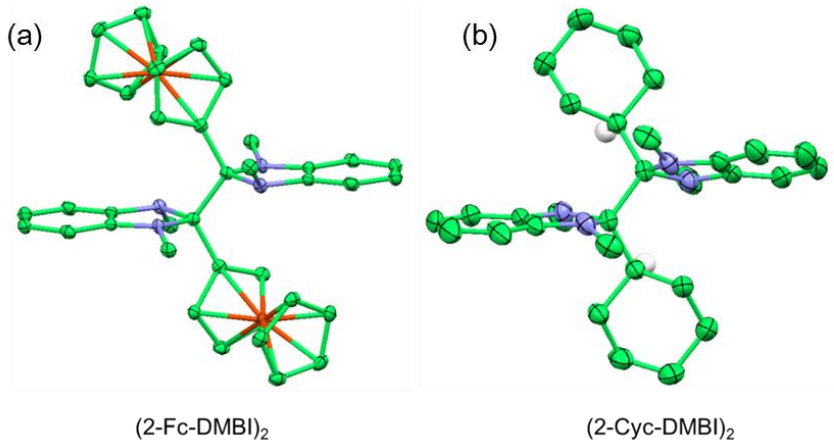

Figure 2.6 Molecular structures of dimers as determined by X-ray crystallography. (a) For (2-Fc-DMBI)$_2$, only one of two very similar crystallographically distinct molecules are shown. (b) Hydrogen atoms are excluded for clarity except for the methine hydrogen atoms of the Cyc groups for (2-Cyc-DMBI)$_2$.

The central inter-monomer C—C bond lengths are 1.595(5) and 1.601(5) Å for the two independent molecules of (2-Fc-DMBI)$_2$, and 1.640(3) Å for (2-Cyc-DMBI)$_2$, both of which are longer than those of standard C(sp^3)–C(sp^3) single bonds (ca. 1.54 Å[20]), but not exceptionally long for hexa-substituted ethanes. In the literature, the central C—C bond length as long as 1.599(3), 1.635, and 1.636(5) Å were reported for (FcMe$_2$C)$_2$,[21] (PhEt$_2$C)$_2$,[22] and a dimer of mesitylene manganese tricarbonyl linked through methyl-substituted positions of both mesitylene rings,[23] respectively. In the dimers of 19-electron sandwich compounds with tetra- and penta-substituted ethane moieties reported previously, the central C—C bonds are 1.553(3)–1.60(3) Å,[12] which are comparable to the (2-Y-DMBI)$_2$ series. This difference in the bond length for (2-

Cyc-DMBI)$_2$ and (2-Fc-DMBI)$_2$ are reproduced in DFT calculations (described in next section), where the central C—C bond are 1.62, 1.58, and 1.58 Å for Y = Cyc, Fc, and Rc derivatives, respectively.

2.2.2.4 DFT calculations

All calculations were performed with the Gaussian 09 (Revision B.01) software suite,[24] done by Dr. Chad Risko at Georgia Tech. Geometry optimizations of neutral and cationic states for the monomers and dimers were carried out via density functional theory (DFT) with the M06 functional[25] and the 6-31G(d,p) and LANL2DZ basis sets for the first-row atoms and transition-metal atoms, respectively.

As shown in Figure 2.7, the highest occupied molecular orbitals (HOMOs) obtained from DFT calculations are qualitatively similar for all three dimers: they are all contributed from an anti-bonding interaction between the local HOMOs of the two *o*-phenylenediamine fragments and the σ-orbital associated with the central C—C bond. There are also additional minor destabilizing contributions from the C—Y σ-orbitals, and small coefficients on the metal centers in the metallocenyl species. DFT calculations were also used to estimate the ionization energy (IEs) for dimers and monomer radicals. Although, the energies are calculated in gas-phase, and the solid-state IEs are relevant to determining whether or not a given acceptor can be doped in a film are typically ca. 1 eV lower.[26] The calculation can potentially give insights into the trend of reactivity for a series of similar compounds. Moreover, the dissociation energies for dimer and dimer radical cations, and the spin densities for the monomers are also calculated, all of which will be discussed in the following section. DFT

calculations help us to better understand the doping mechanisms and compare the doping strength of different DMBI dimer dopants.

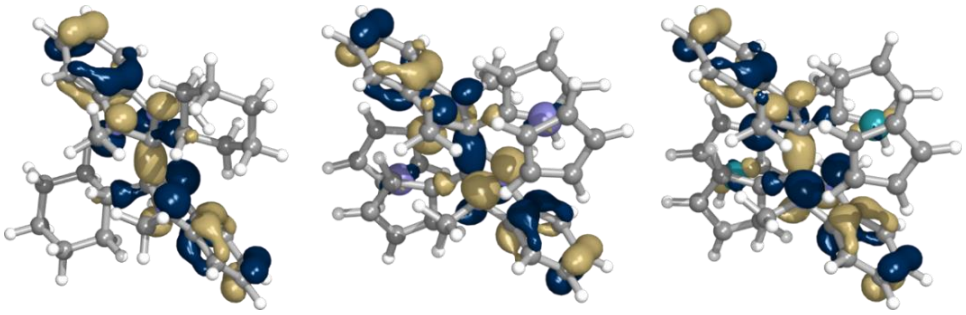

Figure 2.7 Highest occupied molecular orbitals for $(2\text{-Y-DMBI})_2$ species with, from left to right, Y = Cyc, Fc, and Rc.

2.2.2.5 Electron spin resonance (ESR) spectroscopy

ESR measurements were conducted by Dr. Ben Naab using the equipment in Dr. Glenn L Millhauser's group at University of California Santa Cruz. Solutions of the pure dimers (ca. 1 mM) in chlorobenzene were investigated in quartz ESR tubes using an X-band Bruker ESR spectrometer operating at 9.44 GHz with a Bruker SHQ cavity. Solutions of $(2\text{-Fc-DMBI})_2$ showed a structureless ESR signal (g = 2.009) at comparable concentrations at room temperature. Its intensity increases with temperature. The spectrum was consistent with that predicted for 2-Fc-DMBI$^{\bullet}$ by simulation of a spectrum with WINSIM[27] using isotropic Fermi contact couplings obtained from DFT calculations and a linewidth of 0.45 G (Figure 2.8).

ΔH_{diss} can be determined by measuring spectra as a function of temperature, using the following equation:

Equation 2.1
$$-\frac{\Delta H_{diss}}{RT}+\frac{\Delta S_{diss}}{R}=\ln K_{diss}=\ln\frac{[D^{\bullet}]^2}{[D_2]}$$

The ESR intensity (I_{ESR}), either obtained from the doubly integrated 1st

derivative spectrum, or from the peak-to-peak height in the 1st derivative spectrum in this case when line-shape is invariant with temperature. I_{ESR} is proportional to [D•] and experimentally found to be inversely proportional to temperature. [D_2] is regarded as a constant, since the extent of dissociation is small. Thus:

Equation 2.2 $$\ln\left[I_{ESR}T\right] = -\frac{\Delta H_{diss}}{2RT} + c$$

where c is constant, allowing ΔH_{diss} to be obtained from a plot of the logarithm of the product of intensity and temperature vs. the reciprocal temperature. To determine ΔG_{diss} and ΔS_{diss}, [D•] was determined to be 0.97 μM by comparison of the intensity at 320 K, obtained by double integration of the 1st derivative spectrum, of a sample of known initial [D_2] concentration (1.96 mM) to that of a standard sample, a solution in chlorobenzene of the stable nitroxyl radical (2,2,6,6-tetramethylpiperidin-1-yl)oxyl (TEMPO) at the same temperature. Thus, the calculated equilibrium constant is around 4.8×10^{-10} M^{-1}, with ΔH_{diss} = +109 kJ mol^{-1}, ΔS_{diss} = +163 J mol^{-1} K^{-1}, and ΔG_{diss}(300 K) = +60 kJ mol^{-1}.

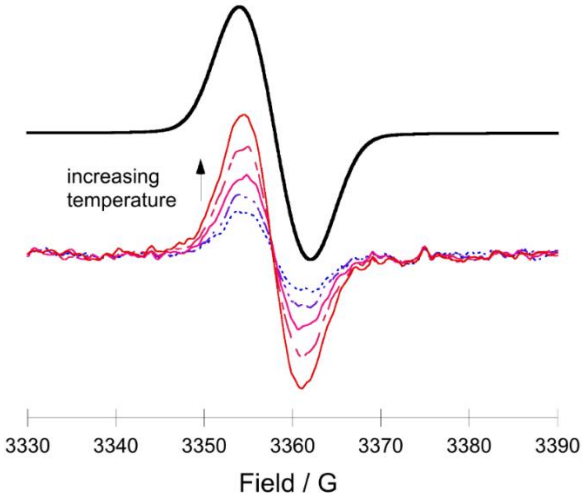

Figure 2.8 ESR spectra obtained for a solution of $(2\text{-Fc-DMBI})_2$ in chlorobenzene in the range 300-320 K (below), compared to a spectrum simulated from isotropic contact couplings obtained from DFT calculations on 2-Fc-DMBI radical.

On the other hand, the radical signal in $(2\text{-Rc-DMBI})_2$ is much weaker, and was only observable at temperatures higher than 330K in chlorobenzene, and $(2\text{-Cyc-DMBI})_2$ produces no radical signal up to 390K in chlorobenzene.

2.3 Characterization of doping effects

2.3.1 Doping mechanism under consideration for the DMBI dimer dopants

Recently, it has been shown that several 19-electron sandwich organometallic dimers can act as powerful n-dopants, and two possible mechanisms are operating as described in Figure 2.9.[11,16] To study the doping mechanism of these DMBI based dimer dopants, 6,13-bis(triisopropylsilylethynyl)pentacene (TIPSp) and phenyl-C_{61}-butyric acid methyl ester (PCBM) were used as the acceptors, both of which are well known solution-processable organic semiconductors with good performance. TIPSp is generally regarded as a hole-transport material, but can act as an electron-transport material when n-doped.[17,28]

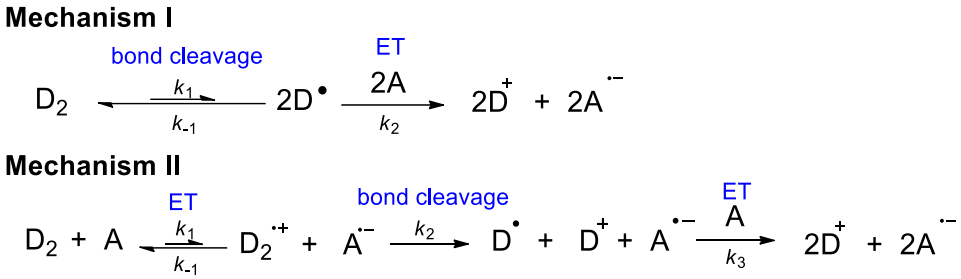

Figure 2.9 Possible mechanisms for dimer doping.

Both n-doping mechanisms are expected to yield the DMBI cations (M^+) and the radical anion of the host electron-transport molecule ($A^{-\bullet}$) through multi-step reactions. For mechanism I, the dimerized dopants cleave first to form monomeric radicals, followed by an electron transfer (ET) to the acceptors. It is only feasible if the dimer is in equilibrium with a small concentration of the corresponding monomer. Based on the ESR results, only $(2\text{-Fc-DMBI})_2$ exhibits small amount of radical concentration (with equilibrium constant around 4.8×10^{-10} M^{-1} at 320 K), while for $(2\text{-Cyc-DMBI})_2$ and $(2\text{-Rc-DMBI})_2$ no radical was detected at room temperature, which indicate that the cleavages of these dimers are more endergonic than $(2\text{-Fc-DMBI})_2$, and less likely to undergo mechanism I. The reduction potential of the cation species can be used to estimate the oxidation potential of the radicals. Figure 2.10 shows the cyclic voltammetry measurement for 2-Y-DMBI^+ salts and $(2\text{-Y-DMBI})_2$, and the results are summarized in Table 2.2. When using TIPSp and PCBM as acceptors, with reduction potential at -1.07 V and -1.4 V (vs. $FeCp_2^{+/0}$), respectively, the subsequent electron transfer step from $2\text{-Y-DMBI}^\bullet$ to the acceptor is exergonic. If the first step is rate-determining, the rates of reaction will be zero-order with respect to the acceptor, and the activation barrier will be independent of the reduction potential of the acceptor.

In mechanism II, the electron transfer from the dimer to acceptors happens first,

then the dimer cation dissociates, given a high energy radical and stable monomeric cation. The last step is the ET from high-energy monomeric radical to another acceptor. According to electrochemical potentials of dopants and acceptors (Figure 2.10 and Table 2.2), the first step will be endergonic. Compared with TIPSp (-1.4 V vs. $FeCp_2^{+/0}$), PCBM has a less cathodic reduction potential at -1.07 V (vs. $FeCp_2^{+/0}$), where it is more possible that a direct somewhat exergonic electron transfer (ET) from dimer to acceptor can occur at an appreciable rate. The second step, with the formation of corresponding stable monomeric cation, is likely to be rapid and irreversible. As shown in Table 2.1, the rates of reaction will be first-order of both the dimer and acceptor with the assumption that the first step is the rate-determining step.

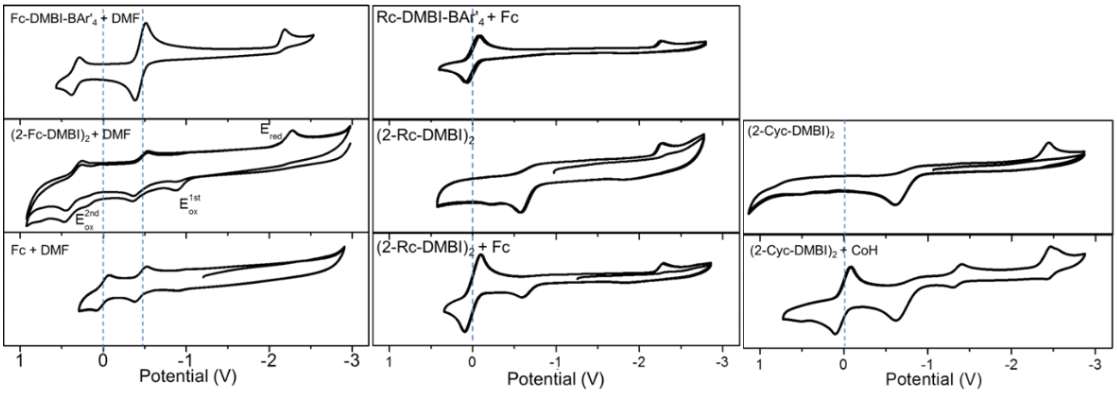

Figure 2.10 Cyclic voltammograms (50 mV s^{-1}, THF, 0.1 M nBu_4NPF_6, vs. ferrocenium/ferrocene) recorded for 2-Y-$DMBI^+BAr'_4^-$ and $(2\text{-Y-DMBI})_2$. DMF, CoH, and Fc denote decamethylferrocene, cobaltocenium hexafluorophosphate, and ferrocene respectively, which are used as internal references.

The electrochemical data (Figure 2.10 and Table 2.2) shows that there is a large variation in the potential at which the D_2 dimers are oxidized. This may lead to rates of reaction via mechanism II increasing in the order Rc < Cyc < Fc.

Table 2.1 Comparison of Proposed Mechanisms for n-Doping with DMBI Dimers

mechm	products	Rate-determining step	rate law[a]	$\Delta G^{\ddagger}$ dependence on Acceptor[a]	$\Delta S^{\ddagger}$
I	$M^{+}A^{\bullet-}$ (+ A^{2-})	Dimer dissociation	$d[M_2]/dt = -k[M_2]$	no	>0
II	$M^{+}A^{\bullet-}$	Electron transfer	$d[M_2]/dt = -k[M_2][A]$	yes	<0

[a]Assuming that in each case the first step is rate-determining step.

Table 2.2 Electrochemical data,[a] estimated free energies of reaction with TIPSp and PCBM, DFT-calculated adiabatic ionization energies (IEs) for dimeric and monomeric 2-Y-DMBI compounds, and DFT-calculated dissociation energetics.

	E vs. $FeCp_2^{+/0}$ / V [a]		IE / eV [d]			ΔU_{diss} / kJ mol^{-1} (eV)	
Y	$E_{pa}(D_2^{+/0})$ [b]	$E_{1/2}(D^{+/0})$ [c]	$D_2 \rightarrow D_2^{\bullet+} + e$ [e]	$D^{\bullet} \rightarrow D^{+} + e$	$0.5D_2 \rightarrow D^{+} + e$ [f]	$D_2 \rightarrow 2D^{\bullet}$	$D_2^{\bullet+} \rightarrow D^{+} + D^{\bullet}$ [e]
Cyc	–0.64	–2.45	5.06	3.72	4.81	210 (2.17)	81 (0.84)
Fc	–0.89	–2.24	4.69	3.93	4.79	165 (1.71)	91 (0.94)
Rc	–0.59	–2.29	4.68	3.80	4.73	181 (1.87)	97 (1.00)

[a] In THF / 0.1 M $^{n}Bu_4NPF_6$. [b] Peak potential for the irreversible oxidation of the dimer measured at 100 mV s^{-1}. [c] Half-wave potential for the partially reversible reduction of the cation. [d] Gas-phase adiabatic IEs obtained from DFT calculations. [e] These results should be treated with caution owing to the tendency of DFT to artificially over delocalize odd-electron systems such as these cations due to self-interaction error.[12] Indeed the optimized structures for the $D_2^{\bullet+}$ are all characterized by spuriously long central C—C bonds (3.23-3.34 Å). [f]$IE_{eff}(0.5D_2 \rightarrow D^{+} + e) = IE(D) + 0.5\Delta U_{diss}(D_2)$.

2.3.2 Themodynamic parameters relevant to doping

As noted in Table 2.1, the barriers for the first steps of mechanisms I and II are related to the thermodynamics of dissociation and of electron-transfer from the dimer to the acceptor, respectively. Thus, the overall thermodynamic doping strength depends on both the ease of monomer ionization and the dissociation energetics, and can be expressed as an effective redox potential:

Equation 2.3 $$E_{\text{eff}}(D^+/0.5D_2) = E(D^+/D^\bullet) + (0.5/F)\Delta G_{\text{diss}}(D_2)$$

or an effective ionization energy:

Equation 2.4 $$IE_{\text{eff}}(0.5D_2 \rightarrow D^+ + e) = IE(D^\bullet) + 0.5\Delta U_{\text{diss}}(D_2)$$

Table 2.2 compares $D^+/D^\bullet$ redox potentials for the three Y-DMBI systems along with the irreversible peak oxidation potentials for the corresponding dimers, and DFT adiabatic ionization energies (IEs) for monomeric and dimeric species. For a series of similar compounds with comparable solvation effects, the same trends can be expected.

Since the group-8 metallocenes are well-known to stabilize α-carbocations, one might expect the 2-Y-DMBI$^\bullet$ radicals species where Y is a metallocene to be more reducing than those why Y is an alkyl group,[29,30] thus more reducing 2-Y-DMBI$^\bullet$ monomers. Surprisingly, both experimental and computational data indicate that the reducing capability of the 2-Y-DMBI$^\bullet$ monomers increases in the order Fc < Rc < Cyc. In these DMBI series, the cation is already stabilized by the aromatic benzimidazole ring, thus, the role of metallocenes in stabilizing the cation is presumably less significant than is the case for, for example, stabilizing an unstabilized methylene cation. Evidently the metallocenyl groups stabilize the 2-Y-DMBI$^\bullet$ monomers to a greater extent than the 2-Y-DMBI$^+$ cations. The DFT calculations support this by indicating

that the spin density of 2-Cyc-DMBI$^{\bullet}$ is almost entirely located in the benzimidazoline rings (primarily at the 2-position), but that in the metallocenyl species, there is significant spin delocalization onto the Y substituent (Figure 2.11), especially for 2-Fc-DMBI$^{\bullet}$.

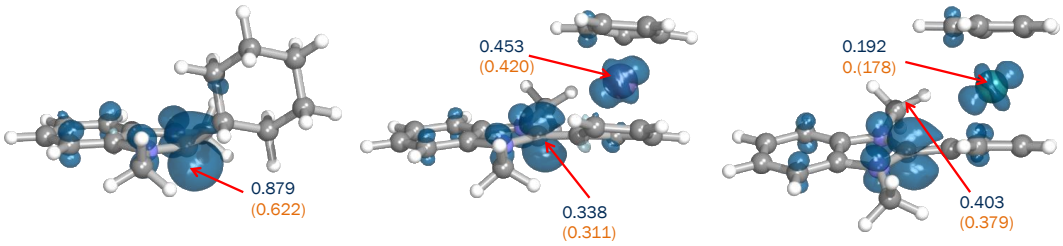

Figure 2.11 DFT-calculated spin densities (0.05 Å^{-3} isosurfaces) for (from left to right) 2-Cyc-, 2-Fc-, and 2-Rc-DMBI$^{\bullet}$ monomers. Spin fractions in the 2-positions of the imidazoline ring and on the metal atoms from Mulliken analyses (from natural population analysis in parentheses) are shown.

The DFT values of ΔU_{diss} for the neutral dimers are also given in Table 2.2: the trend suggests that the rate of reaction through the mechanism I should increase in the order Cyc < Rc < Fc, which is consistent with the ESR results. The value for (2-Cyc-DMBI)$_2$ is similar to those obtained in the same way for the dimeric organometallic n-dopants (IrCp*Cp)$_2$ and (RuCp*(mesitylene))$_2$.[12] In trend in ΔU_{diss} values correlates very well with that in the extent of spin delocalization in the 2-Y-DMBI$^{\bullet}$ monomers noted above. However, the values of ΔU_{diss} do not correlate well with the crystallographic or DFT bond lengths: (2-Cyc-DMBI)$_2$ has the longest and strongest bond, in contrast to the general tendency for C—C bond lengths to decrease linearly with increasing bond strength.[12] However, bond length only depends on steric interactions and sharing of electron-density in the dimer, while the dissociation energy will depend both on how these affect the energy of the dimer and on the stability of the

monomer. Different stability of the monomer causes the overall difference in the ΔU_{diss}. As discussed earlier, this different stability of the monomer can be explained by the delocalization of spin density in radicals (Figure 2.11). A similar lack of correlation between ΔU_{diss} values and bond lengths was also found for dimerized sandwich compounds, where it was also attributable to variations in the stability of the corresponding monomers.[12]

As noted above, the dopant strengths can be gauged by an effective ionization energy obtained from Equation 2.3. These values, based on DFT-calculated quantities, are also given in Table 2.2 and show that all three dimers are expected to exhibit very similar thermodynamic doping abilities: the variations in IE($D^{\bullet}$) and $\Delta U_{diss}(D_2)$, both of which may be demonstrated by the variations in monomer spin delocalization, effectively cancel one another out. A similar cancelation was observed when estimating effective dopant strengths for sandwich-compound dimers.[12] The effective doping strengths for these DMBI dimers are within a similar range to those of the dimeric sandwich compounds (4.4 – 4.8 eV for most compounds examined, 5.4 eV for $(RhCp_2)_2$). Using Equation 2.1, the ESR-derived value of ΔG_{diss}(300 K), E_{eff} for the 2-Fc-$DMBI^+$/0.5(2-Fc-$DMBI)_2$ couple can be estimated to be –1.93 V vs. $FeCp_2^{+/0}$, also similar to values estimated from electrochemical data and DFT calculations for dimeric sandwich compounds (–1.97 to –2.14 V for most examples, –1.72 V for $(RhCp_2)_2$).[12]

2.3.3 Reaction kinetics for $DMBI_2$ dopants in solution

The doping products were characterized through UV−vis−near−IR spectroscopy. The doped products ($PCBM^{\bullet-}$ and $TIPSp^{\bullet-}$) exhibit distinctive absorption

spectra and their salts with organic or organometallic counter-ions can retain reasonable solubility in the same solvents in which the neutral species are soluble, allowing the kinetics to be monitored using vis-NIR spectroscopy.[16,31] The rate laws and activation barriers associated with the different (2-Y-DMBI)$_2$/A reactions were then investigated by using vis-NIR spectroscopy to monitor reactions in the dark in chlorobenzene at various relative dimer and acceptor concentrations by using the pseudo-single-reactant reaction method where either the dimer or the acceptor is present in a large excess.

2.3.3.1 Doping mechanism between DMBI dimers and PCBM

The spectra of mixed solution with PCBM and dimers showed a new band at 1030 nm, which is consistent with previously reported absorption spectra of $PCBM^{-\bullet}$ (Figure 2.12).[31]

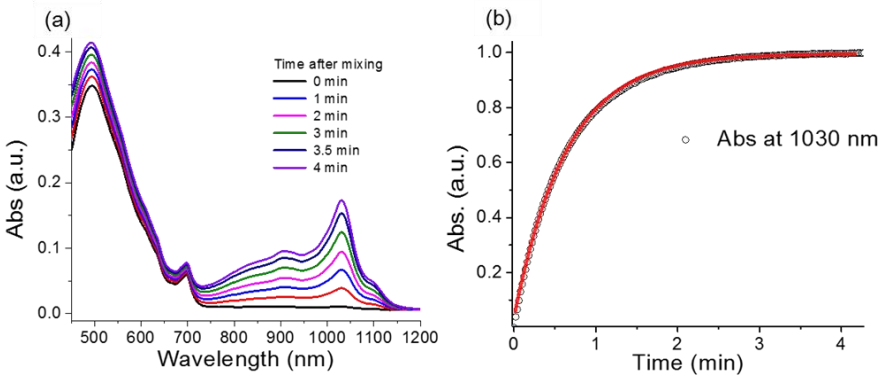

Figure 2.12 (a) UV-vis-NIR spectra of a solution of PCBM (3.7×10^{-4} M) and (2-Cyc-DMBI)$_2$ (1.3×10^{-5} M) in chlorobenzene at various times after mixing. (b) Plots of the absorbances at 1030 nm versus time for the reaction shown in the top left, the red solid lines being fits to a first-order expression.

The reaction of PCBM and (2-Fc-DMBI)$_2$ was complete in a few minutes, even when employing concentrations as low as ca. 10^{-5} M, making the determination of the rate law and rate constants from vis-NIR spectroscopy impractical. The reaction was found to be first-order in both dimer and PCBM for the Cyc and Rc species, with the

reaction occurring more rapidly in the former case (as shown in Figure 2.13 and Figure 2.14). Thus, the observed rates of reaction with PCBM increase as the ease of dimer oxidation increases. Activation parameters for the Y = Cyc and Rc dimers were obtained from Eyring plots of variable-temperature rate-constant data (Table 2.3 and Figure 2.24): values of $\Delta S^{\ddagger}$ are negative, as expected for a bimolecular reaction, and values of $\Delta G^{\ddagger}$(300 K) are close to values the free energies estimated for electron transfer from dimer to PCBM according to $\Delta G_{ET} = F\{E(D_2^{+/0})–E(A^{0/–})\}$. The rate law, the dependence of rate on $E_{pa}(D_2^{+/0})$, and the activation parameters are entirely consistent with the reduction of PCBM by the Cyc and Rc dimers proceeding by mechanism II, with the first step being rate-limiting. Moreover, the reaction of PCBM with (2-Fc-DMBI)$_2$ proceeds much more rapidly than reaction of the same dimer with TIPSp, which is shown below to proceed via mechanism I , at similar concentrations; this suggests (2-Fc-DMBI)$_2$ also reduces PCBM via mechanism II, the faster reaction relative to its Cyc and Rc analogues being consistent with values of $E_{pa}(D_2^{+/0})$.

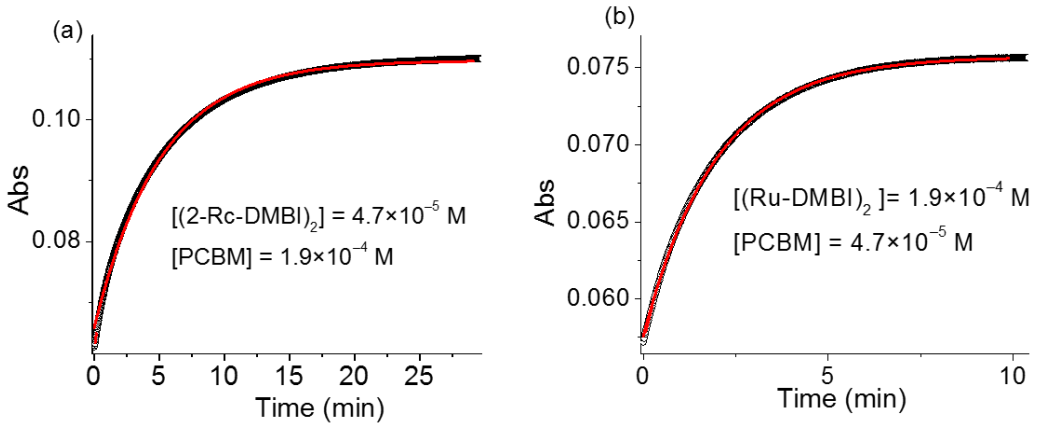

Figure 2.13 (a) Absorbance at 745 nm vs. time for the reaction of PCBM and (2-Rc-DMBI)$_2$, with (2-Rc-DMBI)$_2$ as the limiting reagent. The solid red line is the fitted first-order reaction curve. (b) Absorbance at 745 nm vs. time for the same reaction with PCBM as the limiting reagent. The solid red line is the fitted first-order reaction curve.

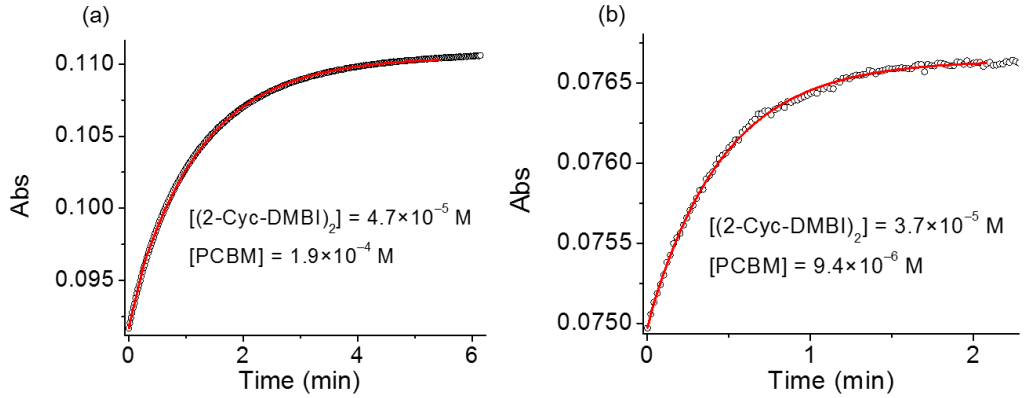

Figure 2.14 (a) Absorbance at 745 nm vs. time for the reaction of PCBM and (2-Cyc-DMBI)$_2$ with (2-Cyc-DMBI)$_2$ as the limiting reagent. The solid red line is the fitted first-order reaction curve. (b) Absorbance at 745 nm vs. time for the same reaction with PCBM as the limiting reagent. The solid red line is the fitted first-order reaction curve.

2.3.3.2 Doping mechanism between DMBI dimers and TIPSp

All (2-Y-DMBI)$_2$/TIPSp combinations in chlorobenzene were found to result in the appearance of the appropriate characteristic radical-anion absorptions, and the identity of product peaks were also confirmed by similarity to the spectrum obtained by exposure of TIPSp solution to Na-K alloy (Figure 2.15), and organometallic dimer doping [RhCpCp*]$_2$.[16] In ^{1}H NMR spectra of (2-Y-DMBI)$_2$/TIPSp mixtures in chlorobenzene-d_5 confirmed the formation of the corresponding 2-Y-DMBI$^+$ cations

and showed broadening of the TIPSp resonances, consistent with the formation of paramagnetic $TIPSp^{\bullet-}$.

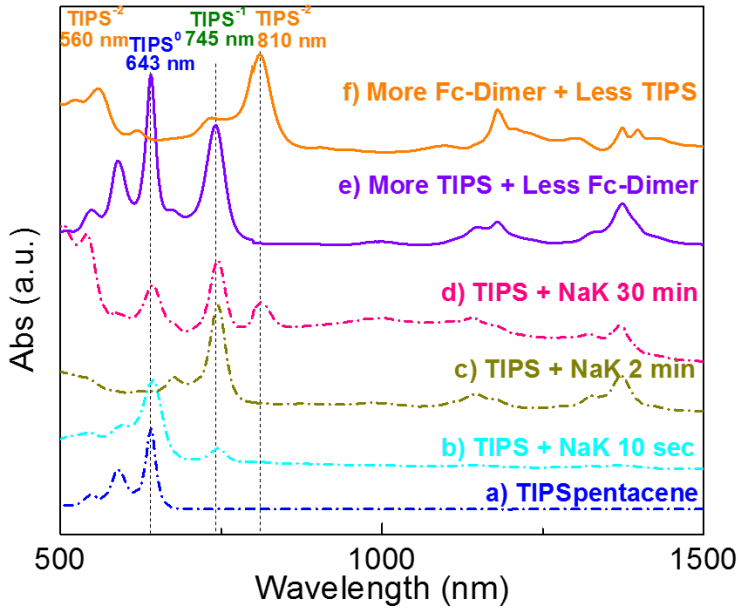

Figure 2.15 UV-vis-NIR spectra of a solution of TIPSp mixed with Na·K and $(2\text{-Fc-DMBI})_2$ at different ratio.

The reduction of TIPSp by $(2\text{-Cyc-DMBI})_2$ proceeds considerably more slowly than that of PCBM. At room temperature in the dark, the reaction is incomplete after 12 h, hampering determination of reaction kinetics. However, from reactions carried out at elevated temperatures the rate law was found to indicate that this reaction also proceeds via mechanism II: when either the dimer or the acceptor is present in large excess, the rate law can be fitted into a first-order curve (Figure 2.16). A value of $\Delta G^{\ddagger}$(300 K) was obtained that is roughly consistent with the electrochemically estimated value of ΔG_{ET} (Figure 2.25 on Page 77, and Table 2.3). The slow room-temperature reaction can also be accelerated by exposure to ambient light (Figure 2.17); as in the previously reported photoinduced reduction of TIPSp using $(IrCp^*Cp)_2$, this reaction presumably proceeding by electron transfer from the dimer to photoexcited

TIPSp.[12]

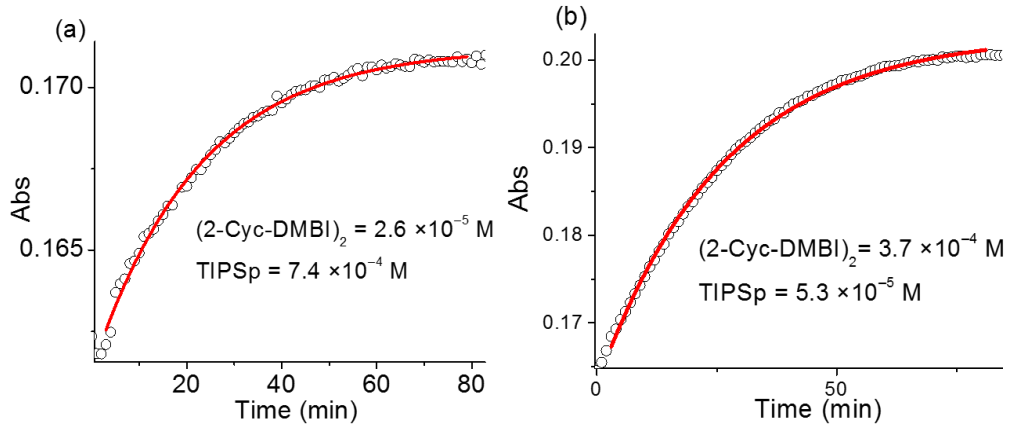

Figure 2.16 (a) Absorbance at 745 nm vs. time for the reaction of TIPSp and (2-Cyc-DMBI)$_2$, when (2-Cyc-DMBI)$_2$ is the limiting reagent. The solid red line is the fitted first-order reaction curve. (b) Absorbance at 745 nm vs. time for the same reaction with TIPSp as the limiting reagent. The solid red line is the fitted first-order reaction curve.

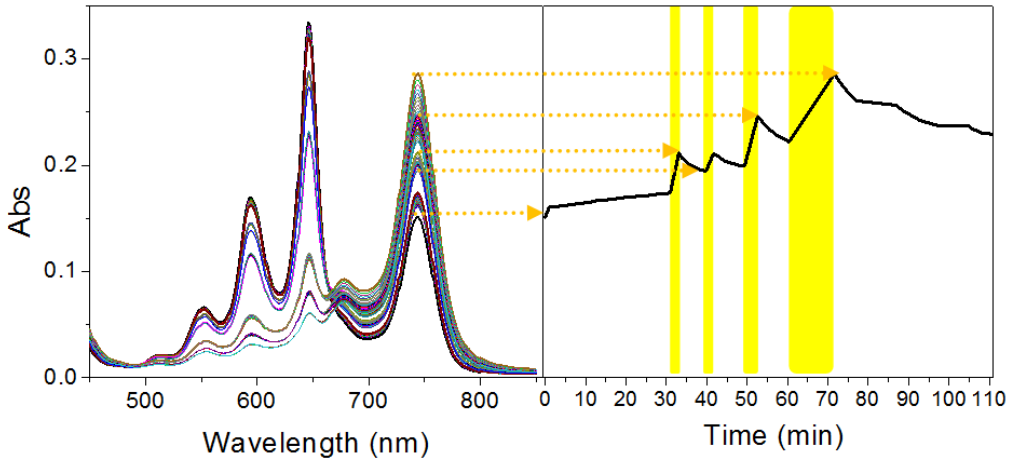

Figure 2.17 Evolution of spectra of a solution of (2-Cyc-DMBI)$_2$ (2.6×10^{-4} M) and TIPSp (1.3×10^{-4} M) in chlorobenzene in the dark and on exposure to laboratory light: a) shows spectra between 450-850 nm and b) shows normalized Absorbance at 745 nm vs. time with the yellow shading indicating the periods in which the samples were exposed to light.

The reactions of Fc and Rc dimers with TIPSp are less straightforward. As in the Cyc case, reduction of TIPSp by (2-Rc-DMBI)$_2$ is slow in the dark at room temperature, but can be accelerated in ambient light (shown in Figure 2.18). However, rate data acquired at elevated temperature in different concentrations cannot be fit to

either of the expected rate laws given in Table 2.1. Plots of the initial rate divided by the initial concentration of dimer vs. the initial concentration of TIPSp are linear with non-zero intercepts, consistent with a rate law of the type

Equation 2.5 $$\frac{d[D_2]}{dt} = -\frac{1}{2}\frac{d[TIPSp^{\bullet -}]}{dt} = -k_I[D_2] - k_{II}[D_2][TIPSp]$$

and, therefore, with both mechanisms I and II contributing to the observed reaction. This is consistent with what has previously been observed for the reaction of $(RhCp^*Cp)_2$ and TIPSp.[16] A series of such plots at different temperatures was used to extract activation parameters for the two pathways (Figure 2.20). Values of $\Delta S^{\ddagger}$ are positive and negative for pathways I and II, respectively, consistent with the expected mechanisms (Table 2.3 on Page 79). The value of $\Delta H^{\ddagger}$ for the reaction of TIPSp and (2-Rc-DMBI)$_2$ by mechanism I is much larger than the value of ΔH_{diss} obtained for the Fc compound from ESR data, consistent with the greater bond strength expected for the Rc species. The value of $\Delta G^{\ddagger}(300)$ for mechanism II is consistent with the electrochemically estimated value of ΔG_{ET}.

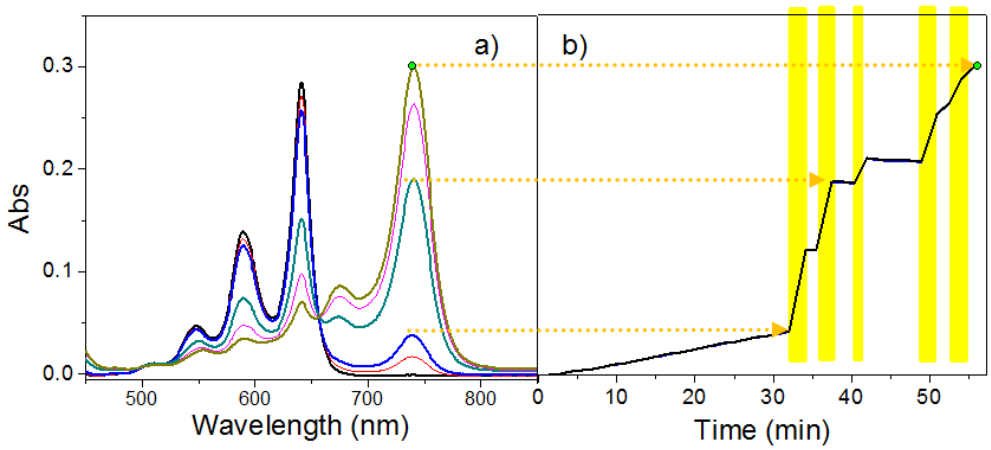

Figure 2.18 Evolution of spectra of a solution of $(2\text{-Rc-DMBI})_2$ (2×10^{-4} M) and TIPSp (2×10^{-4} M) in chlorobenzene in the dark and on exposure to laboratory light: a) shows spectra between 450-850 nm and b) shows normalized Absorbance at 745 nm vs. time with the yellow shading indicating the periods in which the samples were exposed to light.

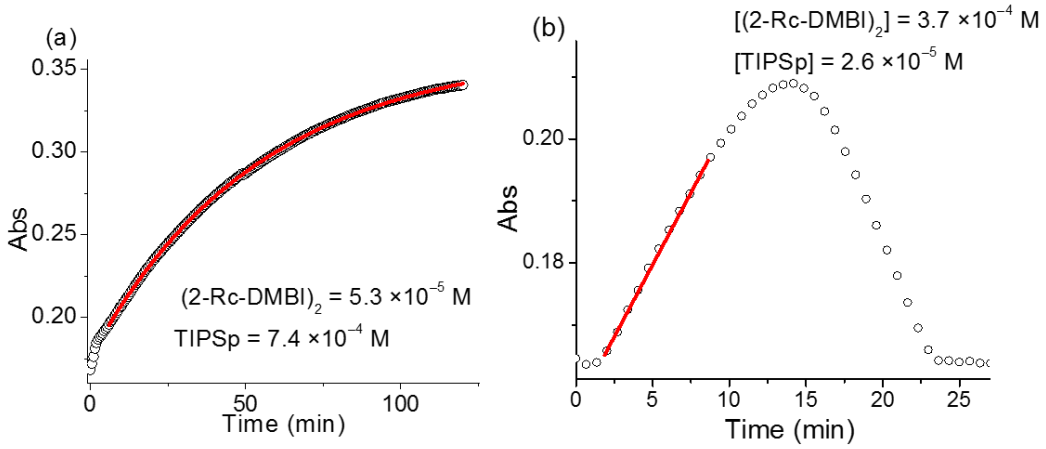

Figure 2.19 (a) Absorbance at 745 nm vs. time for the reaction of TIPSp and $(2\text{-Rc-DMBI})_2$ with $(2\text{-Rc-DMBI})_2$ as the limiting reagent. The solid red line is the fitted first-order reaction curve. (b) Absorbance at 745 nm vs. time for the same reaction with TIPSp as the limiting reagent. The solid red line is the fitted zero-order reaction curve. The decrease in the absorbance at 745 nm begin at 15 min is attributed to the formation of $TIPSp^{2-}$.

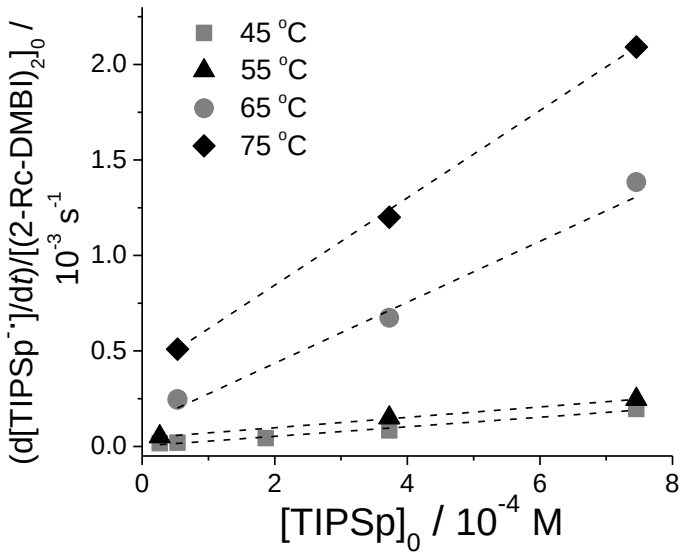

Figure 2.20 Initial rate of reaction of $(2\text{-Rc-DMBI})_2$ and PCBM divided by the initial concentration of dimer versus the initial concentration of acceptor TIPSp. The linear fits at different temperature with non-zero intercept indicate the rate can be expressed as a sum of two mechanisms, where the intercept is the zero-order rate constant, and slope is the first-order rate constant.

At room temperature, the $(2\text{-Fc-DMBI})_2$ reduces TIPSp much more rapidly than do the other dimers at comparable concentrations. In the presence of excess TIPSp, the evolution of the $TIPSp^{\bullet-}$ signals can be modeled with an exponential function, consistent with a reaction first order in the dimer (Figure 2.22). In the presence of excess dimer, however, $[TIPSp^{\bullet-}]$ linearly approaches a maximum and then linearly decreases at a very similar rate while signals attributable to $TIPSp^{2-}$ appear.[16] The independence of the rate on [TIPSp] and the formation of TIPSp on a similar time scale are consistent with the reaction proceeding through mechanism I with the first step being rate determining. Reactions at higher temperatures, however, revealed some dependence of rate on [TIPSp], but the data could not be fitted to a combination of mechanisms I and II as was the case for $(2\text{-Rc-DMBI})_2$ based on Equation 2.5. At the highest temperatures

examined (45 and 55 °C), a plot of initial rate divided by the initial value $[D_2]^{0.5}$ vs. [TIPSp] was found to be linear (Figure 2.23), consistent with the rate law that is expected if mechanism I is operative, but with the second step being rate-limiting:

Equation 2.6

$$\frac{d[D_2]}{dt} = -\frac{1}{2}\frac{d[TIPSp^{\bullet -}]}{dt} = -\frac{1}{2}k_2 K_{diss}^{0.5}[D_2]^{0.5}[TIPSp]$$

where k_2 is the rate constant for electron transfer from the monomer to TIPSp. Equation 2.6 can be derived by assuming D_2 is in pre-equilibrium with $D^{\bullet}$. This equation and that given in Table 2.1 can also be obtained as limits of the general rate equation derived via application of the steady-state approximation.[26] This temperature-dependent change in which step is rate-determining makes it impossible to determine the activation barriers from the temperature range examined.

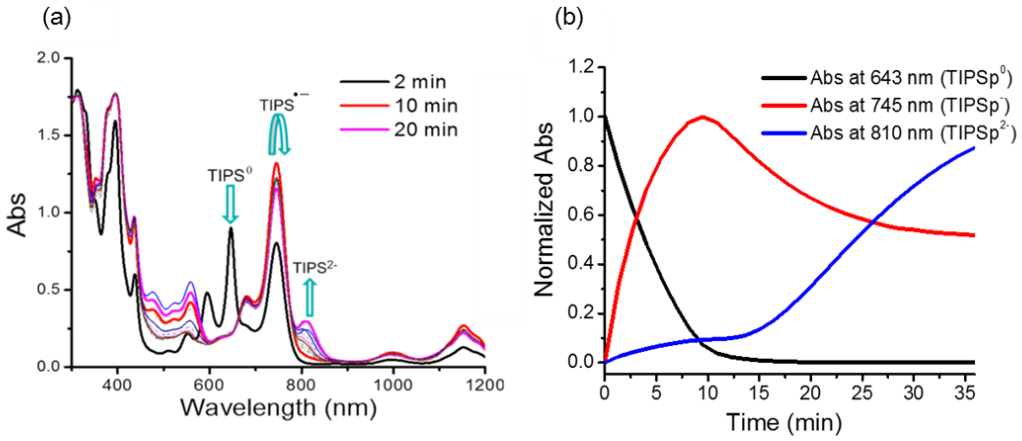

Figure 2.21 (a) UV-vis-NIR spectra of a solution of TIPSp (4×10^{-4} M) and (2-Fc-DMBI)$_2$ (4×10^{-4} M) in chlorobenzene at various times after mixing. (b) Plots of the absorbances at 643 nm, 745 nm and 810 nm versus time for the reaction.

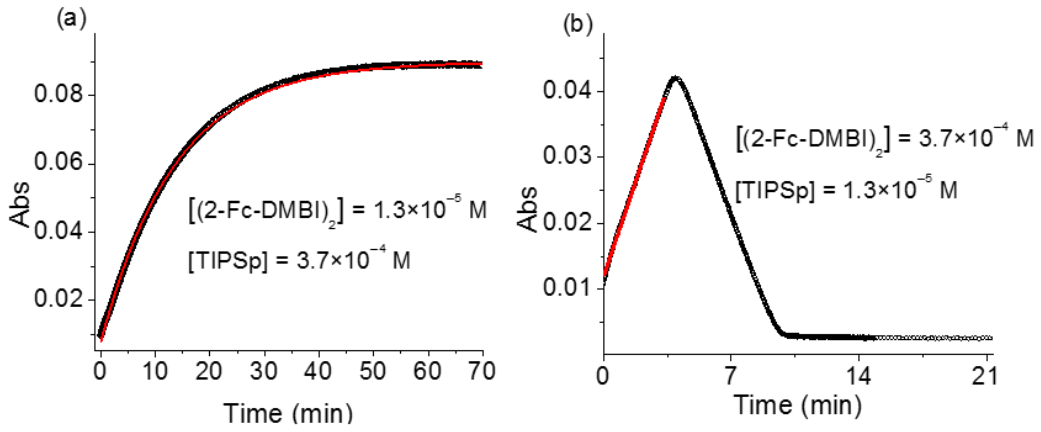

Figure 2.22 (a) Absorbance at 745 nm vs. time for the reaction of TIPSp and (2-Fc-DMBI)$_2$, when (2-Fc-DMBI)$_2$ is the limiting reagent. The solid red line is the fitted first-order reaction curve. (b) Absorbance at 745 nm vs. time for the same reaction with TIPSp as the limiting reagent. The solid red line is the fitted zero-order reaction curve.

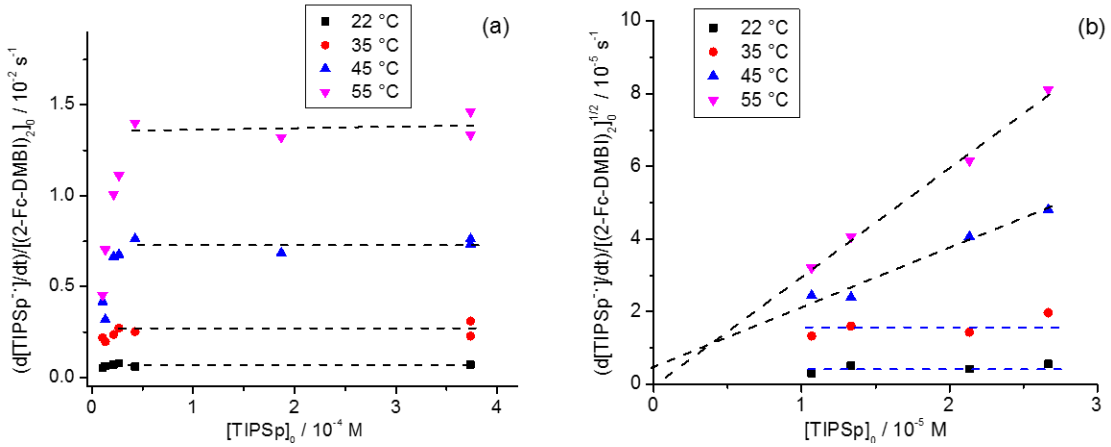

Figure 2.23 (a) Plots of initial rate divided by the square root of initial concentration of (2-Fc-DMBI)$_2$ versus the initial concentration of acceptor TIPSp, and (b) linear fits at low TIPSp concentration.

On the other hand, the formation of $TIPSp^{2-}$ when sufficient (2-Fc-DMBI)$_2$ is itself significant. As discussed above, the effective redox potential for the Fc-$DMBI^+$/0.5(2-Fc-DMBI)$_2$ couple is estimated to be –1.93 V vs. $FeCp_2$, while the potential for the $TIPSp^{-/2-}$ couple is also –1.93 V.[16] Thus, the formation of $TIPSp^{2-}$ appears to be of marginal thermodynamic feasibility. However, the data are not completely comparable, since the electrochemical data for the $D^{+/0}$ couple and the $TIPSp^{-/2-}$ couple were determined in THF in the presence of electrolyte, whereas the

dissociation energetics and the kinetic data were obtained in chlorobenzene, and any ion pairing between Fc-DMBI^{+} and TIPSp^{2-} could increase the thermodynamic feasibility of the reaction. Consistent with the observation of TIPSp^{2-}, (2-Fc-DMBI)$_2$ can also reduce 5,11-Bis(triethylsilylethynyl)-anthradithiophene (TES-ADT, $E^{0/-}$ = 1.71 V vs. $FeCp_2^{+/0}$ in THF) to its radical anion (Figure 2.24).

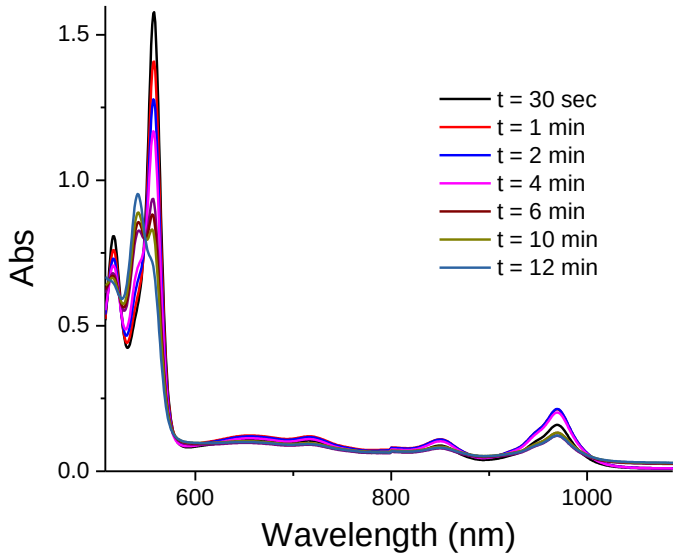

Figure 2.24 Vis-NIR spectra of a mixture of (2-Fc-DMBI)$_2$ (1.45×10^{-4} M) and TES-ADT (2.90×10^{-4} M) in chlorobenzene.

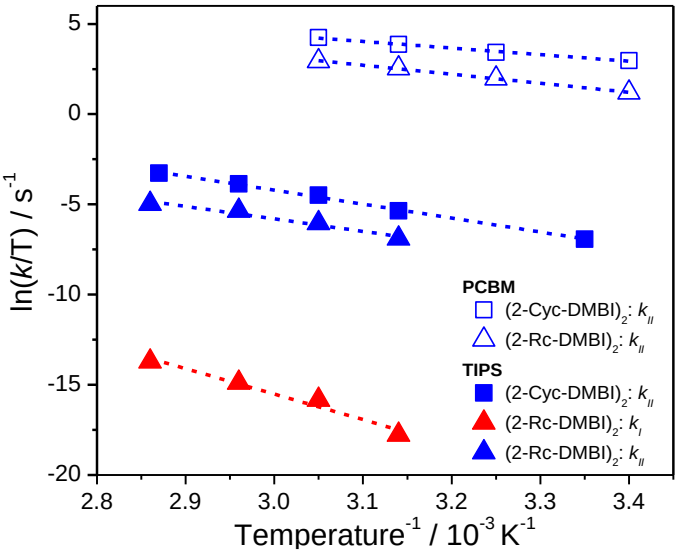

Figure 2.25. Eyring (bottom) plots for variable-temperature rate-constant data for TIPSp doped with (DMBI)$_2$.

In all, based on these mechanism studies, it is shown that the choice of 2-

substituent, Y, in (2-Y-DMBI)$_2$ dimers has a significant effect on their oxidation potentials and their dissociation energies, which in turn influence the kinetics of their reaction with acceptors dramatically. The Y = Fc derivative has both the weakest bond, due to the role of the ferrocenyl moiety in stabilizing the radical monomer, and the most cathodic oxidation potential. Thus, (2-Fc-DMBI)$_2$ is the most reactive one of the species examined: it can react with PCBM (a relatively easily reduced acceptor) through an electron-transfer mechanism (II); and react with TIPSp (a more challenging acceptor) through a mechanism where dimer dissociation is the first step (I). (2-Rc-DMBI)$_2$ and (2-Cyc-DMBI)$_2$ also react with PCBM through the electron-transfer mechanism, but successively more slowly, consistent with their increasingly anodic oxidation potentials. The reduction of TIPSp by (2-Rc-DMBI)$_2$ and (2-Cyc-DMBI)$_2$ proceed considerably even more slowly than that of PCBM, but can be thermal- or photo-activated. This is similar to the previously reported photo-induced reduction of TIPSp using (IrCp*Cp)$_2$, where the reaction can proceed by electron transfer from the dimer to photoexcited TIPSp.[12] For (2-Rc-DMBI)$_2$ dimer, which has intermediate bond strength and the most anodic oxidation potential, both mechanisms are operative with TIPSp, similar to previous observation for the reaction of (RhCp*Cp)$_2$ and TIPSp;[16] whereas for (2-Cyc-DMBI)$_2$, which has the strongest bond and an intermediate redox potential, reacts with TIPSp only through the electron-transfer mechanism.

Table 2.3 Summary of Mechanisms and Activation Parameters for Solution Reactions of (2-Y-DMBI)2 with PCBM and TIPSp.

A	Y	ΔU_{diss} (ΔG_{diss})[a] / kJ mol^{-1}	ΔG_{ET}[b] / kJ mol^{-1}	Mechanism	$\Delta H^{\ddagger}$ / kJ mol^{-1}	$\Delta S^{\ddagger}$ / J mol^{-1} K^{-1}	$\Delta G^{\ddagger}$ (300) / kJ mol^{-1}
PCBM	Cyc	+210 (c)	+41	II	+29.9 ± 0.3	–71.2 ± 3.3	+51.2 ± 1.4
PCBM	Fc	+165 (+60)	+17	II	c	c	c
PCBM	Rc	+181 (c)	+46	II	+45.4 ± 3.5	–95.4 ± 11.2	+74.0 ± 6.8
TIPSp	Cyc	+210 (c)	+78	II	+64.2 ± 1.9	–44.6 ± 5.8	+77.6 ± 3.6
TIPSp	Fc	+165 (+60)	+54	I	c	c	c
TIPSp	Rc	+181 (c)	+82	I	+118.1 ± 8.7	+27.8 ± 18.3	+109.8 ± 14.2
				II	+69.1 ± 2.7	–73.4 ± 15.1	+91.2 ± 7.2

[a]ΔU_{diss} from DFT calculations (Table 2) and ΔG_{diss} from ESR measurements; these are related to $\Delta G^{\ddagger}$ for mechanism I. [b]ΔG_{ET} (related to $\Delta G^{\ddagger}$ for mechanism II) estimated for the reaction $D_2 + A \rightarrow D_2^{\bullet+} + A^{\bullet-}$ from electrochemical data in Table 2 and from values of $E_{1/2}^{0/-}$ = –1.07 and –1.45 V for PCBM and TIPSp, respectively. [c]Not determined.

2.3.4 Film doping experiments

Except the solution doping mechanism studies, the doping behaviors of DMBI dimers were also characterized in films of electron-transport polymer and fullerene derivatives by UPS and conductivity measurements.

For the film doping studies, the electron-transport polymer poly{[*N,N'*-bis(2-octyldodecyl)-naphthalene-1,4,5,8-bis(dicarboximide)-2,6-diyl]-*alt*-5,5*'*-(2,2*'*-bithiophene)}, P(NDI2OD-T2), was used as the host materials. It has relative large EA (3.95 eV), compared with TIPSp (EA 3.0–3.1 eV).[17] An electron mobility as high as ~1 $cm^2V^{-1}S^{-1}$ have been reported for P(NDI2OD-T2).[32] The doped P(NDI2OD-T2) films were first studied by ultraviolet photoelectron spectroscopy (UPS) (Figure 2.26). All three dimer dopants led to large shifts of the Fermi level E_F to ca. 1.7 eV away from the onset of ionization from filled states (E_{HOMO}) at a doping ratio of 2.4 mol%. The saturation of the shift (pinning) of E_F with increasing doping levels has been observed previously for both p- and n-doped organic semiconductors, and it is thought to reflect the approach of E_F to the tail of the Gaussian density of states near the band edges.[17] Indeed, the transport gap for this polymer determined by UPS and inverse photoelectron spectroscopy is ca. 1.6 eV, indicating that the pinning in the present case occurs at or very near to the onset of empty LUMO-derived states.[17]

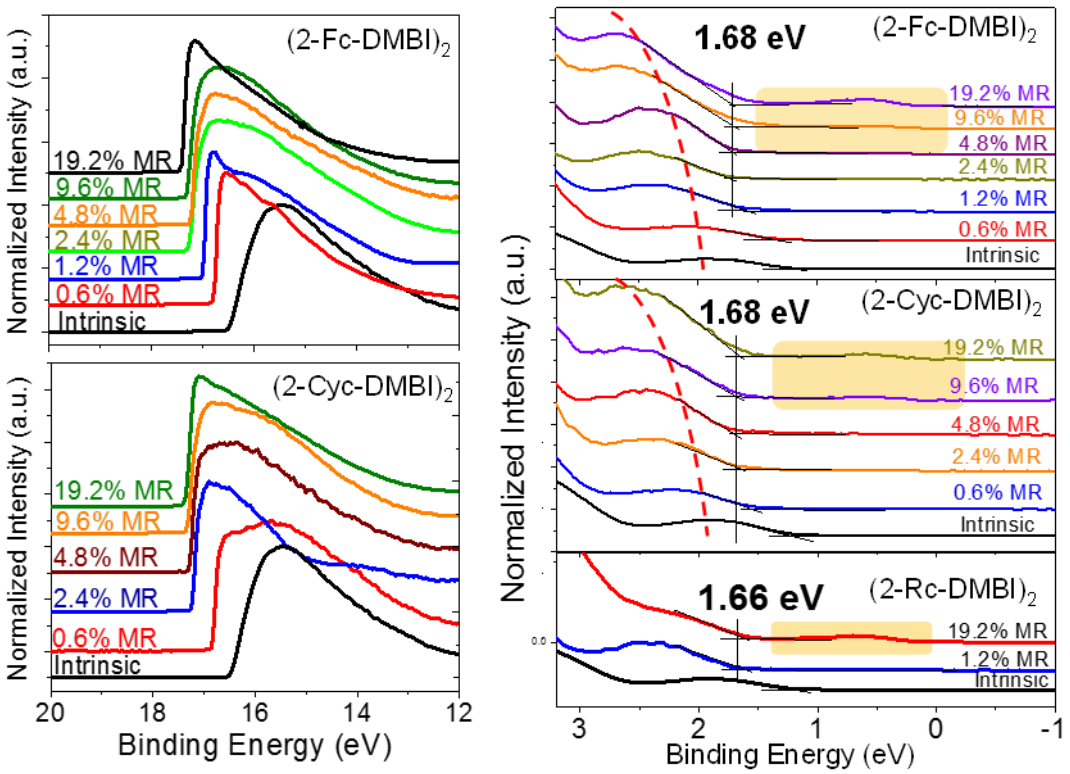

Figure 2.26 UPS spectra of doped P(NDI2OD-2T) films at various dimer doping concentrations showing the secondary electron edge (left), and the onset of ionization (right).

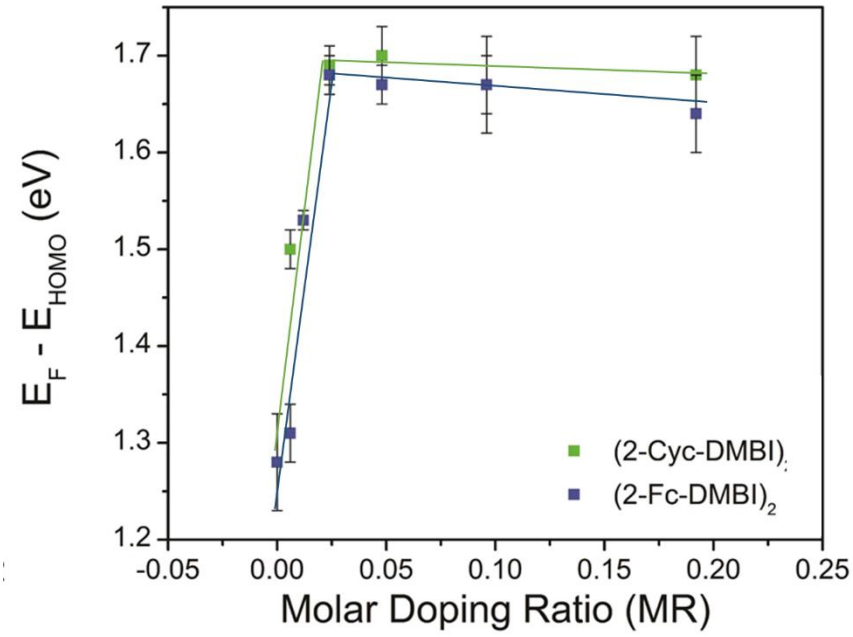

Figure 2.27 UPS measurements of doped P(NDI2OD-T2) showing the shift of E_F away from E_{HOMO} with increasing dopant concentration.

The conductivity measurements of the doped films were carried out by Dr. Ben Naab at Stanford, using a four-point probe technique. P(NDI2OD-T2) and $PC_{61}BM$

were solution-processed with dopants, and C_{60} was vacuum-deposited with dopants. For all material combinations, the doped films exhibited greater conductivity than the intrinsic host, and the variation in the film conductivities was summarized in Table 2.4. The conductivities for $PC_{61}BM$ and C_{60} are ca. 10^{-8} S cm^{-1} before doping, and increase to 10^{-2} and ~10 S cm^{-1}, respectively at the optimized doping ratio. Compared with previously reported DMBI-H and DMBI-I dopants, these dimers exhibit a stronger doping effect in a more diverse array of materials.[8,10] For solution processed P(NDI2OD-T2) film, the conductivity increases from ca. 10^{-8} S cm^{-1} to 10^{-3} cm^{-1} when doped with $(2\text{-Rc-DMBI})_2$ and $(2\text{-Cyc-DMBI})_2$, and slightly low conductivity when doped with $(2\text{-Fc-DMBI})_2$, which may be related to the aggregated morphology observed under AFM.[18]

Table 2.4 Summary of the maximum conductivities obtained for doped P(NDI2OD-T2), $PC_{61}BM$, and C_{60}.

Dopants	Host	Max σ (S cm^{-1})	Wt%(Mol%)
$(2\text{-Fc-DMBI})_2$	P(NDI2OD-T2)	7.6×10^{-5}	20 (26)
	$PC_{61}BM$	1.9×10^{-3}	5.0 (6)
	C_{60}	8.0×10^{-2}	20 (20)
$(2\text{-Rc-DMBI})_2$	P(NDI2OD-T2)	3.0×10^{-3}	10 (12)
	$PC_{61}BM$	1.6×10^{-2}	10 (11)
	C_{60}	1.0×10^{-1}	20 (18)
$(2\text{-Cyc-DMBI})_2$	P(NDI2OD-T2)	2.8×10^{-3}	5.0 (11)
	$PC_{61}BM$	4.7×10^{-2}	5.0 (10)
	C_{60}	12	18 (26)

2.4 Conclusions

New benzimidazole-based dimers, $(2\text{-Y-DMBI})_2$, were successfully synthesized and characterized. They are both solution- and vacuum-processable, and can be used to n-dope electron transport materials (ETMs) with electron affinities (EAs) as low as ca.

3 eV. Compared with previously reported DMBI-H and DMBI-I dopants, these dimers exhibited a stronger doping effect, evidently by higher conductivity and larger UPS shifts, in a more diverse array of materials. Kinetic data indicate that the choice of 2-substituent has a significant effect on the kinetics of their reaction with acceptors: (2-Fc-DMBI)$_2$ and (2-Cyc-DMBI)$_2$ are feasible in dissociation and electron transfer mechanisms respectively, while (2-Rc-DMBI)$_2$ doping process is operated in both mechanisms. Moreover, the reactions of both the Y = Cyc and Rc species with TIPSp are very slow at room temperature in the dark, but can be accelerated by exposure to visible light, suggesting that it may be possible to process films of these components rapidly in air, with only minimal decomposition of the dimer and minimal formation of the doping product, and subsequently accomplish the doping through exposure to light. These doping behaviors are similar to previous reported dimers of 19-electron sandwich compounds.

In all, it was found that carefully design of the dimer structure could enable a dopant that has both strong reducing ability, and enough air-stability to be handled in air. Well controlled dissociation energy and redox potential are important factors to determine the reaction pathway, air-stability and doping ability. The mechanistic information could be useful in the development of new dopants/reductants with different properties. Further work about these DMBI dimers will include doping studies with 2D materials, specifically graphene and TMDCs, which will be discussed in Chapter 3 and 4, respectively.

2.5 Experimental

2.5.1 Sample preparation and characterization

All operations were carried out under an atmosphere of nitrogen or argon, unless stated otherwise. Spectrophotometric grade (99.9%) cholorobenzene and *o*-dichlorobenzene were purchased from Alfa Aesar or Sigma-Aldrich and dried over CaH_2 or 4 Å molecular sieves. THF was distilled from sodium benzophenone. After drying, all solvents were collected in Schlenk flasks and degassed by at least three "freeze-pump-thaw" cycles. 6,13-Bis-tri(isopropylsilylethynyl)pentacene (≥99%, HPLC) and C_{60} (>99.5%, sublimation) were purchased from Sigma-Aldrich and used as received. $PC_{61}BM$ was purchased from NanoC. Sodium amalgams used for the dimerizations were freshly prepared before each reaction. Sodium tetrakis(3,5-bis(trifluoromethyl)phenyl)borate ($NaBAr'_4$), and *N*,*N*'-dimethyl-*o*-phenylenediamine were synthesized according to literature reported methods.[19,33-35] Poly{[*N*,*N*'-bis(2-octyldodecyl)-naphthalene-1,4,5,8-bis(dicarboximide)-2,6-diyl]-*alt*-5,5'-(2,2'-bithiophene)} P(NDI2OD-T2) and ruthenocenecarboxaldehyde (RcCHO) were synthesized by Dr. Tissa Sajoto and Dr. Stephen Barlow, respectively. ^1H, ^{13}C, COSY and NOESY NMR spectra were recorded either on a Bruker AMX 400 or 500 MHz NMR spectrometers. The chemical shifts (δ) are reported in parts per million (ppm) relative to a tetramethylsilane (TMS, 0.00 ppm) internal standard. ESI-MS was performed at the University of Washington mass spectrometry center for all of the dimers. A (Leica DM4000M) optical microscope was used to characterize the spin-coated $PC_{61}BM$ films. Atomic force microscopy was executed in the tapping mode on

a Multimode Nanoscope III (Digital Instruments/Veeco Metrology Group).

2.5.2 Synthesis

General procedure for 1,3-dimethyl-2-metallocenyl-2,3-dihydro-1*H*-benzo[*d*]imidazoles, Fc-DMBI-H and Rc-DMBI-H:

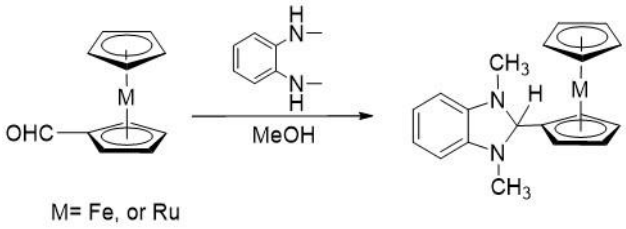

Two drops of acetic acid were added to a mixture of the appropriate metallocene carboxaldehyde (2 mmol), *N*,*N*′-dimethyl-*o*-phenylenediamine (272 mg, 2 mmol), and methanol in a 50 ml flask and the mixture was stirred vigorously. Precipitation was observed within 5 min. After stiring for another 15 min, the crude product was collected by filtration. The solids were then recrystallized from isopropanol to yield Fc-DMBI-H as orange crystals (430 mg, 67%) and Rc-DMBI-H as white needles (438 mg, 58%). **2-Fc-DMBI-H:** ^{1}H NMR (300 MHz, C_6D_6) δ 6.80 (dd, *J* = 5.5, 3.2 Hz, 2H), 6.33 (dd, *J* = 5.4, 3.2 Hz, 2H), 4.62 (s, 1H), 4.12 (t, *J* = 1.9 Hz, 2H), 3.96 (s, 5H), 3.92 (t, *J* = 1.9 Hz, 2H), 2.54 (s, 6H). ^{13}C NMR (75 MHz, CD_3CN) δ 140.14, 118.86, 105.54, 88.82, 87.85, 68.88, 67.79, 66.31, 34.50. Anal. Calcd. for $C_{19}H_{20}N_2Fe$: C, 68.67; H, 6.07; N, 8.44. Found C, 68.53; H, 6.19; N, 8.44. **2-Rc-DMBI-H:** ^{1}H NMR (400 MHz, C_6D_6) δ 6.85 (dd, *J* = 5.4, 3.2 Hz, 2H), 6.38 (dd, *J* = 5.4, 3.2 Hz, 2H), 4.67 (t, *J* = 1.7 Hz, 2H), 4.51 (s, 1H), 4.43 (s, 5H), 4.39 (t, *J* = 1.7 Hz, 2H), 2.55 (s, 6H). ^{13}C{^{1}H} NMR (101 MHz, C_6D_6) δ 142.34, 119.29, 105.77, 91.49, 88.84, 71.26, 69.90, 69.58, 34.63. Anal. Calcd. for $C_{19}H_{20}N_2Ru$: C, 60.46; H, 5.34; N, 7.42. Found: C, 60.19; H, 5.17; N, 7.35.

General procedure for 1,3-dimethyl-2-metallocenyl-2,3-dihydro-1*H*-benzo[d]imidazolium tetrakis(3,5-bis(trifluoromethyl)phenyl)borate salts, Fc-DMBI-BAr'$_4$ and Rc-DMBI-BAr'$_4$:

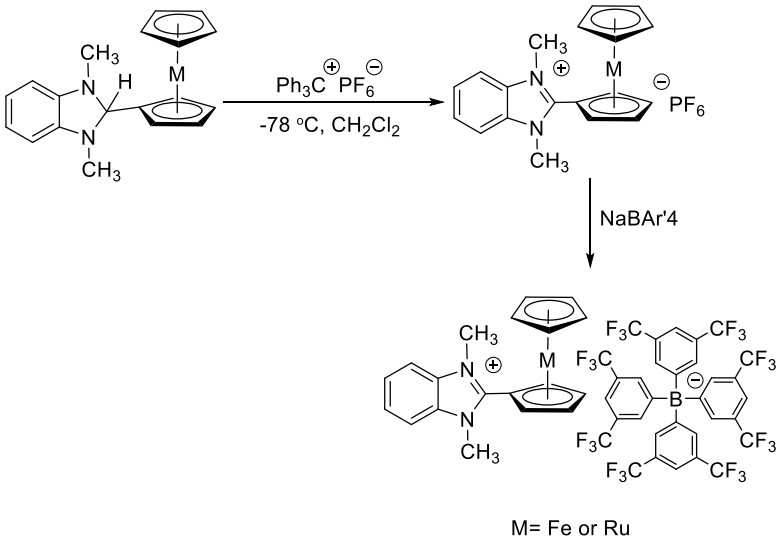

In a 50 ml round-bottomed flask, a solution of the appropriate DMBI-H derivative (0.2 mmol) in dichloromethane (4 ml) was cooled to –20 °C. A solution of triphenylmethyl hexafluorophosphate (77.66 mg, 0.2 mmol) in dichloromethane (5 ml) solution was added dropwise. The mixture was stirred for 30 min at –20 °C, then brought to room temperature for another 2 h. Upon warming, the color changed from yellow to red (Fc-DMBI), or white to yellow (Rc-DMBI). The solvent was removed under reduced pressure, and the solid residue was washed with hexane (3 × 100 mL), then dried to afford the benzimidazolium hexafluorophosphate salt. A equimolar mixture of the benzimidazolium hexafluorophospate salt (0.1 mmol) and sodium tetrakis[3,5-bis(trifluoromethyl)phenyl]borate (0.1 mmol) in dichloromethane (20 ml) was stirred for 30 min. The solution was concentrated and passed through a short silica gel column, eluting with dichloromethane to give pure tetrakis[3,5-

bis(trifluoromethyl)phenyl]borate salts, Fc-DMBI-BAr'$_4$ as a red solid (109 mg, 85%) and Rc-DMBI-BAr'$_4$ as a yellow solid (117 mg, 79%). **2-Fc-DMBI$^+$-BAr'$_4$:** ^{1}H NMR (500 MHz, CD_3CN) δ 7.82 (dd, *J* = 6.2, 3.1 Hz, 2H), 7.78 (s, 8H), 7.71 (s, 4H), 7.67 (dd, *J* = 6.2, 3.1 Hz, 2H), 5.04 (t, *J* = 1.9 Hz, 2H), 4.91 (t, *J* = 1.9 Hz, 2H), 4.46 (s, 5H), 4.19 (s, 6H). $^{13}C\{^1H\}$ NMR (126 MHz, CD_3CN) δ 161.54 (1:1:1:1 q, J_{BC} = 50 Hz, Ar' C_{ipso}), 152.37, 134.52 (Ar' C_o), 132.36, 128.86 (qq, J_{CF} = 32, ca. 3 Hz, Ar' C_m), 127.68, 124.33 (q, J_{CF} = 273 Hz, CF_3), 117.51(septet, J_{CF} = ca. 4 Hz, Ar' C_p), 117.06 , 112.09, 72.38, 71.39, 70.54, 33.24. ^{19}F NMR (471 MHz, CD_3CN) δ -64.52 (s). Anal. Calcd. for $C_{51}H_{31}BF_{24}FeN_2$: C, 51.28; H, 2.62; N, 2.35. Found: C, 51.38; H, 2.60; N, 2.42. **2-Rc-DMBI-BAr'$_4$:** ^{1}H NMR (400 MHz, CD_3CN) δ 7.77 (dd, *J* = 6.2, 3.2 Hz, 2H), 7.70 (s, 8H), 7.67 (s, 4H), 7.65 (dd, *J* = 6.3, 3.2 Hz, 2H), 5.27 (t, *J* = 1.8 Hz, 2H), 5.10 (t, *J* = 1.8 Hz, 2H), 4.79 (s, 5H), 4.06 (s, 6H). $^{13}C\{^1H\}$ NMR (101 MHz, CD_3CN) δ 161.63 (1:1:1:1 q, J_{BC} = 50 Hz, Ar' C_{ipso}), 151.01, 132.38 (Ar' C_o), 129.45, 126.54, 128.98 (qq, J_{CF} = 31, ca. 3 Hz, Ar' C_m), 124.5 (q, J_{CF}= 273 Hz, CF_3), 117.56 (septet, J_{CF} = ca. 4 Hz, Ar' C_p), 112.39, 73.81, 73.12, 73.12, 68.66, 33.53. ^{19}F NMR (471 MHz, CD_3CN) δ -64.50. Anal. Calcd. for $C_{51}H_{31}BF_{24}RuN_2$: C, 49.41; H, 2.52; N, 2.26. Found: C, 49.34; H, 2.58; N, 2.33.

General procedure for (2-Fc-DMBI)$_2$ and (2-Rc-DMBI)$_2$:

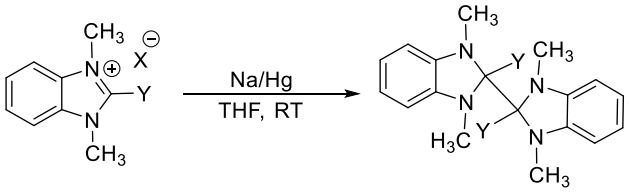

X = BAr'$_4$ {Ar' = 3,5-$(CF_3)C_6H_3$}
Y = ferrocenyl, ruthenocenyl

Sodium-amalgam (1 wt%) was prepared by adding small pieces of sodium

metal (280 mg, 12 mmol) to vigorously stirred Hg (28 g, 0.14 mol) under a flow of nitrogen. A solution of the relevant DMBI-BAr'$_4$ salt (2 mmol) in THF (10 ml) was added into the flask, and the mixture was stirred at room temperature for 2 h, filtered through Celite, and evaporated THF under reduced pressure. The solid residue was transferred into a glovebox, re-dissolved in a minimum amount of benzene, and passed through a short triethylamine-treated silica gel column, eluting with benzene to yield pure dimers, (2-Fc-DMBI)$_2$ (503 mg, 38%) as a rusty solid, and (2-Rc-DMBI)$_2$ (450 mg, 30%) as a white solid. **(2-Fc-DMBI)$_2$:** ^{1}H NMR (500 MHz, C_6D_6) δ 6.80 (dd, *J* = 5.3, 3.1 Hz, 4H), 6.11 (dd, *J* = 5.3, 3.1 Hz, 4H), 4.10 (br s, 4H), 3.96 (t, *J* = 1.8 Hz, 4H), 3.77 (s, 10H), 2.58 (s, 12H). ^{13}C{^{1}H} NMR (101 MHz, C_6D_6): δ 140.56, 134.99, 127.90, 117.85, 101.42, 69.69, 68.85, 67.27, 32.60; ESI-MS *m/z*: 331.1 (M/2$^+$). Anal. Calcd. for $C_{38}H_{38}Fe_2N_4$: C, 68.90; H, 5.78; N, 8.46. Found: C, 69.18; H, 5.93; N, 8.29. **(2-Rc-DMBI)$_2$:** ^{1}H NMR (500 MHz, C_6D_6) δ 6.79 (dd, *J* = 5.2, 3.1 Hz, 4H), 6.06 (dd, *J* = 5.2, 3.1 Hz, 4H), 4.64 (t, *J* = 1.6 Hz, 4H), 4.40 (t, *J* = 1.6 Hz, 4H), 4.19 (s, 10H), 2.58 (s, 12H). ^{13}C{^{1}H} NMR (101 MHz, C_6D_6): δ 140.41, 117.88, 101.81, 94.22, 91.94, 72.37, 71.45, 69.51, 32.46; ESI-MS = 337.1(M/2$^+$). Anal. Calcd. for $C_{38}H_{38}Ru_2N_4$: C, 60.62; H, 5.09; N, 7.44. Found: C, 60.33; H, 5.38; N, 7.15.

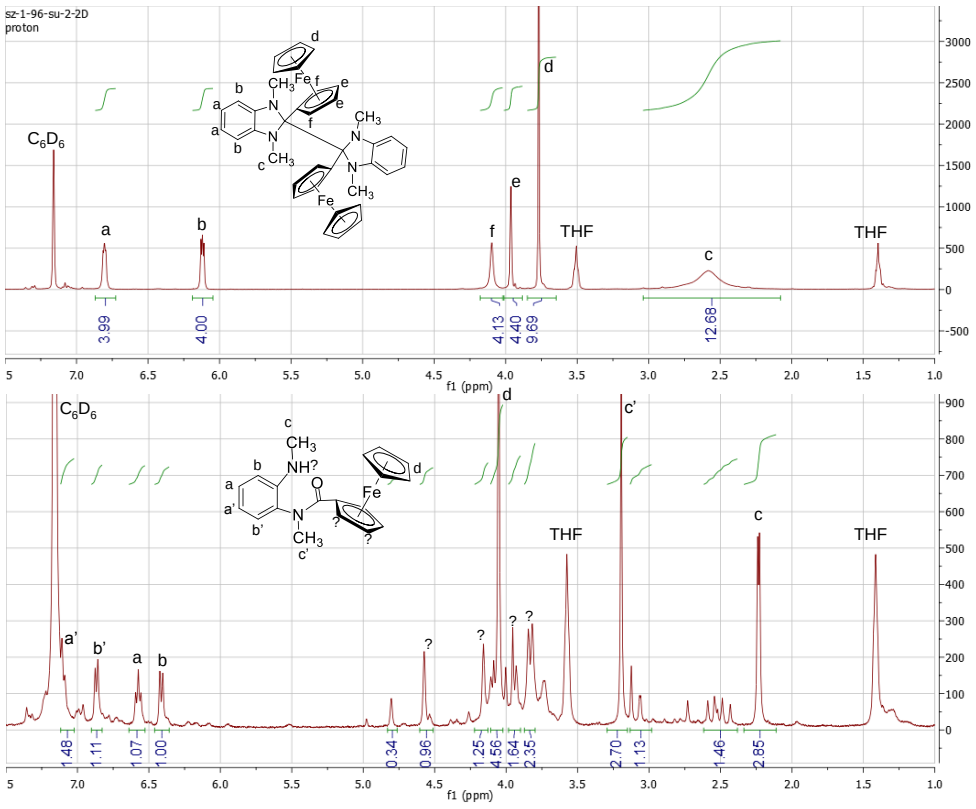

Figure 2.28 ^{1}H NMR for (2-Fc-DMBI)$_2$ in C_6D_6 (top), and same solution after exposure to air and heating over 150 °C, showing formation of the corresponding amide.

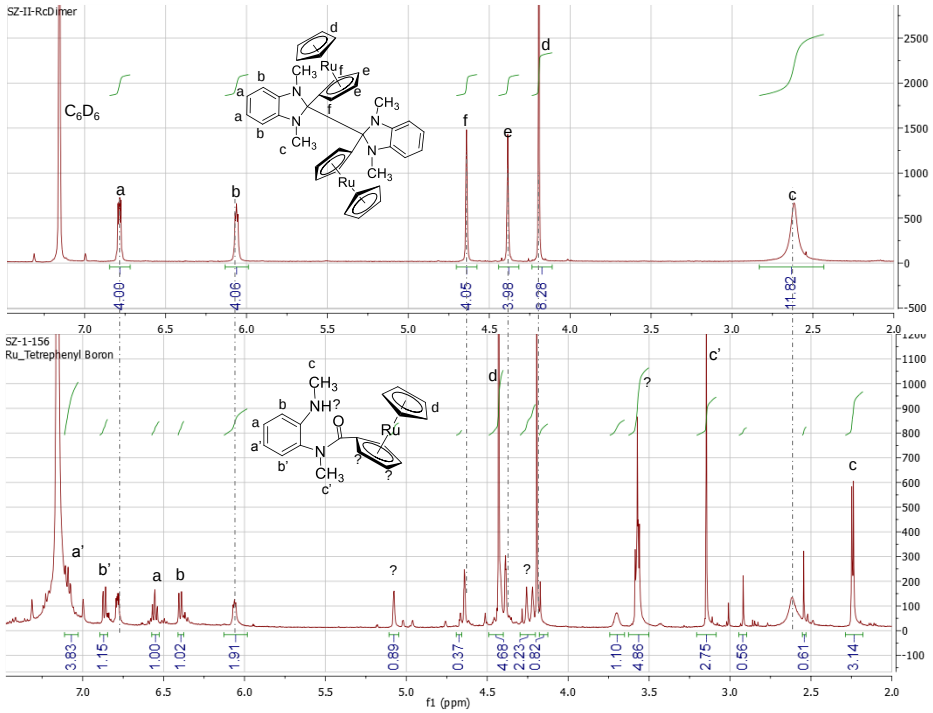

Figure 2.29 ^{1}H NMR spectrum for (2-Rc-DMBI)$_2$ in C_6D_6 (top), and same solution after exposure to air and heating over 150 °C showing partial conversion to the corresponding amide.

2.5.3 Instrumental

UV-Vis-NIR Kinetic Measurements. Measurements were performed on a Varian Cary 5E UV-Vis-NIR spectrometer. All of the samples were prepared in a glove-box at room temperature. Upon mixing, the solutions were transferred to a clean 1 mm path length PTFE-stopcock-sealed quartz cuvette (175 – 2700 nm), and the UV-Vis-NIR measurement was started as rapidly as possible. The temperature for the cuvette holder was controlled by a Quantum Northwest TC 125 temperature controller.

Ultraviolet Photoelectron Spectroscopy. UPS Spectra were measured on Kratos Axis Ultra^{DLD} XPS/UPS system, using He-I lamp radiation at 21.2 eV. All samples were spin coated in a glovebox, and transferred through a Kratos air-sensitive transporter without air exposure. UPS was acquired at 5 eV pass energy and 0.05 eV step size with the aperture and iris set to 55 μm. The Fermi level was calibrated using sputtered clean silver. From the secondary electron edge (SEE) of the spectra, the work function (φ) can be calculated for each film by subtracting the SEE from the total radiation energy (21.22 eV). The position of the valence-band maximum can be determined from the onset of photoemission.

Details of Crystal Structure Determinations

The crystal structures for the dimers were determined by Dr. Evgheni V. Jucov in the group of Dr. Tatiana Timofeeva at New Mexico Highlands University. Parameters relating to data collection and the structural refinements are summarized below in Table S1.

Table 2.5 Selected Crystal and Refinement Parameters for the Crystal Structure Determinations.

	$(2\text{-Cyc-DMBI})_2$	$(2\text{-Fc-DMBI})_2$
Crystal growth	Hexane, –20 °C	Layering C_6D_6 solution with heptane
Crystal appearance	Colorless slab	Orange plate
Crystal size / mm^3	0.18 × 0.10 × 0.08	0.20 × 0.10 × 0.05
Empirical formula	$C_{30}H_{42}N_4$	$C_{38}H_{38}Fe_2N_4$
FW	458.67	662.42
Diffractometer	Bruker-Nonius X8 CCD	Bruker APEX-II CCD
λ Å	1.54178	0.71073
T / K	150[a]	100
Crystal System	Trigonal	Triclinic
Space group	$P3_221$	$P\overline{1}$
a / Å	10.8746(15)	9.893(4)
b / Å	10.8746(15)	11.047(4)
c / Å	19.181(4)	13.583(5)
α / °	90	80.276(5)
β / °	90	87.345(5)
γ / °	120	85.280(5)
V / $Å^3$	1964.4(7)	1457.4(10)
Z	3	2
ρ(calcd) / Mg m^{-3}	1.163	1.510
μ / mm^{-1}	0.522	1.032
F(000)	750	836
θ range for data / °	4.70-68.39	4.17-25.00
Index ranges	$-11 \le h \le 13$	$-11 \le h \le 11$
	$-13 \le k \le 10$	$-13 \le k \le 13$
	$-18 \le l \le 23$	$-16 \le l \le 16$
Reflections collected	24907	11384
Independent reflection (R_{int})	2404 (0.0372)	5084 (0.0246)
Reflections with $I > 2\sigma(I)$	2357	4450
T_{min}, T_{max}	0.859, 0.942	0.6645, 0.7460
Data / restraints / parameters	2404 / 0 / 156	5084 / 0 / 401
Goodness-of-fit on F^2	1.041	0.999
Final $R1$, $wR2$ [$I >$	0.0383, 0.1045	0.0339, 0.0863

2 (*I*)]		
Final *R*1, *wR*2 (all data)	0.0389, 0.1053	0.0399, 0.0896
Largest peak and hole / e Å^{-3}	0.235, –0.213	0.403, –0.367

[a] At temperatures below ~125K, additional diffuse diffraction was observed, consistent with a reduction of symmetry. On warming these extra spots disappeared, and were completely gone at 150K.

2.6 References

(1) Kahn, A.; Koch, N.; Gao, W. *J. Polym. Sci.* **2003**, *41*, 2529.

(2) Zhan, X.; Facchetti, A.; Barlow, S.; Marks, T. J.; Ratner, M. A.; Wasielewski, M. R.; Marder, S. R. *Adv. Mater.* **2011**, *23*, 268.

(3) Lüssem, B.; Riede, M.; Leo, K. *Phys. Status Solidi (a)* **2013**, *210*, 9.

(4) Parthasarathy, G.; Shen, C.; Kahn, A.; Forrest, S. R. *J. Appl. Phys.* **2001**, *89*, 4986.

(5) Kido, J.; Matsumoto, T. *Appl. Phys. Lett.* **1998**, *73*, 2866.

(6) Werner, A. G.; Li, F.; Harada, K.; Pfeiffer, M.; Fritz, T.; Leo, K. *Appl. Phys. Lett.* **2003**, *82*.

(7) Li, F.; Werner, A.; Pfeiffer, M.; Leo, K.; Liu, X. *J. Phys. Chem. B* **2004**, *108*.

(8) Peng, W.; Torben, M.; Benjamin, D. N.; Karl, L.; Moritz, R.; Zhenan, B. *J. Am. Chem. Soc.* **2012**, *134*.

(9) Li, C.-Z.; Chueh, C.-C.; Ding, F.; Yip, H.-L.; Liang, P.-W.; Li, X.; Jen, A. K. Y. *Adv. Mater.* **2013**, *25*, 4425.

(10) Peng, W.; Joon Hak, O.; Guifang, D.; Zhenan, B. *J. Am. Chem. Soc.* **2010**, *132*.

(11) Guo, S.; Kim, S.; Mohapatra, S.; Qi, Y.; Sajoto, T.; Kahn, A.; Marder, S.; Barlow, S. *Adv. Mater.* **2012**, *24*, 699.

(12) Mohapatra, S. K.; Fonari, A.; Risko, C.; Yesudas, K.; Moudgil, K.; Delcamp, J. H.; Timofeeva, T. V.; Brédas, J.-L.; Marder, S. R.; Barlow, S. *Chem. Eur. J.* **2014**, *20*, 15385.

(13) Limmert, M.; Hartmann, H.; Zeika, O.; Werner, A.; Ammann, M. In *Eur. Pat. Appl.* 2007; Vol. EP 1837926 A1 20070926.

(14) Zeika, O.; Limmert, M.; Gruessing, A.; Lux, A.; Hartmann, H.; Werner, A. In *Eur. Pat. Appl.* 2007; Vol. EP 1837927 A1 20070926.

(15) Weber, C.; Bradley, C.; Lonergan, M. *J. Mater. Chem. A* **2014**, *2*, 303.

(16) Guo, S.; Mohapatra, S.; Romanov, A.; Timofeeva, T.; Hardcastle, K.; Yesudas, K.; Risko, C.; Brédas, J.-L.; Marder, S.; Barlow, S. *Chem. Eur. J.* **2012**, *18*, 14760.

(17) Qi, Y.; Mohapatra, S. K.; Bok Kim, S.; Barlow, S.; Marder, S. R.; Kahn, A. *Appl. Phys. Lett.* **2012**, *100*, 083305.

(18) Naab, B. D.; Zhang, S.; Vandewal, K.; Salleo, A.; Barlow, S.; Marder, S. R.; Bao, Z. *Adv. Mater.* **2014**, *26*, 4268.

(19) Zhu, X.-Q.; Zhang, M.-T.; Yu, A.; Wang, C.-H.; Cheng, J.-P. *J. Am. Chem. Soc.* **2008**, *130*, 2501.

(20) Sutton, L. E.; Mitchell, A.; Sommerfeld, A.; Cross, L. *Tables of interatomic distances and configuration in molecules and ions, Supplement 1956-1959*; Chemical Society, 1965.

(21) Wadepohl, H.; Lieth, C.-W. V. D.; Paffen, F.-J.; Pritzkow, H. *Chem. Ber.* **1995**, *128*, 317.

(22) Rüchardt, C.; Beckhaus, H.-D. *Angew. Chem. Int. Ed.* **1985**, *24*, 529.

(23) Gaudet, M. V.; Hanson, A. W.; White, P. S.; Zaworotko, M. J. *Organometallics* **1989**, *8*, 286.

(24) Frisch, M. J.; Trucks, G. W.; Schlegel, H. B.; G. E. Scuseria; Robb, M. A.; Cheeseman, J. R.; Scalmani, G.; Barone, V.; Mennucci, B.; Petersson, G. A.; Nakatsuji, H.; Caricato, M.; Li, X.; Hratchian, H. P.; Izmaylov, A. F.; Bloino, J.; Zheng, G.; Sonnenberg, J. L.; M. Hada; Ehara, M.; Toyota, K.; Fukuda, R.; Hasegawa, J.; Ishida, M.; Nakajima, T.; Honda, Y.; Kitao, O.; Nakai, H.; Vreven, T.; Montgomery, J. A.; Peralta, J. E.; Ogliaro, F.; Bearpark, M.; Heyd, J. J.; Brothers, E.; Kudin, K. N.; Staroverov, V. N.; Keith, T.; Kobayashi, R.; Normand, J.; Raghavachari, K.; Rendell, A.; Burant, J. C.; Iyengar, S. S.; Tomasi, J.; Cossi, M.; Rega, N.; Millam, J. M.; Klene, M.; Knox, J. E.; Cross, J. B.; Bakken, V.; Adamo, C.; Jaramillo, J.; Gomperts, R.; Stratmann, R. E.; Yazyev, O.; Austin, A. J.; Cammi, R.; Pomelli, C.; Ochterski, J. W.; Martin, R. L.; Morokuma, K.; Zakrzewski, V. G.; Voth, G. A.; Salvador, P.; Dannenberg, J. J.; Dapprich, S.; Daniels, A. D.; Farkas, O.; Foresman, J. B.; Ortiz, J. V.; Cioslowski, J.; Fox, D. J. In *Gaussian 09, Revision B.01*; Gaussian Inc.: Wallingford CT, 2010.

(25) Zhao, Y.; Truhlar, D. *Theor. Chem. Acc.* **2008**, *120*, 215.

(26) Zhang, S.; Naab, B. D.; Jucov, E. V.; Parkin, S.; Evans, E. G. B.; Millhauser, G. L.; Timofeeva, T. V.; Risko, C.; Brédas, J.-L.; Bao, Z.; Barlow, S.; Marder, S. R. *Chem. Eur. J.* **2015**, *21*, 10878.

(27)http://www.niehs.nih.gov/research/resources/software/tox-pharm/tools/index.cfm, accessed Apr. 2015.

(28) Naab, B.; Himmelberger, S.; Diao, Y.; Vandewal, K.; Wei, P.; Lussem, B.; Salleo, A.; Bao, Z. *Adv. Mater.* **2013**, *25*, 4663.

(29) Watts, W. E. In *Comprehensive Organometallic Chemistry*; Wilkinson, G., Stone, F. G. A., Abel, E. W., Ed.; Pergamon: London, 1988; Vol. 8.

(30) Gleiter, R.; Bleiholder, C.; Rominger, F. *Organometallics* **2007**, *26*, 4850.

(31) Naab, B.; Guo, S.; Olthof, S.; Evans, E.; Wei, P.; Millhauser, G.; Kahn, A.; Barlow, S.; Marder, S.; Bao, Z. *J. Am. Chem. Soc.* **2013**, *135*, 15018.

(32) Yan, H.; Chen, Z.; Zheng, Y.; Newman, C.; Quinn, J. R.; Dötz, F.; Kastler, M.; Facchetti, A. *Nature* **2009**, *457*, 679.

(33) Chen, Z.; Zheng, Y.; Yan, H.; Facchetti, A. *J. Am. Chem. Soc.* **2009**, *131*, 8.

(34) Brookhart, M.; Grant, B.; Volpe, A. F. *Organometallics* **1992**, *11*, 3920.

(35) Sanders, R. *J. Organomet. Chem* **1996**, *512*, 219.

CHAPTER 3 n- and p-Doping of Graphene and CNTs with Various Solution- processed Redox-active Species

3.1 Introduction

Ever since Dr. Andre Geim and Dr. Kostya Novoselov were able to isolate graphene in 2004, later winning the Nobel Prize for this discovery,[1,2] graphene has emerged as a viable alternative to commonly used materials in various applications due to its unique properties: it is the strongest material ever discovered, with an ultimate tensile strength of 130 GPa, yet it remains extremely light and flexible; it is highly transparent, absorbing only 2% in visible range (for single layer graphene); it has a thermal conductivity that is 10 times greater than copper; and has an electrical mobility of 1500 $cm^2 V^{-1} s^{-1}$ with a theoretical potential limit that is much higher.[2]

One of the applications envisaged for large-area graphene is as the transparent conductive electrode (TCE) in flexible electronics.[3,4] The most commonly used material is indium titanium oxide (ITO); however, intrinsically, ITO is brittle, and not as flexible as would be ideal for future flexible electronics applications.[5-7] Moreover, the supply of indium is unreliable, leading to large price surges. Apart from graphene, other possible alternatives to ITO for TCE applications include metallic nanowires,[5,8] conducting polymers,[9,10] and carbon nanotubes (CNTs).[11,12] The sheet resistance and transmittance of these materials is summarized in Figure 3.1 using the solar spectrum as a reference for transmission evaluation. Many of these materials have fulfilled standard requirements on the transmission values of TCE, and can be fabricated by low-cost processes, such as spin coating, spray coating and even roll-to-roll processes.

However, many of the TCE candidates still the have problems of large sheet resistance, high surface roughness, and poor thermal and/or chemical stability. For chemical vapor deposition (CVD) grown graphene, the sheet resistance is normally in the range between 1000 to 2000 Ω/sq, and the highest quality CVD grown graphene has a sheet resistance of ca. 125 Ω/sq,[3] while commercial available ITO has sheet resistance of 10 to 20 Ω/sq. Before graphene becomes a truly viable alternative, the issue of its resistance must be resolved. Doping is an effective way to tailor the electrical properties, and it can be used to introduce charge carriers and decrease the sheet resistance.

In this chapter, doping studies of two TCE candidates, graphene and CNTs, were conducted, with the aim to tailor their electrical properties and decrease the sheet resistances. After a brief discussion of the electronic properties of graphene and the state of art for graphene doping strategies, chemical doping of graphene using sub-monolayer adsorption of redox-active molecules is studied, and shown to increase its conductivity while maintaining transparency. The n-doped single-layer (SGL) graphene films using dimeric and monomeric dopants were characterized by GFET, two- and four-point probe measurements, UPS, and XPS. Detailed analysis of $(2\text{-Fc-DMBI})_2$ and 2-H-Fc-DMBI is conducted to quantify the doping ability of different dopants, calculate the electron-transfer efficiency, and compare the doping strength. This chapter also demonstrates the p-doping of SGL graphene using four oxidants, and a large reduction of the sheet resistance was observed. As well as graphene, metallic and semiconducting CNTs were also characterized using the same doping strategies, characterized by the transistor and sheet resistance measurements. Detailed synthesis, transfer methods, and

device fabrications are described in the Experimental Section (on Page 141).

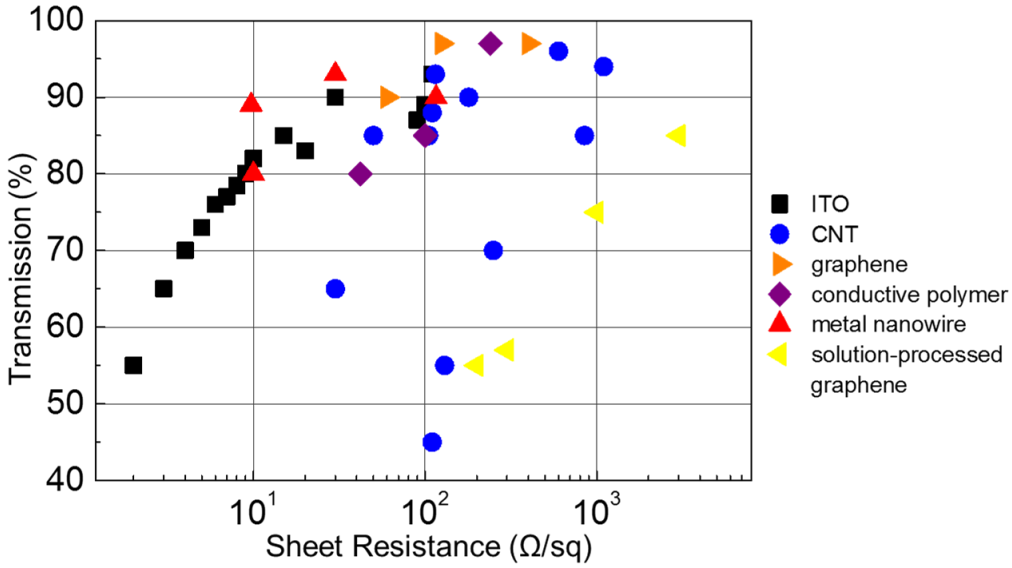

Figure 3.1 Sheet resistance versus optical transmission for popular transparent electrodes, including ITO,[13] CNTs,[11,12,14] graphene,[3,15] conductive polymer,[9,16,17] metal nanowire,[5,8,18] and solution-processed graphene.[19]

3.2 Modulation of electronics properties of graphene

Graphene contains only sp^2 hybrid carbon atoms with s, p_x and p_y atomic orbitals on each carbon atom forming three strong σ bonds with three surrounding atoms. Overlap of the remaining p_z orbital on each carbon atom forms a filled band of π orbitals and empty band of π* orbitals, which known as valence band and conduction band, respectively. The valence and conduction bands touch at the Brillouin zone corners, which leaves graphene a zero-band-gap semi-metal.[20] Figure 3.2 shows the energy spectrum of graphene and zoom-in of the energy bands at one point (Dirac point). Thus, graphene has zero band gap in its pristine state and is a semimetal, with I_{ON}/I_{OFF} ratios typically less than 10 in transistor measurements.[21] There are many ongoing experiments attempting to controllably open a band gap using a variety of approaches as discussed in Chapter 1.[21,22]

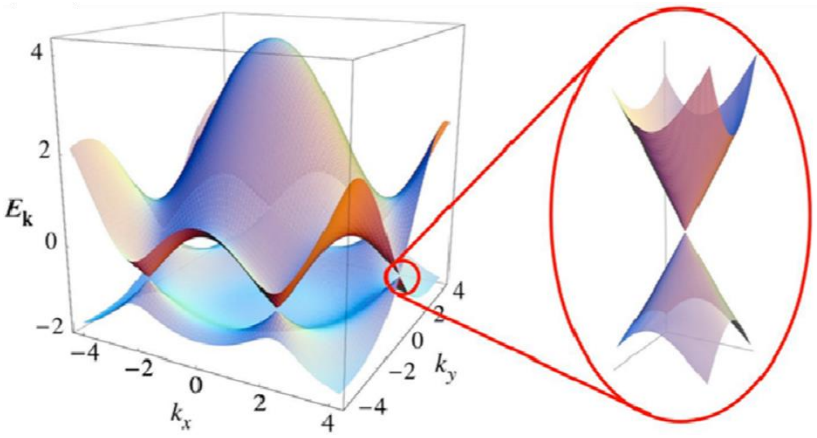

Figure 3.2 Electronic dispersion in the honeycomb lattice. Inset of the energy bands close to one of the Dirac points. Adapted from Neto, *et al.*[20]

In its undoped state, the Fermi level (E_F) corresponds to the point with lowest density of states (DOS) where the two bands meet, and the conductivity of graphene is at its minimum. The E_F can be controlled by application of external electric and magnetic fields, or by altering sample geometry and/or topology.[20] As shown in Figure 3.3, the charge-carrier density can be increased by applying a gate voltage, where the Dirac cones can be emptied or filled by applied negative or positive voltage, respectively. In this case, an external electric field is needed to increase the carrier density, and thus, the conductivity of the graphene.

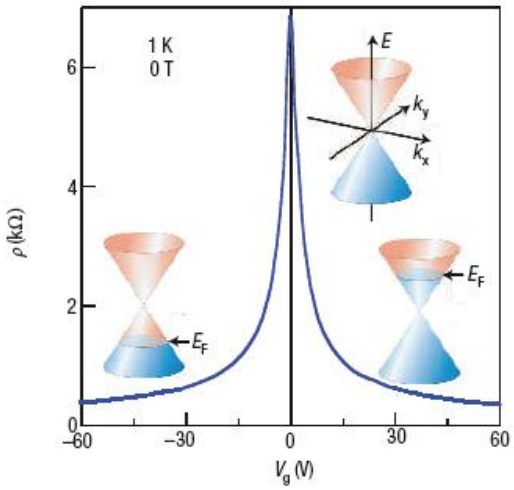

Figure 3.3 Typical resistivity as function of gate voltage in a GFET. The filling or emptying if the Dirac cones is shown. Reproduced from Geim, *et al*.[23]

Alternatively, a more practical way to permanently induce charge carriers into graphene is via adsorption of electron- and hole-donating molecules, while electro-gating graphene can serve as a research tool to characterize the doping effects.[22,24-28] As summarized in Table 3.1, there are precedents using various species leading to n- or p-doping effects.

Table 3.1 Literature reported doping methods of graphene.

	N-Type	**P-Type**
(1) Metal atoms	Potassium (K)[29]	Antimony (Sb) and gold (Au)[30]
2) (2) Gases	Ammonia (NH_3)[28,31]	NO_2 and Br_2[32-35]
(3) Substitution of carbon with foreign atoms	Nitrogen (N)[36,37]	Boron (B)[37]
(4) Organic molecules	PEIE, APTS, and H-N-DMBI [38-40]	FTS and F_4-TCNQ[22,38,41,42]

Firstly, metal atoms with low ionization energy (IE), such as potassium (K) or sodium (Na),[22,29] or high electron affinity (EA) including bismuth (Bi), antimony (Sb) and gold (Au),[30,43] have been used on the surface of graphene to induce n- or p-doping effects, respectively. These techniques will require deposition in an ultra-high vacuum (UHV) chamber through high-energy evaporation method to deposit atomically thin

metal layers, which may damage the graphene, and the resulting metal cations act as charge-scattering centers, significantly reducing the mobility. Moreover, low IE metals are highly reactive, so this doping method is difficult to implement in device technology. Secondly, absorption of gases on the surface through physi- and/or chemisorption has also been used for graphene modification, examples include using ammonia (NH_3) for n-doping, and NO_2 or Br_2 for p-doping effects.[28,32,33,35,44,45] The physisorbed gases, such as Br_2, can be easily de-doped in vacuum with low temperature annealing. Chemisorption, on the other hand, happens through substitution of the original atom, which could disturb the original band structure, and degenerate the device.[46] Thirdly, substitution of the carbon by incorporating foreign atoms into the basal plane of graphene can also lead to strong doping effects: n-doping is achieved through adding atoms with more valence electrons than carbon, such as nitrogen, while p-doping by substituting carbon with atoms with fewer valence electrons, such as boron. In this case, the band structure of the graphene is modified, where larger on/off ratio is observed, but with the cost of losing conductivity and mobility.[36,37] However, the detailed mechanism of substitutional doping still remains uncertain.

The fourth kind of modification method used for graphene is the use of organic (or metal-organic) molecules. As shown in Figure 3.4, molecules with electron-withdrawing groups or electron-rich groups, such as PEIE, APTS, and FTS, can induce a partial charge transfer of a Lewis acid-base type of interaction. Molecular reductants and oxidants, such as H-N-DMBI and F_4-TCNQ, have also been used on the graphene surface where an irreversible fully charge transfer happens. For example, previously

mentioned H-N-DMBI is applied for graphene doping. The E_F of graphene can be tuned significantly by spin-coating the dopant solutions on the graphene sheets at different concentrations.[40] For p-doping, the most widely used dopant has been 2,3,5,6-tetrafluorocyanoquino-dimethane (F_4-TCNQ), given its large electron affinity (estimated at 5.24 eV[47]), a consequence of the electron withdrawing fluorine atoms and cyano groups present. The hole transfer is accompanied by a significant surface dipole due to the electron cloud rearrangement after the charge transfer.[48] However, F_4-TCNQ is very volatile, inter-diffuses in organic films,[49,50] and shows low solubility in most solvents, which has limited its application. In previous works in the Marder group, the n- dopant $(RhCpCp^*)_2$ and p-dopant molybdenum tris-[1,2-bis(trifluoromethyl)ethane-1,2-dithiolene], $Mo(tfd\text{-}COCF_3)_3$ (shown in Figure 3.4) were used to dope SGL CVD graphene.[51] Controllable n- and p-doping of graphene was realized by using solutions of redox-active metal–organic dopants. The doped graphene films were characterized by graphene field-effect transistors (FETs), XPS and UPS. Large carrier densities can be achieved (characterized by FETs) and the WF can be tuned over a range of 1.8 eV.[51]

In this chapter, the types of redox-active molecules used for graphene doping are expanded, and the graphene is served as a test bed for a series of dopants, where the doping power are compared under the same conditions. This is important to recognize the strengths of existing dopants to inform future dopant design. The doped films were also characterized systematically using FETs, XPS, and UPS. More importantly, the sheet resistance of the doped graphene films were measured through different techniques, which confirmed the strong doping effects.

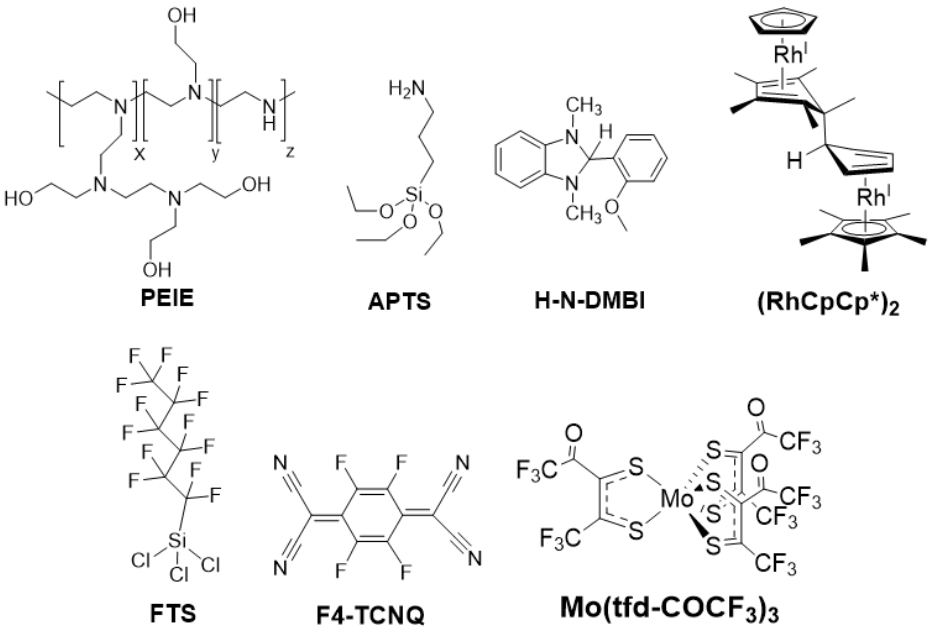

Figure 3.4 Chemical structure of chemicals used for graphene modification.

3.3 Techniques used in this chapter

This section will give a brief introduction about the techniques used in this chapter, include the field-effect transistor (FET), and four- and two-point probe method for sheet resistance and contact resistance measurements.

As mentioned earlier, the electrical properties of graphene can be measured in a transistor configuration. Figure 3.5(a) illustrates the side view of a bottom-gated, bottom-contact FET, where gold contacts were deposited on a dielectric insulator (typically SiO_2) that was grown from highly doped Si. CVD graphene is transferred on top. The charge carrier density can be tuned by applying a gate voltage at the doped silicon substrate. This gate voltage induces a surface charge density as in Equation 3.1:

Equation 3.1
$$\boldsymbol{n = \frac{\epsilon_r \epsilon_0 V_G}{te} = \frac{C_G V_G}{e}}$$

where $\epsilon_r \epsilon_0$ is the permittivity of the dielectric, t is its thickness, and V_G is the gate voltage applied. The permittivity and thickness can be accounted for in a capacitance

per area C_G.

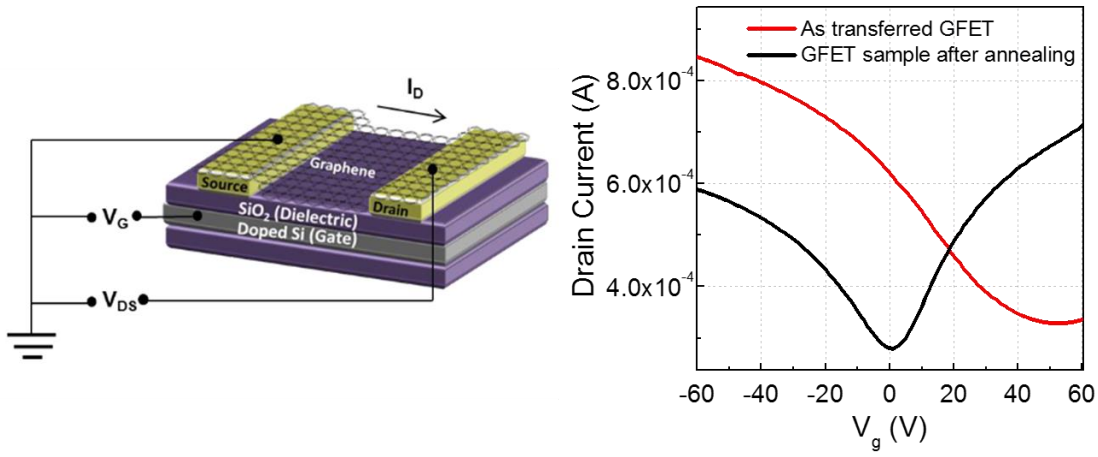

Figure 3.5 (a) Setup of the transistor with graphene as the active layer,[52] (b) GFET transfer characteristics before and after thermal annealing under N_2.

As shown in Figure 3.5(b), the as-transferred GFET sample is p-doped unintentionally. This is typical for CVD graphene, which often involves the removal of the graphene from its metal growth substrate, followed by transfer to a target substrate for device fabrication. This process involves exposing the graphene to both aqueous and atmospheric gas environments, resulting in the attachment of a host of chemical groups to the graphene. Large surface-to-volume ratio makes graphene extremely sensitive to the environment. The O_2 and H_2O trapped between graphene and SiO_2 substrate can induce p-doping effects.[53] A common method for desorption of chemical groups, oxygen, and moisture from graphene is through thermal annealing. Thus, all GFET samples used in this research were annealed in the glovebox at 200 °C for few minutes until the neutrality point (where the conductivity drops to a finite minimum value) was back to zero after removal of the physisorbed species.

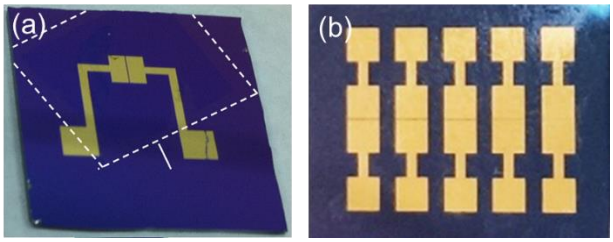

Figure 3.6 Optical images for the FETs used in this research. (a) FET with 50 µm channel length, and have graphene transferred on the top, (b) FETs with various channel length (20 to 60 µm) for contact resistance measurements.

In this research, the sheet resistance measurements were measured by using both two-point probe and four-point probe methods. The contact resistances in n- and p-doped GFETs were also measured. In the two point probe method, two voltage probes are at a fixed spacing distance and are moved together along the material surface. Current is sent through one probe and exits through the second probe. The graphene used in this research only shows Ohmic behavior. By combining both the voltage and current measurements into the two surface probes, the material surface resistance between the two probes can be calculated using the equation:

Equation 3.2 $$R_T = \frac{\partial V_{SD}}{\partial I_{SD}} = R_{ch} + 2R_C = \frac{L}{W\mu C(V_G - V_T)} + 2R_C = \alpha L + 2R_C$$

$$R_{ch} = \alpha L = R_{sh}\frac{L}{W},$$

Equation 3.3 $$\text{thus, } R_{sh} = \alpha \cdot W$$

where, R_T is the total resistance, R_{ch} is the channel resistance. R_c is the contact resistance. V_{SD} and I_{SD} are the source-drain voltage and current, respectively. L is the channel length, and W is the channel width, as shown in Figure 3.7(a). V_G is the gate voltage and V_T is the intrinsic threshold voltage, μ is the intrinsic mobility, C is the capacitance of the gate dielectric. R_{ch} is proportional to the channel length while other parameters keep constant. Thus, by measuring the R_T at various the channel length, the linear plot of R_T

versus L will give the information about the sheet resistance (R_{sh}) and R_c, which can be calculated from the intercept and the slope of the linear fit (shown inFigure 3.7 (c)).

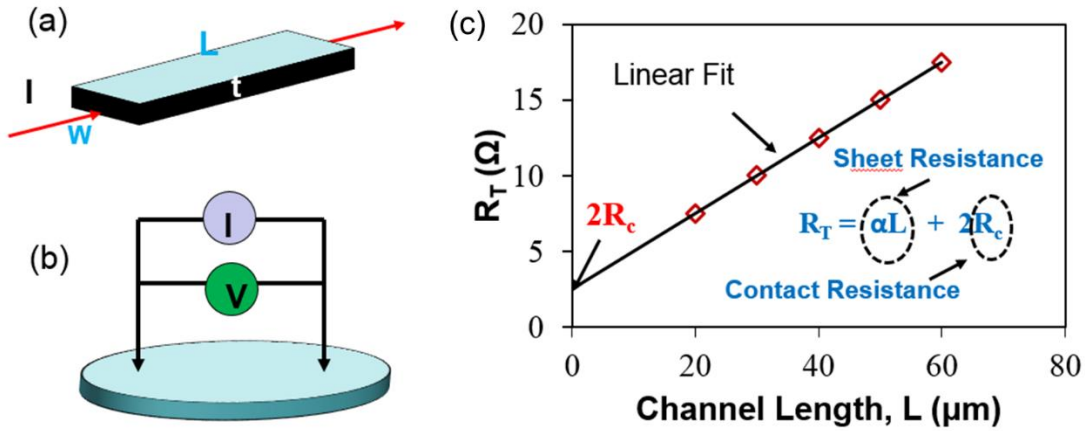

Figure 3.7 (a) Geometry for defining sheet resistance, while the current is parallel to the direction of the double-arrow near the letter "L". (b) Two-point probe test setup. (c) The linear fit of the total resistance (R_T) and different channel length, from which the R_{sh} and R_c can be calculated.

In contrast to the two-point method, the four-point method uses the two additional probes to measure the voltage potential of the material surface. These probes do not carry any current, thus eliminating the parasitic resistances R_c and R_{sp} measured in the two-point probe method. When the electrodes are considered to be two infinite parallel plates as shown in Figure 3.8 (infinite as compared with the channel length L), the current density can be expressed as:

Equation 3.4 $$R_{sh} = R\frac{W}{L} = \frac{V}{I}\cdot\frac{W}{L}$$

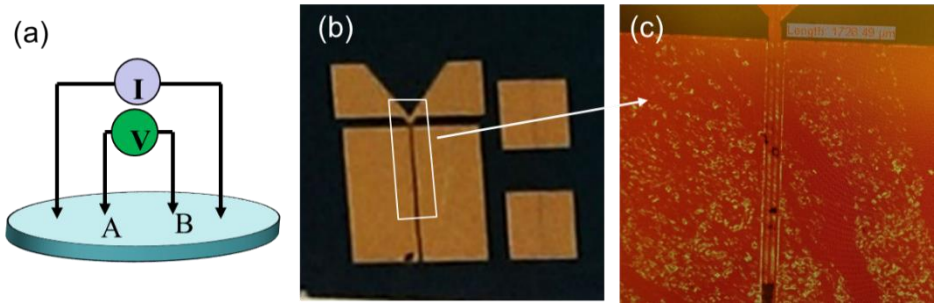

Figure 3.8 (a) Four-point probe test setup. (b) Four-point probe measurement device used for this research, and (c) zoom in region of channel.

In addition to the above mentioned techniques, the doped graphene films were also characterized by using UPS to track work function (φ) changes and estimate numbers of charge carrier transfer per dopant, and XPS to determine quantity of the molecular species adsorbed and assess changes in the donor/acceptor system.

3.4 Selection of dopants and the surface treatment for graphene

In this chapter, graphene is used as a test bed for a series of redox-active molecules, where their doping strengths are compared under the same conduction. The molecules used for doping studies in this chapter are shown in Figure 3.9. The benzimidazole-based dimer $(2\text{-Y-DMBI})_2$ discussed in Chapter 2 and their monomer derivatives H-2-Y-DMBI, were used to n-dope CVD graphene. Detailed characterization and comparison were conducted on $(2\text{-Fc-DMBI})_2$ and 2-H-Fc-DMBI. Different doping mechanisms in these two types of molecules lead to different doping effects on graphene films. For p-dopants, oxidants with different redox potentials, include $(Bu_4N)[Ni(mnt)_2]$, $Ni(tfd)_3$, $Mo(tfd)_3$, and Magic blue, were studied on graphene, while sheet resistances, UPS and XPS were measured on the doped films.

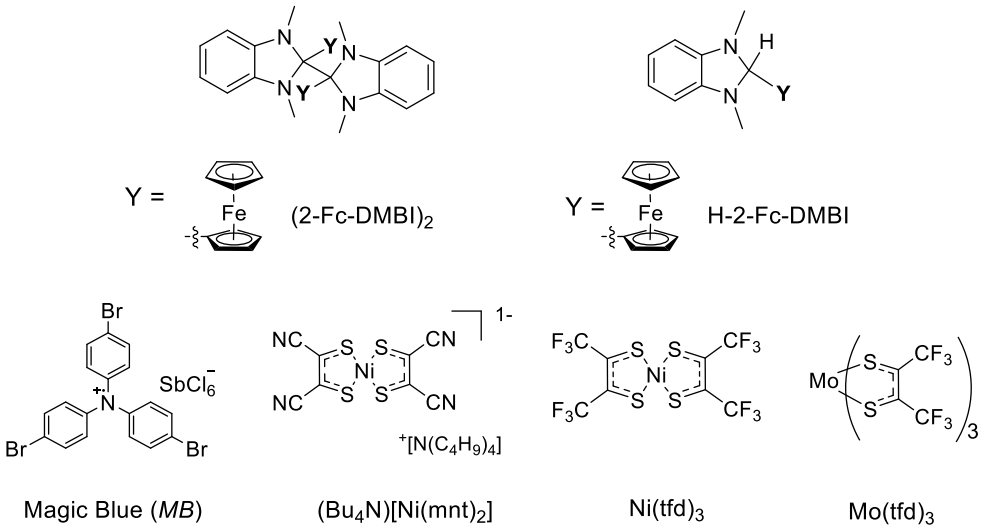

Figure 3.9 n- and p-Dopants used in this study.

3.5 n-Doping of mono-layer graphene using molecular dimeric and monomeric reductants

3.5.1 Transistor and sheet resistance measurements

The patterning of the devices follows general photolithography procedures. The detailed device fabrication procedures are described in the Experimental Section 3.10.3 (Page 143). CVD-grown SGL graphene was transferred onto patterned SiO_2 and annealed inside a glovebox until the neutrality point (VNP) was zero. Samples were then exposed to toluene solutions of dopants, $(2\text{-Y-DMBI})_2$ and H-2-Y-DMBI for various times, followed by rinsing with additional toluene to remove any weakly physisorbed material. All sample modifications and characterizations were done without exposure to air.

Previous studies have shown that the doping products for both DMBI dimer and monomer dopants in organic semiconductors are the $DMBI^+$ cation species. Electron transfer can occur from dopants into the conduction band of graphene, resulting in transfer of two e- per dimer (homolysis of the C-C dimer bridge of $(2\text{-Y-DMBI})_2$) and

one hydride (or one electron and one hydrogen radical, which caused by the C-H cleavage) per 2-H-Y-DMBI, leaving a $DMBI^+$ cation salt on the surface of graphene. The characterization of the doping products was conducted using XPS, and will be discussed in the following section.

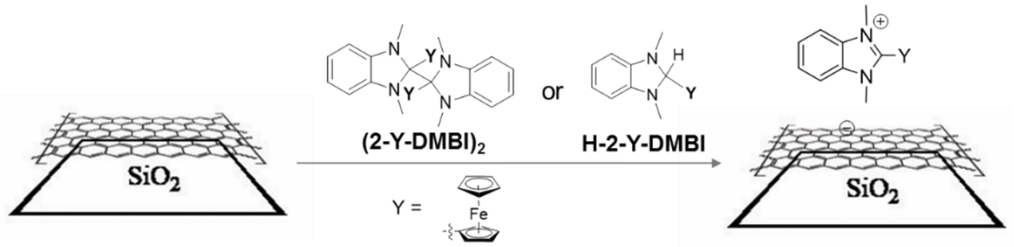

Figure 3.10 Treatment of graphene with DMBI dimer and monomer dopants, and their proposed products.

Changes in electrical behavior were determined by measuring the transfer characteristics of a bottom-gated, bottom-contact GFET. Figure 3.11 shows the transfer characteristics of the transistors before and after successive treatments with (2-Fc-DMBI)$_2$ and 2-H-Fc-DMBI. For (2-Fc-DMBI)$_2$, a short immersion time (*ca.* 1 s) in a low concentration solution (0.025 mM) gave a significant shift of the neutrality point to negative voltage (V_{NP} = –34 V), consistent with n-doping. Equation 3.1 was used to estimate the electron density in the conduction band, *n*, from V_{NP} and the capacitance per unit area of the gate dielectric (300 nm SiO_2, C_G = 115 aF μm^{-2}), resulting in a value of $n = 2.4 \times 10^{12}$ e cm^{-2}. After longer treatments (10 s, 1 min) on the same sample with a 2.5 mM solution, the neutrality point was no longer observable due to the –100 V limit imposed by the dielectric, precluding determination of *n* from Equation 3.1. The increase in conductivity of up to 150% appears to be limited by the on/off ratio of the pristine graphene. One the other hand, 2-H-Fc-DMBI gave a weaker doping effect as compared with the dimer, which is reflected in the shift of V_{NP}, even after 10 min

dipping it can only reach –83 V, representing $n = 5.8 \times 10^{12}$ e cm^{-2}.

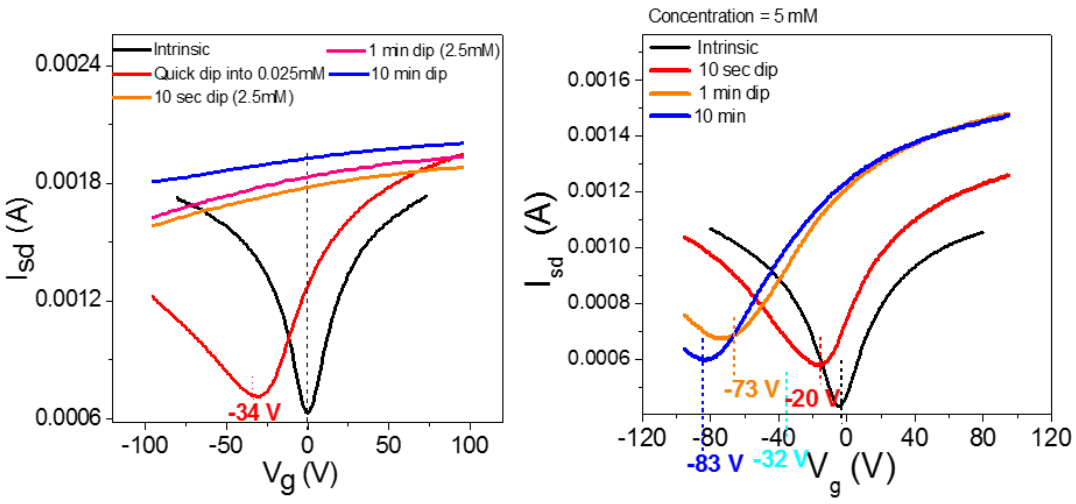

Figure 3.11 GFET transfer characteristic before and after treatment with $(2\text{-Fc-DMBI})_2$ and 2-H-Fc-DMBI at various dipping times.

3.5.2 Effects of doping on the sheet resistance and contact resistance

The sheet resistance of doped SGL graphene were measured by both the four-point probe and two-point probe methods using the previous mentioned methods. Table 3.2 and Table 3.3 summarized the sheet resistance measured by four-point probe method for graphene films doped by $(2\text{-Fc-DMBI})_2$ and 2-H-Fc-DMBI at various treatment time. The overall trend is consistent with the GFET results. The sheet resistances at 0 V gate voltage were highlighted in bold. For $(2\text{-Fc-DMBI})_2$ doping, the sheet resistance can be reduced from 3090 Ω/sq to 121 Ω/sq. A smaller doping effect was observed when 2-H-Fc-DMBI is applied, the resistance was reduced from 3120 Ω/sq to 898 Ω/sq. Then, gate voltage was applied to induce extra charge carries; the highest sheet resistance for each treatment at different gate voltage was highlighted in red. As shown Table 3.2, more positive gate voltage leads to smaller sheet resistance, which is consistent with the n-doping behaviors; as the dopant treatment time increase, the difference of sheet resistance at different gate voltage becomes smaller, showing

that the gate voltage has less effects on the carrier concentration. This is also consistent with the GFET results for $(2\text{-Fc-DMBI})_2$ doping. As shown Table 3.3 for 2-H-Fc-DMBI doping on the other hand, gives the highest sheet resistance at V_g = –10 V for the first two treatments, then –20 V for the 10 s dipping in 5 mM solution, which represent the position of V_{NP}. This is also consistent with relative weaker doping effects observed for 2-H-Fc-DMBI by the GFET measurement.

Table 3.2 Summary of the sheet resistance measured by four-point probe method for n-doped graphene by $(2\text{-Fc-DMBI})_2$ at different treatment time.

Doping level	Sheet Resistance (Ω/sq)						
	V_G=30	V_G=20	V_G=10	V_G=0	V_G= –10	V_G= –20	V_G= –30
Pristine	1050	1450	2640	3090	1350	912	724
0.025 mM - Dip	603	693	828	1060	1350	1670	2080
2.5 mM - Dip	402	451	467	491	501	523	554
2.5 mM – 10s	271	276	280	285	291	298	307
2.5 mM – 10min	152	154	155	157	159	162	165
2.5 mM overnight	118	119	120	121	122	142	165

Table 3.3 Summary of the sheet resistance measured by four-point probe measurements for n-doped graphene by 2-H-Fc-DMBI at different treatment time.

Doping level	Sheet Resistance (Ω/sq)						
	V_G= 30	V_G= 20	V_G=10	V_G= 0	V_G= –10	V_G= –20	V_G= –30
Pristine	913.1	1331	1780	3120	2010	1610	1010
0.05 mM - Dip	1320	1710	2020	2340	2780	2470	2110
5 mM - Dip	1100	1340	1670	1930	2290	2060	1760
5 mM – 10s	881	1050	1330	1610	1910	2130	1970
5 mM – 10min	487	616	735	914	1170	1390	1520
5 mM overnight	446	583	647	898	1010	1270	1430

Figure 3.12 showed the *I-V* curves for the two-point probe measurement of the intrinsic graphene and of graphene subjected to a10 s dipping treatment with $(2\text{-Fc-DMBI})_2$. The total resistance measurements can be calculated. By measuring the total resistance at different channel lengths (L), both the sheet resistance and contact

resistance can be calculated through the linear plot of R_T versus L, based on Equation 3.3. Figure 3.13 summarizes the linear fits of the total resistance at different channel length for n-doped graphene by $(2\text{-Fc-DMBI})_2$ at different treatment times. The calculated results are summarized in Table 3.4 and Table 3.5.

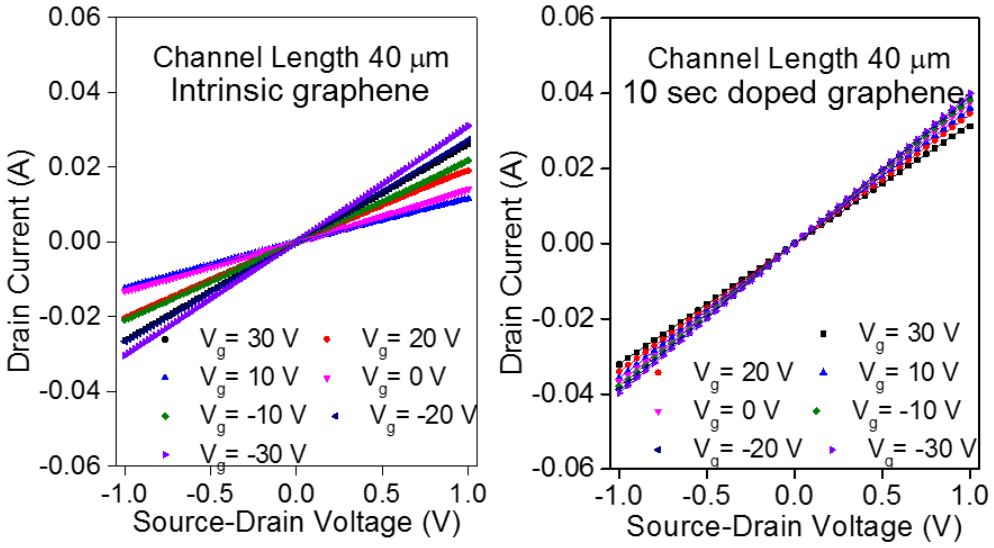

Figure 3.12 I-V curve for the total resistance measurements at different gate voltage.

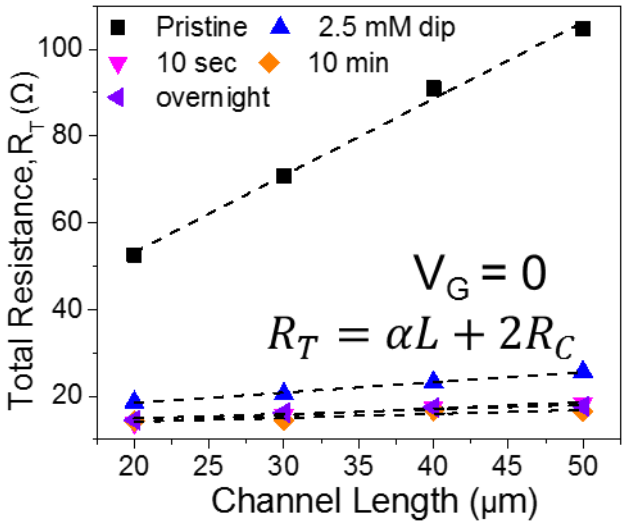

Figure 3.13 Linear fit of the total resistance at different channel length for n-doped graphene by $(2\text{-Fc-DMBI})_2$, no gate voltage was applied.

Table 3.4 Summary of the sheet resistance measured by two-point probe method for n-doped graphene by $(2\text{-Fc-DMBI})_2$ at different treatment time.

Doping level	Sheet Resistance (Ω/sq)						
	V_G=30	V_G=20	V_G=10	V_G=0	V_G= –10	V_G= –20	V_G= –30
Pristine	669	869	1350	3530	1760	1060	807
2.5 mM - Dip	398	421	445	475	511	553	595
2.5 mM – 10s	279	287	296	304	314	325	336
2.5 mM – 10min	156	186	180	180	191	189	193
2.5 mM overnight	213	214	208	211	214	215	212

As shown in Table 3.4 the sheet resistance measured by the by two-point probe method are consistent with the results acquired by the four-point probe method (Table 3.2). Table 3.5 summarizes the results of the contact resistance at different doping treatment condition, where the contact resistance initially decreases, then increases slightly as doping time increases. As the graphene is n-doped, charge carriers are added. This increases the charge carrier density, which allows easier flow of current, causing the contact resistance to decrease. However, as charge carriers are added, the difference in work functions of gold and graphene becomes greater, thus, the larger electron injection barrier. This eventually causes an increase in contact resistance. Figure 3.14 shows an energy diagram of the n-doped graphene and the gold electrode.

Table 3.5 Contact resistance measurements for n-doped graphene at different doping concentration.

Graphene Doping Levels	Contact Resistance (Ω)						
	V_G= –30	V_G= –20	V_G= –10	V_G=0	V_G=10	V_G=20	V_G=30
Pristine	8.36	8.51	8.83	8.94	11.07	9.52	8.96
2.5 mM – Dip	6.90	6.85	6.85	6.85	6.82	6.76	6.72
2.5 mM – 10s	5.48	5.50	5.51	5.52	5.51	5.53	5.53
2.5 mM – 10min	6.13	6.13	6.07	6.15	6.11	6.00	6.29
2.5 mM – Overnight	6.43	6.39	6.36	6.36	6.37	6.32	6.29

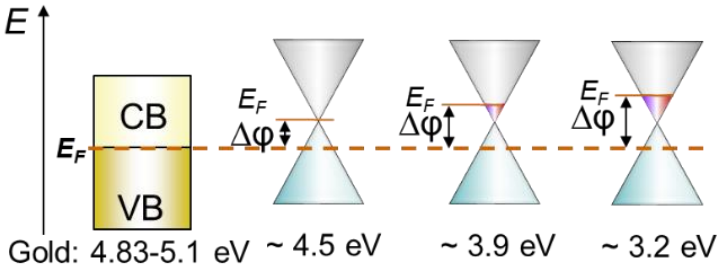

Figure 3.14 Energy diagram of the n-doped graphene and the gold electrode. The work function of the doped graphene is measured by the UPS.

3.5.3 UPS and XPS analysis

Direct characterization of the energy-level shifting upon doping was conducted by UPS. Doping treatments were performed inside a glove box, and UPS/XPS measurements were performed in high vacuum (ca. 10^{-9} mbar) without exposure to air. UPS was used to determine the work function ϕ (ϕ = 21.22 eV – E_{SEE}, where SEE denotes the secondary electron edge, Figure 3.15) and the position of the valence band maximum (E_{VBM}) relative to the Fermi level E_F. The valence band region is examined first for the undoped sample (in black). The pristine sample of graphene used for doping had a WF of 4.50 ± 0.08 eV, and the low binding energy valence band section of the spectrum showed emission all the way to zero binding energy (the Fermi level). Upon n-doping, the conduction band will start filling, and hence the Fermi level (E_F) will move closer to the vacuum level, and give smaller WF. The decrease of WF is accentuated by vacuum level shift as well, because of the interface dipole formed between positively charged doping cations and negatively charged graphene film. As shown in Figure 3.15, the WF decreases slightly (–0.28 eV) with the quick exposure to dilute solution, with the slight dip in the emission at a BE = 0.25 eV mentioned previously, which is attributed to the Dirac point shift from E_F (still aligned with the

spectrometer, at BE = 0) due to filling of the graphene conduction band by electron transfer from the dimer. 10 s treatment with the 2.5 mM solution leads to a further decrease in WF (–0.59 eV relative to pristine) with the Dirac point at BE = 0.31 eV. A 10 min treatment with the concentrated solution gave an additional decrease of –1.27 eV to render a WF of 3.23 ± 0.05 eV, with $E_D - E_F$ = 0.55 eV.

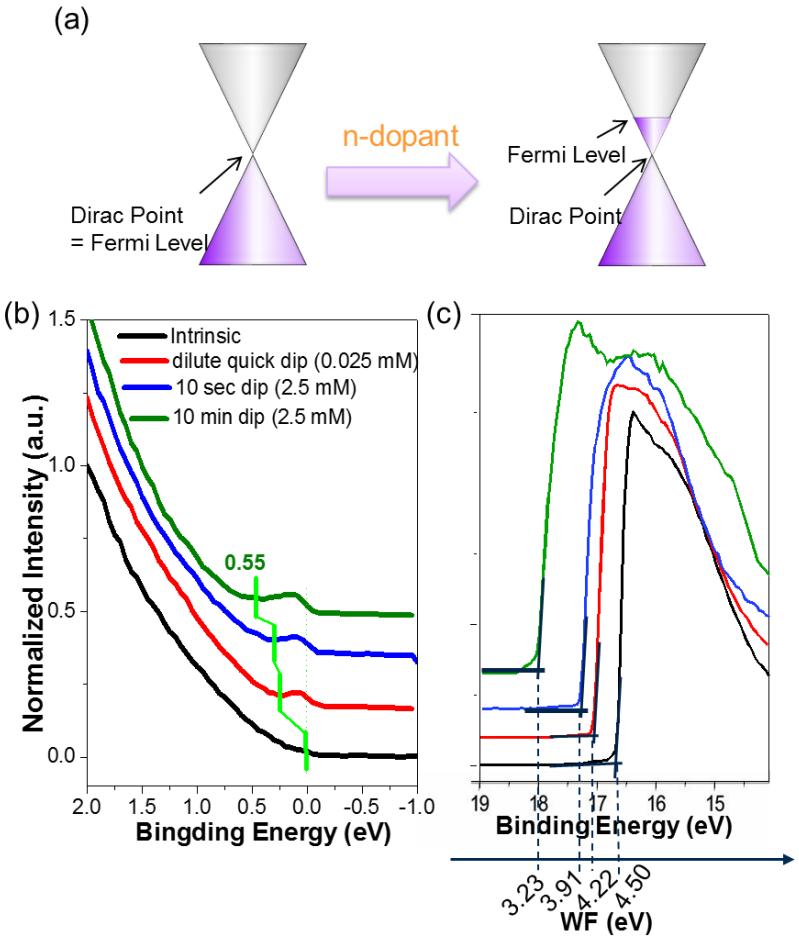

Figure 3.15 (a) Valence band region for graphene and after successive treatments with $(2\text{-Fc-DMBI})_2$ solution, (b) the UPS secondary electron edge was used to determine the WF of graphene before and after successive treatments.

As shown in Figure 3.16, there are two components of the WF shifts: one is from the filling of the conduction band, which is reflected in the $E_D - E_F$, another is attributed to the surface dipole resulting from the formation of a layer of $(2\text{-Fc-DMBI})^+$ cations on top of a negatively charged graphene sheet. The contribution to the WF

change from filling of the conduction band was used to determine the number of charge carriers introduced, *n*, according to Equation 3.5. This equation is derived from consideration of the band structure of graphene near the K point, where it shows linear dispersion $E_{\pm}(k) \approx \hbar v_F |k - K|$ as discussed in the literature.[54,55] The value of *n* estimated from Equation 3.5 for the short immersion in dilute solution,[27] 4×10^{12} cm^{-2}, agrees well with that obtained from GFET data (2.4×10^{12} cm^{-2}).

Equation 3.5 $$n = \frac{1}{\pi}\left(\frac{\Delta\varphi_{ET}}{\hbar v_F}\right)^2$$

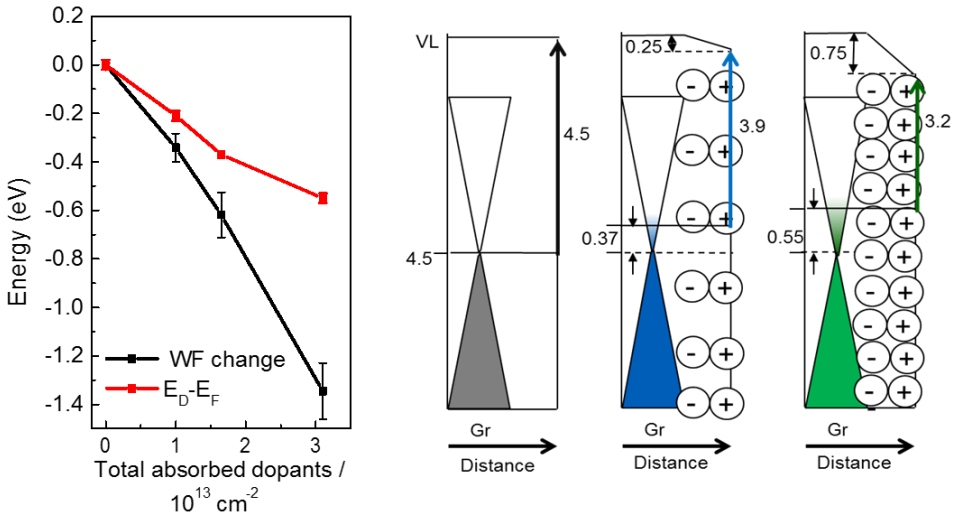

Figure 3.16 WF and E_F shifts determined in UPS as a function of total Fe adsorbed (determined from XPS) for $(2\text{-Fc-DMBI})_2$ doping.

WF and E_F shifts for 2-H-Fc-DMBI doped films were also determined by the UPS, and summarized in Figure 3.17. Smaller WF and E_F shifts were observed compared with the $(2\text{-Fc-DMBI})_2$ doped film.

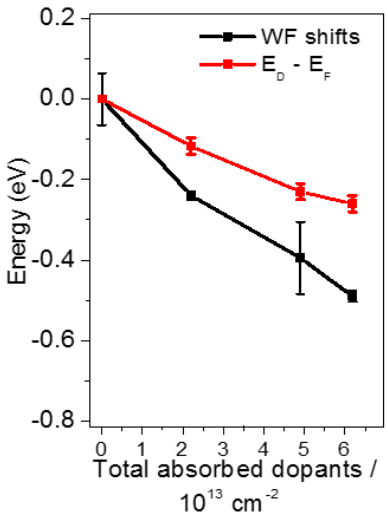

Figure 3.17 WF and E_D – E_F shifts for 2-H-Fc-DMBI doped graphene films, as a function of total Fe adsorbed (determined from XPS).

XPS was used to investigate the number and the nature of dopant-related species on the surface. XPS samples were transferred under inert atmosphere without exposure to air. Figure 3.18 shows the XPS high resolution N 1s peak from the doped graphene films (quick dip into the dilute solution), compared with the thick film of the dopants and cation species. The concentration of the monomer solution is twice the concentration of the dimer solution for better comparison (5 mM versus 2.5 mM). (2-Fc-DMBI)$_2$ and 2-H-Fc-DMBI gave the same doping product, the 2-Fc-DMBI$^+$ cation, consistent with the previous work on organic semiconductors doping studies. For both doped films, N 1s peaks can be deconvoluted into two peaks: a main peak at 402.3 eV, attributed to the 2-Fc-DMBI$^+$ cation, and small shoulder at 400.5 eV, attributed to the unreacted dopants. As shown on Figure 3.18, the reacted versus unreacted species on (2-Fc-DMBI)$_2$ doped graphene film is 83:17, while for 2-H-Fc-DMBI doped film, this ratio is 54:46. These differences in reactivity on the graphene surface may be due to both thermodynamics and kinetics and can be attributed to the different chemical

reactions that are coupled to the electron-transfer reactions required to form stable $DMBI^+$ cations and n-doped semiconductor. In the case of $(2\text{-Fc-DMBI})_2$, a C—C bond is broken, whereas in DMBI-H derivatives a C—H bond is broken, leading to the formation of additional side products, the identity of which is unclear in the case of graphene doping. This is consistent with the previous UPS results that $(2\text{-Fc-DMBI})_2$ leads to larger WF and E_F shift than 2-H-Fc-DMBI on SGL graphene. Similar results were observed for other 2D materials doping, which will be discussed in Chapter 4.

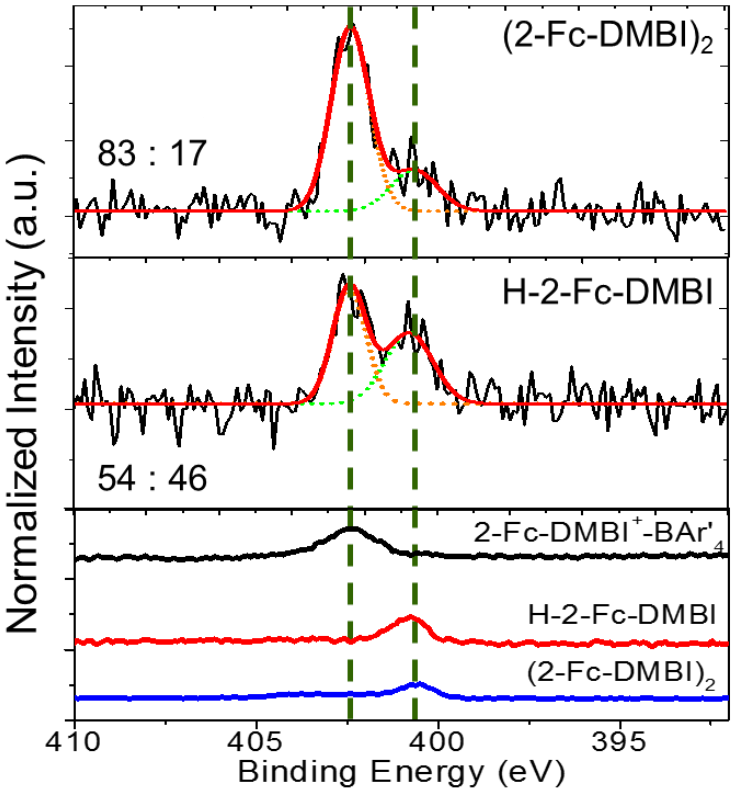

Figure 3.18 XPS spectra for N 1s peak for $(2\text{-Fc-DMBI})_2$ and 2-H-Fc-DMBI treated graphene, compared with the thick films of $(2\text{-Fc-DMBI})^+$ $BAr'_4{}^-$, 2-H-Fc-DMBI, and $(2\text{-Fc-DMBI})_2$.

The density of dopant monomer cations that fit in a close-packed arrangement can be estimated to determine an expected Fe/C ratio for a monolayer (C from the graphene only), and compared with the ratio obtained from the XPS results. Figure 3.19

shows the estimation of molecular footprint, based on the crystallographic data from $(2\text{-Fc-DMBI})^{+}BAr'_4{}^{-}$. If the monomer cations are assumed to oriented with the benzimidazole moiety parallel to the graphene surface, the footprint of the cations can be regarded as an approximately 12.27 × 8.48 Å rectangle with an area of 104.0 $Å^2$. For graphene the unit cell encompassing 2 carbons is 5.24 $Å^2$. Thus, a close-packed monolayer of such cations on top of mono-layer graphene will lead to $\frac{Fe}{C_{graphene}}$ = 0.026. The theoretical monolayer coverage of doping product on graphene can now be compared with the experimental data from XPS, as summarized in Table 3.6 and Table 3.7.

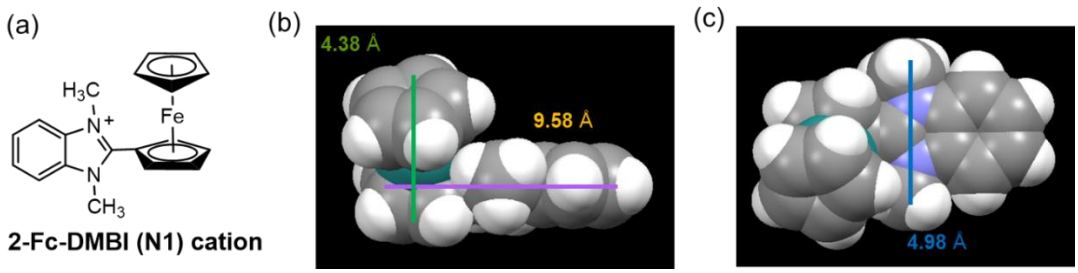

Figure 3.19 (a) Chemical structure of $(2\text{-Fc-DMBI})_2$ and 2-H-Fc-DMBI doping product. (b) Side view of space-filling model of the doping product monomeric cation. (c) Top view of space-filling model of the monomeric cation. Molecular length and width are estimated from crystallography defining planes from the H atoms at the edges of the molecule. A closest separation of the van der Waals radius of non-bonded H of 1.20 Å was considered, which defines of 12.27 Å of length and 8.48 Å of width, for an effective footprint of 104.0 $Å^2$.

Table 3.6 Estimates of $(2\text{-Fc-DMBI})_2$ coverage (% of close-packed monolayer) and the number of dopants on the surface of graphene.

	Quick dip into 0.025 mM	10 sec into 2.5 mM	10 min into 2.5 mM
% of close packed ML (XPS)	2.6±0.2	16±1	61±2
$\varphi_{treated}$-$\varphi_{pristine}$ (eV) (UPS SEE)	–0.34±0.06	–0.62±0.09	–1.3±0.11
E_D-E_F /eV (UPS VB)	–0.21±0.05	–0.37±0.05	–0.55±0.55
n calculated from E_D-E_F (cm^{-2})	(4.6±0.3) $\times10^{12}$	(14.3±0.3) $\times10^{12}$	(31.6±0.3) $\times10^{12}$
Electrons transferred per adsorbed dopant (UPS+XPS)	0.91±0.2	0.46±0.3	0.34±0.2

As mentioned earlier, the number of charge carriers introduced through n-doping can be calculated based on E_F shifts relatively to the Dirac point. The amount of the dopants on the graphene surface has been determined from the XPS. Thus, electrons transferred per adsorbed dopant can be calculated. As summarized in Table 3.6 and Table 3.7 for $(2\text{-Fc-DMBI})_2$ and 2-H-Fc-DMBI doping, the extent of electron transfer decreases at the highest dopant coverages. The electron transfer efficiency for 2-H-Fc-DMBI is smaller than $(2\text{-Fc-DMBI})_2$, which is consistent with previous observation in XPS analysis of the N 1s peak, and UPS characterized energy level shifts.

Table 3.7 Estimates of 2-H-Fc-DMBI coverage (% of close-packed monolayer) and the number of dopants on the surface of graphene.

	Quick dip into 0.05 mM	10 sec into 5 mM	10 min into 5 mM
% of close packed ML (XPS)	11 ± 0.2	25.2 ± 1	31.7 ± 2
$\varphi_{treated}$-$\varphi_{pristine}$ (eV) (UPS SEE)	–0.24 ± 0.01	–0.39 ± 0.09	–0.49 ± 0.01
E_D-E_F /eV (UPS VB)	–0.11 ± 0.02	–0.23 ± 0.02	–0.26 ± 0.0.2
n calculated from E_D-E_F (cm^{-2})	(2.46 ± 0.3) $\times10^{12}$	(5.53± 0.3) $\times10^{12}$	(7.06 ± 0.3) $\times10^{12}$
Electrons transferred per adsorbed dopant (UPS+XPS)	0.22 ± 0.01	0.15 ± 0.01	0.10 ± 0.01

3.6 p-Doping of mono-layer graphene with various oxidants

A similar study was performed on graphene using p-dopant**s**. Figure 3.20 shows the GFET results after successive treatments of graphene with four p-dopants, labelled as **1**, **2**, **3**, and **4**, and their reduction potential versus Fc/Fc^{+}. Based on their redox potential, the doping strength is **4** > **2** > **3** >**1**. However, it is worth pointing out that the redox potentials are measured by the cyclic voltammetry in solution, which may not reflect their doping strength when applied on the surface. Moreover, **1** is charged molecule while the other three are neutral, the favorable interaction between dopant anion and the doped positively charged graphene film (or unfavorable dopant anion and anion interaction) is not taken into account.

Similar with the n-dopant, the increase in conductivity seems to be limited by the intrinsic on/off ratio of the pristine graphene, as further treatments with more concentrated solutions and for more extended periods of time give limited increase in conductivity. Additional immersion times and higher concentrations give neutrality points outside the measureable range. Dopant **4** (Magic Blue) gave the largest V_{NP} shifts among the four dopants with the same doping treatment time and doping concentration, compared with the other three dopants. This is consistent with the fact that it has the most cathodic reduction potential. On the other hand, as shown in Figure 3.20(a-c), the doping strength is **2** >**1** >**3**, based on the V_{NP} shifts, even though **3** has more cathodic reduction potential than **1**.

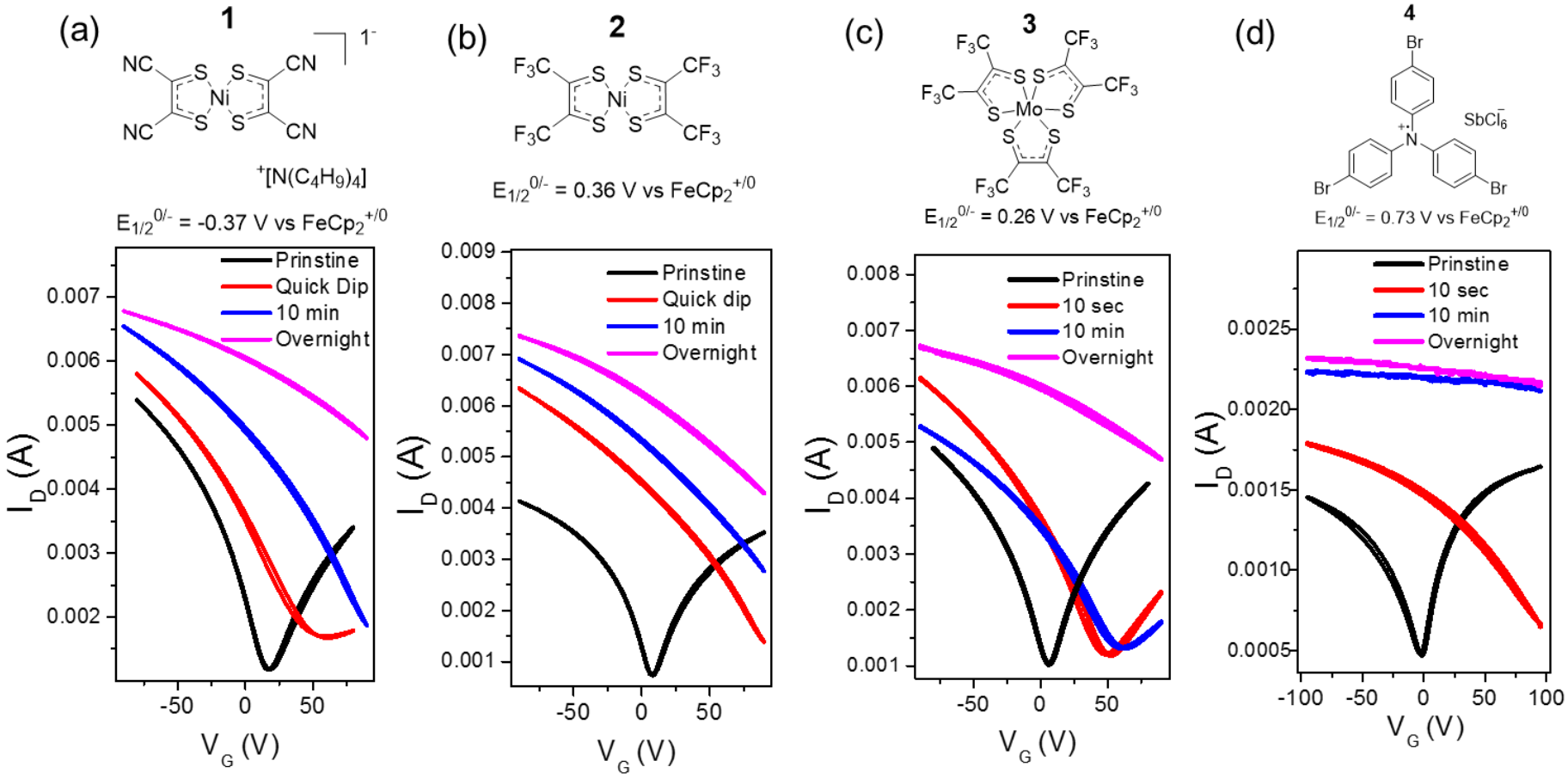

Figure 3.20 GFET of mono-layer p-doped by four p-dopants, labelled as **1**, **2**, **3**, and **4**, and their reduction potential versus $FcCp_2^{+/0}$.

The sheet resistance of doped mono-layer graphene were measured by both the four-point and two-point probe methods, and results summarized in Table 3.8 (no gate voltage is applied). The overall trend is consistent with the GFET results: **3** gave smallest reduction of the sheet resistance among the four molecules (ca. 305 Ω/sq upon the overnight treatment); **1** and **2** gave comparable doping effects, and can reduce the sheet resistance to below 200 Ω/sq; **4**, on the other hand, initially gave lowest sheet resistance compared with the other three dopants, however, longer treatment time (overnight) led to the increase of the resistance. This may be caused by the unstable nature of the tris(4-bromophenyl)ammoniumyl radical cation species. There are visible crystals formed on the surface of the graphene after the overnight treatment. Moreover, it should be noted that, the sheet resistance measured here is not necessary proportional to the number of carriers, since other factors (such as scattering) might also play a role in the overall sheet resistance.

Table 3.8 Sheet resistance measurement for p-dopant mono-layer graphene. Standard deviation (SD) for each dopant treatment is aquired from four samples, measured by two two-point probe devices and two four-point probe devices.

Doping level	Sheet Resistance (Ω/sq) at $V_G = 0$			
	1	**2**	**3**	**4**
Pristine	1830 ± 60	1910 ± 40	1650 ± 50	1760 ± 40
5 mM – Dip	472 ± 35	412 ± 28	507 ± 41	315 ± 37
5 mM – 10s	319 ± 31	307 ± 38	475 ± 29	282 ± 35
5 mM – 10min	265 ± 23	278 ± 15	465 ± 16	193 ± 31
5 mM – Overnight	167 ± 17	193 ± 30	305 ± 22	510 ± 54

The contact resistance for **4** doped graphene film was also characterized. Figure 3.21 shows a graphical representation of the zero gate voltage data. There is a clear downward trend in the y-intercept as doping level increases, corresponding to a

downward trend in contact resistance. Table 3.9 shows the contact resistance data collected from all gate voltages at different levels of doping. The contact resistance decreases from 8.94 Ω to 6.14 Ω at zero gate voltage. The changes in the contact resistance shown in the data follow the trend expected. For p-doping, as the doping time increases, holes are increasingly added to the graphene. Figure 3.22 shows how the Fermi level of the graphene changes as it is doped for increasing amounts of time. The Fermi level of pristine graphene is higher than that of gold, so as holes are added, the difference between the work functions decreases, thus, lower hole injection/extraction barriers, and lower contact resistance is expected.

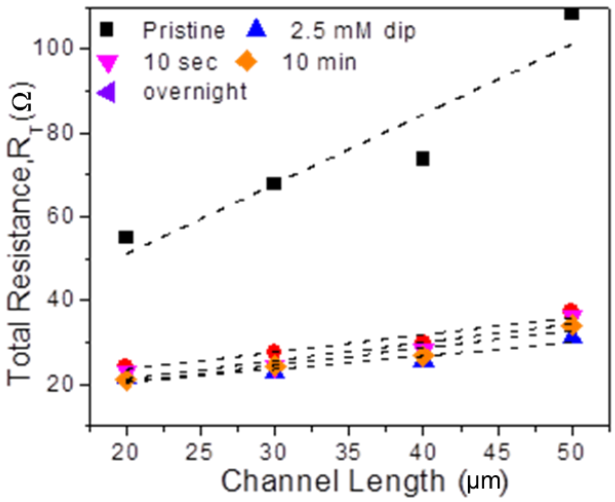

Figure 3.21 Total resistance of p-doped graphene transistor at different channel length.

Table 3.9 Contact resistance measurements for p-doped graphene by **3** at different doping concentration.

Graphene Doping Levels	Contact Resistance (Ω)						
	V_G= –30	V_G= –20	V_G= –10	V_G=0	V_G=10	V_G=20	V_G=30
Pristine	7.50	7.56	7.76	8.94	9.74	6.64	6.09
0.025 mM – dip	7.77	7.76	7.72	7.68	7.60	7.45	7.16
2.5 mM – dip	7.08	7.10	7.12	7.15	7.18	7.22	7.30
2.5 mM – 10 sec	6.61	6.47	6.30	6.29	6.53	6.50	6.59
2.5 mM – 10 min	6.76	6.60	6.48	6.14	5.83	5.32	4.50

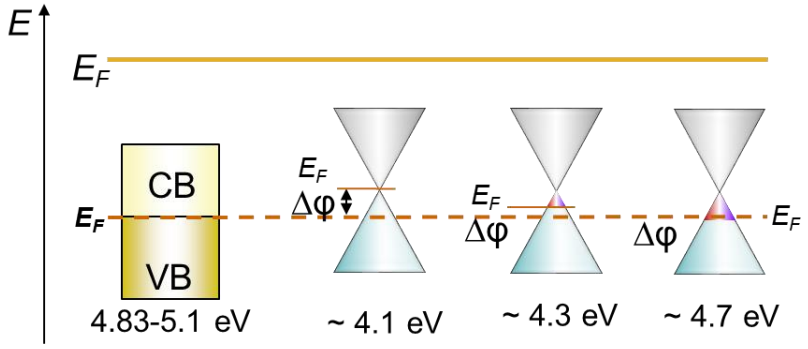

Figure 3.22 p-doping of graphene and band-energy level alignment.

Figure 3.23 shows representative UPS secondary electron edges (SEE) for pristine graphene and after successive treatments with the p-dopants. An increase in the work function, determined as the SEE shifts to lower binding energies, is observed for all the p-dopants treated graphene films. In contrast to n-doped samples, the Dirac point is not observed below the Fermi level, since there is emission all the way to zero binding energy (E_F) upon the p-doping. **4** gave the largest work function shifts, which increases significantly from 4.1 eV (pristine) to 5.1 eV (10 min treatment). The overall trend for the doping strength of these four dopants characterized by the WF shifts is **4** > **2** > **1**> **3**, consistent with the GFET and sheet resistance measurements, but not with their redox potentials.

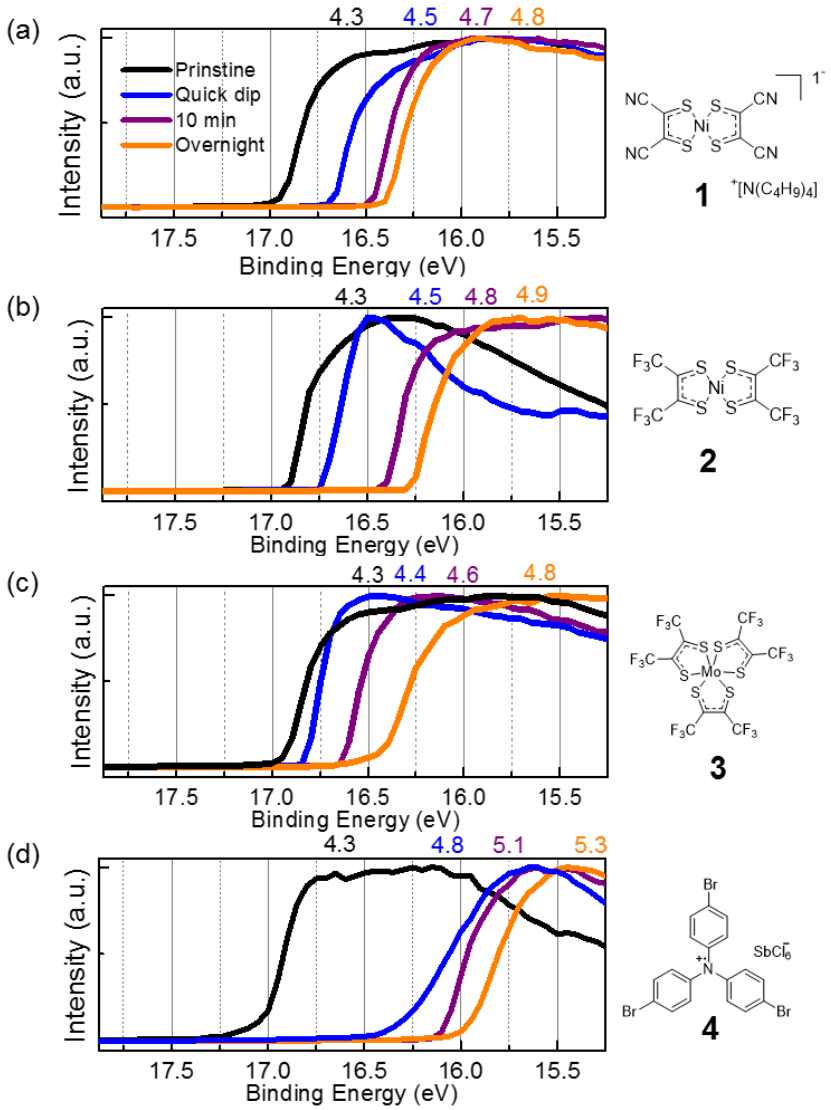

Figure 3.23 UPS for p-doped mono-layer graphene by dopant **1**, **2**, **3** and **4**.

Detailed XPS analysis was conducted on **4** doped graphene films. XPS reveals increasing surface concentrations of Cl and Sb as treatment time increases (Figure 3.25), which is consistent with the expected doping mechanism. As shown in Figure 3.25(a), during the doping process, tris(4-bromophenyl)ammoniumyl radical cation accepts an electron from the graphene to form neutral tris(4-bromophenyl)amine, which is assumed to remain in solution and/or to be washed away in the following rinsing step, and leaving the hexachloroantimonate counter ion to balance the charges introduced to the film. This is supported by the fact that longer doping treatments lead to significant

growth of the Cl 2p peak, but no obvious increase in the Br 3d peak. Assuming all the dopants fully reacted (only anions present on the surface), the coverage can calculated based on the anion to graphene ratio relative to the theoretical value, which is estimated from how many dopant monomers can fit in a close packed arrangement on the surface of graphene. Thus, the concentration of **4** could be deduced from the Cl/C ratio.

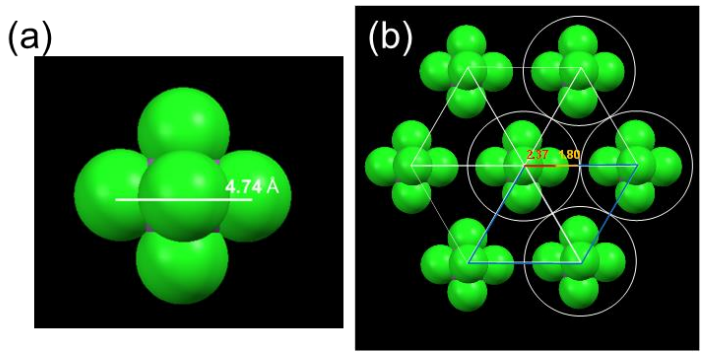

Figure 3.24 (a) Chemical structure and (b) space-filling model of $SbCl_6^-$. Molecular dimensions were estimated from crystallography of $SbCl_6^-$ salts in the literature.[56] (c) Top view of a close packed model for monolayer of $SbCl_6^-$treating the molecules as circular disks. A van der Waals radius of non-bonded Cl of 1.80 Å was used.[57] The sum of the disk areas inside the rhombus defined by blue lines is 91% that of the rhombus.

As shown in Figure 3.24, the unit cell was viewed as a rhombus, and its area calculated to be 60.2 $Å^2$.[2] Since each ion contains six Cl atoms, by comparison with graphene, for which the unit cell encompassing 2 carbons is 5.24 $Å^2$, we can estimate that $\frac{Cl}{C_{graphene}}$ = 0.26. The theoretical monolayer coverage of Magic Blue doping product on graphene can now be compared with the experimental data from XPS. We obtain a coverage of 62 ± 3 % of a molecular monolayer for a 10 min immersion in a dilute solution, which is indeed a sub-monolayer.

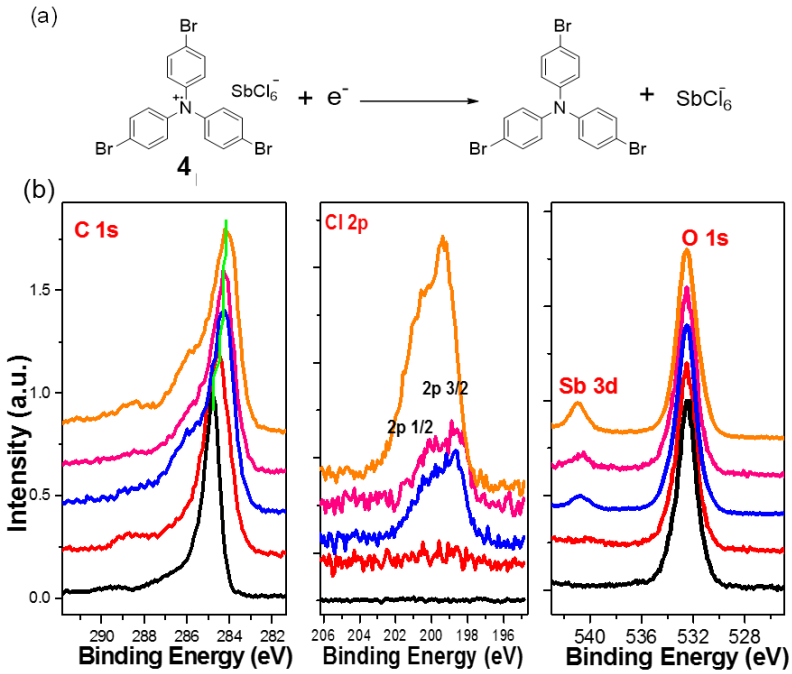

Figure 3.25 (a) Doping reaction for **1** "Magic Blue". (b) XPS comparison of pristine graphene and after treatments with 1 (left) C 1s, (middle) Cl 2p region, (right) O 1s and Sb 3d region.

Figure 3.26 shows Ni 2p peaks for the doping products of **1** and **2** on graphene films, as compared with the thick film of the two dopants and dianion derivative of the **1**, $[Ni(mnt)_2]^{2-}$ $(Bu_4N)_2^+$. The peak positions for **1** and **2** doping products aligned well with the Ni 2p peak position in $[Ni(mnt)_2]^{2-}$, revealing that the formation of the same products after the doping process.

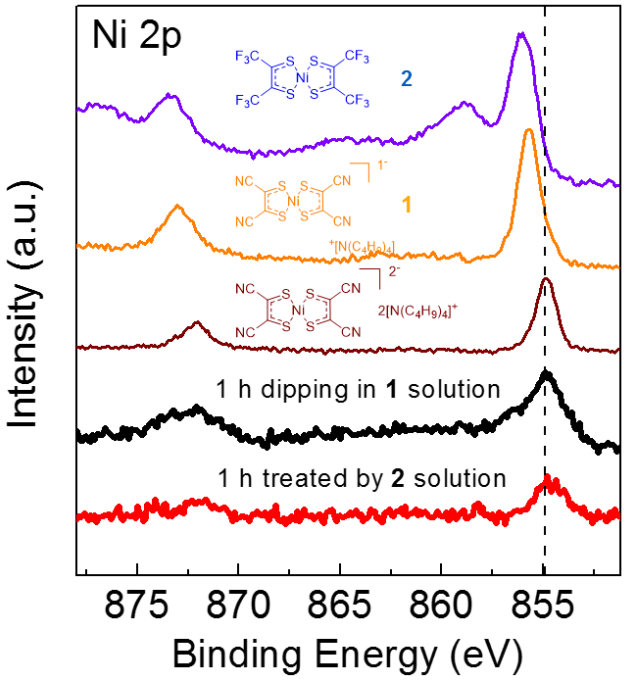

Figure 3.26 XPS spectra for Ni 2p peak for **1** and **2** 1 hour treated graphene, compared with the thick films of **1**, **2**, and $[Ni(mnt)_2]^{2-}$ $(Bu_4N)_2^+$.

3.7 n- and p-Doping of multi-layer graphene

As mentioned earlier, the large area graphene sheets used in this research was synthesized through the low-pressure CVD method. The as-grown graphene film is mostly single layer with sheet resistance in the range of 1000 to 2000 Ω/sq. The sheet resistance of a single layer of graphene is not sufficiently low for OPV applications. Even after doping, the lowest sheet resistance for the single layer CVD graphene used in this research is ca. 100 Ω/sq (discussed in Chapter 3), which is still much higher than ITO (10 to 20 Ω/sq for commercial available grades). In principle, the sheet resistance of graphene can be decreased through increase the number of the graphene layers. In principle, the sheet resistance of multi-layer graphene is described by the equation:

Equation 3.6 $$R_s = (\sigma_{2d} N)^{-1}$$

where σ_{2d} is the conductivity of monolayer, and N is the number of layers.[58] Thus,

stacking multi-layers together through a layer-by-layer transfer method is a viable method for reducing sheet resistance. As shown in Figure 3.27, the sheet resistance can be reduced from ca. 1500 Ω/sq to 800 Ω/sq going from a one- to three-layered graphene film through the layer-by-layer transfer method, and five-layered graphene has the sheet resistance as low as ca. 500 Ω/sq. It should be noted that, this experimentally observed sheet resistance reduction of the graphene film with increased number of layers does not follow Equation 3.6, mainly because of the organic residue (left from the transfer step) on the surface of each layer.

Figure 3.28 shows the optical image and optical transparency measurement for multi-layer graphene films. The transmittance reduced from ca. 97% to 91% for 1–3-layered graphene, then to ca. 84% for a 5-layered film. It has previously been reported that each graphene layer has approximately 2.3% opacity.[59] Thus, the transparency of the graphene films used in this research agrees well with the literature reported value.

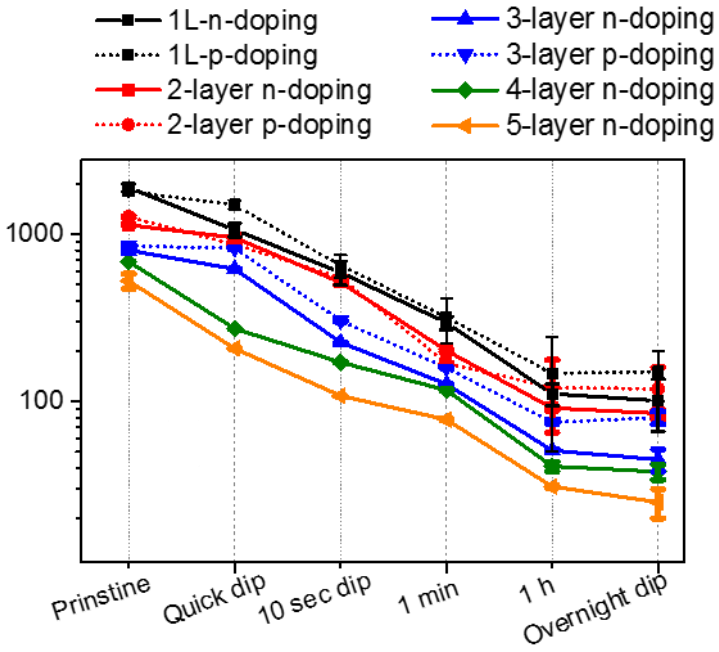

Figure 3.27 Sheet resistance measurements of multi-layer graphene treated by (2-Fc-DMBI)$_2$ and Magic Blue at various time.

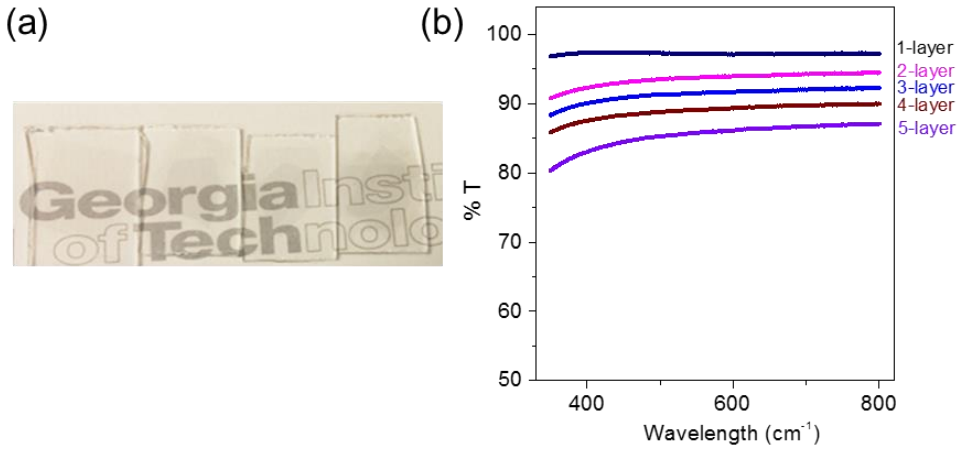

Figure 3.28 (a) Optical image of, from left to right, one to four layers of graphene on glass substrates. (b) Transmittance spectra of the one to five layers graphene in the visible range.

3.8 n- and p-Doping of CNTs

Apart from graphene, CNTs film is another possible alternative to ITO to be used as the flexible transparent electrode. The single-wall carbon nanotubes have the ability to be either metallic or semi-conducting depending on the "twist" of the tube. As shown in Figure 3.29, the zigzag and chiral nanotubes are semiconducting, and

armchair tubes are metallic. Due to the nature of SWNT batch synthesis, 2/3 of the SWNTs in the network are semiconducting, with the remaining 1/3 being metallic in electronic behavior. The metallic and semiconducting SWNTs can be separated by ultracentrifugation.

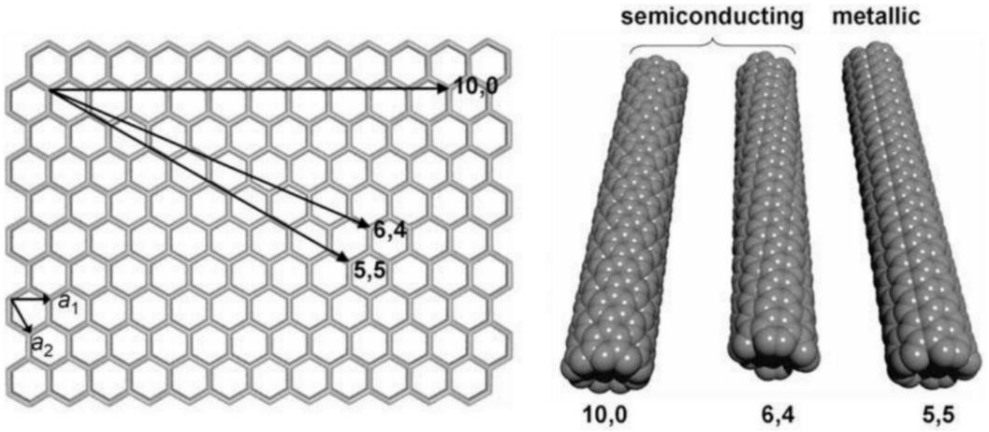

Figure 3.29 Different "twist" of the SWNTs to represent the zigzag (left), chiral (center), and armchair (right) for the semiconducting and metallic nanotubes. Adapted from Campidelli, *et al*. [60]

CNTs are generally randomly distributed in a 2-D array. Because of the 1-D nature of SWNTs, they can be modeled as electronic "conducting sticks".[61] Electrical charges are conducted across the film by traveling along the "conducting sticks". The random network arrangement of SWNT films permits statistical averaging to compensate for electrical anisotropy in the film. With sufficient SWNT nanotube networks can be fabricated that exhibit metallic behavior in spite of the fact that 2/3 of the network are semiconducting.[62] The converse is true for low density networks. The metallic SWNTs in low density films are not sufficiently numerous to form pure metallic pathways in the film. The random architecture also provides mechanical stability to the network. In this regard, the film can maintain electrical contact points even under extreme bending, which make it suitable for flexible electronics

applications.[60]

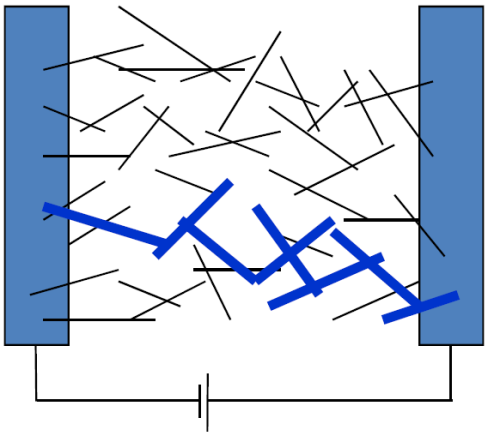

Figure 3.30 Schematic of SWNT film architecture. Possible conduction pathway is illustrated in bold.

The CNTs used in this research are well-separated metallic and semiconducting CNTs with 99% purity, purchased from Nanointegris Technologies Inc. (item No. HS28030 and HS28030). Detailed procedures for the preparation of the CNT films are discussed in the Experimental Section 3.10.4 on Page 143. As shown in Figure 3.31, three CNT films were prepared: both CNT#1 and CNT#1 are made from the metallic CNT solutions, while CNT#3 are prepared from the semiconducting CNT suspension. The thickness of the CNT films were determined by the AFM. As shown in Figure 3.32, the thickness for the three CNT films are 135, 38, and 30 nm, respectively for the CNT#1, CNT#2 and CNT#3.

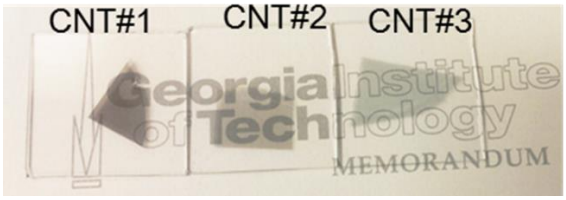

Figure 3.31 Optical images for the three CNT films used in this research. CNT#1 and CNT#1 are films of metallic nanotubes with thickness of 135 nm and 38 nm, respectively. CNT#3 is a semiconducting film with 30 nm thickness.

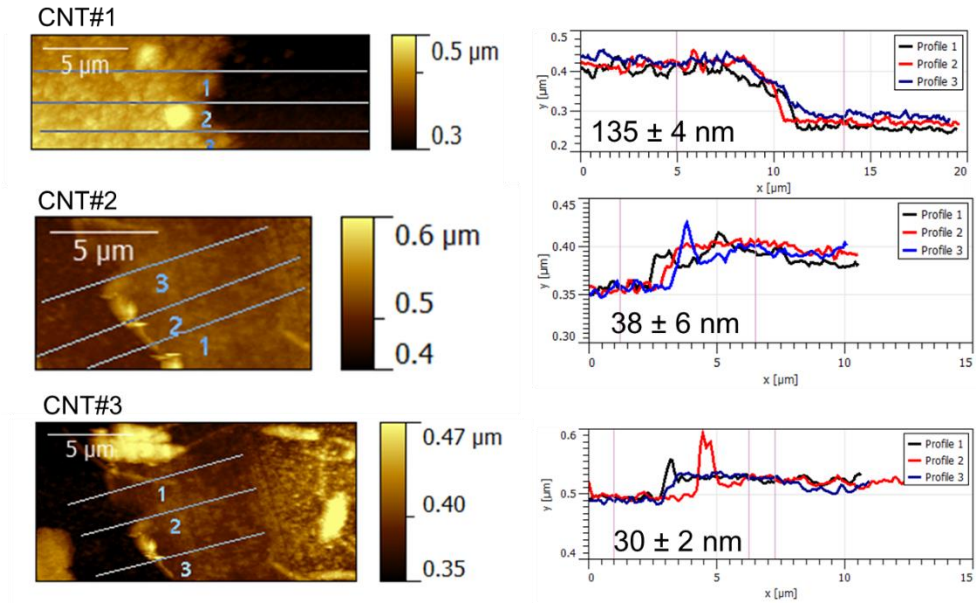

Figure 3.32 Thickness measurements of CNT films using AFM.

The sheet resistance for the two metallic CNT films were measured by the four-point probe method. The summary of the sheet resistance at different treatment time are shown in Figure 3.33, by using $(2\text{-Fc-DMBI})_2$ and Magic Blue (**4**) as n- and p-dopants at the concentration of 2.5 mM and 5 mM, respectively, As described earlier, CNTs are randomly distributed in a 2-D array, CNT#1 with thicker films will have more connected "conducting sticks" for the electrical charges to transfer, thus has lower sheet resistance. The sheet resistance for CNT#1 was reduced from 260 Ω/sq for the pristine film, to 18 Ω/sq and 32 Ω/sq upon n- and p-doping, respectively; while that of the thinner film CNT#2 was reduced from 540 Ω/sq to 63 Ω/sq and 101 Ω/sq, respectively.

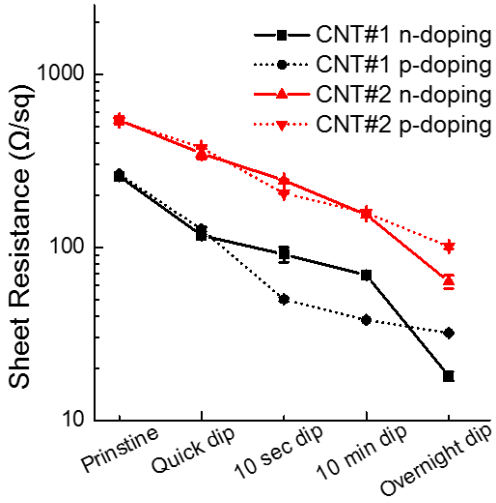

Figure 3.33 Sheet resistance measurements of CNTs doped by $(2\text{-Fc-DMBI})_2$ and Magic Blue.

The results from the AFM analysis of pristine and doped surfaces are provided in Figure 3.34, with RMS roughness values labeled. The AFM data indicates that CNT films have high surface roughness (ca. 7 nm), especially compared with graphene and ITO surface used in this research (Figure 3.35). Slightly increase of the surface roughness is observed upon n- and p-doping.

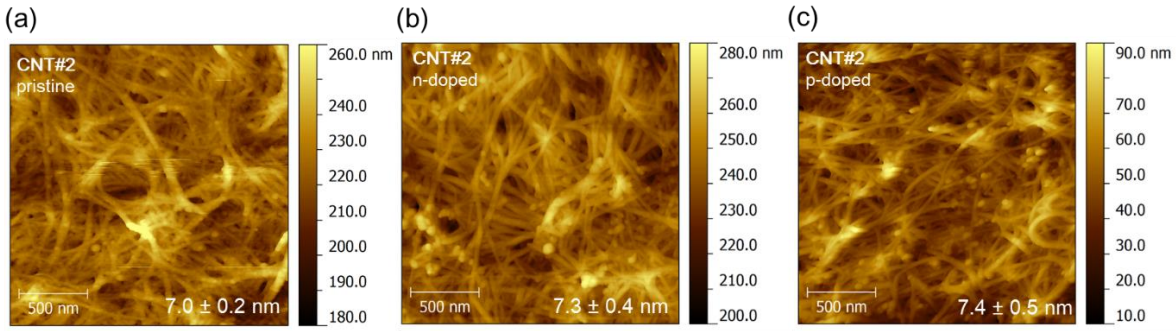

Figure 3.34 Comparison of tapping-mode AFM images of three CNT films before and after the dopants treatments.

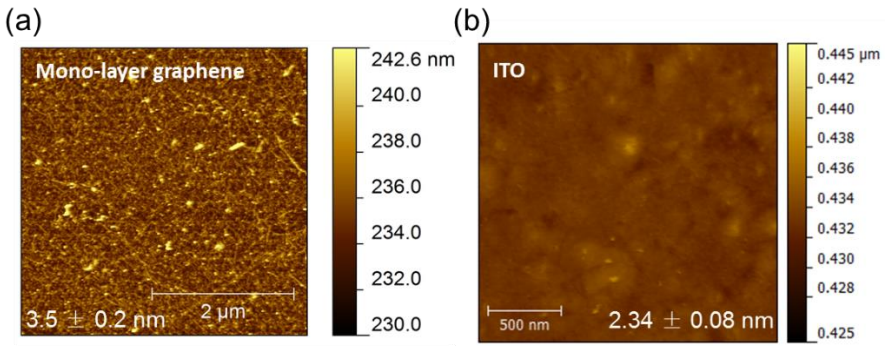

Figure 3.35 AFM topography images for graphene (a) and ITO surface (b).

To investigate different doping effects on semiconducting CNTs, FETs were measured on two different sample that were dip-coated in p- and n-dopants. Figure 3.36 shows the representative transfer characteristic of a CNT FET before and after doping with dopant on a semi-logarithmic scale. The CNTs used in this research are p-channel materials. Upon p-doping by Magic Blue, significantly shifts of the threshold voltage V_{th} to positive voltage was observed, together with the increase of both I_{on} and I_{off}. The mobility μ, is calculated from the linear region using equation:

Equation 3.7
$$\mu = \frac{L}{WC_iV_{ds}}\frac{\partial I_{ds}}{\partial V_g}$$

where, I_{ds} is the drain-source current, V_{ds} and V_g are the drain-source voltage and gate voltage respectively, W is the channel width (2 mm), L is the channel length (50 µm). C_i is the geometric capacitance of the dielectric layer, which is 1.15×10^{-4} F/m^2 for the 300 nm SiO_2 used in this research. As summarized in Table 3.10, the mobility of the films increased from 0.34 cm^{2}V^{-1}s^{-1} to 0.80 cm^{2}V^{-1}s^{-1}, with quick dipping into 5 mM Magic Blue (**4**) solution. Longer dopant treatment time leads to the degeneration of the transistors and decrease of the mobility. On the n-doping side, as increasing the immersion time into the dimer solution, the CNT film is transferred from a hole-transport material into an ambipolar material, and then, into a electron-transport

material. The mobility decreases from 0.34 $cm^2V^{-1}s^{-1}$ (hole-mobility) to the order of 10^{-2} $cm^2V^{-1}s^{-1}$ (electron mobility) (**Error! Reference source not found.**). In all, the ehavior of CNT FET devices can be tuned by controlling the doping time, and dopant type.

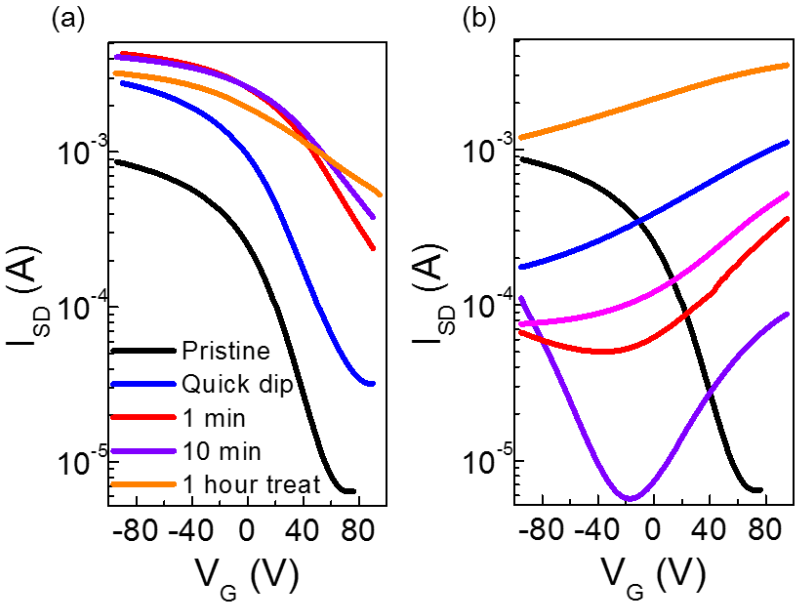

Figure 3.36 CNT FET measurements. (a) p-doped by Magic Blue (**4**). (b) n-doped by $(2\text{-Fc-DMBI})_2$.

Table 3.10 p-Doped CNT FET mobility measurements.

	Doping level	**Mobility, μ_h, ($cm^2V^{-1}s^{-1}$)**	**$I_{ON/OFF}$**
Pristine	none	0.34	~160
p-dope	Quick dip	0.80	~80
	1 min	0.50	~20
	10 min	0.43	~10
	1 h	0.19	~6

Table 3.11 n-Doped CNT FET mobility measurements.

	Doping level	**Mobility ($cm^2V^{-1}s^{-1}$)**	**$I_{ON/OFF}$**
Pristine	none	0.34 (μ_h)	~160
n-dope	Quick dip	1.4×10^{-2} (μ_e)	~20
	10 sec	2.8×10^{-2} (μ_e)	~6
	1 min	3.9×10^{-2} (μ_e)	~6
	10 min	5.2×10^{-2} (μ_e)	~6
	1 h	5.6×10^{-2} (μ_e)	~3

3.9 Conclusions

Controllable n- and p-doping of graphene using solutions of redox-active dopants has been demonstrated. Large carrier densities can be achieved and the work function can be tuned over a range of 2.1 eV, depending on the nature of the dopant, concentration of the dopant solution, and the exposure time. The WF shift consists of two components: a Fermi-level shift and the vacuum level shift. The former one is from the population (or depopulation) of the graphene band structure through electron transfer to or from graphene, while the latter one is caused by the surface dipole created by the charges generated. Resistivity is decreased due to the partial filling or emptying of graphene's bands, and the sheet resistance for monolayer graphene can be reduced by more than 90% upon n- and p-doping without losing transparency (summarized in Figure 3.37). Compared with previous work done in the Marder group:[52] larger WF shifts were achieved in this research (2.1 eV as compared with 1.8 eV) mainly caused by the stronger doping effect on p-side (by Magic Blue); the sheet resistance for the doped graphene films were also measured, as opposed to the indirect interpretation from the FET results in previous research;[51] various n- and p-dopants were tested and compared on graphene, which can be served as a guideline for future doping studies on

different systems.

The n- and p-dopants were also applied to metallic and semiconducting CNTs, and strong doping effects were characterized by the sheet resistance and FET measurement. This research demonstrates that these dopants can potentially be applied to modulate the electronic properties of graphene and CNTs for use as TCE in a variety of electronic devices (LEDs, OFETs, organic photovoltaics, etc) where WF tuning and high conductivity are required. Organic field-effect transistors, diodes, and solar cells with doped graphene electrodes were fabricated and will be discussed in Chapter 5.

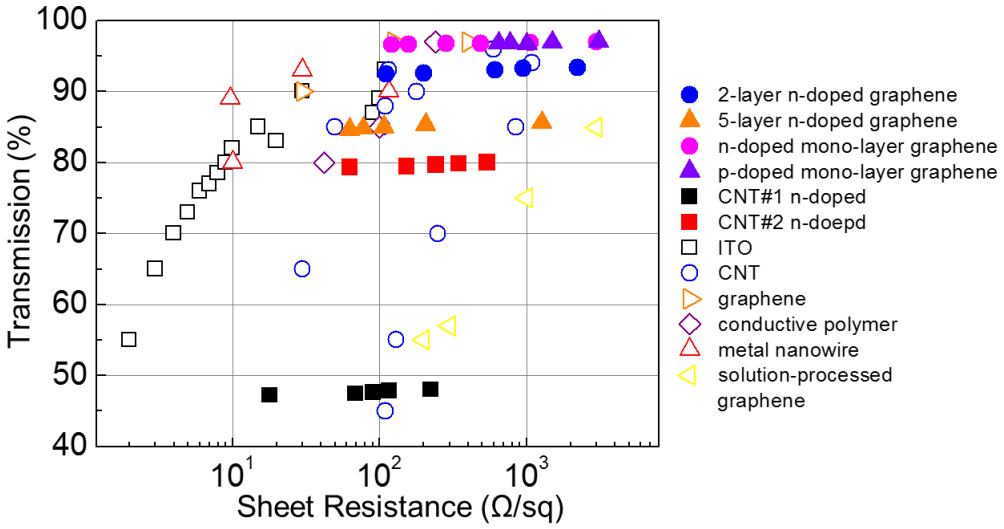

Figure 3.37 Summary of the sheet resistance versus optical transmission for the doped multi- and mono-layer graphene, compared with the literature reported transparent electrodes, including ITO,[13] CNT,[11,12,14] graphene,[3,15] conductive polymer,[9,16,17] metal nanowire,[5,8,18] and solution-processed graphene.[19]

3.10 Experimental

3.10.1 Materials and equipments

The Cu foils for graphene grown were purchased from Alfa Aesar (item No. 14482). Solvents used in the doping studies were purified in a MBRAUN solvent purification system with moisture absorbing filters. Toluene was additionally dried over

CaH_2, distilled and subjected to three freeze-pump-thaw cycles. All the sample treatment and GFET measurements were carried out in a Unilab MBRAUN glovebox (< 0.1 ppm of water, < 0.5 ppm oxygen). Glassware was dried in oven for at least 1 h, prior to bringing into the glovebox. All GFET samples were annealed in the glovebox at 200 °C for few minutes until the neutrality point was back to zero after removal of the physisorbed species. All the dopants treated samples, include graphene and CNTs were rinsed by the fresh solvent for at least three times with shaking to remove the physisorbed molecules, then dried by a rubber ball. GFET devices were measured using a probe station equipped with a HP 4156 semiconductor parameter analyzer under a nitrogen atmosphere. All measurements were also carried out under inert atmosphere, unless stated otherwise.

UPS/XPS Spectra were measured on Kratos Axis Ultra^{DLD} system at a base pressure of 10^{-9} Torr, using He-I lamp radiation and monochromatic Al Kα line, respectively. All the sample treatments were done in a glovebox, and transferred through a Kratos air-sensitive transporter without air exposure. UPS was acquired at 5 eV pass energy and 0.05 eV step size with the aperture and iris set to 55 μm. The Fermi level was calibrated using sputtered clean silver. From the secondary electron edge (SEE) of the spectra, the work function (φ) can be calculated for each film by subtracting the SEE from the total radiation energy (21.22 eV). The position of the valence-band maximum can be determined from the onset of photoemission. XPS peak fits were done with Vision Processing Software 2.2.8 using mixed Gaussian/Lorentzian distributions to minimize *chi* squared value.

All AFM images were acquired under atmospheric conditions using a commercial Agilent 5600 LS equipped with an AC-AFM controller. Cantilevers (NSC35/NoAl from Mikromasch) used for all the measurements were made from n-type silicon (phosphorus doped), utilizing cantilevers of 130 ± 5 μm in length. Image acquisition was performed using PicoView 1.10, and image processing performed using the open source program Gwyddion version 2.20.

3.10.2 Synthesis and transfer of graphene

The graphene samples used in all experiments discussed in this chapter were grown through the chemical-vapor deposition (CVD) method. 25 μm thick Cu foil (Alfa Aesar, item No. 14482) was loaded into a quartz tube and heated by a horizontal split-tube furnace. As depicted in Figure 3.38, under a base pressure of ~90 mTorr, the furnace was heated up to 1000 °C with an Ar (50 sccm)/H_2 (20 sccm) mixture continuously flowing. This helps to remove oxide from the Cu foil and to increase the grain size of the Cu, as this is critical for large area and uniform synthesis of graphene films. Subsequently, growth was performed at the same temperature for 20 min under a flow of a CH_4 (35 sccm)/H_2 (20 sccm) mixture. After growth, the furnace was shut down and opened, which allow the quartz to rapid cool down to room temperature under the same gas flow rate.

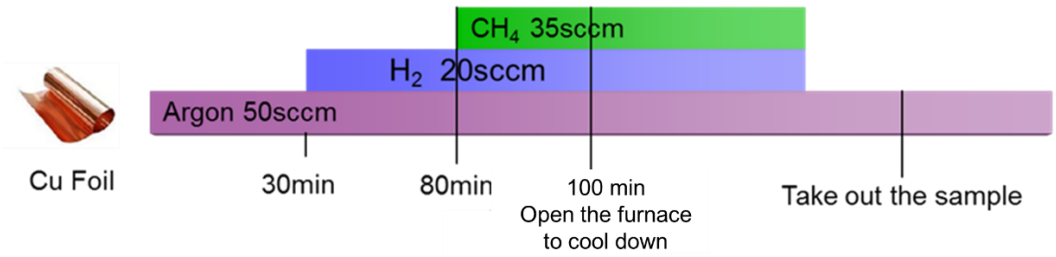

Figure 3.38 Chemical-vapor deposition (CVD) growth of graphene used in this chapter.

As shown in Figure 3.39, to transfer the graphene onto the target substrate, PMMA (9% volume dissolved in anisole) was deposited on the graphene by spin coating, then cured at 180 °C for ca. 5 min in an oven. The Cu foil was then etched with either 30 vol. % iron(III) nitrate, $Fe(NO_3)_3$, aqueous solution or ammonium persulfate (0.1 M) for few hours, leaving the PMMA/graphene film. After washing in DI water two times, the film was then treated with 10 vol. % HCl solution for 10 min when $Fe(NO_3)_3$ was used as the etching solution, to remove the residue. The sample was washed again in deionized (DI) water several times to remove residual HCl and any contaminants bound to the graphene. For all these washing and acid treatments, a piece of clean glass slide was used to transfer bilayer PMMA/graphene from one batch to another to reduce any folding or mechanical force on the film.

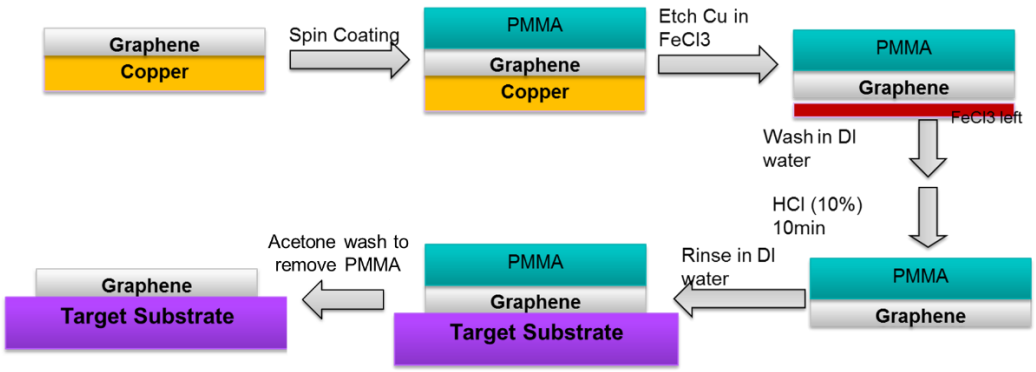

Figure 3.39 Graphene transfer procedures.

3.10.3 Device Fabrication of FET and four-point probe devices

The patterning of the devices follows the general photolithography procedures. The process began with four-inch silicon dioxide wafer (300 nm thermally grown SiO_2 on top of highly doped Si), which was spun coated with a primer (P-20), then with SC 1813 photoresist to have 3 nm film, both at 3000 rpm for 30 sec. Care was taken to ensure no bubbles were left after the spin-coating was complete. The wafer was then soft-baked on a hot plate at 115 °C for four minutes. The Karl Suss Mask MA6 Aligner was used to expose the wafer to the pattern the mask, following by dipping into the developer MF-319 for 1 min. SC 1813 used here is a positive photoresist, which will leave the exposed area become soluble when exposed to the UV light. The Denton Explorer E-Beam Evaporator was used to deposit 3 nm chromium followed by 50 nm gold. Then, the wafer was unloaded from the evaporator and dipped into the acetone to remove the unwanted photoresist and metal layers. Figure 3.6 and Figure 3.8 (page 105 and 107) show the completed set up of the devices with different patterns.

3.10.4 Preparation of the CNT films

Both the metallic and semiconducting CNTs solutions (0.01 mg/mL in aqueous

solution) were purchased from Nanointegris Technologies with 99% purity (item No. HS28030 and HS28030). The fabrication procedures are adapted from the literature reported methods.[63] The CNT solution was diluted to ~1-10 μg/mL using 1% w/v sodium dodecyl sulfate (SDS) in water. As shown in Figure 3.40, the diluted CNT solution was subsequently vacuum filtered through mixed cellulose ester (MCE) membranes (GE Osmonics) with a diameter of 47 mm and a pore size of 100 nm. The thickness of the CNT films was controled by how much diluted solution was added each portion. Solutions smaller than 30 mL may result in regions of thick/thin SWNT deposits on the membrane filter. As shown in Figure 3.40, a thin film of nanotubes accumulates on the surface of the filter. The resulting CNT film was allowed to sit for approximately 15 min to let it fully dry, then gently rinsed with ~1 mL of 2-propanol, followed by ca. 30 mL of water; he film was then allowed to set again for approximately 15 min. To transfer the CNT film onto target substrates, it was first cut into the target size carefully, thoroughly wetted with isopropyl alcohol (IPA) and applied onto transparent substrates. Once the membrane was placed on the substrate and membrane was allowed to dry, the film was quickly placed on the acetone vapor bath to allow the membrane to begin dissolution. The membrane/SWNT/substrate was placed into 4 sequential acetone baths to dissolve the membrane such that only the SWNT film remained on the substrate. Each acetone bath soaking time was approximately 45 min. Three CNT films were transferred onto the glass substrates, as shown in Figure 3.40.

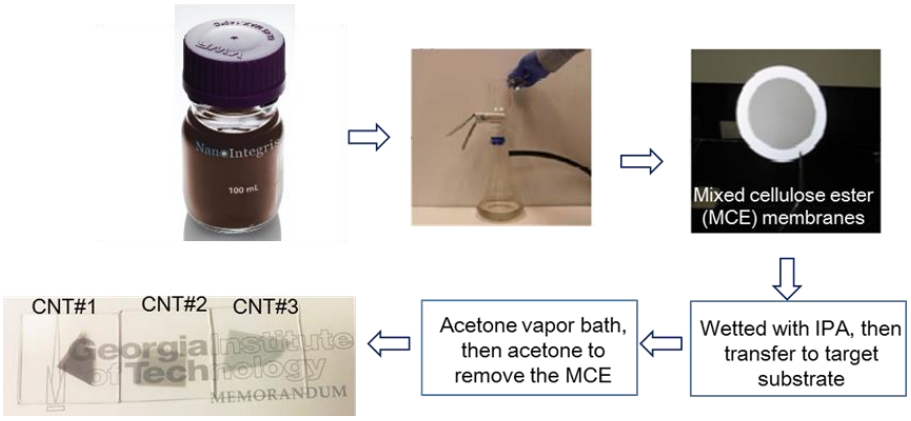

Figure 3.40 Preparation and transfer of CNT films.

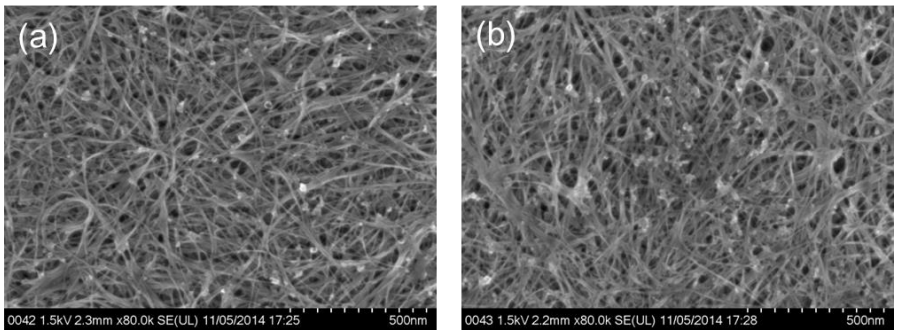

Figure 3.41 SEM images of CNTs before and after doping by $(2\text{-Fc-DMBI})_2$. Acquired on Hitachi SU8230.

3.11 References

(1) Novoselov, K. S.; Geim, A. K.; Morozov, S. V.; Jiang, D.; Zhang, Y.; Dubonos, S. V.; Grigorieva, I. V.; Firsov, A. A. *Science* **2004**, *306*, 666.

(2) Geim, A. K.; Novoselov, K. S. *Nat. Mater.* **2007**, *6*, 183.

(3) Bae, S.; Kim, H.; Lee, Y.; Xu, X.; Park, J.-S.; Zheng, Y.; Balakrishnan, J.; Lei, T.; Kim, H. R.; Song, Y. I. *Nat. Nanotechnol.* **2010**, *5*, 574.

(4) Kim, K. S.; Zhao, Y.; Jang, H.; Lee, S. Y.; Kim, J. M.; Kim, K. S.; Ahn, J.-H.; Kim, P.; Choi, J.-Y.; Hong, B. H. *Nature* **2009**, *457*, 706.

(5) Wu, H.; Kong, D.; Ruan, Z.; Hsu, P.-C.; Wang, S.; Yu, Z.; Carney, T. J.; Hu, L.; Fan, S.; Cui, Y. *Nat. Nano.* **2013**, *8*, 421.

(6) Minami, T. *Thin Solid Films* **2008**, *516*, 1314.

(7) Pang, S.; Hernandez, Y.; Feng, X.; Müllen, K. *Adv. Mater.* **2011**, *23*, 2779.

(8) Karim, S.; Toimil-Molares, M.; Balogh, A.; Ensinger, W.; Cornelius, T.; Khan, E.; Neumann, R. *Nanotechnology* **2006**, *17*, 5954.

(9) Yang, Y.; Heeger, A. *Appl. Phys. Lett.* **1994**, *64*, 1245.

(10) Xia, Y.; Sun, K.; Ouyang, J. *Adv. Mater.* **2012**, *24*, 2436.

(11) Gruner, G. *J. Mater. Chem.* **2006**, *16*, 3533.

(12) Li, J.; Hu, L.; Wang, L.; Zhou, Y.; Grüner, G.; Marks, T. J. *Nano Lett.* **2006**, *6*, 2472.

(13) Kim, N.-R.; Lee, J.-H.; Lee, Y.-Y.; Nam, D.-H.; Yeon, H.-W.; Lee, S.-Y.; Yang, T.-Y.; Lee, Y.-J.; Chu, A.; Nam, K. T. *J. Mater. Chem. C* **2013**, *1*, 5953.

(14) Kymakis, E.; Stratakis, E.; Koudoumas, E. *Thin Solid Films* **2007**, *515*, 8598.

(15) Wang, X.; Zhi, L.; Müllen, K. *Nano lett.* **2008**, *8*, 323.

(16) Cao, Y.; Treacy, G. M.; Smith, P.; Heeger, A. J. *Appl. Phys. Lett.* **1992**, *60*, 2711.

(17) Kim, Y. H.; Lee, J.; Hofmann, S.; Gather, M. C.; Müller‐Meskamp, L.; Leo, K. *Adv. Funct. Mater.* **2013**, *23*, 3763.

(18) Kang, M. G.; Guo, L. J. *Adv. Mater.* **2007**, *19*, 1391.

(19) Wu, J.; Agrawal, M.; Becerril, H. A.; Bao, Z.; Liu, Z.; Chen, Y.; Peumans, P. *ACS Nano* **2009**, *4*, 43.

(20) Neto, A. C.; Guinea, F.; Peres, N.; Novoselov, K. S.; Geim, A. K. *Rev. Mod. Phys.* **2009**, *81*, 109.

(21) Cooper, D. R.; D'Anjou, B.; Ghattamaneni, N.; Harack, B.; Hilke, M.; Horth, A.; Majlis, N.; Massicotte, M.; Vandsburger, L.; Whiteway, E.; Yu, V. *ISRN Condens. Matter Phys.* **2012**, *2012*, 56.

(22) Liu, H.; Liu, Y.; Zhu, D. *J. Mater. Chem.* **2011**, *21*, 3335.

(23) Geim, A. K.; Novoselov, K. S. *Nat. Mater.* **2007**, *6*, 183.

(24) Wang, H.; Wang, Q.; Cheng, Y.; Li, K.; Yao, Y.; Zhang, Q.; Dong, C.; Wang, P.; Schwingenschlögl, U.; Yang, W. *Nano Lett.* **2011**, *12*, 141.

(25) Liang, J.; Jiao, Y.; Jaroniec, M.; Qiao, S. Z. *Angew. Chem. Int. Ed.* **2012**, *51*, 11496.

(26) Pontes, R. B.; Fazzio, A.; Dalpian, G. M. *Phys. Rev. B* **2009**, *79*, 033412.

(27) Pi, K.; McCreary, K.; Bao, W.; Han, W.; Chiang, Y.; Li, Y.; Tsai, S.-W.; Lau, C.; Kawakami, R. *Phys. Rev. B* **2009**, *80*, 075406.

(28) Wang, X.; Li, X.; Zhang, L.; Yoon, Y.; Weber, P. K.; Wang, H.; Guo, J.; Dai, H. *Science* **2009**, *324*, 768.

(29) Bianchi, M.; Rienks, E.; Lizzit, S.; Baraldi, A.; Balog, R.; Hornekær, L.; Hofmann, P. *Phys. Rev. B* **2010**, *81*, 041403.

(30) Gierz, I.; Riedl, C.; Starke, U.; Ast, C. R.; Kern, K. *Nano Lett.* **2008**, *8*, 4603.

(31) Hugo, E. R.; Prasoon, J.; Awnish, K. G.; Humberto, R. G.; Milton, W. C.; Srinivas, A. T.; Peter, C. E. *Nanotechnology* **2009**, *20*, 245501.

(32) Li, B.; Zhou, L.; Wu, D.; Peng, H.; Yan, K.; Zhou, Y.; Liu, Z. *ACS Nano* **2011**, *5*, 5957.

(33) Yaya, A.; Ewels, C. P.; Suarez-Martinez, I.; Wagner, P.; Lefrant, S.; Okotrub, A.; Bulusheva, L.; Briddon, P. R. *Phy. Rev. B* **2011**, *83*, 045411.

(34) Vinogradov, N. A.; Simonov, K.; Generalov, A.; Vinogradov, A.; Vyalikh, D.; Laubschat, C.; Preobrajenski, A. *J. Phys. Condens. Matter* **2012**, *24*, 314202.

(35) Chen, Z.; Darancet, P.; Wang, L.; Crowther, A. C.; Gao, Y.; Dean, C. R.; Taniguchi, T.; Watanabe, K.; Hone, J.; Marianetti, C. A. *ACS Nano* **2014**, *8*, 2943.

(36) Wei, D.; Liu, Y.; Wang, Y.; Zhang, H.; Huang, L.; Yu, G. *Nano lett.* **2009**, *9*, 1752.

(37) Panchakarla, L.; Subrahmanyam, K.; Saha, S.; Govindaraj, A.; Krishnamurthy, H.; Waghmare, U.; Rao, C. *Adv. Mater.* **2009**, *21*, 4726.

(38) Yang, H.; Li, F.; Shan, C.; Han, D.; Zhang, Q.; Niu, L.; Ivaska, A. *J. Mater. Chem.* **2009**, *19*, 4632.

(39) Zhou, Y.; Fuentes-Hernandez, C.; Shim, J.; Meyer, J.; Giordano, A. J.; Li, H.; Winget, P.; Papadopoulos, T.; Cheun, H.; Kim, J. *Science* **2012**, *336*, 327.

(40) Wei, P.; Liu, N.; Lee, H. R.; Adijanto, E.; Ci, L.; Naab, B. D.; Zhong, J. Q.; Park, J.; Chen, W.; Cui, Y. *Nano lett.* **2013**, *13*, 1890.

(41) Pinto, H.; Jones, R.; Goss, J.; Briddon, P. *Phys. Status Solidi A* **2010**, *207*, 2131.

(42) Pinto, H.; Jones, R.; Goss, J.; Briddon, P. *J. Phys.: Condens. Matter* **2009**, *21*, 402001.

(43) Park, J.; Lee, W. H.; Huh, S.; Sim, S. H.; Kim, S. B.; Cho, K.; Hong, B. H.; Kim, K. S. *J. Phys. Chem. Lett.* **2011**, *2*, 841.

(44) Hwang, E. H.; Adam, S.; Das Sarma, S. *Phys. Rev. B* **2007**, *76*, 195421.

(45) Wehling, T. O.; Novoselov, K. S.; Morozov, S. V.; Vdovin, E. E.; Katsnelson, M. I.; Geim, A. K.; Lichtenstein, A. I. *Nano Lett.* **2008**, *8*, 173.

(46) Lin, Y.-C.; Lin, C.-Y.; Chiu, P.-W. *Appl. Phys. Lett.* **2010**, *96*, 133110.

(47) Gao, W.; Kahn, A. *J. Appl. Phys.* **2003**, *94*, 359.

(48) Chen, W.; Chen, S.; Qi, D. C.; Gao, X. Y.; Wee, A. T. S. *J. Am. Chem. Soc.* **2007**, *129*, 10418.

(49) Drechsel, J.; Pfeiffer, M.; Zhou, X.; Nollau, A.; Leo, K. *Synth. Met.* **2002**, *127*, 201.

(50) Duhm, S.; Salzmann, I.; Broker, B.; Glowatzki, H.; Johnson, R. L.; Koch, N. *Appl. Phys. Lett.* **2009**, *95*, 093305.

(51) Paniagua, S. A.; Baltazar, J.; Sojoudi, H.; Mohapatra, S. K.; Zhang, S.; Henderson, C. L.; Graham, S.; Barlow, S.; Marder, S. R. *Mater. Horiz.* **2014**, *1*, 111.

(52) Paniagua-Barrantes, S. *Ph.D. Thesis, Georgia Institute of Technology* **2013**.

(53) Ryu, S.; Liu, L.; Berciaud, S.; Yu, Y.-J.; Liu, H.; Kim, P.; Flynn, G. W.; Brus, L. E. *Nano Lett.* **2010**, *10*, 4944.

(54) Novoselov, K. S.; Geim, A. K.; Morozov, S. V.; Jiang, D.; Katsnelson, M. I.; Grigorieva, I. V.; Dubonos, S. V.; Firsov, A. A. *Nature* **2005**, *438*, 197.

(55) Pisana, S.; Lazzeri, M.; Casiraghi, C.; Novoselov, K. S.; Geim, A. K.; Ferrari, A. C.; Mauri, F. *Nature Mater.* **2007**, *6*, 198.

(56) Davlieva, M. G.; Lindeman, S. V.; Neretin, I. S.; Kochi, J. K. *New J. Chem.* **2004**, *28*, 1568.

(57) Housecroft, C. E.; Sharpe, A. G. *Inorganic Chemistry*; Pearson / Prentice Hall: Essex, UK, 2008.

(58) Loh, K. P.; Tong, S. W.; Wu, J. *J. Am. Chem. Soc.* **2015**.

(59) Nair, R.; Blake, P.; Grigorenko, A.; Novoselov, K.; Booth, T.; Stauber, T.; Peres, N.; Geim, A. *Science* **2008**, *320*, 1308.

(60) Campidelli, S.; Meneghetti, M.; Prato, M. *Small* **2007**, *3*, 1672.

(61) Hu, L.; Hecht, D.; Grüner, G. *Nano Lett.* **2004**, *4*, 2513.

(62) Cao, Q.; Hur, S. H.; Zhu, Z. T.; Sun, Y. G.; Wang, C. J.; Meitl, M. A.; Shim, M.; Rogers, J. A. *Adv. Mater.* **2006**, *18*, 304.

(63) Kim, J. H.; Nam, K.-W.; Ma, S. B.; Kim, K. B. *Carbon* **2006**, *44*, 1963.

CHAPTER 4 n- and p-Doping of 2D TMDC Materials

4.1 Introduction

Layered transition-metal dichalcogenides (TMDCs) are an emerging class of two-dimensional materials with unique thickness-dependent optical and electrical properties.[1,2,3] Unlike graphene, TMDCs offer a wide range of band gaps, which makes these materials very attractive for various device applications, such as field-effect transistors (FETs) with high on/off ratios,[1] chemical sensors,[4-9] and p-n diodes,[10] and integrated circuits.[11] MoX_2 and WX_2 (where X is S or Se), in particular, have tunable bandgaps and strong absorption of incident solar illumination at sub-10 nm thickness, which make them very attractive for transistors and optoelectronics applications.[12-15]

However, several significant challenges remain that limit their widespread use beyond proof-of-concept demonstration. Most of the TMDCs currently used in the research are produced by the by mechanical exfoliation, which is limited to small sizes (few microns).[2,16,17] Much progress has already been achieved with large-area CVD growth of MoS_2 and WSe_2.[18,19] However, the large sheet resistance and/or contact resistance existing at the metal/semiconductor interfaces decrease the overall device performance.[20] Further studies are needed to optimize the film quality and uniformity of these large area TMDCs.

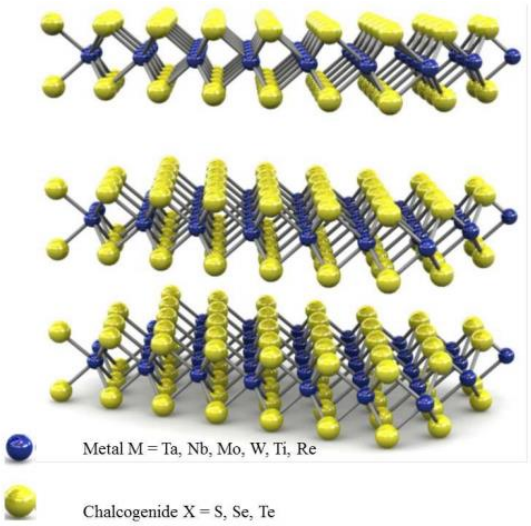

Figure 4.1 2D Transition metal dichalogenides. Adapted from Qing, *et al*.[2]

n- or p-Doping can play an important role in these electronics applications. It is a powerful tool for modifying the electrical and optical properties, leading to dramatically increased conductivities and decreased barriers to charge-carrier injection or extraction. For TMDCs, which have a wide range of bandgaps (unlike graphene), applying dopants to increase the current and induce a Fermi level shift, could subsequently enable modulations of electrical and optical properties. This is essential for their successful use as electronic or optoelectronic devices.[21-24]

While chemical doping has been extensively used to modify organic semiconductors,[25] carbon nanotubes,[26] and graphene,[26,27] little has been done so far on TMDCs. The reported strategies used to modify TMDCs include: 1) doping with metals, such as potassium for n-doping, and gold for p-doping; however, the small size of metal ions makes them easily diffuse within the doped device, and damage the crystal structure by implanting;[28-32] 2) gases, such as NH_3 and NO_2, which can undergo physi- and/or chemisorption;[22,33] and 3) organic molecules, such as polyethyleneimine (PEI) [34] and benzyl viologen.[35] In the second case, the physisorbed gases can be easily

desorbed because the weak van der Waals interactions is not enough to sustain stable charge transfers; while the chemisorption of gases happens through covalent bonding may disturb the original band structure. For example, the O from NO_2 can directly bond to W (in WSe_2) after a thermal disassociation and cause a degeneration of the transistor.[31] Organic molecules, on the other hand, can either go through a partial charge transfer of a Lewis acid-base type interaction, such as PEI,[34] or a full charge transfer through an oxidation-reduction reaction, such as benzyl viologen.[35]

Most of these previous studies demonstrated the feasibility of molecular doping using exfoliated TMDC flakes, but few studies on large-area TMDCs doping. In this chapter, doping studies of wafer-scale TMDCs (including MoS_2 and WSe_2) using redox-active molecules will be discussed, with the aim to explore to which extent the work function (WF) and electrical behavior for large-area TMDCs can be tuned. MoS_2 and WSe_2 were n- and p-doped by the redox-active molecules, and the doped films were characterized by electrical measurements, UPS, XPS, and Raman spectroscopy.

4.2 Doping studies of MoS_2

The tri-layer MoS_2 samples used in this research was synthesized by Phillip Campbell in the group of Dr. Eric Vogel, grown on a highly doped Si wafer with 260 nm thermal SiO_2 using the literature reported method.[36] The pristine MoS_2 sample used in this research shows n-channel behavior, $(2\text{-Fc-DMBI})_2$ and 2-H-Fc-DMBI were chosen as the n-dopants. As discussed in the previous chapter, two different doping mechanisms are expected these dopants. For 2-Fc-DMBI-H, the hydride or hydrogen transfer was involved in the doping process. Thus, the doping ability depends on both

the electron affinity (EA) and hydrogen accepting ability of doped materials; while dimers only involve electron transfer to form two monomeric cations. In the case of 2-H-Fc-DMBI/MoS_2 doping, the fate of the H atom is unknown. MoS_2 films were also treated with a p-dopant tris(4-bromophenyl)ammoniumyl hexachloroantimonate[37] ("Magic Blue"), which is stable in dry air and dry CH_2Cl_2. As discussed in Chapter 3, treatment with Magic Blue is expected to form the neutral tri(4-bromophenyl)amine and leave $SbCl_6^-$ anions on the surface.

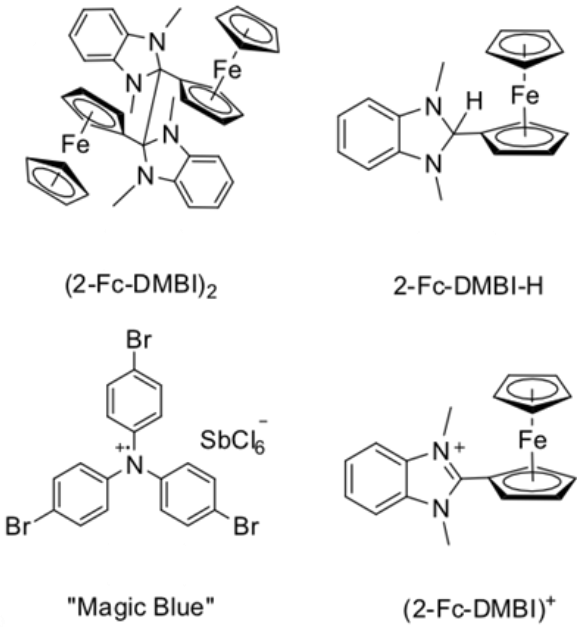

Figure 4.2 Molecules used in this study. The cation 2-Fc-$DMBI^+$ is also shown and is the expected product of doping with both $(2\text{-Fc-DMBI})_2$ and 2-H-Fc-DMBI;

4.2.1 FET characterization

The MoS_2 FETs were fabricated and measured by Dr. Alexey Tarasov in the group of Dr. Vogel. Electrical measurements were performed on back-gated field-effect transistors made from wafer-scale trilayer MoS_2. The device schematic and its optical image are presented in Figure 4.3. Since the pristine MoS_2 sample shows n-channel behavior, 30 nm Ti and 30 nm Au were chosen as the top electrodes across which the

drain-source voltage V_{ds} is applied. A highly doped Si wafer serves as both the substrate and the back-gate where gate voltage V_{bg} is applied.

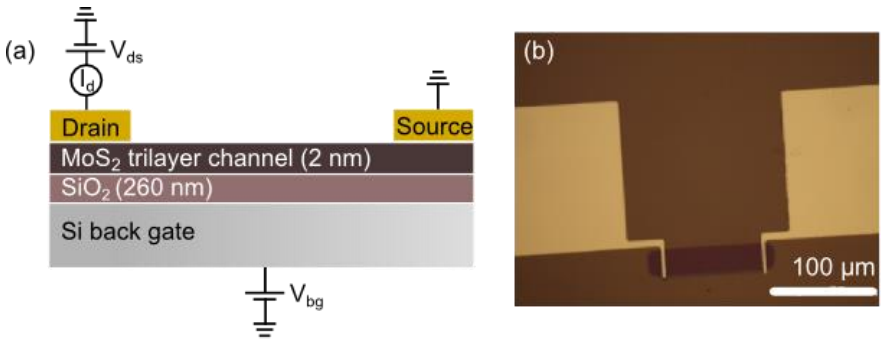

Figure 4.3 (a) Schematics of a back-gated MoS_2 transistor. b) Optical image of the MoS_2 transistor.

Three different samples were dip-coated in solutions of the dopants presented above for up to 10 min. The concentration of $(2\text{-Fc-DMBI})_2$ is 2.5 mM, while 2-H-Fc-DMBI and Magic Blue is 5 mM. Each sample contained several tens of transistors. Doping treatments were performed inside a glove box. After a short exposure to air during the transfer step (ca. 1 min), the electrical measurements were performed in high vacuum (ca. 10^{-6} mbar). The electrical measurements are summarized in Figure 4.4. It shows a representative transfer characteristic of a MoS_2 FET before and after doping with $(2\text{-Fc-DMBI})_2$ on a semi-logarithmic scale: even a short immersion into the $(2\text{-Fc-DMBI})_2$ solution significantly shifts the threshold voltage of the transistor V_{th} (defined as the voltage necessary to achieve a current of 10^{-10}A) to more negative values, as indicated by the arrow. After this measurement, the sample was treated in the same solution for 10 min and measured again. An even more pronounced V_{th} shift and a further current increase are observed. Figure 4.5 shows the transistor measurements for 2-H-Fc-DMBI doped MoS_2, where significant shift of V_{th} were also observed. These

results are consistent with n-doping of the channel.

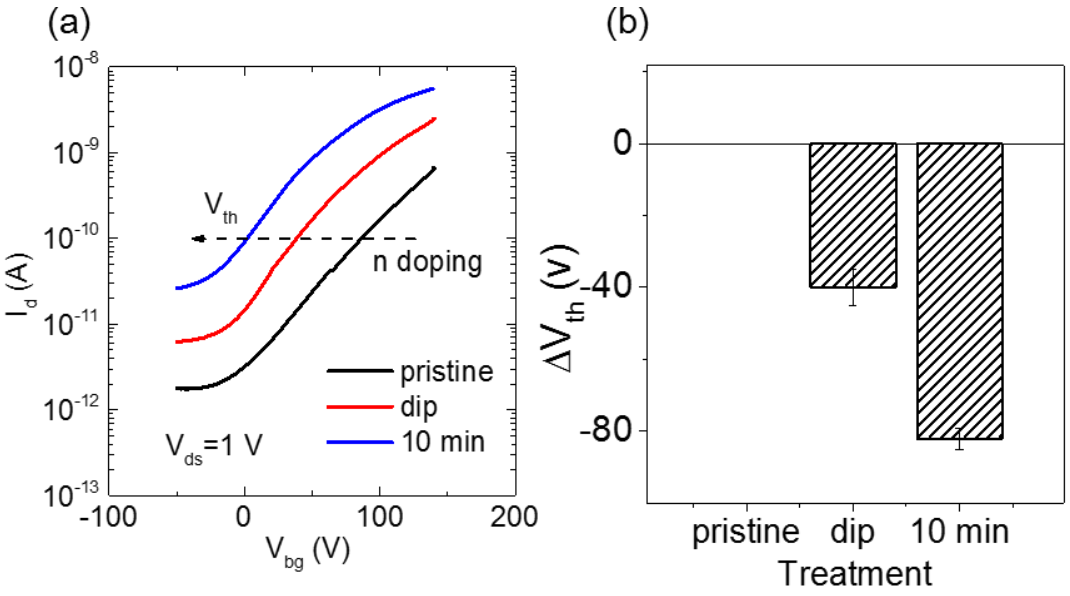

Figure 4.4 Representative transfer characteristics of a MoS_2 FET before and after doping with $(2\text{-Fc-DMBI})_2$. (b) Effects of $(2\text{-Fc-DMBI})_2$ on the threshold voltage V_{th}. Several transistors were measured in each case. FETs were measured by Dr. Alexey Tarasov.

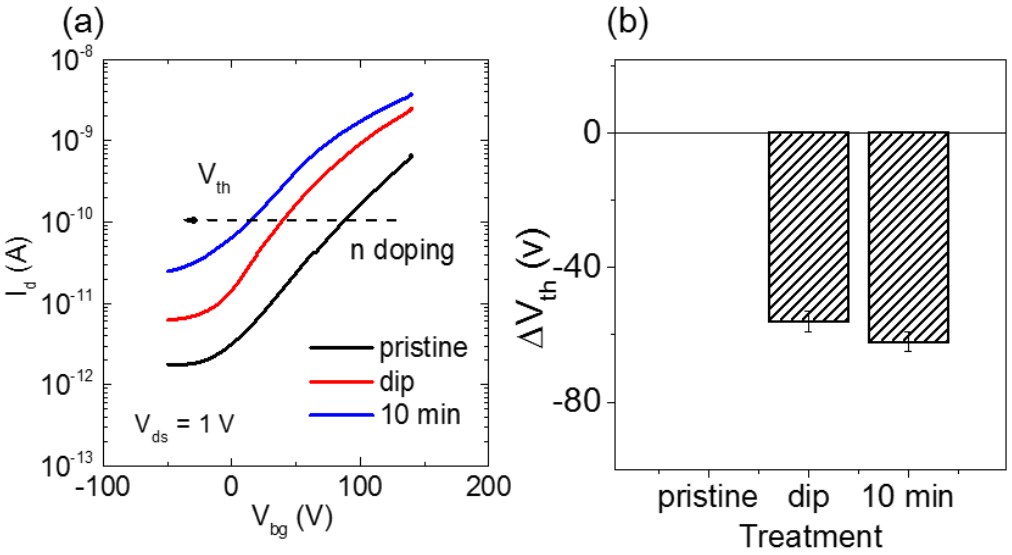

Figure 4.5 Representative transfer characteristics of a MoS_2 FET before and after doping with 2-H-Fc-DMBI. (b) Effects of 2-H-Fc-DMBI on the threshold voltage V_{th}. Several transistors were measured in each case. FETs were measured by Dr. Alexey Tarasov.

Extracted threshold voltage shifts, ΔV_{th}, are plotted relative to the pristine

sample (i.e. $V_{th,\ pristine}$ = 0 V) in Figure 4.4(b) and Figure 4.5(b), where the error bars indicate the standard deviation from averaging the results obtained with different devices. Both n-dopants induce a significant negative ΔV_{th} shift, but with a larger effect for $(2\text{-Fc-DMBI})_2$ than 2-H-Fc-DMBI. This is consistent with previous observation that $(DMBI)_2$ dimers are stronger dopants for graphene than DMBI-H derivatives, as discussed in Chapter 3. These differences in dopant strength may be due to both thermodynamics and kinetics. As discussed earlier, different reaction mechanisms are coupled to the electron-transfer process of these two dopants, even though both will form stable $DMBI^+$ cations and n-doped semiconductor. In the case of the dimers a C—C bond is broken, whereas in DMBI-H derivatives a C—H bond is broken, leading to the formation of additional side products, the identity of which is unclear in the case of MoS_2 doping.

In contrast, the Magic Blue treatment shifts the transfer curves to more positive gate values and decreases the overall electron current (Figure 4.6). This is consistent with the expected effects of p-doping of MoS_2. However, a significant p-channel behavior (or hole transport) was not observed at negative gate voltages. A detailed discussion will be presented below, together with the analysis of UPS data. The extracted threshold voltage shifts, ΔV_{th}, are plotted relative to the pristine sample in Figure 4.6(b).

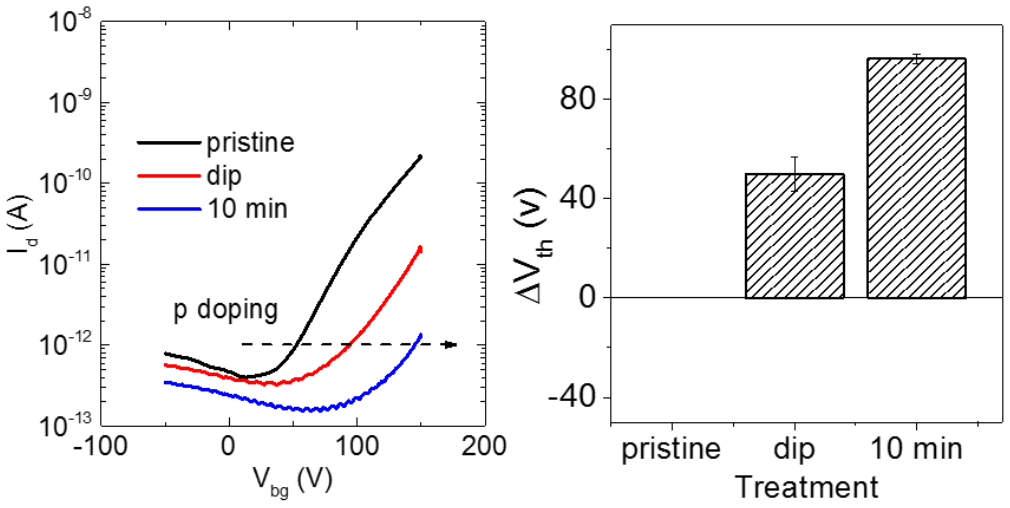

Figure 4.6 Representative transfer characteristics of a MoS_2 FET before and after doping with Magic Blue. (b) Effects of Magic Blue on the threshold voltage V_{th}. Several transistors were measured in each case. FETs were measured by Dr. Alexey Tarasov.

Based on these ΔV_{th} shifts, the charge density n in MoS_2 after doping can be estimated using the following expression:

Equation 4.1 $$n = \frac{C_{bg}\Delta V_{th}}{e}$$

where $e = 1.6\times10^{-19}$ C is the electron charge, and $C_{bg} \approx 1.33\times10^{-8}$ Fcm^{-2} is the estimated back-gate capacitance $C_{bg} = \varepsilon_0\varepsilon_r/d$, with $\varepsilon_0 = 8.85\times10^{-12}$ F/m being the vacuum permittivity, ε_r =3.9 the relative permittivity of SiO_2, and d = 260 nm the oxide thickness. With ΔV_{th} values from Figure 4.4(b) and Figure 4.5(b), after 10 min treatment, the densities of electrons introduced by $(2\text{-Fc-DMBI})_2$ and 2-H-Fc-DMBI are: 6.3×10^{12} cm^{-2} and 5.2×10^{12} cm^{-2}, respectively; and the density of carriers removed by Magic Blue is 8.0×10^{12} cm^{-2} (Figure 4.6). The induced charge densities can be controlled by changing the treatment time or the solution concentration, providing effective control over the doping level.

These values are slightly lower than the n-doping densities previously reported for doping few-layer exfoliated flakes of MoS_2 with potassium (~1×10^{13} cm^{-2})[38] and

benzyl viologen (~1.2×10^{13} cm^{-2}).[35] It may be caused by the brief exposure to air after the doping treatment and before the transistor measurement in the present procedure. Moreover, the MoS_2 used in this research has different material quality as the exfoliated ones, thus different density of states. It should also be noted that the extremely high electron densities induced by doping in these previous reports resulted in a dramatic loss of the current on/off ratio,[35,38] which is not observed in this doping study.

4.2.2 Band structure characterization

The effect of molecular surface doping can be understood in terms of changes to the band structure of a semiconductor. The tri-layer MoS_2 used in this research has an optical band gap of ~1.8 eV (derived from absorption measurements), which is higher than the reported value for the exfoliated trilayer MoS_2 (~1.5 eV[39]). As described in Figure 4.7, the band structure of an n-type semiconductor is illustrated for 3 different cases: untreated or pristine (center), p-doped (left), and n-doped (right). Upon p-doping, E_F shifts closer to the VBM because of emptying of states close to the VB edge by electron transfer (denoted by ϕ_{SF}), while the E_{vac} is increased across the interface due to the formation of a surface dipole between the resultant positively charged semiconductor and negatively charged dopant ions (denoted by ϕ_{SD}). Both of these effects are expected to contribute to the increasing of ϕ upon p-doping, i.e. $\Delta\phi = \Delta\phi_{SF} + \Delta\phi_{SD}$. Conversely, E_F and E_{vac} are shifted to the opposite direction when the material is n-doped, thereby decreasing the work function ϕ (right part).

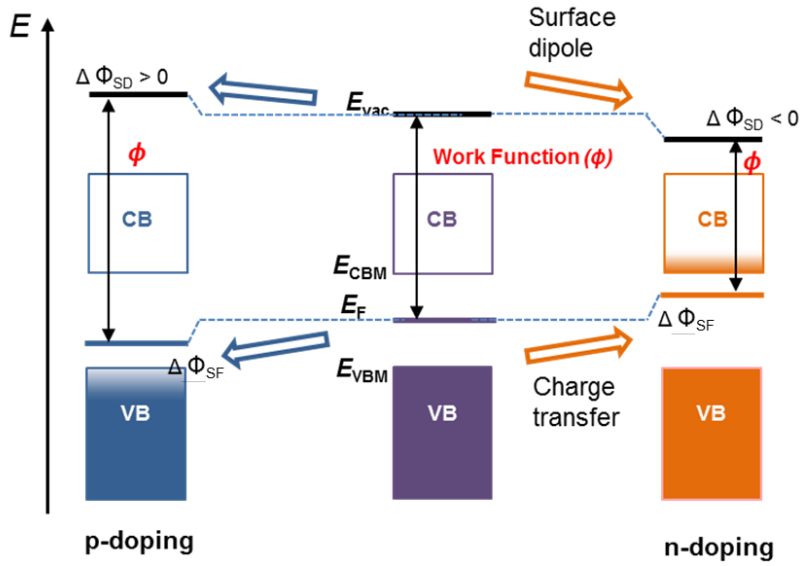

Figure 4.7 Effect of molecular surface doping on the band structure of an n-type semiconductor.

UPS is used to determine the work function ϕ and the position of E_{VBM} relative to E_F. Figure 4.8 shows the high binding energy cutoff regions (i.e., secondary edge) of the UPS spectra for the sample doped with $(2\text{-Fc-DMBI})_2$. The secondary electron edge (SEE) shifts to increasingly higher binding energy with increasing dopant treatment time. The work function of pristine MoS_2 is ϕ = 4.63 eV, similar to previous reports,[40] and decreases significantly by ~1 eV after 10 min $(2\text{-Fc-DMBI})_2$ treatment. Figure 4.8 also shows the corresponding low binding energy part of the UPS spectra close to the Fermi energy (E_F = 0 eV). Prior to doping, the Fermi level of pristine MoS_2 is located at ~1.32 eV above the VBM which in the upper half of the band gap. This is consistent with the n-type nature of MoS_2, which could be either intrinsic due to sulfur vacancies[41-44] or extrinsic due to defects at the substrate/MoS_2 interface.[45] With increasing doping time, the onset of ionization (E_{VBM}) shifts to higher binding energy. Importantly, consistent with the electrical measurements, $(2\text{-Fc-DMBI})_2$ gives larger WF and E_F shift than 2-H-Fc-DMBI, as shown in Figure 4.9.

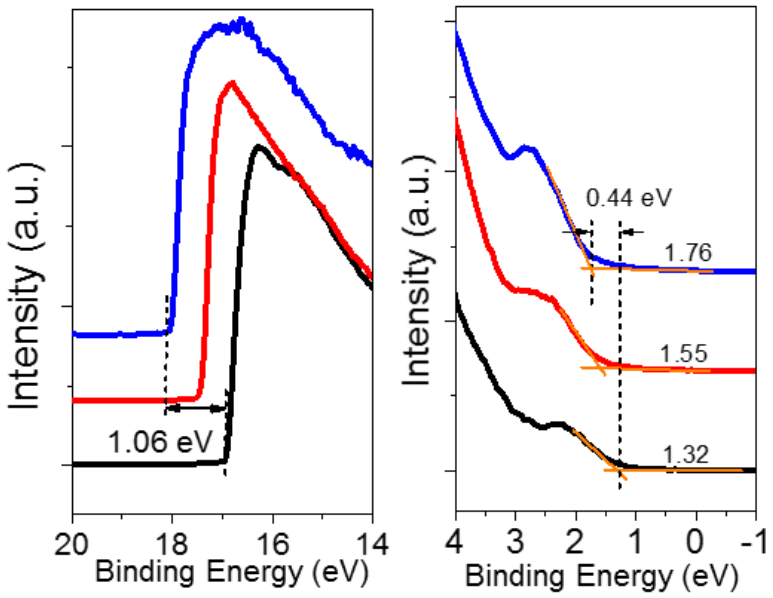

Figure 4.8 UPS of MoS_2 before and after doping with $(2\text{-Fc-DMBI})_2$: secondary electron edge shifts (SEE) of MoS_2 after various treatment times (left); low binding energy region (near the Fermi energy $E_F = 0$ eV) (right).

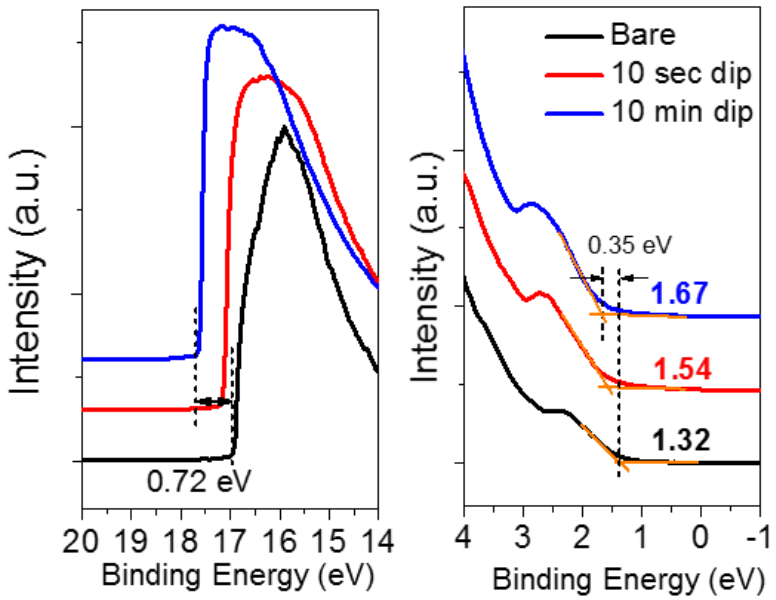

Figure 4.9 UPS of MoS_2 before and after doping with 2-H-Fc-DMBI: secondary electron edge shifts (SEE) of MoS_2 after various treatment times (left); low binding energy region (near the Fermi energy $E_F = 0$ eV) (right).

On the other hand, after successive treatments of MoS_2 with Magic Blue (Figure 4.10), an increase in the work function is observed. The SEE shifts to lower binding energies with increasing treatment times, and the VBM shifts to lower binding energy

relative to E_F.

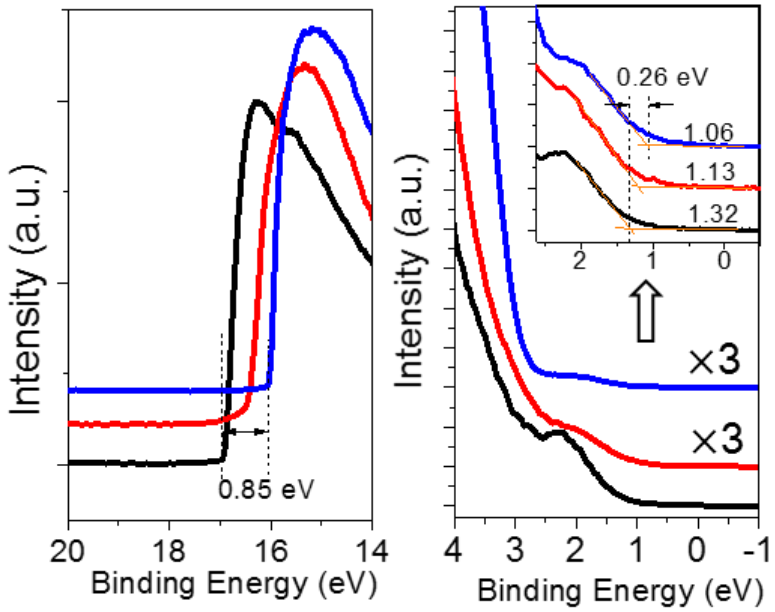

Figure 4.10 UPS of MoS_2 before and after doping with Magic Blue: secondary electron edge shifts (SEE) of MoS_2 after various treatment times (left); low binding energy region (near the Fermi energy E_F = 0 eV) (right).

As mentioned above, the total ϕ change consists of two different contributions: one from the shift of the vacuum level, E_{vac}, arising from surface dipole formation (ϕ_{SD}), and another from the shift of E_F relative to the VBM contributed from the (de)population of semiconductor states on doping (ϕ_{SF}). Figure 4.11 summarizes the total change in work function $\Delta\phi$ and ϕ_{SF}. The contribution from the surface dipole is the difference $\Delta\phi_{SD} = \Delta\phi - \Delta\phi_{SF}$. In all cases, both effects make significant contribution, and the relative importance of the dipole contribution generally increasing with the treatment time. For a given treatment time, both contributions from $(2\text{-Fc-DMBI})_2$ doping are larger than those using 2-H-Fc-DMBI, consistent with the electrical measurements discussed above.

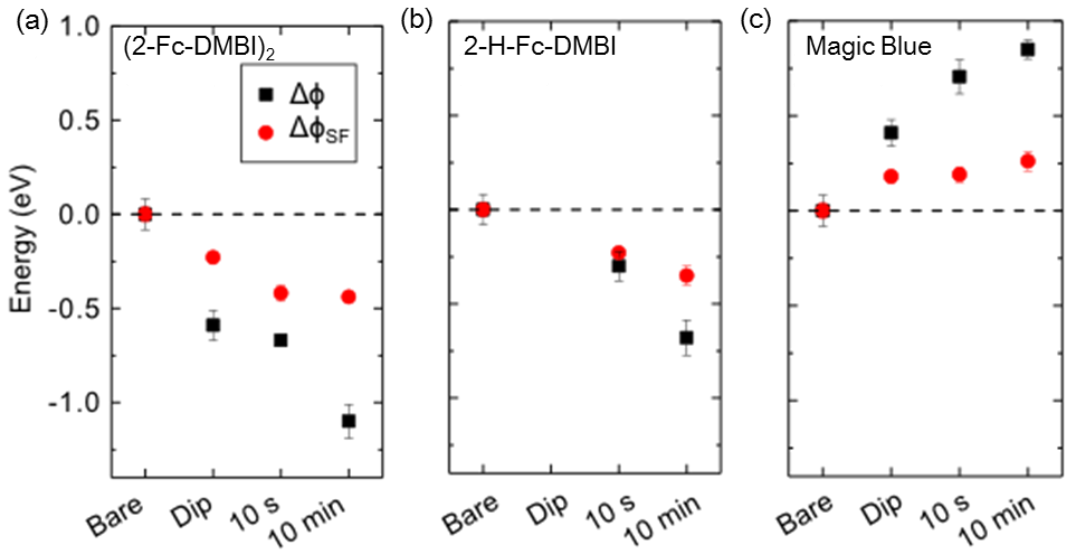

Figure 4.11 Summary of total work function shifts $\Delta\phi$ (black squares) and the contribution to the WF change from state filling/emptying $\Delta\phi_{SF}$ (red circles) for different dopants and treatment times, shown relative to the pristine value (energy = 0 eV, dashed line).

4.2.3 XPS characterization

XPS was also used to investigate the doping effects. As seen in Figure 4.12 and Figure 4.13, the binding energy (BE) of the main Mo 3d peak of n-doped MoS_2 shifts to a higher value. This upshift of peaks is attributed to the population of semiconductor states upon n-doping, and the Fermi level shift toward the conduction band edge. It is consistent with the E_{VBM} shift characterized by the UPS, and also consistent with previous studies on doped MoS_2 flakes.[46] On the other hand, depopulation of filled states through Magic Blue treatment shifts the MoS_2 Mo 3d peak to lower binding energies since the Fermi level is being lowered relative to the VBM (Figure 4.14).

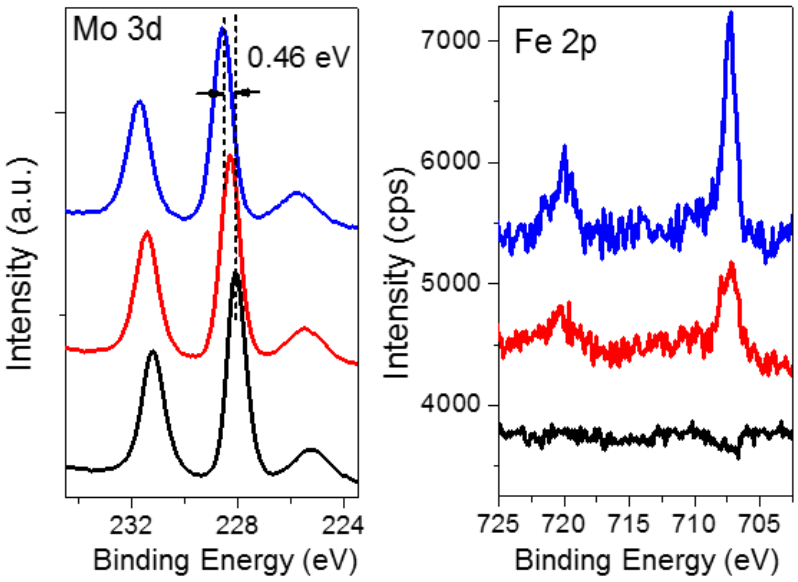

Figure 4.12 XPS core level ionizations characteristic of Mo 3d and Fe 2p from (2-Fc-DMBI)$_2$ doped MoS_2 films.

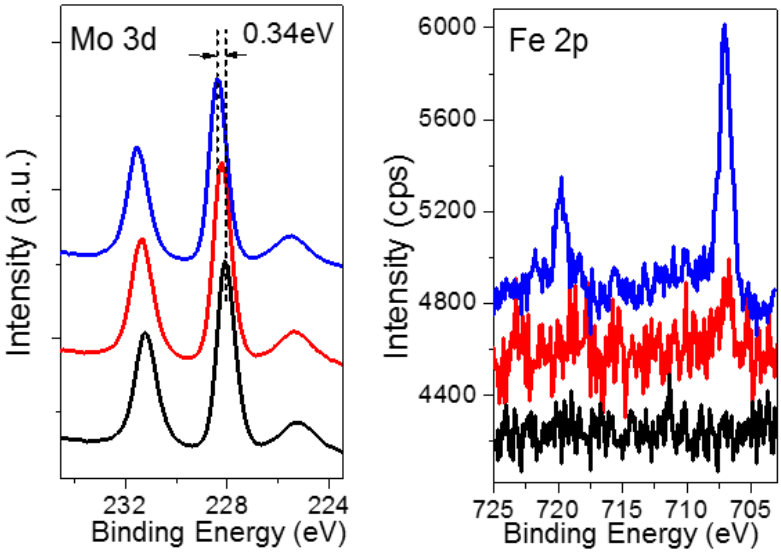

Figure 4.13 XPS core level ionizations characteristic of Mo 3d and Fe 2p from 2-H-Fc-DMBI doped MoS_2 films.

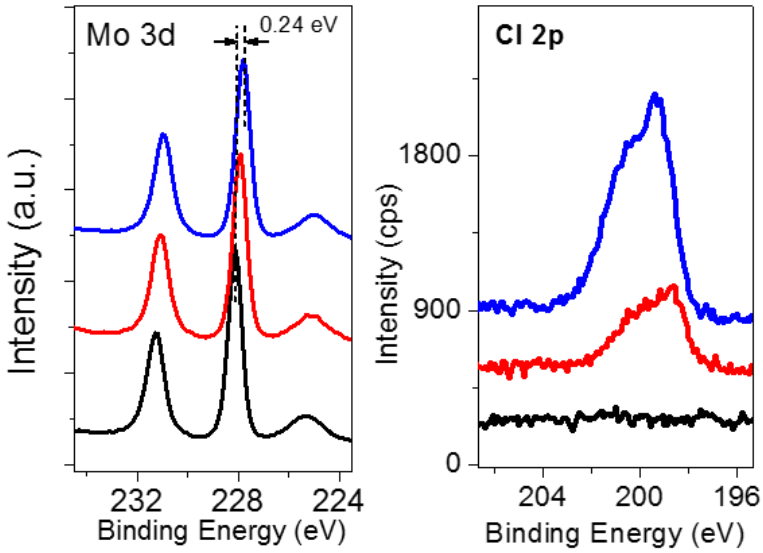

Figure 4.14 XPS core level ionizations characteristic of Mo 3d and Cl 2p from Magic Blue doped MoS_2 films.

Moreover, XPS also reveals increasing surface concentrations of dopants: (2-Fc-DMBI)$_2$ and 2-H-Fc-DMBI are based on the Fe 2p peak (Figure 4.12 and Figure 4.13), while Magic Blue is based on Cl 2p (Figure 4.14). Assuming that all the dopants fully reacted and only cations (or anions) present on the surface for n-dopant (or p-dopant), the surface concentrations of (2-Fc-DMBI)$_2$ and 2-H-Fc-DMBI dopants from the Fe/Mo ratios can be estimated. The coverage is calculated based on the dopant to MoS_2 ratio relative to the theoretical value, which is estimated from how many dopant monomers can fit in a close packed arrangement on the surface of trilayer MoS_2. Similarly, the concentration for Magic Blue can also be estimated based on the Cl/Mo ratio.

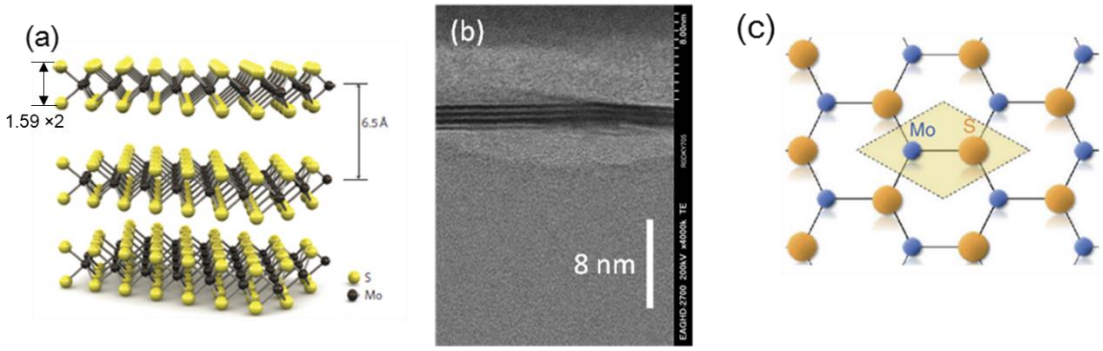

Figure 4.15(a) The interlayer distance for the MoS_2 film is estimated to be 6.5 Å.[47] (b) STEM images reveal good stacking of MoS_2 layers used in this research. (c) A top view of the monolayer MoS_2 lattice, with unit cell parameter is a = 3.12 Å. Thus, the unit cell area is 8.43 $Å^2$.

$(2\text{-Fc-DMBI})_2$ and 2-H-Fc-DMBI are expected to give the same doping product (2-Fc-DMBI^+ cation) as discussed in Chapter 3. The density of dopant monomer cations that fit in a close-packed arrangement can be estimated to determine an expected Fe/Mo ratio for a monolayer, and compared with the ratio obtained from the XPS results. The experimental ratio of the number of Fe atoms over the number of Mo atoms of the three-layer MoS_2 film can be calculated from the peak area ratio after calibration by the sensitivity factors (SF). Figure 4.15 shows a model of multi-layer MoS_2 sample, and STEM images of samples used in this work, which reveals good stacking of three MoS_2 layers.

The photoelectrons originating from the second and third layer of MoS_2 are attenuated on their passage through the film before collection by the analyzer. Equation 4.2 describes the decay of signal from electrons originating at distance t from the surface.

Equation 4.2 $$I = I_S \exp(-\frac{t}{\lambda cos\theta})$$

where I_s is the unscattered intensity, θ the detection angle relative to the surface normal

(zero in the current work), and λ is the inelastic mean free path for the photoelectrons; i.e., at a depth of λ from the surface, only 1/e fraction (36.8%) of all electrons can be detected without undergoing energy loss. For the Mo $3d_{5/2}$ line in MoS_2, for which when using Al Ka radiation, photoelectrons will have a kinetic energy of ca. 1257 eV, λ = 3.4 nm using the inelastic mean free path curve for inorganic materials.[48] Thus, 9.2% and 1.4% of photoelectrons from the Mo atoms on second and third layers (at a distance of 8.1 Å and 14.6 Å), respectively, will be detected by the analyzer without energy loss. Hence, 1.10 Mo atoms will be detected for three-layer MoS_2 in each unit cell. The overall intensity for Mo 3p peak detected by the XPS needs to be divided by 0.37 to compensate the energy loss for photoelectrons emitted from the second and third layer.

As shown in Figure 4.15, the unit cell area for single-layer MoS_2 is 8.43 $Å^2$, which contains one Mo atom, and two S atoms. The density of dopant monomers that fit in a close-packed arrangement was used to estimate the expected Fe/Mo for a monolayer and compared with the obtained ratio from the XPS. As discussed in Chapter 3, the footprint of the cations can be regarded as an approximately 12.27 × 8.48 Å rectangle with an area of 104.0 $Å^2$. Thus, a close-packed monolayer of such cations on top of three-layer MoS_2 will lead to $\frac{Fe}{Mo}$ = 0.073. The theoretical monolayer coverage of $(2\text{-Fc-DMBI})_2$ and 2-H-Fc-DMBI doping product on MoS_2 can now be compared with the experimental data from XPS, as summarized in Table 4.1, and discussed below. The number of dopant cations present on the surface of MoS_2 could also be estimated based on these XPS results, and it should be equal to the number of electrons donated to the doped MoS_2 films, assuming that all the dopants fully reacted, and only cations

are present on the surface.

Table 4.1 Estimates of $(2\text{-Fc-DMBI})_2$ and 2-H-Fc-DMBI coverage (% of close-packed monolayer) and the number of dopants on the surface of the trilayer MoS_2.

		Quick dip	*10 sec dip*	*10 min dip*
$(2\text{-Fc-DMBI})_2$	% of close-packed ML	23 ± 1	40 ± 1	82 ± 2
(M= 2.5 mM)	n of absorbed cations/10^{13} cm^{-2}	2.2 ± 0.5	3.8 ± 0.5	7.9 ± 0.6
2-H-Fc-DMBI	% of close-packed ML	19 ± 2	22 ± 3	56 ± 1
(M = 5 mM)	n of absorbed cations/10^{13} cm^{-2}	1.8 ± 0.4	2.2 ± 0.3	5.4 ± 0.7

For $(2\text{-Fc-DMBI})_2$, a coverage of 23% and 82% of a molecular monolayer was obtained for a quick dip and a 10 min immersion in a dilute toluene solution, respectively. 2-H-Fc-DMBI gives lower coverage than $(2\text{-Fc-DMBI})_2$ (up to 56%), consistent with other evidence that it dopes MoS_2 to a lesser extent than $(2\text{-Fc-DMBI})_2$ under a given set of condition. The change of electron sheet density induced by n-doping with $(2\text{-Fc-DMBI})_2$ is estimated to be 7.9×10^{13} cm^{-2}, which is about 10 times higher than electron sheet densities calculated based on ΔV_{th} ($n_{N1} \approx 6.3\times10^{12}$ cm^{-2}). There are several possible reasons for this discrepancy: (1) the dopants present on the surface are not fully reacted, and both dopant ions and unreacted dopants are present on the surface; (2) some of the electrons transferred from the dopant may be trapped, for example by strong electrostatic interactions with dopant ions, and, therefore, may not contribute to the drain current; (3) the short exposure to air before the electrical measurements may quench some of the electrons in the n-doped devices. Previous results on graphene doping showed that the doping efficiency for $(2\text{-Fc-DMBI})_2$ can be as low as ca. 34% after 10 min dipping (same concentrations were used in both

studies).[27]

A similar approach is used to calculate coverage for p-dopant. Unlike (2-Fc-DMBI)$_2$ and 2-H-Fc-DMBI, Magic Blue is an ionic compound. After the tris(4-bromophenyl)ammoniumyl radical cation accepts an electron from the MoS_2 it forms neutral tris(4-bromophenyl)amine, which is assumed to remain in solution and/or to be washed away in the following rinsing step, leaving the hexachloroantimonate counter ion to balance the charges introduced to the film. This is assumption is supported by XPS results, which show that longer doping treatments lead to significant growth of the Cl 2p peak, but no obvious increase in the Br 3d peak. As discussed in Chapter 3, the unit cell of hexachloroantimonate moiety can be viewed as a rhombus of area 60.2 Å^2. Since each ion contains six Cl atoms, a monolayer of such anions on top of three-layer MoS_2, will lead to $\frac{Cl}{Mo}$ = 0.76. The theoretical monolayer coverage of Magic Blue doping product on MoS_2 can now be compared with the experimental data from XPS, as summarized in Table 4.2. The number of dopant anions present on the surface of MoS_2 can be calculated, which should be equal to the change of charge-carrier density induced by p-doping, assuming that all the dopants fully reacted, and only anions are present on the surface.

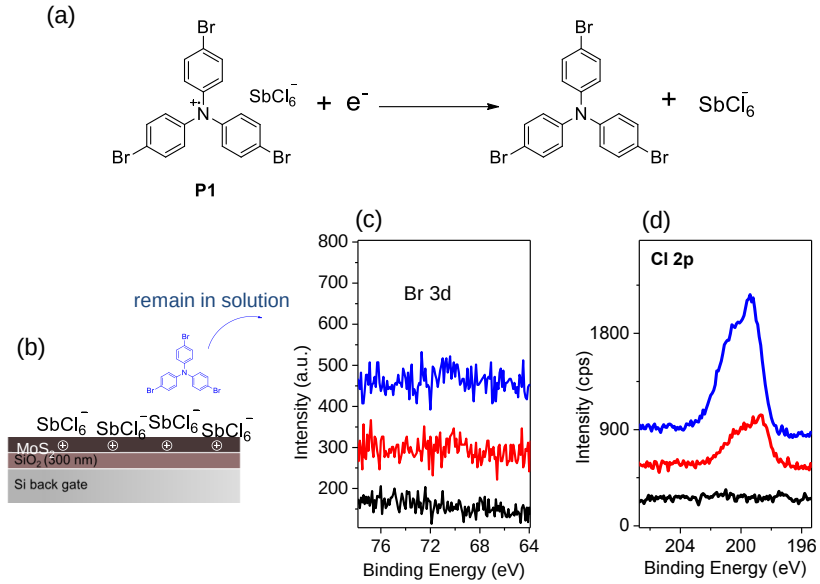

Figure 4.16 (a) Doping reaction for P1. (b) Schematic illustration of the doping reaction of P1 molecules with MoS_2. (c-d) XPS core level spectra of Br 3d and Cl 2p. The black curves are the pristine MoS_2 spectra, the red curves are for a short dip in 5 mM P1 solution, and the blue curves for samples immersed for 10 min in the same solution.

Table 4.2 Estimates of Magic Blue coverage (% of close-packed monolayer) and the number of dopants on the surface of the trilayer MoS_2.

		Quick dip	*10 sec dip*	*10 min dip*
Magic Blue (M= 5 mM)	% of close-packed ML	18 ± 2	27 ± 1	42 ± 2
	n of absorbed cations/10^{13} cm^{-2}	2.9 ± 0.7	4.5 ± 0.6	7.0 ± 0.3

4.2.4 Raman characterization

Raman spectroscopy was performed to further understand the doping effects. Figure 4.17 displays the characteristic MoS_2 double peak before and after the doping treatments with $(2\text{-Fc-DMBI})_2$.The E_{2g}^1 phonon mode represents the in-plane vibrations of Mo and S atoms, whereas the A_{1g} peak is the out-of-plane vibration of S atoms.[49] The peak positions of both vibrational modes for the three dopants treated MoS_2 are plotted in Figure 4.18. For $(2\text{-Fc-DMBI})_2$ doping, a significant red shift of the A_{1g} peak position by ~ 1 cm^{-1} was observed, while the E_{2g}^1 peak position shows almost no change (< 0.2 cm^{-1}). For doping with 2-H-Fc-DMBI, the A_{1g} downshift is smaller than the dimer (<

0.3 cm^{-1}, Figure 4 c), in agreement with the electrical and UPS measurements. All peak shifts are also accompanied by peak broadening and intensity decrease after the treatment. As shown in Figure 4.18(c), an opposite trend is observed upon doping with Magic Blue with both peak positions shifting slightly (by ~ 0.5 cm^{-1}) to higher values (blue shift).

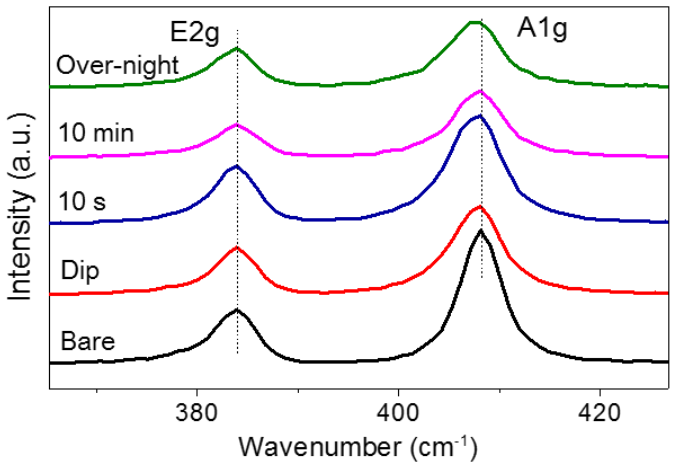

Figure 4.17 Raman spectra of trilayer MoS_2 before and after different treatments with $(2\text{-Fc-DMBI})_2$.

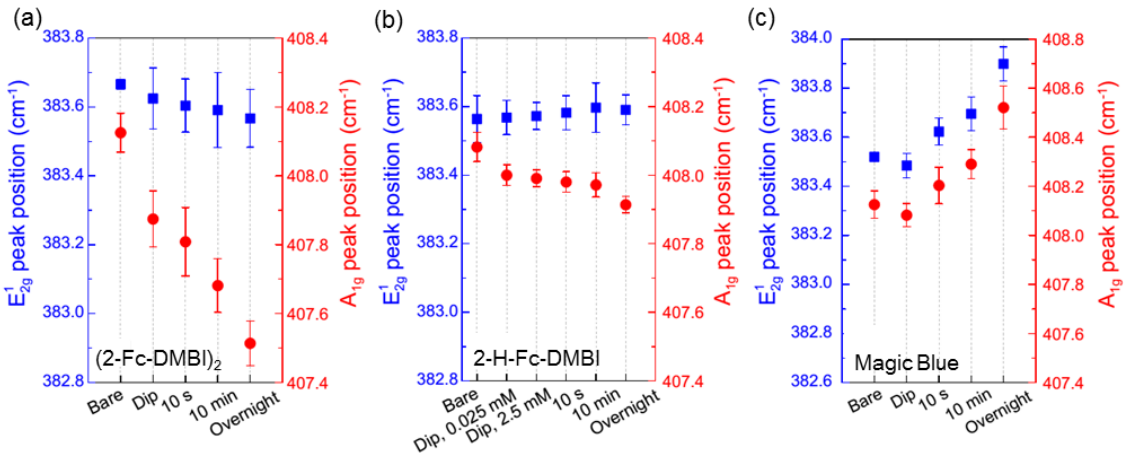

Figure 4.18 Summary of $E_{2g}{}^1$ and A_{1g} peak position shifts upon doping with three dopants.

The n-doping results are consistent with previous work on electrostatic[50] and chemical doping[51] of monolayer MoS_2 flakes. The higher electron concentration in the n-doped MoS_2 increases the electron-phonon scattering, which affects the frequency

and the full width at half maximum (FWHM) of phonons via renormalization of their self-energy.[52] In the case of $(2\text{-Fc-DMBI})_2$ and 2-H-Fc-DMBI doping, this leads to Raman mode softening and peak broadening. The difference between the A_{1g} and $E_{2g}{}^1$ downshifts was previously explained by stronger electron-phonon coupling of the A_{1g} mode based on symmetry arguments: the A_{1g} peak is affected more strongly by n-doping than the $E_{2g}{}^1$ mode.[50] On the other hand, the treatment with Magic Blue depopulates filled states in MoS_2. Therefore, the electron-phonon scattering is reduced and stiffening of both Raman-active modes are observed. Unlike in the case of n-doping, the shifts are similar for both A_{1g} and $E_{2g}{}^1$ phonons, suggesting a similar electron-phonon coupling. It has been recently shown that the presence of the surface dipoles on MoS_2 may lead to similar Raman shifts.[53] However, future experimental and theoretical studies are needed to fully understand this effect.

4.3 Doping studies of WSe_2

The tri-layer WSe_2 samples used in this research were synthesized by Phillip Campbell in the group of Dr. Eric Vogel using the literature reported method.[54] The WSe_2 FET was fabricated and measured by Meng-Yen Tsai in the same group. The pristine WSe_2 sample used in this research is a p-channel material. Magic Blue and a 19-electron sandwich organometallic dimer $(RhCpCp^*)_2$ were used at p- and n-dopants for this study. The monomeric cation $RhCpCp^{*+}$ is the expected product of doping after charge transfer and bond cleavage.

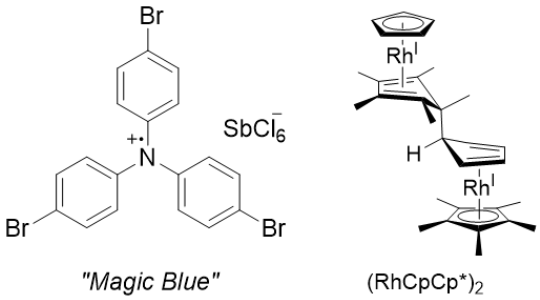

Figure 4.19 p- and n-Dopants used for WSe_2 doping.

Similar to the MoS_2 doping treatment, WSe_2 samples were dip-coated in the dopant solutions of the dopants presented above for up to 10 min. The concentration of Magic Blue was 5 mM, while the dimer $(RhCpCp^*)_2$ was used at 2.5 mM concentration. Each sample contained several tens of transistors and measured by the exact same set-up as the MoS_2 doping. Figure 4.20(a) shows the representative transfer characteristic of a WSe_2 FET before and after doping with Magic Blue on a semi-logarithmic scale. As indicated by the arrow, a short dipping into the dopant solutions shifts the V_{th} (defined as the voltage necessary to achieve a current of 2×10^{-8}A) to more positive values. A more profound V_{th} shift and a further current increase are observed for longer immersion time. Figure 4.21 shows the n-doping effects with $(RhCpCp^*)_2$, where a small shift of V_{th} is observed, together with slightly decrease of both I_{on} and I_{off}.

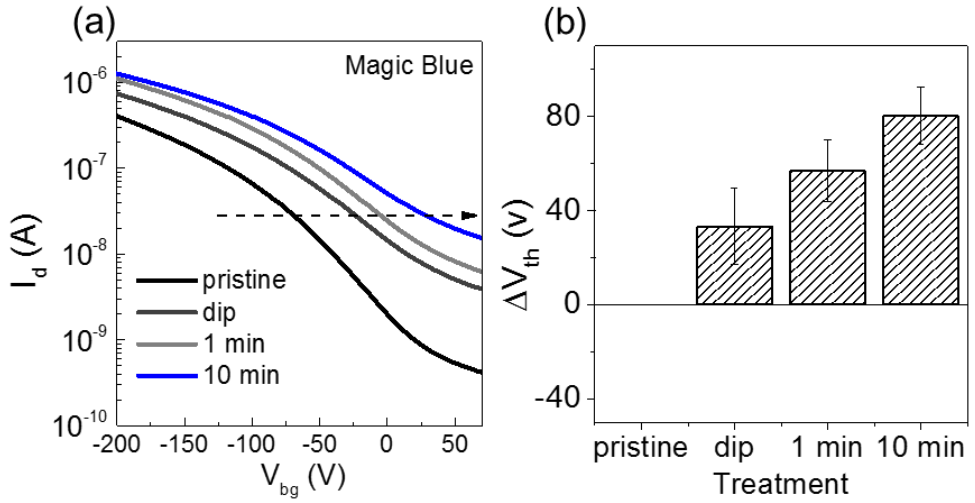

Figure 4.20 (a) Representative transfer characteristics of a WSe_2 FET before and after doping with Magic Blue. (b) Threshold voltage shifts ΔV_{th} are shown relative to the pristine sample ($V_{th,\ pristine}$= 0V). FETs were measured by Meng-Yen Tsai.

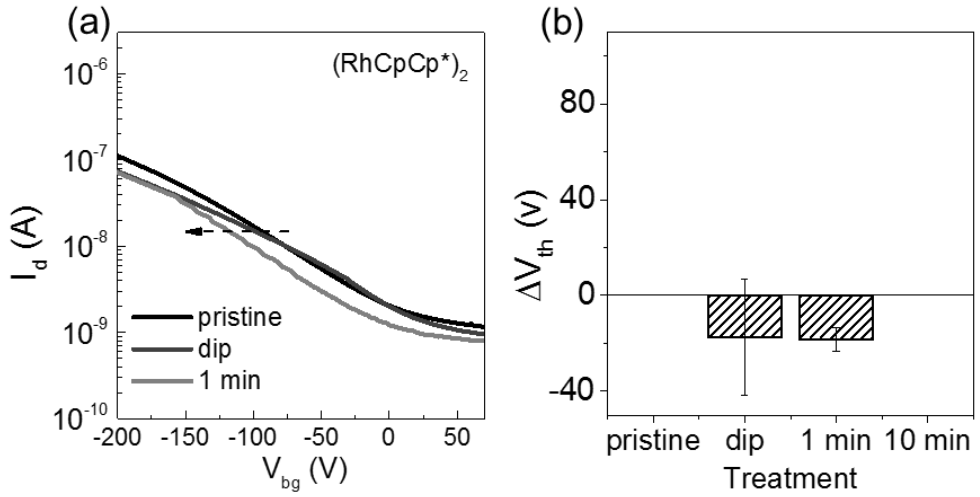

Figure 4.21 (a) Representative transfer characteristics of a WSe_2 FET before and after doping with $(RhCpCp^*)_2$. (b) Threshold voltage shifts ΔV_{th} are shown relative to the pristine sample ($V_{th,\ pristine}$:= 0V). FETs were measured by Meng-Yen Tsai.

Figure 4.20 and Figure 4.21 summarize the extracted threshold voltage shifts, relative to the pristine sample. Using Equation 4.1, the density of holes introduced by Magic Blue can be calculated giving a value of 6.6×10^{12} cm^{-2} for the 10 min treatment. $(RhCpCp^*)_2$ doping, on the other hand, has much less profound effect on the ΔV_{th} shifts, and only an estimated 1.6×10^{12} cm^{-2} density of carriers were removed by the n-dopant.

However, as discussed in the following section, large WF and E_F shifts were observed on the $(RhCpCp^*)_2$ doped films. The absence of electron transport behavior in the transistor may be caused by the high work function electrode (Au, WF = 5.1 eV[55]) used in the WSe_2 device, which may render large injection barriers for the electron transport, thus high contact resistance. However, more experiments, including fabricating WSe_2 FET with low work function metal electrode, need to be conducted to fully clarify the reason.

UPS is used to determine the work function ϕ and the position of E_{VBM} relative to E_F. Figure 4.22 shows the secondary cut off and the low binding energy region shifts of WSe_2 upon doping at various treatment time. The tri-layer WSe_2 used in this research has a band gap of ~1.8 eV (derived from absorption measurements). Prior to doping, the Fermi level of pristine WSe_2 is located ~0.78 eV above the VBM in the lower half of the band gap, consistent with the p-type nature of WSe_2. The work function of pristine WSe_2 is ϕ = 4.1 eV, similar to previous reports,[22] and increases by ca. 0.9 eV after 1 hour dipping into the Magic Blue solution. Moreover, E_{VBM} shifts to lower binding energy, which is consistent with the p-doping effect. Figure 4.23 shows the n-doped WSe_2 film with $(RhCpCp^*)_2$, where the SEE and E_{VBM} shift to the opposite direction. E_{VBM} shifts as large as 0.67 eV are observed, which demonstrates the strong n-doping effect. This is inconsistent with the transistor results, where no obvious n-doping effect is observed. As mentioned earlier, more experiments need to be carried out to fully understand this phenomenon.

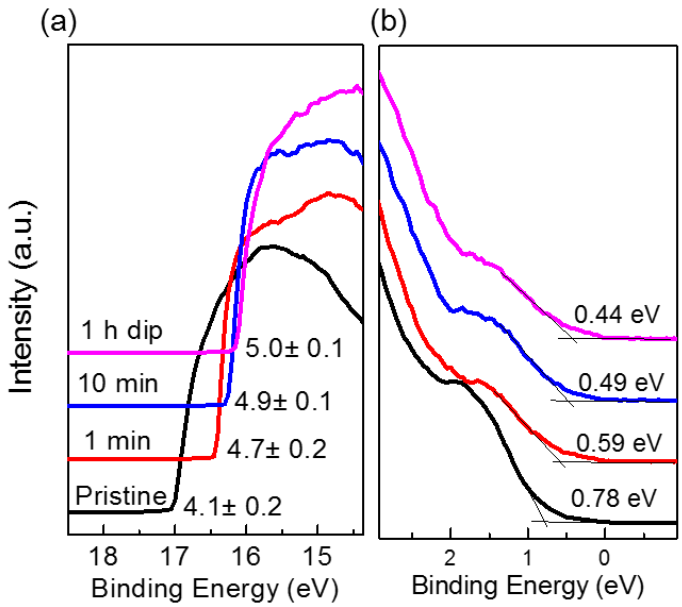

Figure 4.22 UPS spectra of WSe_2 before and after doping with Magic Blue: (a) secondary cut off shfits of WSe_2 upon doping at various treatment time. (b) low binding energy region (near the E_F), the onset of ionization of filled states (E_{HOMO}) relative to 0 binding energy, is used to track the shifts of E_F relative to VBM.

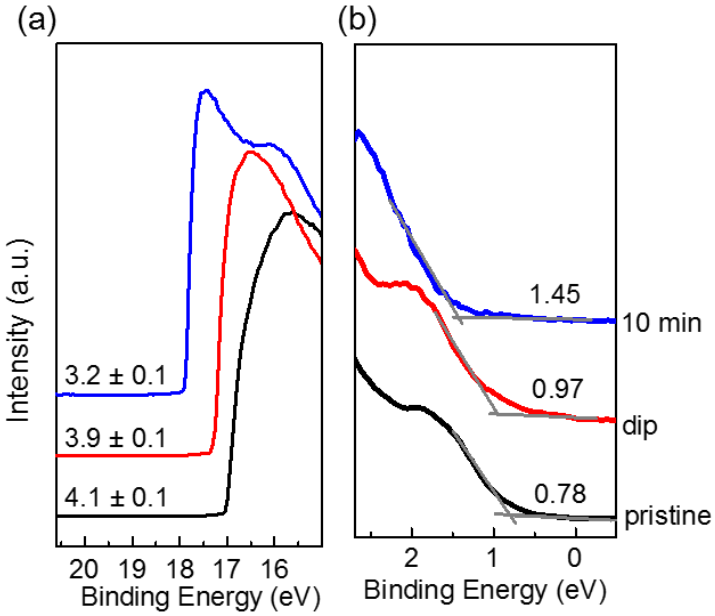

Figure 4.23 UPS spectra of WSe_2 before and after doping with $(RhCpCp^*)_2$: (a) secondary cut off shifts of WSe_2 upon doping at various treatment time. (b) low binding energy region (near the E_F), the onset of ionization of filled states (E_{HOMO}) relative to 0 binding energy, is used to track the shifts of E_F relative to VBM.

The doped surface was then characterized using XPS. Figure 4.24(a) and Figure 4.25(a) show the binding energy (BE) of the main W 4f peak from the p-doped and n-doped films. The downshift (lower binding energy) of W 4f peak in the p-doping case

is attributed to the depopulation of semiconductor states, and the Fermi level shift toward the valence band edge. Meanwhile, n-doping leads to the upshift of the W 4f peak. Importantly, both of these shifts are consistent with the E_F shifts (relatively to the E_{VBM}) characterized by the UPS (Figure 4.22 and Figure 4.23).

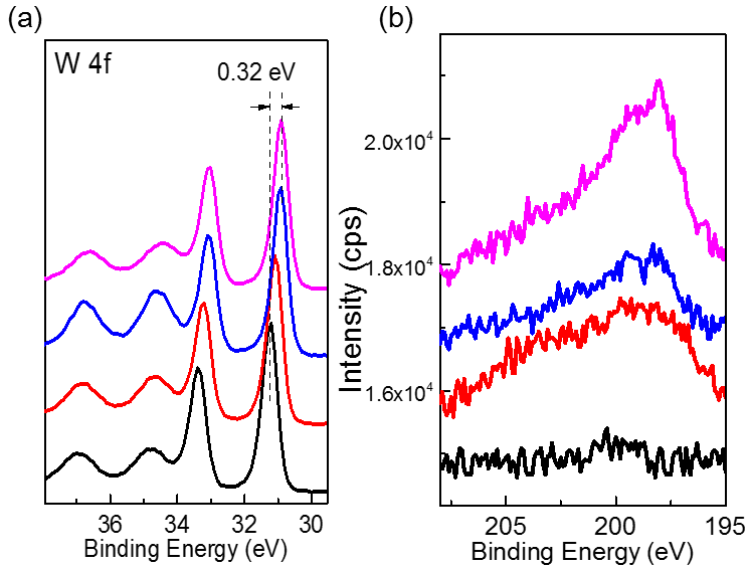

Figure 4.24 XPS surface analysis of WSe_2 before and after doping with Magic Blue: (a) XPS core level spectra of W 4f; (b) Cl 2p from the Magic Blue.

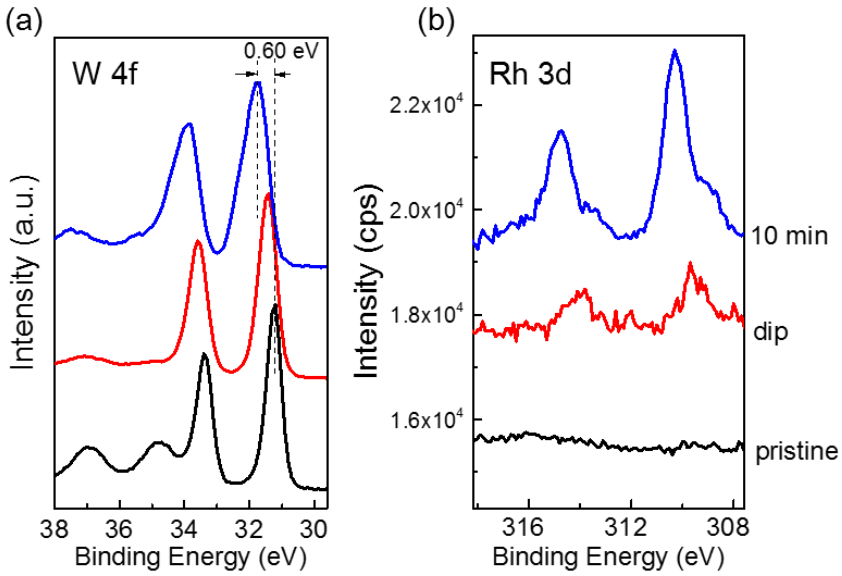

Figure 4.25 XPS surface analysis of WSe_2 before and after doping with Magic Blue: (a) XPS core level spectra of W 4f; (b) Rh 3d from the Magic Blue.

Figure 4.24(b) and Figure 4.25(b) show the increased concentration of the

dopants on the surface based on the Cl 2p and Rh 3d peaks. As mentioned earlier, the coverage can be calculated based on the dopant to WSe_2 relative to the theoretical value. As discussed earlier, for three-layer WSe_2 film, the photoelectrons originating from the second and third layer need to be attenuated on their passage through the film before collection by the analyzer. For Al Kα radiation, electrons emerging from the W $4f_{7/2}$ orbitals (*ca.* 31 eV binding energy) will have a kinetic energy of *ca.* 1455 eV, λ = 3.7 nm using the inelastic mean free path curve for inorganic materials.[48] Based on Equation 4.2, for W atom on the second and third layer (at a distance of 8.57 Å and 15.57 Å, respectively), ca. 9.9% and 1.5% of W 4f photoelectrons can be detected by the analyzer without energy loss, respectively. Thus, the overall intensity for W 4f peak detected by the XPS needs to be divided by 0.37 to compensate the energy loss for photoelectrons emitted from the second and third layer.

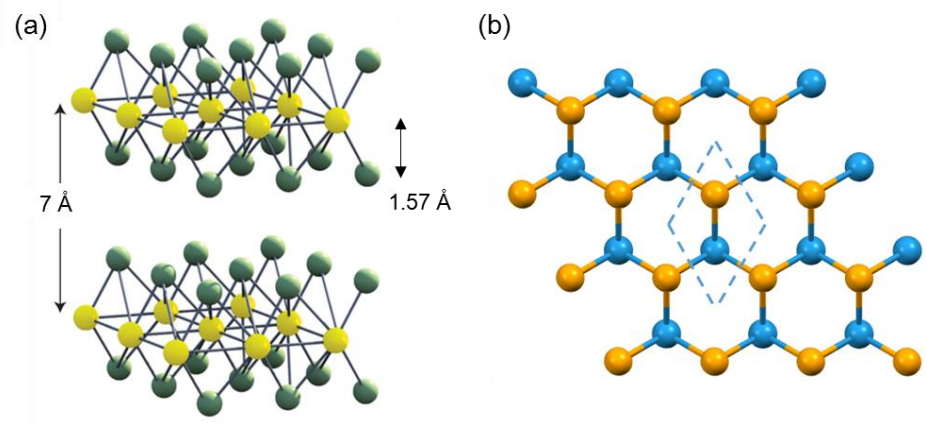

Figure 4.26 (a) The interlayer distance for the MoS_2 film is estimated to be 7 Å.[56] (b) A top view of the monolayer WSe_2 lattice, with unit cell area 9.32 $Å^2$.[57]

As shown in Figure 4.26, the unit cell area for single-layer WSe_2 is 9.32 $Å^2$, which contains one W atom, and two Se atoms. As described in Chapter 3, the unit cell of $SbCl_6^-$ that can be viewed as a rhombus of area 60.2 $Å^2$. Thus, the theoretical

monolayer coverage of Magic Blue doping product on WSe_2 is $\frac{Cl}{W}$ = 0.84. A coverage of 28 ± 7 % of a molecular monolayer was obtained for a 10 min immersion in the dilute solution of Magic Blue, thus the change of hole sheet density induced by p-doping with Magic Blue can be estimated as 4.1×10^{13} cm^{-2}. As in the case of MoS_2 doping, this value is much larger than the density of holes calculated from the FET results. As explained earlier, possible reasons include that the dopants are not fully reacted, and the charge carries introduced from the dopant is not all free carries, some of which do not contribute to the current.

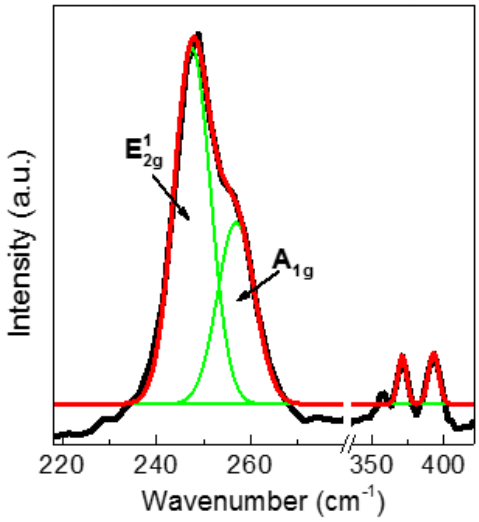

Figure 4.27 Raman spectra of trilayer WSe_2 used in this research.

Figure 4.27 shows the Raman spectra of the tri-layer WSe_2 used in this research. The $E_{2g}{}^1$ phonon mode represents the in-plane vibrations of W and Se atoms, whereas the A_{1g} peak is the out-of-plane vibration of Se atoms. As shown in Figure 4.27, $E_{2g}{}^1$ and A_{1g} peaks are overlapped, which is consistent with the reported literature for the tri-layer WSe_2 films.[58] The Raman spectra were fitted using Gaussian functions to extract the peak positions for both vibrational modes. For Magic Blue doping, a significant down shift of both A_{1g} and $E_{2g}{}^1$ peaks are observed, which is caused by the

change of the hole-phonon scattering in the doped film. This observation is also consistent with previous work on p-doping of WSe_2 films.[31] In contrast to what is seen for MoS_2 doping, A_{1g} and $E_{2g}{}^1$ shift to about the same extent, but this could be an artifact since these two peaks are heavily overlapped. On the n-doping side, blue shifts are observed for A_{1g} and $E_{2g}{}^1$ peak, presumably caused by the lower charge carrier concentration in the film. This is the first demonstration of an n-doping effect on WSe_2, future experimental and theoretical studies are needed to fully understand this.

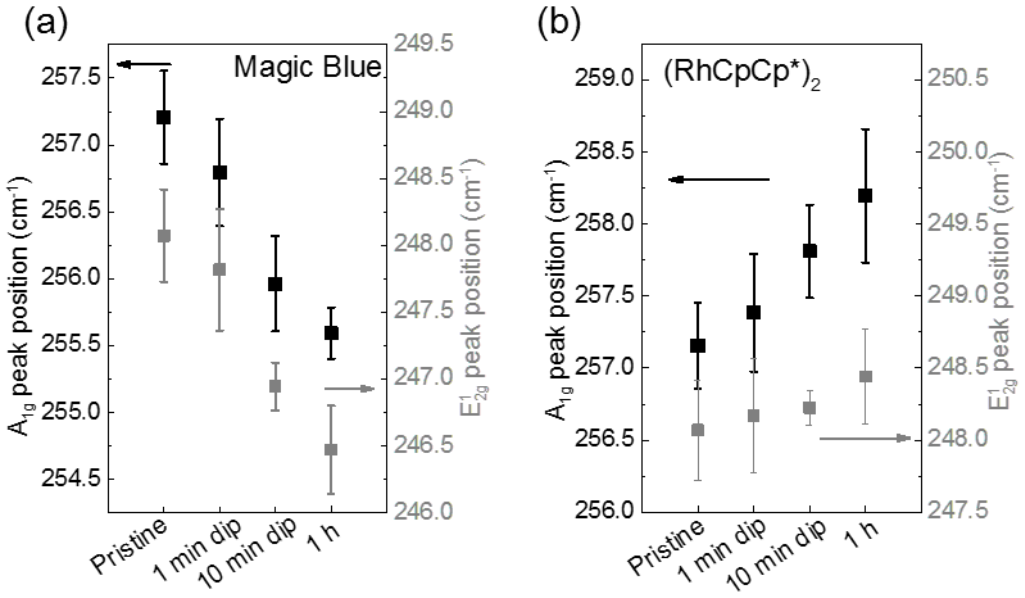

Figure 4.28 Summary of $E_{2g}{}^1$ and A_{1g} peak position shifts upon doping with Magic Blue and $(RhCpCp^*)_2$ dopants.

4.4 Conclusions

In conclusion, controllable surface doping of wafer-scale trilayer MoS_2 and WSe_2 using solutions of redox-active molecular dopants were studied, and large carrier densities can be achieved (on the order 10^{12} cm^{-2}) as characterized by FET. The work function of both materials can be tuned over a large range of up to ca. 2 eV. The change in work function arises from a combination of electron transfer from the adsorbed

dopants to the channel, as well as the resultant surface dipoles. For MoS_2 doping, the dimer of a benzimidazoline radical $(2\text{-Fc-DMBI})_2$ and its monomer derivative 2-Fc-DMBI-H have been shown to be effective solution-processable n-dopants, which largely facilitate the electron transport properties. Electrical measurements, UPS, XPS and Raman results indicate that the dimer exhibits a stronger doping effect than the monomer, consistent with previous studies of their strength as dopants for organic semiconductors[59] and graphene. For WSe_2 doping, the p-dopant Magic Blue works effectively to tune the WF and increase the carrier density in the film. Compared with previous literature work, this is the first observation of work function and Fermi level shifts in p-doped MoS_2 and n-doped WSe_2; controllable doping can be realized through tuning the dopant type, treatment time, and the solution concentration. Future work on the TMDCs materials will investigate interface modification between the channel materials (TMDCs) and the dielectric layer (SiO_2 or AlO_x).

4.5 Experimental

4.5.1 General details

All operations were carried out under an atmosphere of nitrogen or argon, unless stated otherwise. Spectrophotometric grade (99.9%) toluene was purchased from Alfa Aesar and dried over CaH_2. After drying and distillation under inert atmosphere, it was collected in Schlenk flasks and degassed by at least three "freeze-pump-thaw" cycles before transferring into the glovebox. Dichloromethane was purchased from Sigma-Aldrich (anhydrous grade solvent packed under argon) and used as received. Tris(4-bromophenyl)ammoniumyl hexachloroantimonate ("Magic Blue") was purchased from

Sigma-Aldrich and used as received. N-dopants $(2\text{-Fc-DMBI})_2$ and 2-H-Fc-DMBI were synthesized as discussed in Chapter 2,[60] and discussed in Chapter 2. $(RhCpCp^*)_2$ was synthesized by Dr. Karttikay Moudgil.[61]

4.5.2 Sample doping treatment

Doping treatments were carried out inside a Unilab MBRAUN glovebox (< 0.5 ppm of water, < 0.5 ppm oxygen). All three n-dopants were dissolved in anhydrous deoxygenated toluene to make a 2.5 mM (dimer) or 5 mM (monomer) solution, respectively. The differences being chosen to reflect that the two dopants can contribute two and one electrons, respectively. Magic Blue was dissolved in CH_2Cl_2 to make a 5 mM solution. Samples were then exposed to dopant solutions for various times, followed by rinsing in fresh solvent 3 times with shaking to remove physisorbed materials, and dried out with N_2 from a rubber bulb.

4.5.3 Characterization of the samples

All the FET measurements were performed using a LakeShore Cryotronics probe station and a Keithley 4200-SCS parameter analyzer at room temperature, and were conducted by Dr. Alexey Tarasov and Meng-Yen Tsai. The as-fabricated transistors were first tested in ambient and in high vacuum (~ 10^{-7} Torr), then dip-coated in dopant solutions inside a glove box and measured again in vacuum.

XPS and UPS Spectra were acquired on Kratos Axis UltraDLD XPS/UPS system, under a base pressure of 10^{-9} Torr, using the monochromatic Al Kα line and He-I lamp radiation (21.2 eV), respectively. Samples were transferred through a Kratos air-sensitive transporter without air exposure. Both MoS_2 and WSe_2 films were

transferred onto a gold substrate for the UPS and XPS measurements using a PMMA-based technique,[62] since their intrinsic conductivity is too low for measurement. All samples were characterized at normal take-off angle (90°), and grounded with the spectrometer via a metallic clip on the TMDCs film. The Fermi level was calibrated using atomically clean silver. XPS survey scans were run at 160 eV pass energy and the high resolution scans at 20 eV pass energy. UPS was acquired at 5 eV pass energy. The peak fits of high resolution XPS scans were done with Vision Processing Software 2.2.8 using mixed Gaussian/Lorentzian distributions to minimize *chi* squared value. From the binding energy corresponding to the secondary electron edge (SEE) of the UPS spectra, the work function is calculated based on equation $\varphi = 21.22\ \text{eV} - \text{SEE}$. From the onset of photoemission, the position of the valence band maximum was determined.

Raman spectroscopy was acquired in a Renishaw InVia microscope spectrometer with laser excitation at either 488 nm (for MoS_2) or 532 nm (for WSe_2), and collection using a 50× objective in backscattering configuration. For all of the Raman measurements, the samples were transferred from the glovebox using a sealed microscope stage (Linkam TS 1500) to avoid air exposure during transfer and measurements steps. A quartz window was used to allow optical access to the sample during the measurements. All Raman peaks were fitted with Gauss-Lorentzian line shapes to determine the peak position, the linewidth, and the intensity of the E^1_{2g} and A_{1g} Raman peaks.

4.6 References

(1) Radisavljevic, B.; Radenovic, A.; Brivio, J.; Giacometti, V.; Kis, A. *Nat. Nanotechnol.* **2011**, *6*, 147.

(2) Wang, Q. H.; Kalantar-Zadeh, K.; Kis, A.; Coleman, J. N.; Strano, M. S. *Nat. Nanotechnol.* **2012**, *7*, 699.

(3) Jariwala, D.; Sangwan, V. K.; Lauhon, L. J.; Marks, T. J.; Hersam, M. C. *ACS Nano* **2014**, *8*, 1102.

(4) He, Q.; Zeng, Z.; Yin, Z.; Li, H.; Wu, S.; Huang, X.; Zhang, H. *Small* **2012**, *8*, 2994.

(5) Late, D. J.; Huang, Y.-K.; Liu, B.; Acharya, J.; Shirodkar, S. N.; Luo, J.; Yan, A.; Charles, D.; Waghmare, U. V.; Dravid, V. P.; others *ACS Nano* **2013**, *7*, 4879.

(6) Li, H.; Yin, Z.; He, Q.; Li, H.; Huang, X.; Lu, G.; Fam, D. W. H.; Tok, A. I. Y.; Zhang, Q.; Zhang, H. *Small* **2012**, *8*, 63.

(7) Liu, B.; Chen, L.; Liu, G.; Abbas, A. N.; Fathi, M.; Zhou, C. *ACS Nano* **2014**, *8*, 5304.

(8) Perkins, F.; Friedman, A.; Cobas, E.; Campbell, P.; Jernigan, G.; Jonker, B. *Nano Lett.* **2013**, *13*, 668.

(9) Sarkar, D.; Liu, W.; Xie, X.; Anselmo, A. C.; Mitragotri, S.; Banerjee, K. *ACS Nano* **2014**, *8*, 3992.

(10) Bratschitsch, R. *Nat. Nanotechnol.* **2014**, *9*, 247.

(11) Wang, H.; Yu, L.; Lee, Y.-H.; Shi, Y.; Hsu, A.; Chin, M. L.; Li, L.-J.; Dubey, M.; Kong, J.; Palacios, T. *Nano Lett.* **2012**, *12*, 4674.

(12) Baugher, B. W. H.; Churchill, H. O. H.; Yang, Y.; Jarillo-Herrero, P. *Nat. Nanotechnol.* **2014**, *9*, 262.

(13) Pospischil, A.; Furchi, M. M.; Mueller, T. *Nat. Nanotechnol.* **2014**, *9*, 257.

(14) Ross, J. S.; Klement, P.; Jones, A. M.; Ghimire, N. J.; Yan, J.; Mandrus, D. G.; Taniguchi, T.; Watanabe, K.; Kitamura, K.; Yao, W.; Cobden, D. H.; Xu, X. *Nat. Nanotechnol.* **2014**, *9*, 268.

(15) Yu, X.; Prevot, M. S.; Guijarro, N.; Sivula, K. *Nat. Commun.* **2015**, *6*, 7596.

(16) Anto Jeffery, A.; Nethravathi, C.; Rajamathi, M. *J. Phys. Chem. C* **2014**, *118*, 1386.

(17) Lukowski, M. A.; Daniel, A. S.; Meng, F.; Forticaux, A.; Li, L.; Jin, S. *J. Am. Chem. Soc.* **2013**, *135*, 10274.

(18) van der Zande, A. M.; Huang, P. Y.; Chenet, D. A.; Berkelbach, T. C.; You, Y.; Lee, G.-H.; Heinz, T. F.; Reichman, D. R.; Muller, D. A.; Hone, J. C. *Nat. Mater.* **2013**, *12*, 554.

(19) Najmaei, S.; Liu, Z.; Zhou, W.; Zou, X.; Shi, G.; Lei, S.; Yakobson, B. I.; Idrobo, J.-C.; Ajayan, P. M.; Lou, J. *Nat. Mater.* **2013**, *12*, 754.

(20) Liu, H.; Si, M.; Najmaei, S.; Neal, A. T.; Du, Y.; Ajayan, P. M.; Lou, J.; Ye, P. D. *Nano Lett.* **2013**, *13*, 2640.

(21) Tarasov, A.; Zhang, S.; Tsai, M.-Y.; Campbell, P. M.; Graham, S.; Barlow, S.; Marder, S. R.; Vogel, E. M. *Adv. Mater.* **2015**, *27*, 1175.

(22) Zhao, P.; Kiriya, D.; Azcatl, A.; Zhang, C.; Tosun, M.; Liu, Y.-S.; Hettick, M.; Kang, J. S.; McDonnell, S.; Kc, S.; Guo, J.; Cho, K.; Wallace, R. M.; Javey, A. *ACS Nano* **2014**, *8*, 10808.

(23) Kiriya, D.; Tosun, M.; Zhao, P.; Kang, J. S.; Javey, A. *J Am Chem Soc* **2014**, *136*, 7853.

(24) Yuchen, D.; Han, L.; Neal, A. T.; Mengwei, S.; Ye, P. D. *IEEE Electron Device Lett.* **2013**, *34*, 1328.

(25) Holmes, R. J.; Brütting, W.; Adachi, C. *Physics of Organic Semiconductors*; John Wiley & Sons, 2012.

(26) Maiti, U. N.; Lee, W. J.; Lee, J. M.; Oh, Y.; Kim, J. Y.; Kim, J. E.; Shim, J.; Han, T. H.; Kim, S. O. *Adv. Mater.* **2014**, *26*, 40.

(27) Paniagua, S. A.; Baltazar, J.; Sojoudi, H.; Mohapatra, S. K.; Zhang, S.; Henderson, C. L.; Graham, S.; Barlow, S.; Marder, S. R. *Mater. Horiz.* **2014**, *1*, 111.

(28) Choi, M. S.; Qu, D.; Lee, D.; Liu, X.; Watanabe, K.; Taniguchi, T.; Yoo, W. J. *ACS Nano* **2014**, *8*, 9332.

(29) Fang, H.; Tosun, M.; Seol, G.; Chang, T. C.; Takei, K.; Guo, J.; Javey, A. *Nano Lett.* **2013**, *13*, 1991.

(30) Chen, M.; Nam, H.; Wi, S.; Ji, L.; Ren, X.; Bian, L.; Lu, S.; Liang, X. *Appl. Phys. Lett.* **2013**, *103*, 142110.

(31) Chen, C.-H.; Wu, C.-L.; Pu, J.; Chiu, M.-H.; Kumar, P.; Takenobu, T.; Li, L.-J. *2D Mater.* **2014**, *1*, 034001.

(32) Shi, Y.; Huang, J.-K.; Jin, L.; Hsu, Y.-T.; Yu, S. F.; Li, L.-J.; Yang, H. Y. *Sci. Rep.* **2013**, *3*, 1839.

(33) Late, D. J.; Huang, Y.-K.; Liu, B.; Acharya, J.; Shirodkar, S. N.; Luo, J.; Yan, A.; Charles, D.; Waghmare, U. V.; Dravid, V. P.; Rao, C. N. R. *ACS Nano* **2013**, *7*, 4879.

(34) Du, Y.; Liu, H.; Neal, A. T.; Si, M.; Ye, P. D. *IEEE Electron Device Lett.* **2013**, *34*, 1328.

(35) Kiriya, D.; Tosun, M.; Zhao, P.; Kang, J. S.; Javey, A. *J. Am. Chem. Soc.* **2014**, *136*, 7853.

(36) Tarasov, A.; Campbell, P. M.; Tsai, M.-Y.; Hesabi, Z. R.; Feirer, J.; Graham, S.; Ready, W. J.; Vogel, E. M. *Adv. Funct. Mater.* **2014**, *24*, 6389.

(37) Connelly, N. G.; Geiger, W. E. *Chem. Rev.* **1996**, *96*, 877.

(38) Fang, H.; Tosun, M.; Seol, G.; Chang, T. C.; Takei, K.; Guo, J.; Javey, A. *Nano Lett* **2013**, *13*, 1991.

(39) Mak, K. F.; Lee, C.; Hone, J.; Shan, J.; Heinz, T. F. *Phys. Rev. Lett.* **2010**, *105*, 136805.

(40) Sup Choi, M.; Lee, G.-H.; Yu, Y.-J.; Lee, D.-Y.; Hwan Lee, S.; Kim, P.; Hone, J.; Jong Yoo, W. *Nat. Commun.* **2013**, *4*, 1624.

(41) Amani, M.; Chin, M. L.; Birdwell, A. G.; O'Regan, T. P.; Najmaei, S.; Liu, Z.; Ajayan, P. M.; Lou, J.; Dubey, M. *Appl. Phys. Lett.* **2013**, *102*, 193107.

(42) Chuang, S.; Battaglia, C.; Azcatl, A.; McDonnell, S.; Kang, J. S.; Yin, X.; Tosun, M.; Kapadia, R.; Fang, H.; Wallace, R. M. *Nano Lett.* **2014**, *14*, 1337.

(43) Qiu, H.; Xu, T.; Wang, Z.; Ren, W.; Nan, H.; Ni, Z.; Chen, Q.; Yuan, S.; Miao, F.; Song, F.; Long, G.; Shi, Y.; Sun, L.; Wang, J.; Wang, X. *Nat. Commun.* **2013**, *4*.

(44) Santosh, K.; Longo, R. C.; Addou, R.; Wallace, R. M.; Cho, K. *Nanotechnology* **2014**, *25*, 375703.

(45) Lu, C.-P.; Li, G.; Mao, J.; Wang, L.-M.; Andrei, E. Y. *Nano Letters* **2014**, *14*, 4628.

(46) Lin, J. D.; Han, C.; Wang, F.; Wang, R.; Xiang, D.; Qin, S.; Zhang, X.-A.; Wang, L.; Zhang, H.; Wee, A. T. S.; Chen, W. *ACS Nano* **2014**, *8*, 5323.

(47) Radisavljevic, B.; Radenovic, A.; Brivio, J.; Giacometti, V.; Kis, A. *Nat. Nanotechnol.* **2011**, *6*, 147.

(48) Seah, M. P.; Dench, W. A. *Surf. Interface Anal.* **1979**, *1*, 2.

(49) Li, H.; Zhang, Q.; Yap, C. C. R.; Tay, B. K.; Edwin, T. H. T.; Olivier, A.; Baillargeat, D. *Adv. Funct. Mater.* **2012**, *22*, 1385.

(50) Chakraborty, B.; Bera, A.; Muthu, D.; Bhowmick, S.; Waghmare, U.; Sood, A. *Phys. Rev. B* **2012**, *85*, 161403.

(51) Lin, J. D.; Han, C.; Wang, F.; Wang, R.; Xiang, D.; Qin, S.; Zhang, X.-A.; Wang, L.; Zhang, H.; Wee, A. T. S. *ACS Nano* **2014**, *8*, 5323.

(52) Bera, A.; Sood, A. K. In *MoS2*; Wang, Z. M., Ed.; Springer: 2014, p p. 155.

(53) Zhou, K.-G.; Withers, F.; Cao, Y.; Hu, S.; Yu, G.; Casiraghi, C. *ACS Nano* **2014**.

(54) Campbell, P. M.; Tarasov, A.; Joiner, C. A.; Tsai, M.-Y.; Pavlidis, G.; Graham, S.; Ready, W. J.; Vogel, E. M. *Nanoscale* **2016**, *8*, 2268.

(55) Sachtler, W.; Dorgelo, G.; Holscher, A. *Surf. Sci.* **1966**, *5*, 221.

(56) Pospischil, A.; Furchi, M. M.; Mueller, T. *Nat. Nano.* **2014**, *9*, 257.

(57) Coehoorn, R.; Haas, C.; Dijkstra, J.; Flipse, C.; De Groot, R.; Wold, A. *Phys. Rev. B* **1987**, *35*, 6195.

(58) Zeng, H.; Liu, G.-B.; Dai, J.; Yan, Y.; Zhu, B.; He, R.; Xie, L.; Xu, S.; Chen, X.; Yao, W. *Sci. Rep.* **2013**, *3*.

(59) Naab, B. D.; Zhang, S.; Vandewal, K.; Salleo, A.; Barlow, S.; Marder, S. R.; Bao, Z. *Adv. Mater.* **2014**, *26*, 4268.

(60) Naab, B. D.; Zhang, S.; Vandewal, K.; Salleo, A.; Barlow, S.; Marder, S. R.; Bao, Z. *Adv Mater* **2014**, *26*, 4268.

(61) Fischer, E. O.; Wawersik, H. *J. Org. Chem.* **1966**, *5*, 559.

(62) Liu, K.-K.; Zhang, W.; Lee, Y.-H.; Lin, Y.-C.; Chang, M.-T.; Su, C.-Y.; Chang, C.-S.; Li, H.; Shi, Y.; Zhang, H.; Lai, C.-S.; Li, L.-J. *Nano Lett.* **2012**, *12*, 1538.

CHAPTER 5 Doped Graphene Electrodes in Organic-semiconductor Devices

5.1 Introduction

Device function in most electronic devices (*e.g.*, light-emitting diodes, thin-film transistors, solar cells) involves the flow of charges from electrodes into the semiconducting layer, or vice versa. In inorganic semiconductors, Ohmic contact at the interface is realized through the degenerate doping of the semiconductor at the interface, where the charge carriers can tunnel through the narrow depletion region.[1] For organic semiconductors, however, dopants are not widely used at the interface, and the charge-carrier injection efficiency is mainly depends on the alignment of material energy levels – the IE or EA, depending whether the material transports holes or electrons – of the organic layer with respect to the Fermi level of the contacts.[2,3]

The work function of a given metal or metal oxide electrode material in its intrinsic state depends on its band structure and surface condition (different cleaning methods lead to different WF). The WF of ITO, for example, after normal solvent cleaning procedure is about 4.6 eV, but can reach 5.3 eV after plasma cleaning.[4] However, when low-work function transparent electrodes are needed for effective electron injection, ITO cannot fulfill this role in its intrinsic state, and interface modifications are needed to tune the WF. Interface modification has been demonstrated to enhance the carrier injection or extraction in organic transistors,[5,6] light-emitting diodes[7-9] and solar cells.[10-12]

As discussed in Chapter 3, graphene is one of the promising next-generation

conducting materials, and has the potential to replace ITO in electrical and optical devices.[13-16] There is immense interest in the application of graphene as an electrode material in organic semiconductors and flexible devices.[14,17,18] For example, ITO-free organic photovoltaics (OPVs) with single-layer (SGL) graphene electrode as the cathode have been reported by Park *et al.* with the power conversion efficiency (PCE) of 7.1%, which is among the best reported efficiency for graphene electrode single junction OPVs.[19] Higher efficiency has been reported for tandem cells (8.48%), where Au-modified SGL graphene nanoribbons was used as the anode.[20] For organic field-effect transistors (OFET), Lee *et al.* reported the use of graphene electrode for pentacene transistors, where much lower contact resistance was observed as compared to the gold electrode. Consequently, improved the output and transfer currents and hole mobilities (0.40 – 1.01 $cm^2 V^{-1} s^{-1}$) were obtained than the gold counterpart (0.16 – 0.28 $cm^2 V^{-1} s^{-1}$).[21] However, for more practical applications, the engineering of graphene films, such as through their synthesis, transfer, and doping, is still necessary to further improve device performance.[22,23]

Besides the needs for good conductivity and high transparency of the electrode, the performance and current density for semiconducting electronic devices also strongly rely on the carrier injection efficiency through the contact between electrodes and semiconducting material layers.[17,24] Much research has demonstrated that the Fermi level, carrier density and work function of graphene can be easily tuned by various surface treatment.[25-30] As discussed in Chapter 3, by using redox-active molecules, the WF of graphene can be tuned over a large range of 2 eV, and the sheet resistance can

be reduced for more than 90% without losing the transparency in the visible range.

In this chapter, interface engineering of graphene electrode for three different organic semiconductor devices was studies. Organic diodes, photovoltaics (OPVs), and field-effect transistors (OFETs) with doped graphene electrodes were fabricated, and the device performance was compared with undoped graphene or conventional metal or metal oxide electrodes. The choice of n- or p-dopants was determined by the energy levels and transport properties of the semiconductors. The molecules used in this chapter are shown in Figure 5.1. In organic diodes and OPVs, trilayer (3-L) graphene prepared by layer-by-layer transfer method, was used because of the high current density normally observed in this material relative to that for SGL graphene; while for OFETs, the device performance of which is not so sensitve to the sheet resistance of the electrode, SGL graphene was used. The transferred graphene films were patterned using conventional photolithography methods, followed by the O_2 plasma etching. Control devices with metal electrode were fabricated using the exact same photo-mask. For the dopant treatment, the graphene electrode was immersed in the dopant solutions for various time, and the degree of doping was controlled by varying the immersion time based on the experimental results discussed in Chapter 3. The organic semiconductor layers were then deposited onto the patterned dopant-treated graphene electrode through spin-coating or vacuum deposition. Finally, the metal top electrode was thermally depositted onto the organic layers. In organic diodes and OPVs, the dimensions of the device area were defined by the overlapping area between the bottom graphene electrode and top metal electrode; and in OFETs, the dimension was

determined by the size of the electrode. The device performances were characterized, and the devices with doped graphene electrodes showed comparable to, or even better than, that of similar devices with metal or metal-oxide electrodes. Interface engineering of the graphene electrode through doping proved to be an effective method to tune the device performance.

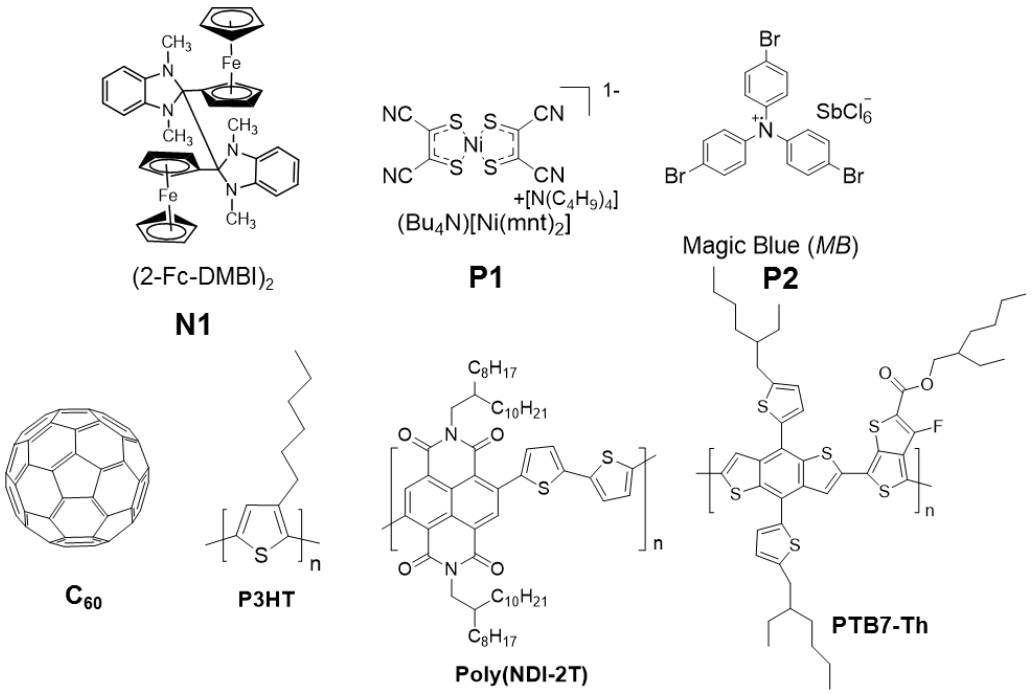

Figure 5.1 Molecular structure of the dopants (first row) and organic semiconductors used in this chapter.

5.2 Graphene electrode diodes with simple sandwich structures

The graphene electrodes were first tested in organic diodes. The carrier transport properties were characterized using a simple sandwich structure, and the impacts of doped graphene contacts on carrier injection at the organic polymer/electrode interface were studied, as compared to pristine graphene and to ITO electrodes. The hole-only device consists of ca. 150 nm P3HT film sandwiched between a graphene or ITO bottom electrode and a Ca/Al layer, where the bottom electrode is ITO, pristine or p-

doped graphene. The electron-only device had P(NDT-2Th) film (ca. 150 nm) sandwiched between bottom electrode and MoO_x/Ag layer, where the bottom electrode is ITO, or pristine or n-doped graphene. P3HT and P(NDT-2Th) layers were spin-coated under standard conditions, as described in the Experimental section. In these measurements, the charge carriers are transported perpendicularly to the polymer film. Bias is applied to the bottom electrode (ITO or graphene), while the top electrode is grounded.

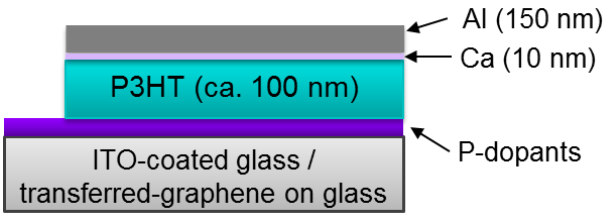

Figure 5.2 Schematic illustration of P3HT diodes with p-doped graphene electrode as compared to pristine graphene and ITO electrode.

The device configuration for P3HT diodes was shown in Figure 5.2. The *J-V* characteristics for devices with different bottom electrode were measured at room temperature inside the glovebox. As shown in Figure 5.3, the current density (*J*) was more readily modulated at positive voltage than the negative voltage. At positive bias, holes were injected from bottom electrode (ITO, pristine or p-doped graphene) into P3HT layer, while at negative bias, holes were injected from the top Ca/Al layer into the polymer, where a large hole-injection barrier is expected (WF for Ca is as low as 2.9 eV). Therefore, the current at negative bias is very low and less affected by the choice of bottom electrode.

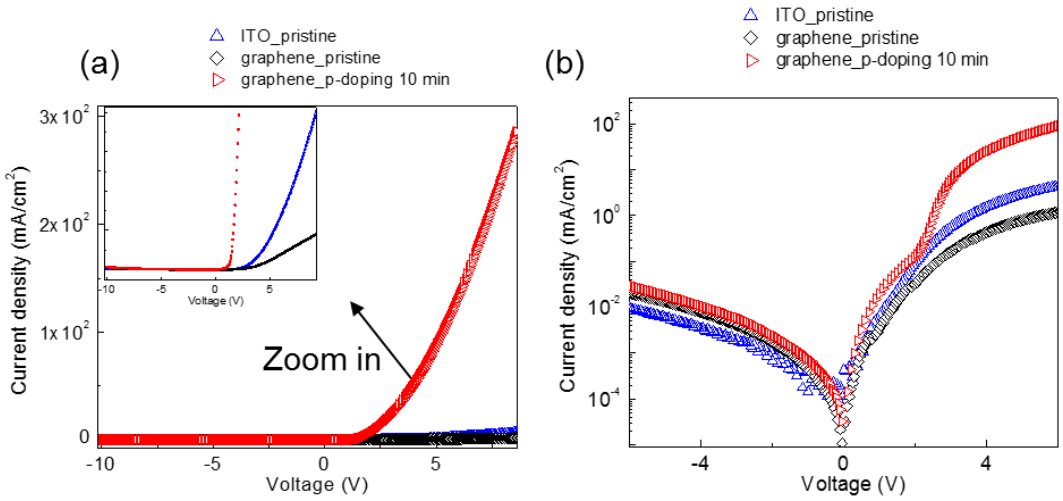

Figure 5.3 *J-V* characteristics of P3HT diodes with p-doped graphene electrode as compared to the pristine graphene and ITO electrode at (a) linear scale and (b) semi-log scale.

UPS measurements indicate that the WF for ITO, pristine graphene and p-doped graphene (10 min dipping into **P1**) is 4.6, 4.5 and 4.9 eV, respectively (discussed in Chapter 3). Given that EA and IP for P3HT is 2.1 eV and 4.6 eV, respectively,[31] the WF offset is not much on the bottom electrode side. Thus, in positive bias regime (positive voltage at bottom electrode), hole injected from the bottom electrode dominates the current, because the injection barriers are much smaller. At low voltage regime (<1.5 V), the current density is first order in the voltage ($J \propto V$) in all three devices, thus, it is in the Ohmic regime. It is known that in the Ohmic regime, the carrier is combination of the parasitic leakage currents and transport of the bulk carriers,[32,33] The *J-V* curves for the three devices almost overlap in low voltage regime (<1.5 V), indicating that the charge transport of P3HT remains the same within three devices and was not affected by the presence of the dopants on the graphene surface in the Ohmic regime. As the bias increases, the current increased dramatically in device with the p-doped graphene electrode, which is about two orders-of-magnitude higher than the ITO and pristine

graphene ones. The *J-V* curve at high voltage regime largely depends on series resistance of the device, which is believed to be dominated by contact resistance.[32-34] The current for the diode with p-doped graphene electrode is much higher than for the pristine graphene and ITO, which confirmed the improvement in hole-injection from the p-doped graphene side. Similar phenomena have been observed within other systems (but not with graphene electrodes): in small-molecule devices, depositing a thin layer of dopant at the organic/electrode interface can lead to a lower injection barrier, which was contributed to the shift of energy levels of organic molecules with respect to the Fermi level (E_F) of the contact.[35,36] In the present case, dopant was used to shift the E_F of the graphene electrode with respect to the organic molecular levels, but the same principle can be applied.

Figure 5.4 shows the device configuration for electron-only P(NDI-2Th) diodes, and the *J-V* characteristics with n-doped graphene electrode as compared to the pristine graphene and ITO electrode are summarized in Figure 5.5. Opposite to the hole-only diodes, electrons can be injected from the bottom electrode at negative bias (applied on the bottom electrode, while the top electrode was grounded), and the electron injection from the top electrode (at positive bias) was blocked by the high work function MoO_x layer. As positive bias, the current densities were negligible for devices with ITO, and with pristine and 1 min doped graphene (in 2.5 mM $(2\text{-Fc-DMBI})_2$ solution).

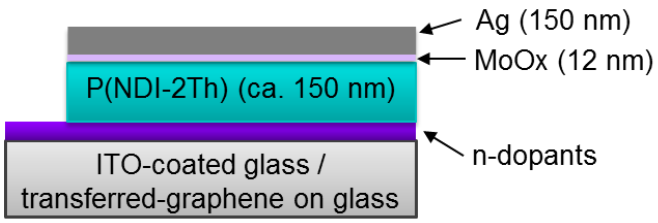

Figure 5.4 Schematic illustration of P(NDI-2Th) diodes with n-doped graphene electrode as compared to pristine graphene and ITO electrode.

In the negative bias regime, electrons injected from the bottom electrode dominate the current. As the voltage becomes increasingly negative, the current density for the device with doped electrode was much higher than the pristine graphene and ITO electrode. As mentioned earlier, ITO and pristine graphene has a WF of 4.6 and 4.5 eV, respectively, while n-doped graphene (1 min treatment in $(2\text{-Fc-DMBI})_2$ dimer solution) have WF of 3.9 eV, and P(NDI-2Th) has EA at 4.0 eV.[37] The lower current densities in ITO and pristine graphene electrode can be explained by the energy mismatch between their WF and the EA of the polymer. These observations confirmed the improvement in electron-injection in the device with n-doped graphene electrode.

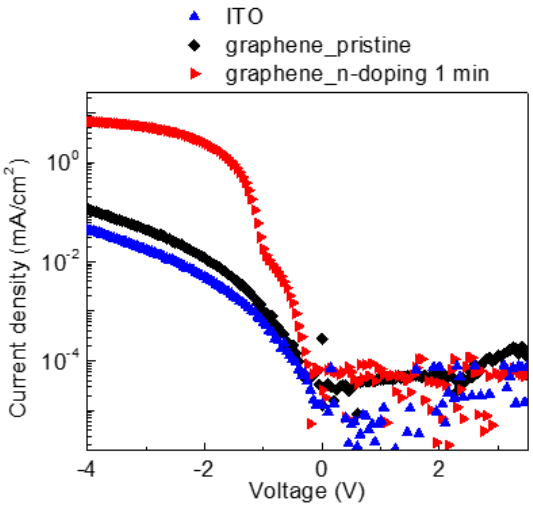

Figure 5.5 *J-V* characteristics of P(NDI-2Th) diodes with n-doped graphene electrode as compared to the pristine graphene and ITO electrode.

The effects of doping on the organic semiconductor layers have also been tested

with graphene electrode diodes. Figure 5.6 shows the device structure used for these measurements, and results are summarized in Figure 5.7. Dopants were added at different weight ratio into the polymer.

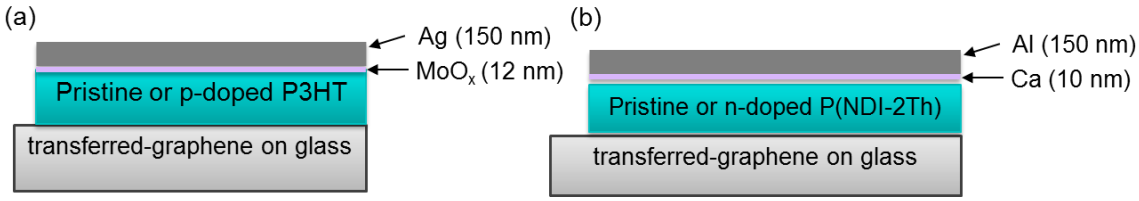

Figure 5.6 (a) Schematic illustration of hole-only P3HT diodes sandwiched between a graphene electrode and a top electrode. (b) Schematic illustration of electron-only P(NDIT-2Th) diodes sandwiched between graphene electrode and top electrode.

The *J-V* characteristics for hole-only devices with different doping ratios of **P1** on graphene electrode were measured at room temperature inside the glovebox (Figure 5.7a). The current in device with pristine P3HT is in the Ohmic regime below 0.2 V, where the current density is first order of the voltage ($J \propto V$). At higher voltage the current approaches the space-charge-limited current regime (SCLC), and the current density is proportional to the square of the voltage ($J \propto V^2$), which indicates that the carriers are accumulating and form a space-charge region. For the doped polymer film, the SCLC regime is not observed within the voltage range of the measurement, presumably caused by the better charge transport in the polymer films. The device with the p-doped graphene electrode has the highest current density, which is more than one order-of-magnitude larger than the pristine one. This observation is consistent with previous observation of p-doped P3HT film.[38] Similarly, for the n-doped P(NDI-2Th) device, the SCLC region was only observed for pristine film; addition of the dopant into the polymer film significantly increases the current density.

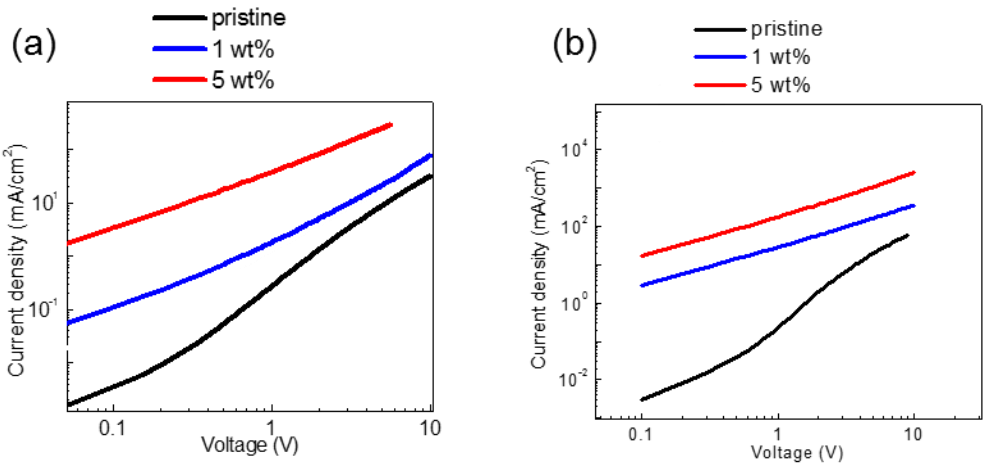

Figure 5.7 (a) *J-V* characteristics of pristine and doped P3HT based hole-only devices; (b) *J-V* characteristics of pristine and doped P(NDI-2Th) based electron-only devices.

5.3 Doped graphene electrodes for OPVs

In order to extend the use of this method to more device applications, OPVs with doped graphene electrodes were also fabricated, in which the carrier transport is also perpendicular to the active layer. Figure 5.8 shows the OPV device structure used in this work. A blend of high-performance pseudo-2D donor polymer PTB7-Th (Figure 5.1) and $PC_{71}BM$ was used as the photoactive layer.

The graphene electrode solar cells were first tested in the conventional device structure as shown in Figure 5.8, where the graphene electrode is used as the hole-collecting electrode. p-Dopant $(Bu_4N)[Ni(mnt)_2]$ (**P1**) was used to decrease the sheet resistance and tune the WF of the graphene electrode. Poly(3,4-ethylenedioxythiophene) polystyrenesulfonate (PEDOT:PSS) was used as the hole-transport layer (HTL) and deposited on the transparent electrode. Because of the hydrophobic nature of the graphene film, the PEDOT:PSS layer was modified with IPA and n-butanol for successful formation of a uniform layer.[39-41] Another way to achieve a uniform PEDOT:PSS layer is vacuum deposit a thin layer of MoO_x, which has abundant

hydroxyl group on the surface. In this research, the first method is used, and the detailed experiment procedures are provided in the Experimental section. As mentioned earlier, the graphene electrode was made by stacking three monolayer graphene sheets grown by CVD method; a pristine 3-L film has a sheet resistance of ca. 800 Ω/sq, but can be decreased to ca. 80 Ω/sq after p-doping. The transmittance remains the same before and after the dopant treatment at ca. 92% (at 550 nm wavelength).

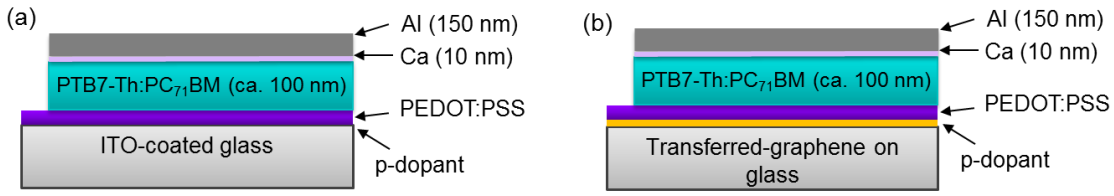

Figure 5.8 Device configuration of conventional PSCs with p-doped graphene as the anode.

The device performance was measured under AM1.5 illumination. The resulting *J-V* characteristics for p-doped graphene-based PSCs were compared with those of ITO and pristine graphene reference device (shown in Figure 5.9), and the resulting photovoltaic parameters were summarized in Table 5.1. The reference device (red curve) with ITO substrate showed comparable results to the literature for PTB7-Th:$PC_{71}BM$ based OPVs.[42-44]

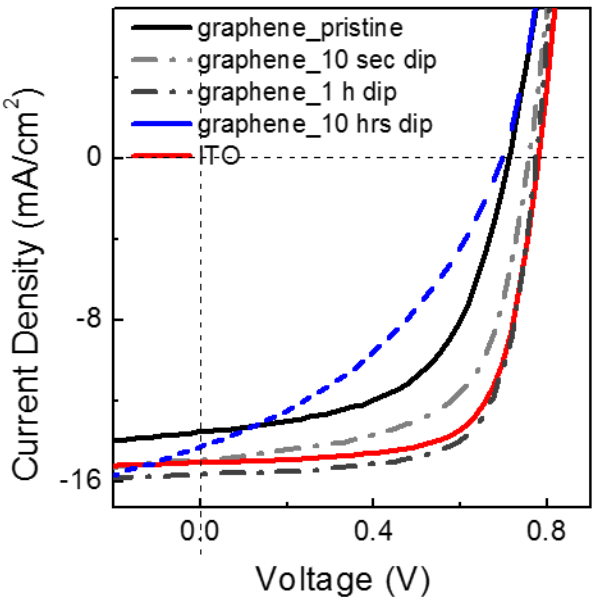

Figure 5.9 Representative *J-V* characteristics of PSCs with PTB7-Th:PCBM bulk heterojunction under AM1.5 illumination (100 mW/cm^2) using ITO, pristine or p-doped graphene (**P1**) as the anode.

Figure 5.9 and Table 5.1 indicate that the best device performance for graphene electrode OPVs is the 1 hour dopant treated sample, which exhibits an open-circuit voltage (V_{oc}) of 0.77 ± 0.01 V, short-circuit current (J_{sc}) of 15.7 ± 0.06 mA/cm^2, and fill factor (*FF*) of (68.9 ± 1.0)%, which yields a total efficiency of approximately 8.33%. These results are comparable to those of ITO-based devices, which were fabricated under the exact same conditions. Lower performances were achieved on pristine graphene electrode and 1 min dopant-treated devices.

Table 5.1 Summary of the solar cell performance using ITO, pristine or p-doped graphene as the anode. Average of 10 to 15 samples.

Sample	J_{sc} (mA/cm^2)	V_{oc} (V)	*FF* (%)	η (%)
Graphene_pristine	13.6 ± 0.5	0.72 ± 0.02	56.4 ± 1.5	5.54 ± 0.39
Graphene_1 min dip	14.9 ± 0.7	0.76 ± 0.01	62.9 ± 0.9	7.18 ± 0.42
Graphene_1 h dip	15.7 ± 0.6	0.77 ± 0.01	68.9 ± 1.0	8.33 ± 0.52
Graphene_10 hrs dip	14.0 ± 0.8	0.71 ± 0.05	35.9 ± 0.5	3.56 ± 0.53
ITO	15.1 ± 0.3	0.78 ± 0.00	68.7 ± 0.2	8.10 ± 0.36
Graphene_1h dip no PEDOT:PSS	13.9 ± 2.1	0.52 ± 0.10	32.7 ± 4.0	2.36 ± 1.21

This phenomenon can be explained by the change of the sheet resistance of the bottom electrode. OPVs exhibit series resistance, which is a combination of the resistance originated from bulk active layer, electrode contacts, and the interfaces, as shown in Equation 5.1:

$$R_{\mathrm{s}} = R_{\mathrm{anode}} + R_{\mathrm{PEDOT:PSS}} + R_{\mathrm{PTB7-Th:PCBM}} + R_{\mathrm{interfacial\,contact}} + R_{\mathrm{Ca/Al}}$$

This series resistance consumes the generated power as it dissipates through the device. The total resistive power loss density (P_{R}) depends on active area of the device, series resistance (R_{s}) and current density (J_{max}) based on equation:

Equation 5.2 $$P_{\mathrm{R}} = R_{\mathrm{s}}\, A\, J_{\mathrm{max}}^{2}$$

which shows that the resistive power loss is proportional to the series resistance. [45,46] Thus, the high sheet resistances of the pristine and 1 min doped tri-layer graphene (ca. 800 and 160 Ω/sq) are expected to result in high series resistance for the devices and, thus, larger power lost. Moreover, the V_{oc} value for 1 hour treated graphene electrode is about 50 mV higher than the devices with pristine graphene. This can be attributed to the increase of the work function of graphene electrode as doped by **P1**.

Longer treatment time (10 hours) of the 3-L graphene films led to obvious decrease of all the parameters, J_{sc}, V_{oc}, and *FF*, and, thus, to a lower efficiency of 3.56 ± 0.53 %. The studies described in Chapter 3 showed that the sheet resistance of 3-L graphene can be largely reduced by **P1** dopant treatment even after the overnight treatment. Thus, the low device performance in this case is not attributable to high series resistance. To explore other possible causes for this impaired performance, 1 hour and 10 hours treated graphene films were characterized by AFM. As shown in Figure 5.10,

there were obvious particles aggregated on the 10 hours treated sample, which were not observed in the 1 hour treated one. The reason of formation of these particles on the surface is still unclear, and further characterization by XPS and/or Mass Spectrometry is needed to determine the chemical composition. However, the high surface roughness of the electrode resulting from the presence of these particles may significantly affect the morphology of layers built up on top, which may have detrimental effects on the device performance. Evidently, as shown in Figure 5.12 for the dark current of the devices, there is large leakage current for the 10 hours treated graphene sample. Moreover, the presence of particles at the interface may also increase the interfacial contact resistance, thus the overall power loss.

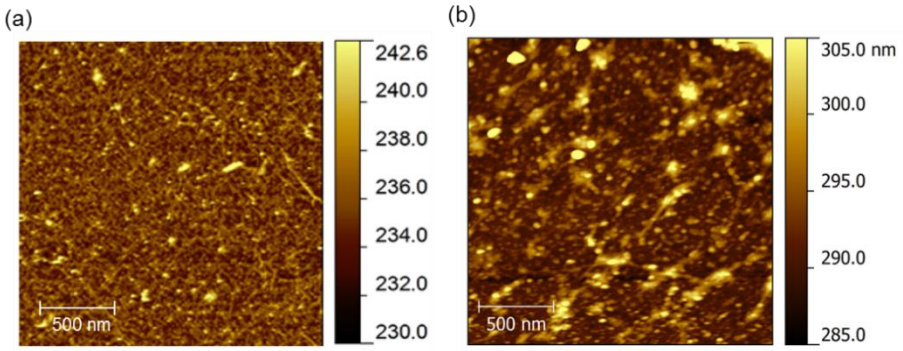

Figure 5.10 AFM images for the 1 hour (a) and 10 hours (b) treated graphene films.

As mentioned earlier, PEDOT:PSS layer was used as a hole-transport layer the OPVs. It can also be used to planarize the bottom electrode, whose rough surface may result in shorts through the thin molecular device. ITO-based OPV devices without a PEDOT:PSS interlayer have been reported in the literature,[47-49], especially when a high work function electrode is used. Graphene-based OPVs without the PEDOT:PSS were, therefore, also fabricated, and the *J–V* characteristics of a representative set of devices are shown in Figure 5.11. The photovoltaic performance decreased considerably

without the PEDOT:PSS layers. As shown in the dark current (Figure 5.13), there is large leakage current in doped graphene electrode cells without the PEDOT:PSS. The possible reasons for the degraded efficiency could be: (1) the high surface roughness of the electrode cause the uneven film of the active layer; (2) different surface energies of the doped graphene film and PEDOT:PSS lead to different qualify of the active layer; (3) thin layer of dopants on the graphene surface cannot effectively block electrons; and (4) exciton quenching happens at the graphene electrode. More experiments would be needed to distinguish between these possibilities.

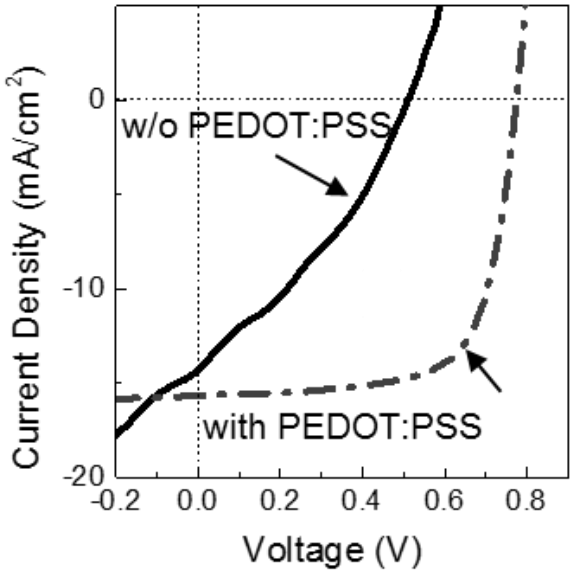

Figure 5.11 Comparison of the *J-V* characteristics for conventional PSCs using p-doped graphene as the anode with or without the PEDOT:PSS HTL. Measured under AM1.5 illumination (100 mW/cm^2).

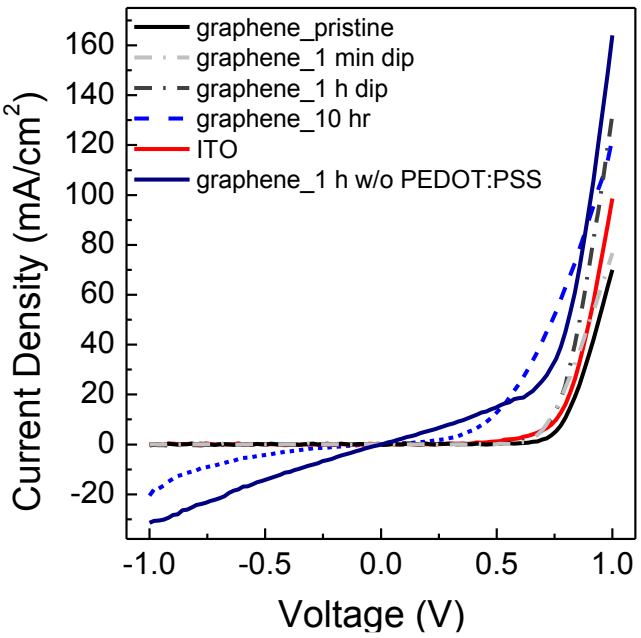

Figure 5.12 Dark *J-V* characteristics for conventional PSCs using p-doped graphene as the cathode as compared with ITO electrode.

Solar cells with inverted structure normally have better stability than those with the conventional structure, because of the use of low work function metal electrode is avoided. For the PTB7-Th:PCBM system, inverted cells are reported to show higher device performance than their conventional counterparts.[44,50,51] Thus, the inverted OPVs with n-doped graphene electrode were also fabricated and characterized in this research. The device structure for the inverted graphene electrode OPVs was shown in Figure 5.13. Sol-gel processed ZnO was used as the electron-transport layer (ETL), because of the air-sensitive nature of the n-doped film, the preparation of the ZnO was slightly different from the commonly used method. The ZnO precursor solution was spun cast on top of substrates inside the glovebox, annealed at 150 °C for 10 min, then brought outside of the glovebox annealed for another 10 min for further oxidization. The detailed preparation procedures is provided in the Experimental section.

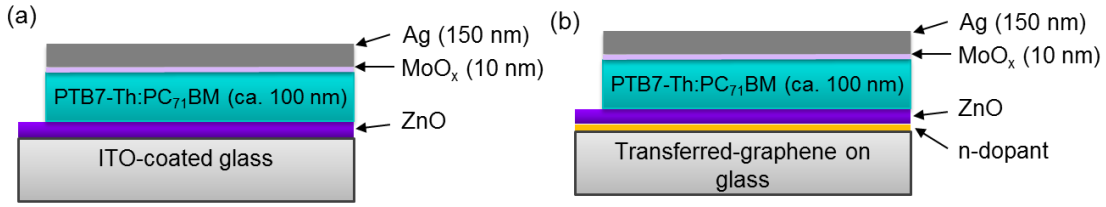

Figure 5.13 Device configuration of inverted PSCs with ITO (a) or n-doped graphene as the cathode (b).

The device performance was also measured under AM1.5 illumination. The resulting *J-V* characteristics for n-doped graphene-based OPVs were compared with that of ITO and pristine graphene reference device (shown in Figure 5.14), and the resulting photovoltaic parameters are summarized in Table 5.2. The inverted device with pristine graphene electrode exhibited lower device performance than the 1 min n-doped one and the ITO control sample. As discussed earlier, this might be caused by the high sheet resistance of the electrode. The sample with pristine graphene electrode exhibits an S-shaped *J-V* curve, as shown in Figure 5.14, which results in a decreased *FF*. One possible reason might be the different quality of the ZnO layer on the pristine graphene as compared with other substrates. AFM characterization of the ZnO films is needed to elucidate this reason. As discussed in Chapter 3, 1 min treatment of graphene with $(2\text{-Fc-DMBI})_2$ dimer (2.5 mM) can significantly reduce the WF from 4.5 eV to 3.9 eV, which increases the WF difference between the two electrode, thus the built-in potential in the device. The V_{oc} increased from 0.71 V to 0.77 V upon n-doping and is in the range of reported values for PTB7-Th:$PC_{71}BM$ based PSCs.[42-44]

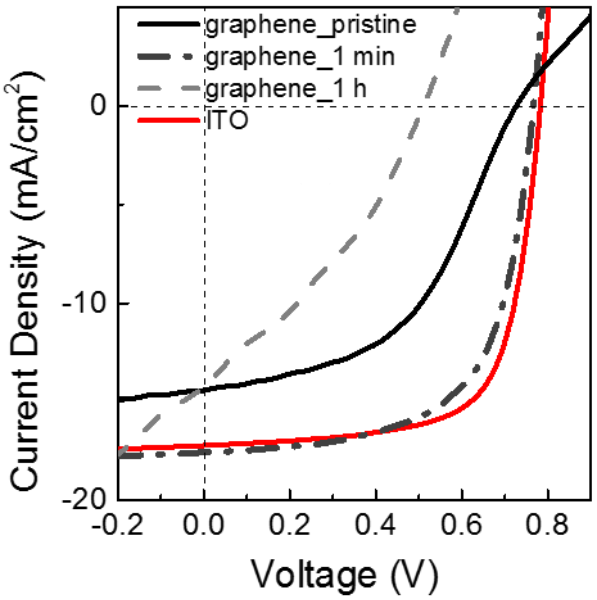

Figure 5.14 Representative *J-V* characteristics of PSCs with PTB7-Th:PCBM bulk heterojunction under AM1.5 illumination (100 mW/cm^2) using ITO, pristine or n-doped graphene as the cathode.

Table 5.2 Summary of the solar cell performance using ITO, pristine or p-doped graphene as the cathode. Average of 10 to 15 samples.

Sample	J_{sc} (mA/cm^2)	V_{oc} (V)	FF (%)	η (%)
Graphene_pristine	15.3 ± 0.3	0.71 ± 0.02	52.2 ± 1.3	5.69 ± 0.51
Graphene_1 min dip	17.6 ± 0.4	0.77 ± 0.03	65.5 ± 2.8	8.87 ± 0.41
Graphene_1 h dip	14.8 ± 0.7	0.51 ± 0.05	32.83 ± 2.6	2.48 ± 0.69
ITO	17.2 ± 0.2	0.78 ± 0.00	69.3 ± 0.8	9.33 ± 0.12
Graphene_1h dip no ZnO	21.2 ± 1.1	0.22 ± 0.10	25.8 ± 1.7	1.26 ± 0.67

As shown in Table 5.2, devices with 1 min immersion into the dopant solution showed comparable performance as the ITO control sample, with a V_{oc} of 0.77 ± 0.03 V, J_{sc} of 17.6 ± 0.04 mA/cm^2, and *FF* of (65.5 ± 2.8)%, which yields a total efficiency of approximately (8.87 ± 0.41)%. Similar to the conventional cells, longer dopant treatment time (1 hour instead of 1 min) degraded the device performance, and leakage current was observed in the dark current.

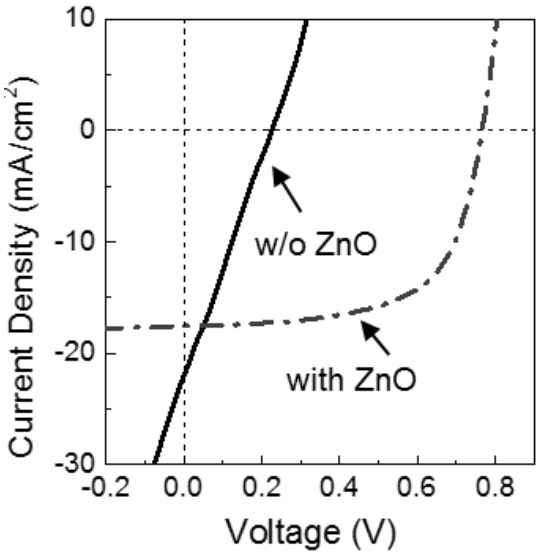

Figure 5.15 Comparison of the *J-V* characteristics for inverted PSCs using n-doped graphene as the cathode with or without the ZnO ETL. Measured under AM1.5 illumination (100 mW/cm^2).

Moreover, as shown in Figure 5.15, for an n-doped graphene electrode device without ZnO layer, the photovoltaic performance also decreased dramatically, and a large leakage current was observed in the dark (Figure 5.16). As discussed previously, there are several possible reasons for this phenomenon, and further characterization of active layer films (such as surface roughness and thickness) and doped graphene films (surface energy and roughness) are needed.

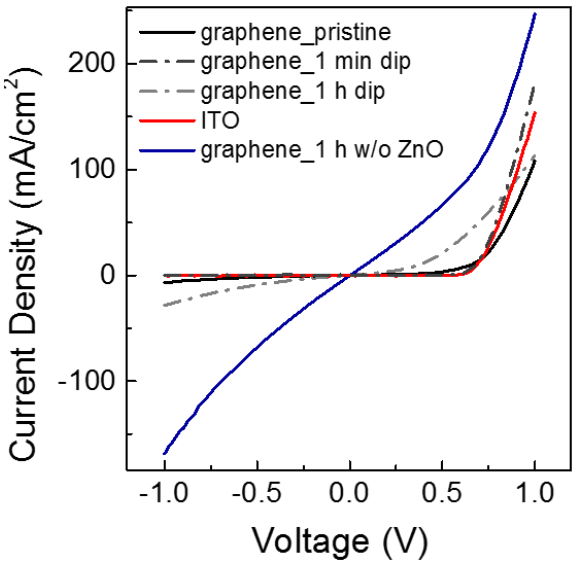

Figure 5.16 Representative dark *J-V* characteristics for inverted PSCs using n-doped graphene as the cathode as compared with ITO electrode.

Overall, OPVs with doped graphene electrodes used as either hole or electron collecting electrodes were demonstrated in this section. It was shown that the dopant treatment is necessary for graphene to be used as the electrode in OPVs, because of the large decrease of the sheet resistance. As mentioned previously, Park *et al.* reported OPVs using SGL graphene electrode for inverted cells where a 7.1% efficiency was achieved. As compared with previous work in the literature, the efficiency reported in this work is among the highest reported value with graphene electrode.[19,52,53]

5.4 Doped graphene electrode for organic field-effect transistors

In both diodes and OPVs, the carrier transport is perpendicular to the polymer film. In this section, lateral transport is investigated with the graphene electrode in OFETs. $(2\text{-Fc-DMBI})_2$ (**N1**) is used to n-dope CVD graphene, and Magic Blue (**P2**) is applied for p-doping. As explained in details previously, CVD-grown graphene was transferred from a copper foil to a SiO_2/Si substrate. Samples were then exposed to dopant solutions for various times, followed by rinsing with additional solvent (toluene

for **N1** and DCM for **P2**) to remove any weakly physisorbed material. The detailed device fabrication procedures are provided in the Experimental section. The feasibility of using doped graphene as source/drain electrodes was demonstrated in both n- and p-channel OFETs.

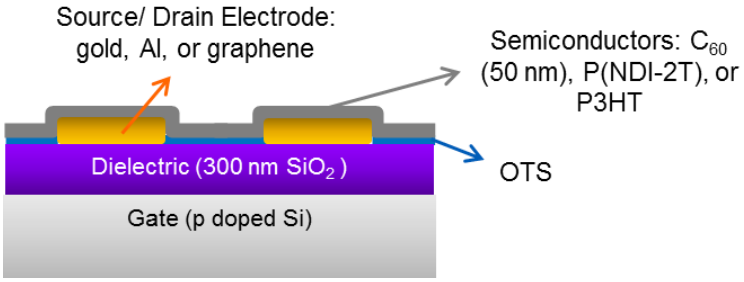

Figure 5.17 (a) Device structure for the bottom-gate, bottom contact OFETs used in this research.

5.4.1 Graphene electrode OFETs with vacuum deposited C_{60}

Graphene electrode OFETs were first tested with n-channel material C_{60}, and Figure 5.17 shows the device structure for the OFETs with either doped graphene or metal source and drain electrodes. The energy levels of C_{60} and work function of different electrode are also shown in Figure 5.18. To the best of our knowledge, this is the first demonstration of using graphene electrode for n-channel transistors, one important reason is: the graphene films under untreated state is normally p-doped by the environment and is normally have a relatively high work function (4.4 to 4.6 eV). Thus, the energy-level alignment of graphene electrode and active layer materials is necessary. The patterned graphene electrodes are soaked into the **N1** solution for 10 min, followed by rinsing with solvent, and annealing at 200 ^{o}C for 10 min. Then 50 nm C_{60} were vacuum-deposited onto the treated graphene electrodes. All the sample treatment and preparation were conducted inside the glovebox, and transfer between different gloveboxes was realized by using a small sealed sample holder.

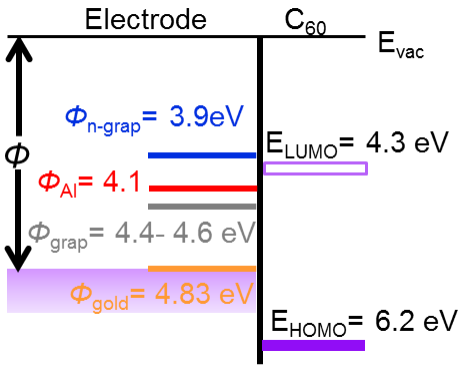

Figure 5.18 Energy level alignment between C_{60} and the electrode (pristine, doped graphene, gold, and Al).

The device performance of C_{60} OTFT devices with different electrodes were characterized and shown in Figure 5.19, where all curves have a clear on-off transition ($I_{on}/I_{off} > 10^5$) and reasonably low threshold voltage (V_T). There was a clear difference of V_T between devices using high work function and low work function electrodes (Au and Al or n-doped graphene, respectively). This is consistent with the expected better energy-level alignment of the EA of C_{60} and WF of the electrodes in the latter case. The mobilities are calculated by extracting the slope of the linear range of $|I_{SD}|^{1/2}$ vs. V_G in the transfer plots of V_G vs. I_{SD}.[54,55] The equation used for the calculation is:

Equation 5.3
$$\left(\frac{\partial I_{SD}^{1/2}}{\partial V_G}\right)_{V_{SD}} = \left[\mu C_{ox}\left(\frac{W}{2L}\right)\right]^{1/2}$$

where I_{SD} and V_{SD} are the source-drain current and voltage; C_{ox} is the capacitance per unit area of the gate dielectric layer, which is 1.15×10^{-4} F m^{-2} in this case; W and L are the channel length (50 μm) and width (2 mm); and μ_h represents the hole mobility in the saturation regime (cm^2 V^{-1} s^{-1}).

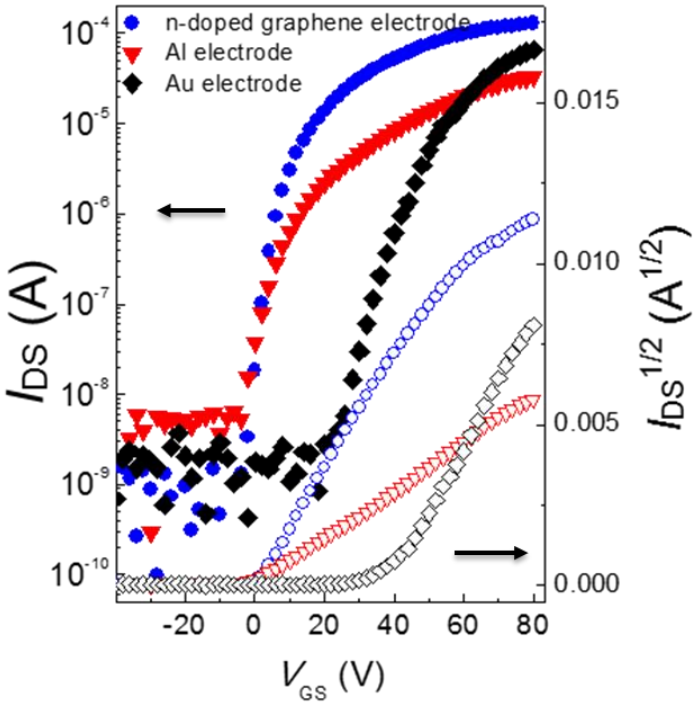

Figure 5.19 *I-V* relations for transfer curves of C_{60} OFET devices with different electrodes: n-doped graphene, Al and Au.

The mobility values for the transistors are summarized in Table 5.3, and all the results are average of ca. 10 devices. The as-prepared n-doped graphene electrode showed slightly higher mobility (0.18 $cm^2 V^{-1} s^{-1}$) than gold electrode devices (0.16 $cm^2 V^{-1} s^{-1}$), and much higher than the Al electrode ones (0.054 $cm^2 V^{-1} s^{-1}$). For Al electrode, because of its low WF, a thin layer of oxide is normally exist on the surface, which will be detrimental to the device performance, especially for these bottom-contact devices. The mobility for the gold electrode C_{60} FETs is comparable to a literature reported value with same device architecture,[56] but much lower than reported values for top-contact devices (1.4 – 6 $cm^2 V^{-1} s^{-1}$)[57-60]. It is known that top-contact OFETs typically show improved device performance than the bottom-contact ones, due in part to the film morphology.[61,62]

Table 5.3 Summary of the comparative transistor performance of graphene and metal-electrode C_{60} OFETs. Average of ca. 10 samples.

Samples		Mobility ($cm^2 V^{-1} s^{-1}$)		$I_{ON/OFF}$	$V_{TH, avg}$ / V	WF(eV)
		Avg	Max			
Graphene	n-doped graphene (2.5 mM for 1 min)	0.18	0.22	10^6	4	3.4-3.9
Au	As prepared	0.16	0.18	10^5	17	4.8-5.1
Al	As prepared	0.054	0.061	10^5	6	4.1
Gold[56]	As prepared	0.02 – 0.65	--	10^6	30	--
Gold[57-60]	As prepared (top-contact)	1.4 - 6	--	10^6	12 - 17	--

To further understand the impact of n-doped graphene electrode on the overall device performance, the contact resistance values were measured for devices with bottom-contact gold and n-doped graphene electrodes. Contact resistance measurements for Al electrode devices were unsuccessful, where the total resistance at different channel length cannot be fitted linearly. This may be caused by the oxidization of the Al surface during the device transfer process. As shown in Figure 5.20, the total resistance values were calculated and plotted at different channel length. The linear fit of the total resistance versus channel length gives the contact resistance according to Equation 3.3. As shown in Figure 5.21, the contact resistance for the graphene electrode devices was about one order of magnitude smaller than that for the gold devices, even though the sheet resistance of n-doped graphene is higher than that of gold. The parameter evaluated here is not refers not to transfer of carriers through the electrode, but to the transfer of charge carriers across the electrode/semiconductor interface. Higher gate voltage leads to smaller contact resistance which is consistent with the literature observation.[56] Better energy alignment between the graphene electrode Fermi level and the EA of C_{60} leads to lower contact resistance than in the gold case. It has been shown that many other carbon-based materials also have lower contact resistance than Au for charge injection (or extraction) into the organic semiconductor materials, and, thus, enhanced charge transport.[63-65] Moreover, different surface energy between graphene and metals may also lead to different packing of the organic semiconductors, some researchers attribute the reason for the lower contact resistance to the influence

of the electrode on the morphology of the semiconductor layers.[63,66,67]

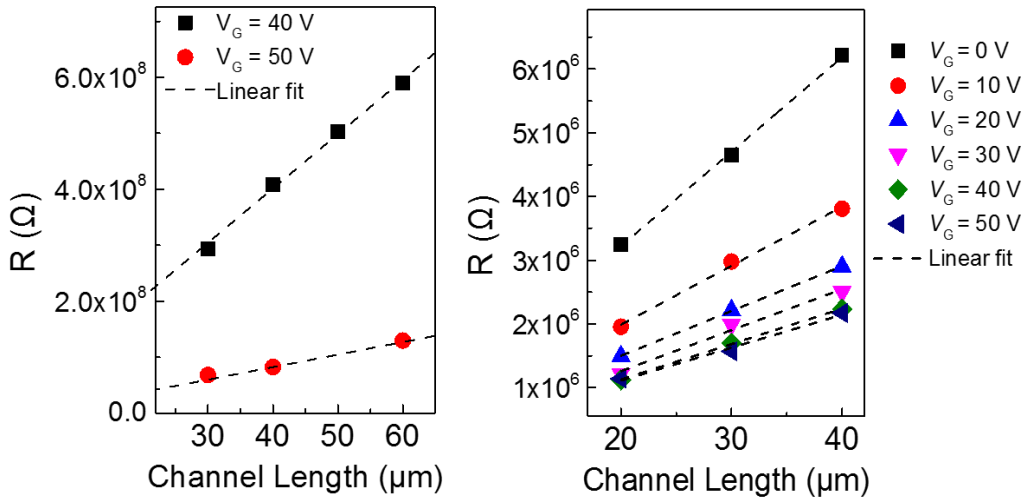

Figure 5.20 Total resistance measurements at different channel length and their linear fit. (Left) Gold electrode C_{60} FET. (Right) Graphene electrode C_{60} FET.

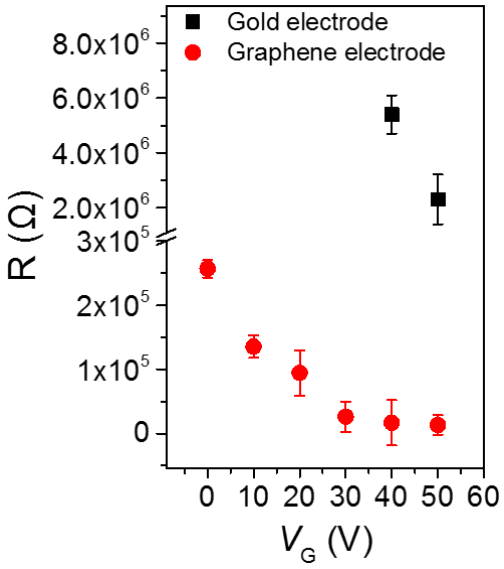

Figure 5.21 Summary of the contact resistance of C_{60} FET with doped graphene and gold electrode at different gate voltage.

Figure 5.14 shows AFM characterization of the morphology of C_{60} deposited on OTS, graphene and gold surface. There is no obvious change in the morphology was observed for C_{60} deposited on gold and graphene.

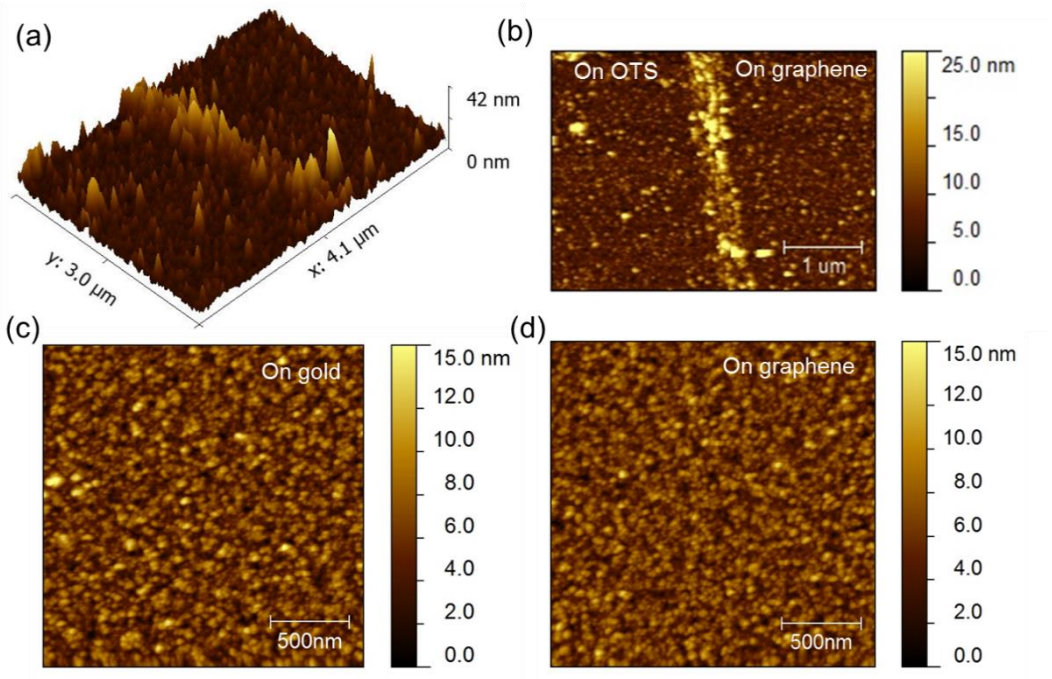

Figure 5.1 AFM images of thermally evaporated C_{60} on different regions of the OFETs.

5.4.2 Graphene electrode OFETs with solution processed polymers

Graphene electrodes were also applied for OFETs based on solution processed polymers: n-channel material P(NDI-2Th) and p-channel material P3HT. Figure 5.22 shows the energy levels of the polymers and the WF of the electrodes used in this research. As with C_{60}, a low WF electrode is needed for P(NDI-2Th); for P3HT to have a better hole injection properties, high work function electrode is needed. Thus, in the former case, n-doped patterned graphene was prepared using the same conditions as for C_{60} devices; in the latter one, graphene electrodes were immersed into the **P2** solution for 10 min. Both processes were followed by rinsing with solvent, and annealing at 200 °C for 10 min. Then, the polymer solutions were spun-coated on the top of the patterned devices. The detailed procedures are provided in the Experimental section.

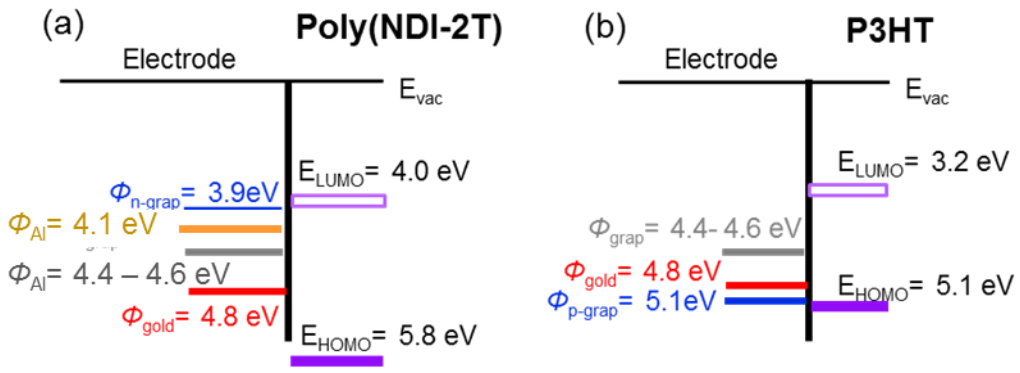

Figure 5.22 (a) Energy-level alignment between Poly(NDI-2T) and the electrode (pristine, doped graphene, and gold). (b) Energy-level alignment between P3HT and the electrode (pristine, doped graphene, Al and gold).

The device performance of the polymer-based FET devices with different electrodes were characterized and shown in Figure 5.23, the mobility (μ), on/off ratio (I_{on}/I_{off}) and the threshold voltage (V_T) are summarized in Table 5.4. The graphene electrode OFETs showed similar mobility values to the metal ones: for P(NDI-2Th), both are on the order of 10^{-3} $cm^2V^{-1}s^{-1}$, which is comparable to the literature value within same device configuration; the mobilities for P3HT films are all on the order of 10^{-3} $cm^2V^{-1}s^{-1}$ as well.

As expected, in P(NDI-2Th) transistor, V_T shifted to lower voltage (meaning that the device is easier to turn on) as the electrode is changed from gold to Al, then n-doped graphene, which is consisted with the observation in C_{60} FETs; in P3HT devices, V_T shifted to more positive voltage with p-doped graphene electrode, which indicates that a more positive voltage is needed to turn off the device. Even though the latter case may not be favorable in the device application, the experiment was a proof-of-concept that the V_T can be shifted according by tuning the WF of the electrode relative to the energy levels of the channel materials. The AFM characterization of the morphology of P3HT

deposited on OTS, graphene and gold substrates are shown in Figure 5.24, and the morphologies on OTS, graphene and gold are quite similar.

In all, this section demonstrated the use of doped graphene in both n- and p-channel transistors. The device performance was evaluated. Bottom contact graphene-electrode devices showed lower contact resistance and comparable mobility than metal electrode transistors.

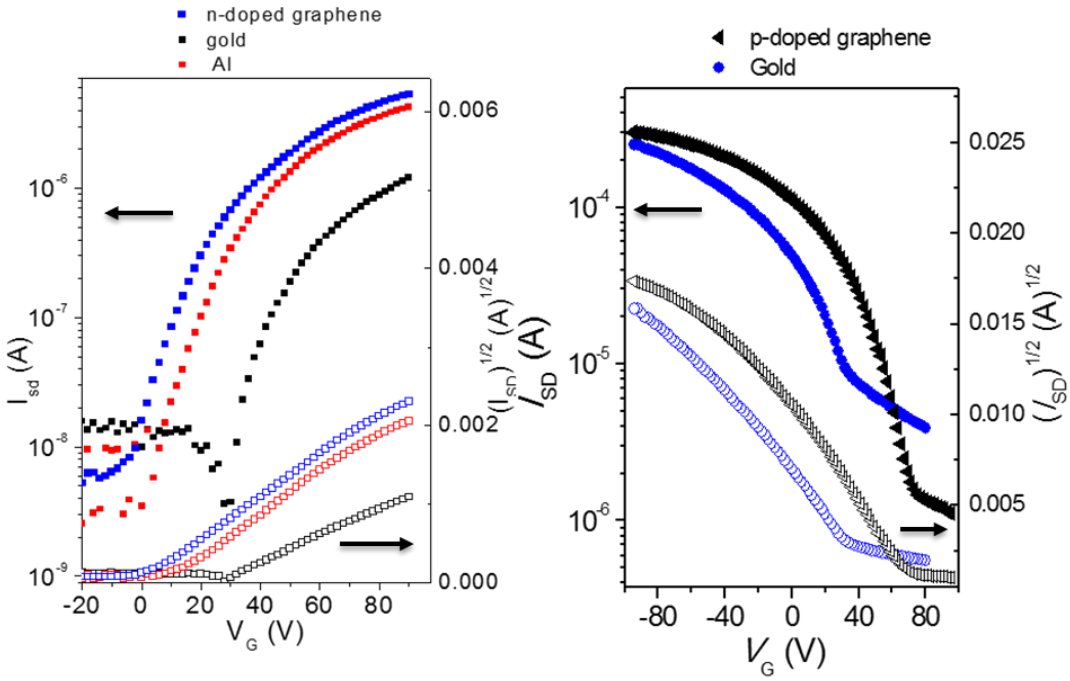

Figure 5.23 *I-V* relations for transfer curves of Poly(NDI-2T) (left) and P3HT (right) OTFT devices with different electrodes: n-doped graphene, Al and Au.

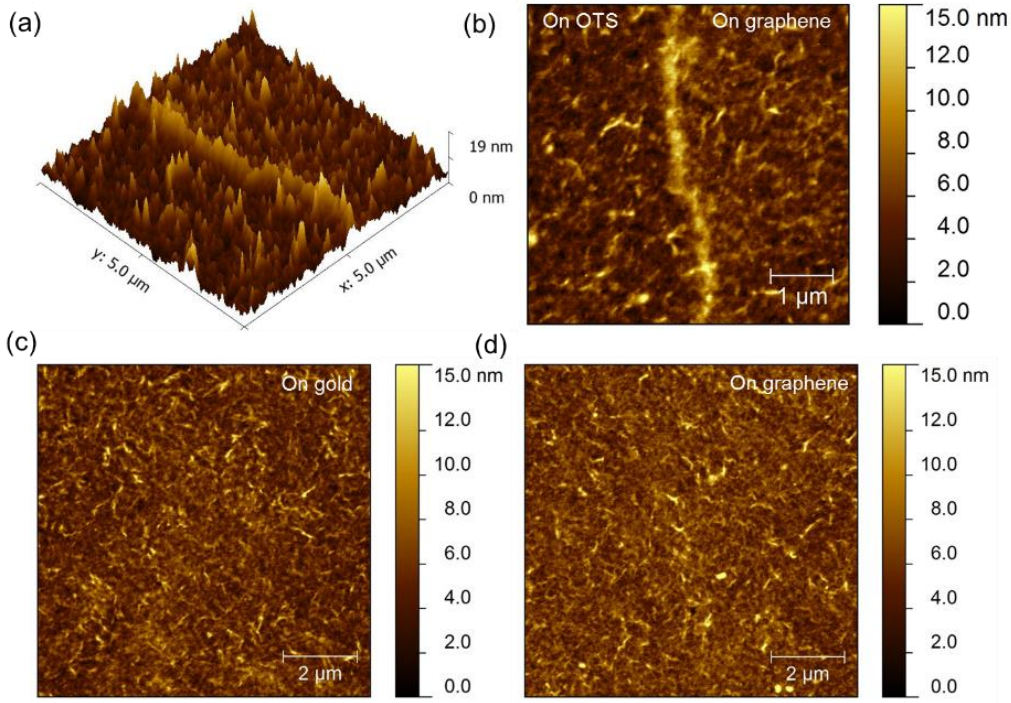

Figure 5.24 AFM images of the P3HT film on different regions of the device.

Table 5.4 Summary of the comparative transistor performance of graphene and metal-electrode P(NDI-2Th) and P3HT OFETs. Average of ca. 10 samples.

Samples		Hole mobility ($cm^2V^{-1}s^{-1}$)		$I_{ON/OFF}$	$V_{TH,\ avg}$/ V	WF(eV)
		Avg	Max			
P(NDI-2Th)	n-doped graphene (2.5 mM for 1 min)	3.4×10^{-3}	3.8×10^{-3}	10^3	2	3.2-3.4
P(NDI-2Th)	Al	3.7×10^{-3}	4.0×10^{-3}	10^3	13	4.1
P(NDI-2Th)	Au	1.6×10^{-3}	2.2×10^{-3}	10^3	29	4.8-5.1
P(NDI-2Th)[68,69]	Au (bottom-gate, top contact)	0.001-0.01	--	10^4	4-20	--
P(NDI-2Th)[69]	Au (bottom-contact, top gate)	0.45-0.85	--	10^4-10^8	15-20	--
P3HT	Au	3.8×10^{-3}	5.0×10^{-3}	10^4	31	4.8-5.1
P3HT	p-doped graphene (0.05 mM dip)	4.8×10^{-3}	5.9×10^{-3}	10^4	43	4.8
P3HT[70]	Au	4.3×10^{-3}	--	10^4	15	--
P3HT[71]	Graphene oxide (20-60 nm)	$(0.3 – 4) \times 10^{-2}$	--	10^4	10	--

5.5 Conclusions

In this chapter, CVD grown mono- or tri-layer graphene sheets were used as the electrodes in three different organic semiconductor devices: organic diodes, OPVs, and OFETs. A versatile approach to fabricate graphene electrode in these device applications has been demonstrated. Compared with previous literature, this is the first comprehensive demonstration of doped graphene electrode used as the hole- and electron-collecting electrode in both perpendicular and lateral transport devices. The WF engineering of graphene through doping is proven to be important to improve the charge-carrier injection efficiency. The doped graphene electrode is suitable for both solution- and vacuum- processed films. In organic diodes and OFETs, application of dopants on graphene leads to the formation of more efficient contacts at the interface without affecting the electronic properties of other components in the device. High efficiency OPVs were demonstrated with doped graphene used as both anode (8.33%) and cathode (8.87%). Even though the device performance is still not superior to that of ITO-electrode devices, the gap in performance has been substantially reduced. Future research directions may include device fabrication of graphene on top of flexible polymer substrates to realize flexible electronics.

5.6 Experimental

5.6.1 General details

All the solvents, include chloroform, dichloromethane (DCM), 1,2-dichorobenzene (DCB), dichlorobenzene isopropanol, n-butanol, toluene, were purchased from Sigma-Aldrich as the anhydrous grade solvents packed under argon.

Toluene was additionally dried over CaH_2, distilled and subjected to three freeze-pump-thaw cycles, while other solvents were used directly without further drying. P3HT was purchased from Rieke Metals Inc. Poly(NDI-2T) was synthesized by Dr. Tissa Sajoto in the Marder group according to the literature.[72] C_{60} was purchased from Alfa Aesar, and was purified using gradient zone sublimation before use. All the sample treatment and GFET measurements were carried out in a Unilab MBRAUN glovebox (< 0.1 ppm of water, < 0.5 ppm oxygen). Glassware was heated dried in oven for at least 1 h, prior to bringing into the glovebox.

The thickness of films was measured by KLA-Tencor P-15 profiler. All AFM images were acquired under atmospheric conditions using a commercial Agilent 5600 LS equipped with an AC-AFM controller. Image acquisition was performed using PicoView 1.10, and image processing performed using the open source program Gwyddion version 2.20.

5.6.2 Device fabrication of graphene electrode diodes and OPVs

Organic diodes and OPVs used the same bottom electrode, either transferred three-layer graphene on glass or ITO. The pre-patterned ITO-coated glass substrates were purchased from Tinwell Technology (item No. TI1678D). Figure 5.25 shows the pattern used in this research. The ITO substrates were cleaned in successive sonication steps using detergent (SDS), deionized water, acetone, and isopropyl alcohol, then exposed to UV–ozone for 10 min. Glass slides used for graphene transfer were cleaned using the same procedures. Graphene substrates used for PSC fabrication were all three-layer CVD graphene transferred layer by layer onto the clean glass substrate using

method described in Chapter 3 (Experimental Section).

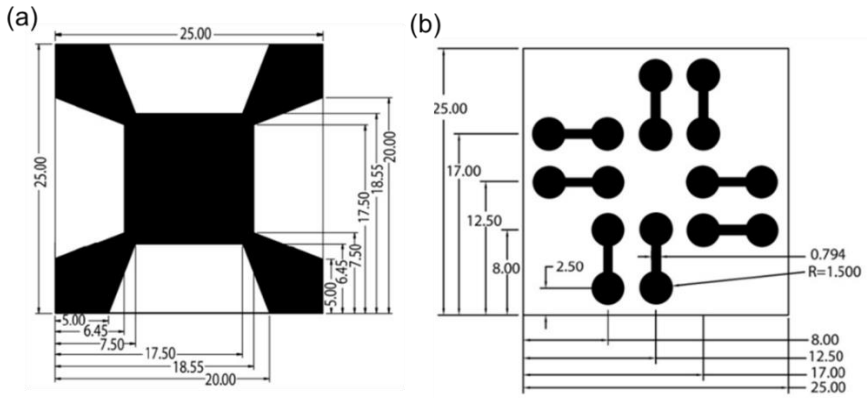

Figure 5.25 (a) The ITO pattern used in this research. (b) The pattern for the top electrode, which is deposited through a shadow mask using a thermal evaporater.[73]

The conventional PSC devices have a structure of glass/ITO or graphene/PEDOT:PSS/active layer/Ca/Al. The PEDOT:PSS (Clevios P VP Al 4083) solution was modified by isopropyl and n-butanol at 1:2:2 volume ratio, then sonicated for 15 min. Different volume ratios between PEDOT:PSS and the alcohols were tried on the pristine electrode cells, and the ratio was optimized as 1:2:2 (v/v/v) PEDOT:PSS:IPA:n-butanol. After filtering with a 0.45 μm nylon syringe filter (Whatman Puradisc), the modified PEDOT:PSS solution was spun cast on top of patterned ITO or graphene substrates at 5000 rpm for 40 s, then placed on the hotplate and annealed at 130 °C for 20 min. The graphene-glass substrates were treated with 5 mM p-dopant solution for various times before the spin-coating of PEDOT:PSS layer. It has been reported in the literature that an additional layer of MoO_x can help prevent the charge recombination at the interface in graphene electrode solar cells, but will largely degrade the performance for ITO electrode cells.[19,74] In these studies, experiments which compare graphene/PEDOT:PSS with or without MoO_x layer were conducted. The device without the MoO_x showed better device performance (high *FF*

and J_{sc}). Thus, the ITO and graphene electrode solar cells were fabricated under the same conditions and allows direct comparison of the results.

The inverted devices have glass/ITO or graphene/ZnO/active layer/MoOx/Ag structure. The ZnO precursor solution was prepared by dissolving zinc acetate in methanol, kept stirring overnight then filtered through a 0.25 μm nylon syringe filter (Whatman Puradisc) before the use. In this study, methanol was used instead of the ethanolamine in 2-methoxyethanol, because previous studies showed that 2-methoxy ethanol solution of zinc acetate cannot form a uniform coating on graphene surfaces because of the hydrophobic nature of graphene. The 3L graphene substrates were treated by 2.5 mM dimer dopant solution for various times in the glovebox. Because of the air-sensitive nature of n-doped graphene, the preparation of ZnO films were first conducted inside the glovebox. The ZnO precursor solution was spun cast on top of substrates at 4000 rpm for 30 s, annealed at 150 °C for 10 min, then brought outside of the glovebox annealed for another 10 min for further oxidization. For comparison, the pristine graphene and ITO coated substrates were prepared under the same condition.

The polymer/PCBM blend solution was prepared by dissolving in chlorobenzene with 1:1.5 ratio at 25 mg/mL total concentration, with 3% DIO. The solution was kept stirring at 60 °C for more than 4 h before spin-coating. The blend solution was spun cast at 100 rpm for 60 s. Approximately a 100 nm thick donor:acceptor active layers were spun cast. The top electrodes were deposited using the shadow masks (Figure 5.25(b)) through a thermal evaporator. The overlap area between the bottom patterned electrode (ITO or graphene) and the shadow mask

resulted in 8 independent cells with an area of 0.07 cm^2.

The current density–voltage (*J*–*V*) characteristics measurement was performed using a Keithley 2400 source meter in a nitrogen-filled glovebox. Solar cell performance was measured using an Air Mass 1.5 G solar simulator with an irradiation intensity of 100 mW cm^{-2}.

5.6.3 Device fabrication of graphene electrode OFET

The graphene electrodes used in this research were patterned using photolithography process as shown in Figure 5.26. Large area graphene pieces (ca. 1.5 $\times$1.5 cm) were transferred on the silicon dioxide substrates (300 nm thermally grown SiO_2 on top of highly doped Si). Then, the graphene substrate was coated with a thin-layer of photoresist, and the electrode patterns were transferred to it using conventional photolithography procedures, as discussed in Chapter 3. After a development step, the transistor substrate was exposed to O_2 plasma with the graphene electrode pattern protected by the photoresist, and the uncovered graphene area was removed. The photoresist was removed by an acetone bath. A 50 nm gold layer was deposited through a shadow mask by the E-beam evaporator (Denton Explorer) for a better contact during the transistor measurements. Controlled transistors with Au or Al as the source and drain contacts were E-beam deposited directly onto the SiO_2 layer using a conventional photolithography lift-off process, as discussed in Chapter 2.

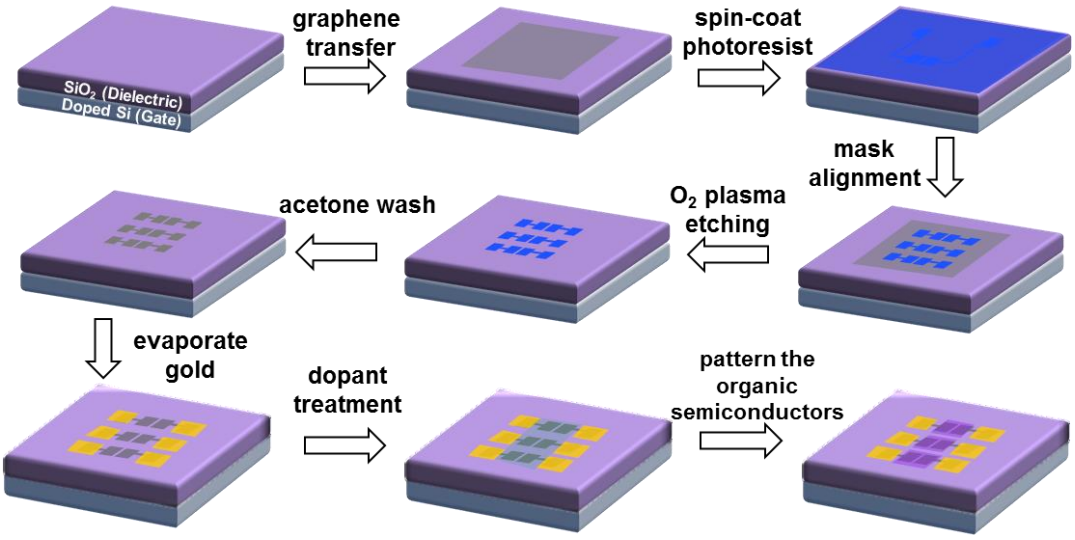

Figure 5.26 Photolithography method to pattern graphene electrodes.

The SiO_2 surface was modified with OTS-18 (n-octadecyltrichlorosilane, purchased from Gelest, Inc.), as shown in Figure 5.27. The substrate was first cleaned under UV/ozone for 30 min. Since UV/ozone treatment will damage the graphene film, a layer of photoresist was used to protect the graphene electrode. Then, the UV/ozone cleaned SiO_2 substrate with either metal (Au or Al) electrode or photo-resist protected graphene electrode were immersed into a 2.54×10^{-3} M (1 μL / mL) solution of OTS-18 in anhydrous toluene overnight inside the glovebox. The substrates were then rinsed by toluene for 3 times, dried under a flow of nitrogen, then rinsed by acetone, methanol and isopropanol, and dried. The contact angle for OTS-18 treated SiO_2 surface is in the range of 95 – 105° with H_2O. Hot solutions of P3HT and Poly(NDI-2T) were prepared with a concentration of 5 mg/mL in chloroform and DCB, respectively, then, were spin-coated onto OTS-18 pretreated FET substrates inside glovebox. Recently, it was shown that UV irradiation could help to enhance formation of anisotropic supramolecular polymer assemblies via favorable π–π stacking (intermolecular interaction).[75,76] The

P3HT/chloroform (5 mg/mL) solution used in this research were treated with the UV source for 10 min. C_{60} was deposited 0.6 Å/s at room temperature using physical vapor deposition (under a pressure of 5×10^{-8} Torr) to final thickness of 50 nm.

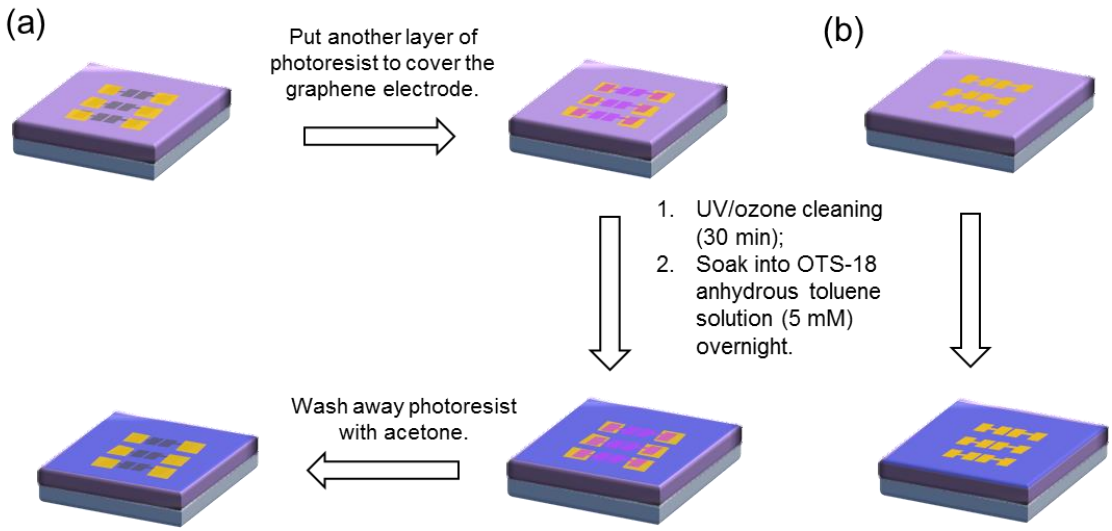

Figure 5.27 Photolithography method to protect the graphene electrode for UV/ozone and subsequent OTS treatment.

All OFET characterizations were performed using a probe station inside a nitrogen filled glovebox using an Agilent 4155C semiconductor parameter analyzer.

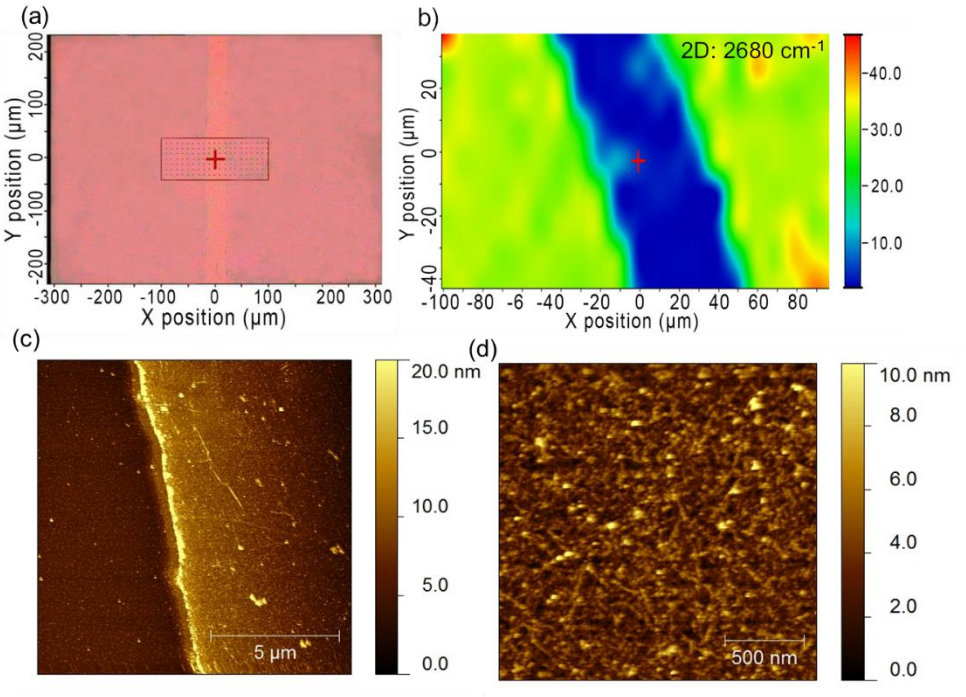

Figure 5.28 (a) Optical microscopy image of the channel of patterned graphene electrode device. (b) Raman mapping of 2D peak at 2680 cm^{-1} across the patterned graphene channel. (c-d) AFM images of the patterned graphene electrode.

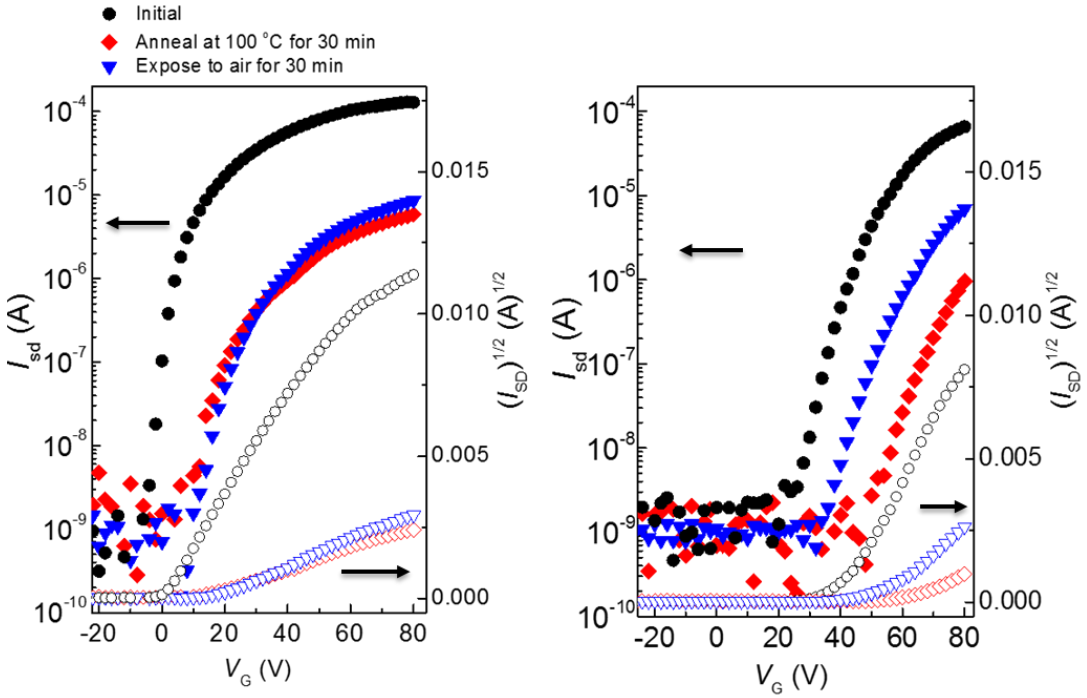

Figure 5.2 Air stability of the C_{60} OTFT devices with different electrodes: graphene (left) and gold (right).

5.7 References

(1) Sze, S. M.; Ng, K. K. *Physics of semiconductor devices*; John wiley & sons, 2006.

(2) Braun, S.; Salaneck, W. R.; Fahlman, M. *Adv Mater* **2009**, *21*, 1450.

(3) Cahen, D.; Kahn, A.; Umbach, E. *Materials Today* **2005**, 32.

(4) Giordano, A. J. *Ph.D. Thesis, Georgia Institute of Technology* **2014**.

(5) Olthof, S.; Singh, S.; Mohapatra, S. K.; Barlow, S.; Marder, S. R.; Kippelen, B.; Kahn, A. *Appl. Phys. Lett.* **2012**, *101*, 253303.

(6) Hamadani, B. H.; Ding, H.; Gao, Y.; Natelson, D. *Phys. Rev. B* **2005**, *72*, 235302.

(7) Wang, Y.; Gao, W.; Braun, S.; Salaneck, W. R.; Amy, F.; Chan, C.; Kahn, A. *Appl. Phys. Lett.* **2005**, *87*, 193501.

(8) He, G.; Schneider, O.; Qin, D.; Zhou, X.; Pfeiffer, M.; Leo, K. *J. Appl. Phys.* **2004**, *95*, 5773.

(9) Huang, J.; Pfeiffer, M.; Werner, A.; Blochwitz, J.; Leo, K.; Liu, S. *Appl. Phys. Lett.* **2002**, *80*, 139.

(10) Uhrich, C.; Wynands, D.; Olthof, S.; Riede, M. K.; Leo, K.; Sonntag, S.; Maennig, B.; Pfeiffer, M. *J. Appl. Phys.* **2008**, *104*, 043107.

(11) Falkenberg, C.; Uhrich, C.; Olthof, S.; Maennig, B.; Riede, M. K.; Leo, K. *J. Appl. Phys.* **2008**, *104*, 034506.

(12) Tress, W.; Leo, K.; Riede, M. *Adv. Funct. Mater.* **2011**, *21*, 2140.

(13) Chae, S. H.; Yu, W. J.; Bae, J. J.; Duong, D. L.; Perello, D.; Jeong, H. Y.; Ta, Q. H.; Ly, T. H.; Vu, Q. A.; Yun, M.; Duan, X.; Lee, Y. H. *Nat. Mater.* **2013**, *12*, 403.

(14) Kim, K. S.; Zhao, Y.; Jang, H.; Lee, S. Y.; Kim, J. M.; Kim, K. S.; Ahn, J.-H.; Kim, P.; Choi, J.-Y.; Hong, B. H. *Nature* **2009**, *457*, 706.

(15) Paniagua, S. A.; Baltazar, J.; Sojoudi, H.; Mohapatra, S. K.; Zhang, S.; Henderson, C. L.; Graham, S.; Barlow, S.; Marder, S. R. *Mater. Horiz.* **2014**, *1*, 111.

(16) Wang, X.; Li, X.; Zhang, L.; Yoon, Y.; Weber, P. K.; Wang, H.; Guo, J.; Dai,

H. *Science* **2009**, *324*, 768.

(17) Baltazar, J.; Sojoudi, H.; Paniagua, S. A.; Zhang, S.; Lawson, R. A.; Marder, S. R.; Graham, S.; Tolbert, L. M.; Henderson, C. L. *Adv. Funct. Mater.* **2014**, *24*, 5147.

(18) Yuchen, D.; Han, L.; Neal, A. T.; Mengwei, S.; Ye, P. D. *IEEE Electron Device Lett.* **2013**, *34*, 1328.

(19) Park, H.; Chang, S.; Zhou, X.; Kong, J.; Palacios, T.; Gradečak, S. *Nano Lett.* **2014**, *14*, 5148.

(20) bin Mohd Yusoff, A. R.; Kim, D.; Schneider, F. K.; da Silva, W. J.; Jang, J. *Energy Environ. Sci.* **2015**, *8*, 1523.

(21) Lee, S.; Jo, G.; Kang, S. J.; Wang, G.; Choe, M.; Park, W.; Kim, D. Y.; Kahng, Y. H.; Lee, T. *Adv. Mater.* **2011**, *23*, 100.

(22) Pang, S.; Hernandez, Y.; Feng, X.; Müllen, K. *Adv. Mater.* **2011**, *23*, 2779.

(23) Loh, K. P.; Tong, S. W.; Wu, J. *J. Am. Chem. Soc.* **2015**.

(24) Liu, H.; Liu, Y.; Zhu, D. *J. Mater. Chem.* **2011**, *21*, 3335.

(25) Ohta, T.; Bostwick, A.; Seyller, T.; Horn, K.; Rotenberg, E. *Science* **2006**, *313*, 951.

(26) Gierz, I.; Riedl, C.; Starke, U.; Ast, C. R.; Kern, K. *Nano Lett.* **2008**, *8*, 4603.

(27) Wehling, T. O.; Novoselov, K. S.; Morozov, S. V.; Vdovin, E. E.; Katsnelson, M. I.; Geim, A. K.; Lichtenstein, A. I. *Nano Lett.* **2008**, *8*, 173.

(28) Hugo, E. R.; Prasoon, J.; Awnish, K. G.; Humberto, R. G.; Milton, W. C.; Srinivas, A. T.; Peter, C. E. *Nanotechnology* **2009**, *20*, 245501.

(29) Jung, N.; Kim, N.; Jockusch, S.; Turro, N. J.; Kim, P.; Brus, L. *Nano Lett.* **2009**, *9*, 4133.

(30) Bianchi, M.; Rienks, E.; Lizzit, S.; Baraldi, A.; Balog, R.; Hornekær, L.; Hofmann, P. *Phys. Rev. B* **2010**, *81*, 041403.

(31) Guan, Z.-L.; Kim, J. B.; Wang, H.; Jaye, C.; Fischer, D. A.; Loo, Y.-L.; Kahn, A. *Org. Electron.* **2010**, *11*, 1779.

(32) Werner, J. H. *Appl. Phys. A* **1988**, *47*, 291.

(33) Dongaonkar, S.; Servaites, J. D.; Ford, G. M.; Loser, S.; Moore, J.; Gelfand, R. M.; Mohseni, H.; Hillhouse, H. W.; Agrawal, R.; Ratner, M. A. *J. Appl. Phys.* **2010**, *108*, 124509.

(34) Manohara, H. M.; Wong, E. W.; Schlecht, E.; Hunt, B. D.; Siegel, P. H. *Nano lett.* **2005**, *5*, 1469.

(35) Qi, Y.; Sajoto, T.; Kröger, M.; Kandabarow, A. M.; Park, W.; Barlow, S.; Kim, E.-G.; Wielunski, L.; Feldman, L. C.; Bartynski, R. A.; Brédas, J.-L.; Marder, S. R.; Kahn, A. *Chem. Mater.* **2010**, *22*, 524.

(36) Olthof, S.; Tress, W.; Meerheim, R.; Lüssem, B.; Leo, K. *J. Appl. Phys.* **2009**, *106*, 103711.

(37) Qi, Y.; Mohapatra, S. K.; Bok Kim, S.; Barlow, S.; Marder, S. R.; Kahn, A. *Appl. Phys. Lett.* **2012**, *100*, 083305.

(38) An, D.; Yinhua, Z.; Andrew, L. S.; Swagat, K. M.; He, W.; Canek, F.-H.; Yadong, Z.; Stephen, B.; Yueh-Lin, L.; Seth, R. M.; Bernard, K.; Antoine, K. *Adv. Funct. Mater.* **2013**.

(39) Noh, Y.-J.; Na, S.-I.; Kim, S.-S. *Sol. Energy Mater. Sol. Cells* **2013**, *117*, 139.

(40) Gao, Y.; Li, J.; Yang, X.; Xiang, Q.; Wang, K. *Electroanalysis* **2014**, *26*, 382.

(41) Park, B.-w.; Pazoki, M.; Aitola, K.; Jeong, S.; Johansson, E. M.; Hagfeldt, A.; Boschloo, G. *ACS Appl. Mater. Interfaces* **2014**, *6*, 2074.

(42) Zhang, S.; Ye, L.; Hou, J. *Adv. Energy Mater.* **2016**, n/a.

(43) Zhang, S.; Ye, L.; Zhao, W.; Liu, D.; Yao, H.; Hou, J. *Macromolecules* **2014**, *47*, 4653.

(44) He, Z.; Xiao, B.; Liu, F.; Wu, H.; Yang, Y.; Xiao, S.; Wang, C.; Russell, T. P.; Cao, Y. *Nat. Photon.* **2015**, *9*, 174.

(45) Choi, S.; Potscavage Jr, W. J.; Kippelen, B. *J. Appl. Phys.* **2009**, *106*, 054507.

(46) Wang, Y.; Tong, S. W.; Xu, X. F.; Özyilmaz, B.; Loh, K. P. *Adv. Mater.* **2011**, *23*, 1514.

(47) Peumans, P.; Forrest, S. R. *Appl. Phys. Lett.* **2001**, *79*, 126.

(48) van de Lagemaat, J.; Barnes, T. M.; Rumbles, G.; Shaheen, S. E.; Coutts, T. J.;

Weeks, C.; Levitsky, I.; Peltola, J.; Glatkowski, P. *Appl. Phys. Lett.* **2006**, *88*, 233503.

(49) Xue, J.; Uchida, S.; Rand, B. P.; Forrest, S. R. *Appl. Phys. Lett.* **2004**, *84*, 3013.

(50) He, Z.; Zhong, C.; Su, S.; Xu, M.; Wu, H.; Cao, Y. *Nat. Photon.* **2012**, *6*, 591.

(51) Zhang, Q.; Kan, B.; Liu, F.; Long, G.; Wan, X.; Chen, X.; Zuo, Y.; Ni, W.; Zhang, H.; Li, M.; Hu, Z.; Huang, F.; Cao, Y.; Liang, Z.; Zhang, M.; Russell, T. P.; Chen, Y. *Nat. Photon.* **2015**, *9*, 35.

(52) Mohd Yusoff, A. R. b.; Kim, D.; Schneider, F. K.; da Silva, W. J.; Jang, J. *Energy Environ. Sci.* **2015**, *8*, 1523.

(53) Yusoff, A. R. b. M.; Lee, S. J.; Shneider, F. K.; da Silva, W. J.; Jang, J. *Adv. Energy Mater.* **2014**, *4*, n/a.

(54) Newman, C. R.; Frisbie, C. D.; da Silva Filho, D. A.; Brédas, J.-L.; Ewbank, P. C.; Mann, K. R. *Chem. Mater.* **2004**, *16*, 4436.

(55) Dimitrakopoulos, C. D.; Mascaro, D. J. *IBM J. RES. DEV.* **2001**, *45*, 11.

(56) Haddock, J. N.; Zhang, X.; Domercq, B.; Kippelen, B. *Org. Electron* **2005**, *6*, 182.

(57) Anthopoulos, T. D.; Singh, B.; Marjanovic, N.; Saricifici, N.; Ramil, A. M.; Sitter, H.; Colle, M.; de Leeuw, D. M. *Appl. Phys. Lett.* **2006**, *89*, 213504.

(58) Itaka, K.; Yamashiro, M.; Yamaguchi, J.; Haemori, M.; Yaginuma, S.; Matsumoto, Y.; Kondo, M.; Koinuma, H. *Adv. Mater.* **2006**, *18*, 1713.

(59) Kitamura, M.; Kuzumoto, Y.; Kamura, M.; Aomori, S.; Arakawa, Y. *Appl. Phys. Lett.* **2007**, *91*, 3514.

(60) Domercq, B.; Kippelen, B.; Zhang, X. **2007**.

(61) Horowitz, G. *J. Mater. Res.* **2004**, *19*, 1946.

(62) Puntambekar, K. P.; Pesavento, P. V.; Frisbie, C. D. *Appl. Phys. Lett.* **2003**, *83*, 5539.

(63) Pang, S.; Tsao, H. N.; Feng, X.; Müllen, K. *Adv. Mater.* **2009**, *21*, 3488.

(64) Koch, N.; Kahn, A.; Ghijsen, J.; Pireaux, J.-J.; Schwartz, J.; Johnson, R.; Elschner, A. *Appl. Phys. Lett.* **2003**, *82*, 70.

(65) Zhang, Y. Y.; Shi, Y.; Chen, F.; Mhaisalkar, S.; Li, L.-J.; Ong, B. S.; Wu, Y. *Appl. Phys. Lett* **2007**, *91*, 223512.

(66) Lee, C.-G.; Park, S.; Ruoff, R. S.; Dodabalapur, A. *Appl. Phys. Lett.* **2009**, *95*, 023304.

(67) Becerril, H. A.; Stoltenberg, R. M.; Tang, M. L.; Roberts, M. E.; Liu, Z.; Chen, Y.; Kim, D. H.; Lee, B.-L.; Lee, S.; Bao, Z. *ACS nano* **2010**, *4*, 6343.

(68) Zhan, X.; Tan, Z. a.; Domercq, B.; An, Z.; Zhang, X.; Barlow, S.; Li, Y.; Zhu, D.; Kippelen, B.; Marder, S. R. *J. Am. Chem. Soc.* **2007**, *129*, 7246.

(69) Yan, H.; Chen, Z.; Zheng, Y.; Newman, C.; Quinn, J. R.; Dötz, F.; Kastler, M.; Facchetti, A. *Nature* **2009**, *457*, 679.

(70) Chang, M.; Choi, D.; Fu, B.; Reichmanis, E. *ACS nano* **2013**, *7*, 5402.

(71) Pang, S.; Tsao, H. N.; Feng, X.; Müllen, K. *Adv. Mater.* **2009**, *21*, 3488.

(72) Chen, Z.; Zheng, Y.; Yan, H.; Facchetti, A. *J. Am. Chem. Soc.* **2008**, *131*, 8.

(73) Grand, G. *Ph.D. Thesis, Georgia Institute of Technology* **2015**.

(74) Park, H.; Shi, Y.; Kong, J. *Nanoscale* **2013**, *5*, 8934.

(75) Choi, D.; Chang, M.; Reichmanis, E. *Adv. Funct. Mater.* **2015**, *25*, 920.

(76) Chang, M.; Lee, J.; Kleinhenz, N.; Fu, B.; Reichmanis, E. *Adv. Funct. Mater.* **2014**, *24*, 4457.

CHAPTER 6 Conclusions and Outlook

6.1 Overview

The field of organic and 2D material-based electronics have led to considerable research over the past decade due to their promise of low-cost, light-weight and flexible circuitry. This dissertation focused on doping studies of these new emerging semiconductors (or semimetal for the graphene case) using redox-active molecules. The objectives of this research were to (1) design and synthesize of new air-stable dimeric based dopants, (2) understand the relationship between the structure and their doping properties, (3) fully characterize the doping properties of dopants in various host materials, and (4) assess the utility of dopants as modified layer in organic semiconductor devices.

The research discussed in this dissertation is on the interface of organic chemistry, physical chemistry, materials science, and device engineering. Specifically, new air-stable dimeric n-dopants were developed, and their doping properties were tuned through synthetic design; kinetics of the redox reaction of newly synthesized dopants in solution with various organic semiconductor acceptors were fully characterized, and their structure-property relationships were explored; the applicability of dopants was tested on various materials of interest, include organic semiconductors, graphene, and TMDCs; and the usage of doped graphene electrode was demonstrated in various device applications.

6.2 Design of new dimeric n-dopants

As discussed in Chapter 1, designing stable n-dopants with strong reducing

power is challenging, because the compounds that dope the hosts through a simple one-electron transfer will be highly air-sensitive when having low enough ionization potentials (IPs) to dope materials with a wide of range of electron affinities (EAs). Previous work in the Marder group identified several dimers of nineteen-electron ($19e^-$) sandwich molecules, such as rhodocene dimer[1] and related Ru, Fe and Ir dimeric sandwich compounds,[2-4] which have moderate air-stability and can n-dope organic semiconductors with EAs as low as ca. 3 eV.[5-8] Monomeric cations are formed which is coupled with the electron transfer and bond cleavage of the dimer. In Chapter 2, the scope of this "air-stable dimer precursor" approach was expanded to the metal-organic and all-organic system, where solution- and vacuum- processable benzimidazole-based dimer dopants, $(DMBI)_2$, were designed and synthesized. Detailed studies of the doping mechanism were conducted for understanding the limitations of their doping efficacy, and for optimizing the processing condition to achieve efficient doping. These DMBI-based dimers behave in a similar way as the $19e^-$ sandwich dimers: exhibit strong reducing power, and can reduce 6,13-bis(triisopropylsilylethynyl)pentacene (TIPSp) whose EA is 3.0 eV (determined by IPES); the substituents (or metal core and ligands in the latter case) have large effects on their doping ability and the kinetics of their reaction with acceptors; and two different reaction mechanisms can occur depending on the choice the donor/acceptor combination. Compared with the $19e^-$ sandwich dimers, DMBI-based dimers can avoid the use of the expensive toxic heavy metals, but the formation of the side-products (amide derivatives) during the synthesis results in lower overall yield. Based on these current results would be how far the reducing ability

of these DMBI-based dimer dopants can be further pushed to reduce materials with even lower EAs.

As discussed in Chapter 2, the overall reducing ability of the dimers can be calculated based on the redox potentials of monomers ($E(M^+/M)$, from cyclic voltammetry measurements) and the bond dissociation energy (estimated by the DFT calculations). Then, the question is how far the reducing ability of these DMBI-based dimer dopants can be further pushed through either decreasing the C—C bond strength or shifting the reduction potential of monomeric cations cathodically.

To shift $E(M^+/M)$, different substitution groups on the benzo-ring can be used. Figure 6.1 summarizes the literature reported redox potentials for DMBI derivatives with different functional groups on the benzo-ring.[9,10] Anodic shifts of the monomer potential are observed with methylation on the benzo ring or through having electron-rich groups, such as alkoxy, attached.[9]

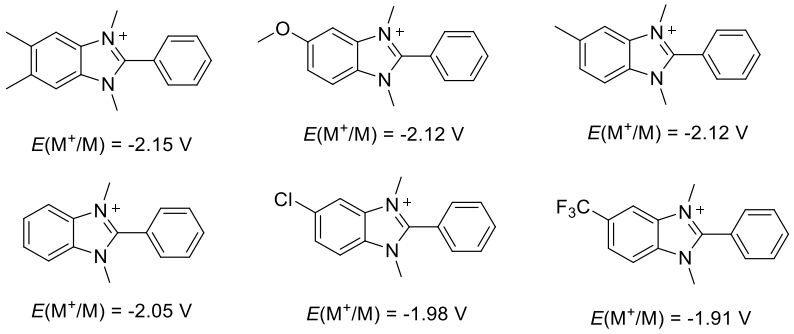

Figure 6.1 Redox potential for several 2-phenylbenzoimidazole, and biimidazole derivatives.[9,10] All values reported versus ferrocene.

To fine tune to the strength of the C—C bond, the strain can be introduced, therefore, decrease the overall activation energy for doping process. More bulky substitution may lead to additional steric strain in the dimers: at the 1 and 3 position of

benzoimidazole, the methyl group could be replaced by an isopropyl group; instead of cyclohexane, a larger alkyl ring could be attached at the 2 position to induce more steric strain. A possible alternative approach to modify the 2 position of benzoimidazole is to synthesize an alkyl chain linked di-benzimidazolium salt first, then reduce it to form the dimer. The steric strain between two benzimidazole moieties can be controlled by the length of the alkyl chain (shown in Figure 6.2).

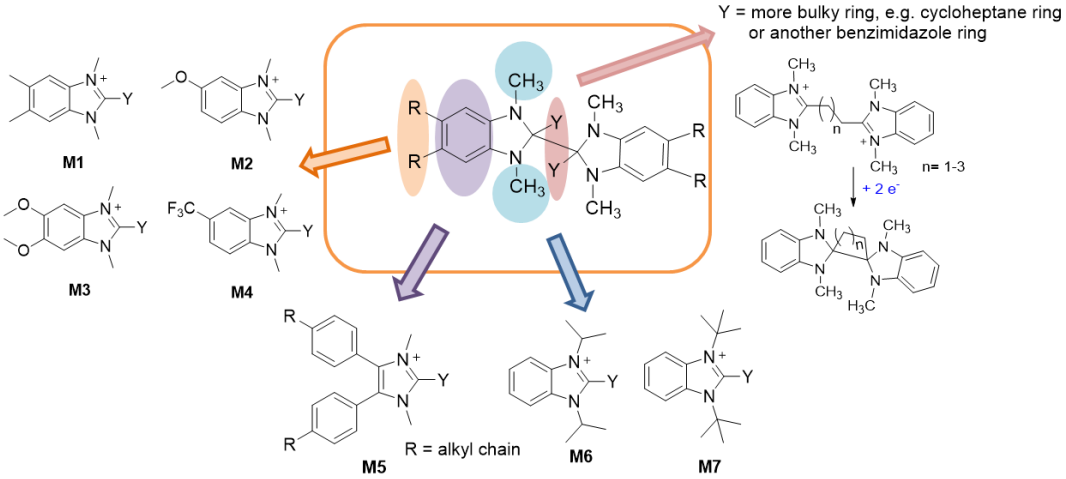

Figure 6.2 Possible design for the new DMBI-based dimers.

However, it can be expected that, as the reducing ability gets stronger, the synthesis of the dimers will become more challenging, and less air-stable. Products other than dimer may also formed through the reduction reaction. Indeed, dimer several 2-aryl analogues have also been tried previously, but no desired dimers were formed. It has also been shown that some previously mentioned organometallic sandwich cations can form hydride monomeric compounds rather than the dimer when they were reduced. Thus, a satisfactory balance has to be achieved between applicable synthesis, dimer stability, and ultimate reducing ability.

6.3 Doping of graphene and its use in organic semiconductors

Chapter 3 focused the controllable doping studies of graphene, while Chapter 5 discussed the device applications of the doped graphene films in the organic semiconductor applications. In Chapter 3, chemical vapor deposition (CVD) synthesized single-layer (SGL) graphene was used as a test bed for a series of dopants where their doping strength (both n- and p-side) were compared. Large carrier densities can be achieved and the WF can be tuned over a range of 2 eV, depending on the nature of the dopant, its concentration, and the exposure time. The sheet resistance of SGL graphene can be reduced by more than 90%. However, compared with ITO, the sheet resistance (ca. 100 Ω/sq) is still not sufficiently low enough for high current device applications, such as OPVs and OLEDs. Thus, multi-layer graphene prepared by layer-by-layer transfer method and metallic carbon nanotubes (CNTs) were also tested for the doping studies: the sheet resistance of three-layer graphene can be reduced form ca. 800 Ω/sq to 50 Ω/sq with 91% transmittance in the visible range; and for CNTs, the resistance can be reduced from ca. 540 Ω/sq to 60 Ω/sq with 80% transmittance. Lower sheet resistance can be achieved with more layers of graphene or thicker films of CNTs, but with the cost of loss transparency. In Chapter 5, the doped graphene layers were applied in three different organic semiconductor devices (diodes, OPVs, and OFETs) as the electrodes. n- and p-Doping of the graphene were proven to be beneficial for the electron- and hole-injection at the electrode/active layer interface. In OPVs, high efficiencies were demonstrated with doped graphene used as both anode (8.33%) and cathode (8.87%) using a blend of high performance low bandgap polymer PTB7-Th

and $PC_{71}BM$ as the photoactive layer, which is comparable to the ITO electrode devices. In OFETs, significant lower contact resistance and comparable mobilities were obtained with doped graphene electrode as compared with metal one. These results open up more questions from both practical application and scientific point of view.

For the device application of graphene to come to fruition, the preparation procedures of high-quality large-area graphene films need to be optimized and simplified, and sheet resistance needs to be further decreased to compete with other transparent electrodes. In this research, a layer-by-layer transfer method was used to obtain multi-layer graphene, which is tedious and time consuming: about three days is required for the growth and transfer to obtain a three-layer graphene, in contrast to only one day for SGL graphene. To avoid this duplication of efforts during the transfer steps, as-grown multilayer graphene can be used. However, the multilayer graphene obtained from CVD method (grown on nickel instead of copper) is usually a stack of 2-5 layers, and the variation in conductivity across the film may disrupt the overall performance. An alternative approach is using graphene oxide, which can be prepared from its water suspensions, followed by a reduction step through thermal desorption of oxygen content, hydrogen plasma, or chemical reaction.[11-13] This will allow a simpler and less expensive processing, and it is suitable for large area applications. In this case, a thicker film is needed to achieve same sheet resistance as compared with multilayer graphene, because of the existence of defects due to the residual oxygenated sites and loss of carbon during the reduction.[14,15] Thus, more transmittance loss in the visible range are expected. Moreover, based on current results, doped CNTs also seems to be a promising

alternative. Organic diodes with CNT electrode have been fabricated, but all the devices were shorted presumably caused by the high surface roughness of the CNT films. Spin-coating a commonly used conductive polymer, such as poly(3,4-ethylene-dioxythiophene) (PEDOT), can reduce the roughness without loss the transparency across the device surface.[16,17] Further experiment would be trying to fabricate OPVs with doped CNTs electrode, where the hole- or electron-transport layer (PEDOT:PSS and ZnO) can be used to modify the surface of CNTs.

It also worth pointing out that most of the dopants used in this research either contains expensive/toxic heavy metals or require multi-step synthesis procedures, which will increase the cost of the dopants as well. It would be desirable to use lost-cost, easy-access dopants for practical device applications. Commercially available hydride reducing reagents sodium borohydride ($NaBH_4$) and its derivative tetrabutylammonium borohydride, $(C_4H_9)_4N(BH_4)$, which is soluble in most organic solvent, have been tried on the graphene films. Obvious n-doping effects were observed based on the preliminary results: the sheet resistance for SGL graphene was reduced from ca. 2000 Ω/sq to 270Ω/sq, together with the reducing of the WF about 0.5 eV. For host materials that are not sensitive to the side-product of the doping reaction and fairly easy to dope, these commercially available chemicals would be more attractive than the dimers discussed in this research. Thus, it might be of interest to thoroughly study their doping mechanisms and understand their doping abilities.

As discussed in Chapter 5, one problem observed from devices with heavily doped graphene electrode is that the presence of the adsorbed dopant molecules on the

surface may also affect the microstructure of the organic semiconductor on the top, and even increase the contact resistance when large quantity of doping products are formed at the interface. Moreover, the existence of unreacted dopants on the surface, which are not electrostatically bonded to the doped film, may cause problems when the organic semiconductor layer is processed from the solution, where the unreacted dopants might be re-dissolved into the solution and dope the active layer. Doping at the interface is desirable to reduce the sheet resistance, but doping through the active layer may adversely affect the device performance. In the current research, this problem was not observed, which may because of the relatively thick semiconductor films employed (ca. 150 to 200 nm), and carefully preparation of the film during the spin-coating step (start spinning once the solution was dropped and use high acceleration). However, for thin-film electronics, the drawbacks of this method may become more obvious. One possible strategy to solve this problem is using underside doping method, where the surface properties of the graphene are maintained. To realize this underside doping, the graphene films with a polymer layer (such as PMMA used for the transfer step) supported on the top can be floated on the surface of dopant solution. The solvent for this treatment needs to be chosen carefully, which should be a good solvent for the dopants without dissolving the polymer support of the graphene film.

Beyond these practical questions when it comes to the device application of using dopants for organic semiconductors, there are also several interesting scientific questions need to be answered: (1) how are energy levels aligned at the interface between the graphene and organic molecules, and what is the role of doping in this

alignment; (2) will there be any difference when different dopants are applied at the interface; and (3) how are the band structure and surface properties of the electrode (such as graphene versus CNTs and graphene oxide) affect the interface alignment. Currently, there are many studies about the energy level alignment at organic/metal and organic/metal oxide interfaces,[18-20] relatively few on the organic/organic interfaces,[21] and no such studies on the organic/graphene interface. To characterize the energy level alignment at organic/graphene interface, a large-area, high-quality graphene film with an ultra-clean surface is needed, which may require the hydrogen annealing at high temperature several times to fully remove the polymer residue from the transfer step. UPS measurements need to be performed on the graphene coated with different thickness of the organic semiconductor films to extract the position of the Fermi level relative to the vacuum level and valance band maximum. When the dopant is applied at the interface, one can anticipate that a small space-charge layer will be created, which will reduce the electrode-induced gap states and Fermi level pinning between them. Thus, simple vacuum level alignment is expected at the interface, where electron- and hole-injection barriers at the interface are simply the difference between the work function of the modified electrode and EA and IE, respectively. However, all of these assumptions need to be tested by experiments.

6.4 Doping and chemical functionalization of TMDCs

For flexible electronics application, other than organic semiconductor and graphene, transition-metal dichalcogenides (TMDCs) have emerged as promising candidates with high carrier mobility and large semiconducting bandgap. For example,

high mobility up to 200 cm^2/Vs has been demonstrated for MoS_2 at room temperature.[22] Moreover, MoS_2 has tunable bandgap from ca. 1.8 eV to 1.3 eV that depends on the number of layers.[23] The carrier mobilities for organic semiconductors are typical below 1 $cm^2\ V^{-1}\ s^{-1}$,[24] while graphene is lack of bandgap, thus, digital transistor and switching cannot be realized.[25] In Chapter 4, doping studies of TMDCs, including MoS_2 and WSe_2, using redox-active molecules were discussed. In both cases, the work function can be tuned over a large range (ca. 2 eV) upon n- and p-doping, and large carrier densities can be achieved (on the order $10^{12}\ cm^{-2}$) as characterized by the FET. The doping strength can be controlled by the dopant type, treatment time, and the solution concentration. For the trilayer MoS_2 used in this research, strong n-doping is desired because of its intrinsic n-channel behavior. Both DMBI dimer dopants and its hydride monomer derivative were applied on the surface, with the dimer giving a larger reduction in work function and a larger increase in current. This is consistent with the observation in organic semiconductor doping. p-Dopant was also applied on the MoS_2 film, which neutralized electrons in the pristine films, and resulted in less strongly n-type MoS_2 than the pristine film, but p-channel behavior was not observed in this case. WSe_2, on the other hand, is p-channel material, thus, p-dopant was used to improve its transistor performance, and n-doping studies were conducted for a proof-of-concept purpose.

From a fundamental science perspective, these studies contribute to expanding the scope of dopable host materials in the semiconductor community by using these strong redox-active solution-processable dopants. Future work on doping and interface modification of these TMDCs films could be explored from two main aspects: (1)

device engineering of the transistor used in current to further push the doping effects, and (2) surface modification of the TMDCs using different strategies.

In the current study, the transistor has a bottom-gate top-contact configuration, and the whole device was treated with the dopant solution. In this case, only the exposed channel region was doped while the interface between the contact and channel materials remained intact. Thus, high contact resistance might still exist at the interface. An alternative method would be to conduct the doping treatment before the deposition of the top electrode to realize the interface doping. Two sets of experiments, where either all the TMDCs film is exposed to the doping treatment or only the contact/active layer interface area is treated with the dopants, can be conducted to elucidate the different contribution of doping effects to the overall electrical performance of the transistors. Moreover, in this research, low WF metal (Ti/Au) and high WF metal (Au) were used as the top-contact for MoS_2 and WSe_2, respectively, because of their intrinsic transport properties. This might be the reason that opposite type of channel behavior was not observed upon p- and n-doping for MoS_2 and WSe_2, respectively, especially when UPS characterization confirmed the large shifts of the Fermi level and WF. Fabricating device with different top contacts will be helpful to fully understand this observation.

Moreover, it would also be interesting to investigate the influence of the dielectric/TMDCs interface modification by using different surface modifiers. The samples used in this research were directly grown and fabricated on the SiO_2 substrate without transferring. Preliminary results (measured by Meng-Yen Tsai in Dr. Vogel's group) showed that the current can be increased dramatically through a simple transfer

step of the film to a new SiO_2 substrate (Figure 6.3). This may be caused by the existence of un-sulfurized (or selenized) metal atoms at the interface, because the TMDCs films were synthesized through a top-to-bottom sulfurization or selenization of the pre-deposited Mo or W film. To further reduce the trap states on the dielectric surface, self-assembly monolayers (SAMs), such as thiols or phosphonic acids, with different dipole inherent within the molecules can applied on the surface. Different surface dipole, thereby different WF, will be induced on the dielectric layer. It would be interesting to explore the effects of different interface dipole on the physical and electrical properties of TMDCs layers.

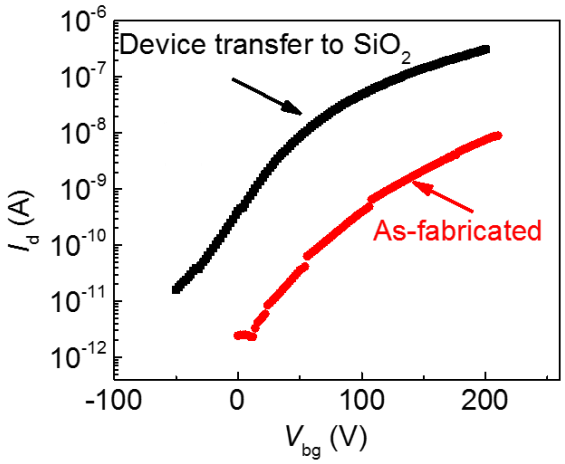

Figure 6.3 Representative transfer curves (I_d versus V_{bg}) of as-fabricated and transferred MoS_2 FETs.

As discussed in the previous section, it would be desirable to use inexpensive dopants for practical device applications. $NaBH_4$ have been applied on the MoS_2 surface, where large work function shift (decreased by ca. 1 eV) and Fermi level shift (ca. 0.5 eV relative to the VBM) were observed. This is even comparable to the doping effects of dimer dopants. Further characterizations of the doped film are needed to fully understand their reaction mechanism and doping strength.

The modification method for TMDCs discussed in this research is surface doping, where the electrical property is improved because of the increased number of charge carriers, and the doping product is electrostatically bonded to the surface. Covalent attachment of functional group on the surface might be of interest to facilitate the carrier transfer as well, with the new bond formed at the defect sites. For example, it has been shown that thiol-containing molecules can be used to fill the sulfur vacancies in MoS_2, which are the main type of intrinsic defects in the film.[26] Organic moieties, such as amide or methyl group, can be grafted onto the chalcogenide layer of TMDCs from their organoiodide precursors. Dramatic changes in the optoelectronic properties were observed.[27] Using molecules which can interact with unsaturated metal atoms at the edge or defect sites or directly bond to the chalcogen atoms might be interesting for surface functionalization and modification of electric and optical properties.

In all, this thesis sought to examine the doping studies of several host materials with promising applications in flexible electronics, through using a series of redox-active molecules. It is the author's hope that the systematic investigation presented in this dissertation can be served as a platform for future scientific studies and development of flexible electronics.

6.5 References

(1) Fischer, E. O.; Wawersik, H. *J. Organomet. Chem.* **1966**, *5*, 559.

(2) Hamon, J.-R.; Astruc, D.; Michaud, P. *J. Am. Chem. Soc.* **1981**, *103*, 758.

(3) Gusev, O. V.; Ievlev, M. A.; Peterleitner, M. G.; Peregudova, S. M.; Denisovich, L. I.; Petrovskii, P. V.; Ustynyuk, N. A. *J. Organomet. Chem.* **1997**, *534*, 57.

(4) Gusev, O. V.; Peterleitner, M. G.; Ievlev, M. A.; Kal'sin, A. M.; Petrovskii, P. V.; Denisovich, L. I.; Ustynyuk, N. A. *J. Organomet. Chem.* **1997**, *531*, 95.

(5) Olthof, S.; Mehraeen, S.; Mohapatra, S. K.; Barlow, S.; Coropceanu, V.; Brédas, J.-L.; Marder, S. R.; Kahn, A. *Phys. Rev. Lett.* **2012**, *109*, 176601.

(6) Guo, S.; Kim, S.; Mohapatra, S.; Qi, Y.; Sajoto, T.; Kahn, A.; Marder, S.; Barlow, S. *Adv. Mater.* **2012**, *24*, 699.

(7) Guo, S.; Mohapatra, S.; Romanov, A.; Timofeeva, T.; Hardcastle, K.; Yesudas, K.; Risko, C.; Brédas, J.-L.; Marder, S.; Barlow, S. *Chem. Eur. J.* **2012**, *18*, 14760.

(8) Qi, Y.; Mohapatra, S. K.; Bok Kim, S.; Barlow, S.; Marder, S. R.; Kahn, A. *Appl. Phys. Lett.* **2012**, *100*, 083305.

(9) Zhu, X.-Q.; Zhang, M.-T.; Yu, A.; Wang, C.-H.; Cheng, J.-P. *J. Am. Chem. Soc.* **2008**, *130*, 2501.

(10) Thummel, R. P.; Goulle, V.; Chen, B. *J. Org. Chem.* **1989**, *54*, 3057.

(11) Becerril, H. A.; Mao, J.; Liu, Z.; Stoltenberg, R. M.; Bao, Z.; Chen, Y. *ACS Nano* **2008**, *2*, 463.

(12) Stankovich, S.; Dikin, D. A.; Piner, R. D.; Kohlhaas, K. A.; Kleinhammes, A.; Jia, Y.; Wu, Y.; Nguyen, S. T.; Ruoff, R. S. *Carbon* **2007**, *45*, 1558.

(13) Gómez-Navarro, C.; Weitz, R. T.; Bittner, A. M.; Scolari, M.; Mews, A.; Burghard, M.; Kern, K. *Nano Lett.* **2007**, *7*, 3499.

(14) Schniepp, H. C.; Li, J.-L.; McAllister, M. J.; Sai, H.; Herrera-Alonso, M.; Adamson, D. H.; Prud'homme, R. K.; Car, R.; Saville, D. A.; Aksay, I. A. *J. Phys. Chem. B* **2006**, *110*, 8535.

(15) Mkhoyan, K. A.; Contryman, A. W.; Silcox, J.; Stewart, D. A.; Eda, G.; Mattevi, C.; Miller, S.; Chhowalla, M. *Nano Lett.* **2009**, *9*, 1058.

(16) Zhang, D.; Ryu, K.; Liu, X.; Polikarpov, E.; Ly, J.; Tompson, M. E.; Zhou, C. *Nano Lett.* **2006**, *6*, 1880.

(17) Park, S.; Vosguerichian, M.; Bao, Z. *Nanoscale* **2013**, *5*, 1727.

(18) Greiner, M. T.; Helander, M. G.; Tang, W.-M.; Wang, Z.-B.; Qiu, J.; Lu, Z.-H. *Nat. Mater.* **2012**, *11*, 76.

(19) Hill, I.; Rajagopal, A.; Kahn, A.; Hu, Y. *Appl. Phys. Lett.* **1998**, *73*, 662.

(20) Vázquez, H.; Dappe, Y.; Ortega, J.; Flores, F. *J. Chem. Phys.* **2007**, *126*, 144703.

(21) Ishii, H.; Sugiyama, K.; Ito, E.; Seki, K. *Adv. Mater.* **1999**, *11*, 605.

(22) Das, S.; Chen, H.-Y.; Penumatcha, A. V.; Appenzeller, J. *Nano lett.* **2012**, *13*, 100.

(23) Chang, H.-Y.; Yang, S.; Lee, J.; Tao, L.; Hwang, W.-S.; Jena, D.; Lu, N.; Akinwande, D. *ACS Nano* **2013**, *7*, 5446.

(24) Chason, M.; Brazis, P. W.; Jie, Z.; Kalyanasundaram, K.; Gamota, D. R. *Proc. IEEE* **2005**, *93*, 1348.

(25) Schwierz, F. *Nat. Nano.* **2010**, *5*, 487.

(26) Yu, Z.; Pan, Y.; Shen, Y.; Wang, Z.; Ong, Z.-Y.; Xu, T.; Xin, R.; Pan, L.; Wang, B.; Sun, L. *Nat. Commun.* **2014**, *5*.

(27) Voiry, D.; Goswami, A.; Kappera, R.; e Silva, C. d. C. C.; Kaplan, D.; Fujita, T.; Chen, M.; Asefa, T.; Chhowalla, M. *Nat. Chem.* **2015**, *7*, 45.

APPENDIX A Benzodithiophene and Benzobisthiazole based Oligomers: Investigation of Photovoltaic Propterties

A.1 Introduction

In organic solar cells (OSCs), the synthetic strategy of incorporating molecular electron donor (D) and acceptor (A) units in an alternating and conjugated manner is a widely used approach to guarantee a high absorption coefficient at low energy.[1-4] Through fine tuning the D and A moieties, the intramolecular charge transfer (ICT), absorption, and the energy levels can be adjusted accordingly. Rational design based on this D-A concept has led to a large number of high-performance hole-transport materials, which are either polymers or small- (or medium-) size molecules. In the past few years, power conversion efficiencies (PCEs) of >11% have been achieved for polymer-based OSCs after careful device optimization,[5] while solution-processable small molecules, on the other hand, have demonstrated PCEs of ~9%.[6] Even though the overall performance of small molecules is still behind that of their polymer counterparts, the gap in performance has been narrowed. There are several advantages of small molecules over their polymeric counterparts, including the good solubility,[7] generally higher open-circuit voltage (V_{oc}), and higher hole-mobility compared with polymers,[8,9] well-defined chemical structures, resulting in elimination of issues associated with batch-to-batch variability of molecular weight (MW) distribution.[10] However, there is the trade-off of poorer film quality, relatively lower J_{sc}, and less thermally stable phases in the solid states. Possible solutions include developing the medium-size conjugated system (with 6-10 units) with appropriate alkyl substituents,[2,11] which possesses the

desirable properties of both polymer and small-molecule classes.

Bazan *et al.* reported a series of high efficiency intermediate-sized conjugated molecules adapting D^1−A−D^2−core− D^2−A−D^1 alternating frameworks, where D^1 and D^2 represent 5′-hexyl-2,2′-bithiophene (BiTh) and dithieno(3,2-*b*;2′,3′-*d*)-silole (DTS), respectively, while pyridal[2,1,3]thiadiazole (PT) was employed as the acceptor moiety, as shown in Figure A.1.[2,10] By varying the center "core", the optical properties, energy levels, thermal resistance, self-organization and ultimately charge carrier mobilities and optoelectronic properties were effectively tuned. High efficiency was achieved using **X2** (ca. 6.4%) in bulk-heterojunction blend with $PC_{60}BM$ in simple conventional device structure without any postdepostion treatment or additive.

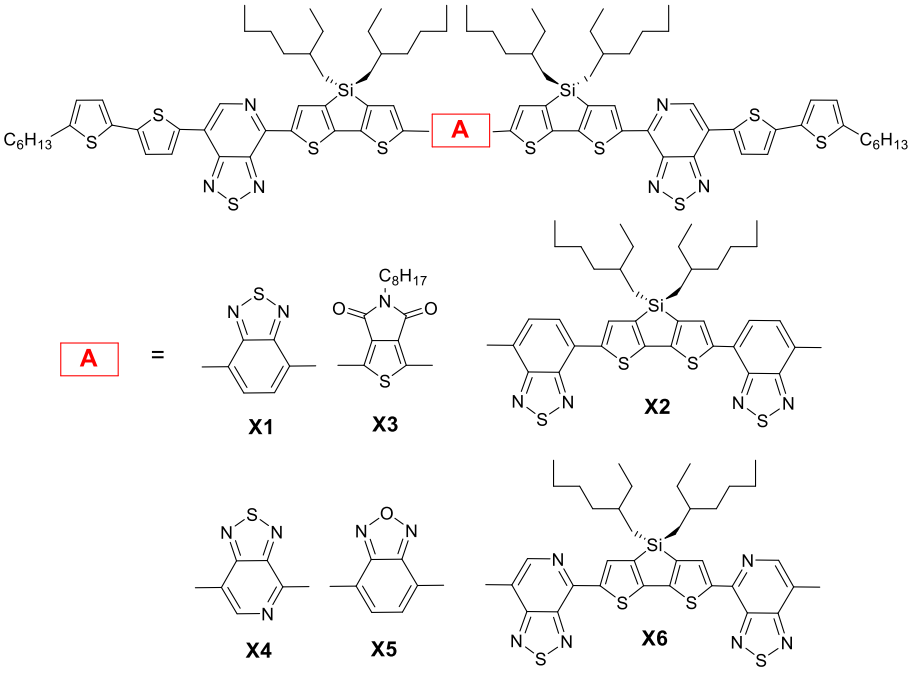

Figure A.1 The chemical structures of medium-sized molecules with various electron-accepting units (**X1** to **X6**), reported by Bazan *et al.*[2]

The studies discussed in this chapter are focusing on evaluating how structural variation affects the bulk properties, which is mainly two-fold: (1) expanding the

backbone to 2D by attaching alkylthienyl side groups, where the π-electrons can delocalize to the conjugated side chain, thus facilitating exciton diffusion and charge transport; and (2) using two different cores, BDT and BBTz, to fine tune the molecular energy levels, optical and thermal properties. The two-dimensional conjugated BDT-based unit has been widely used in polymer systems, in order to extend the conjugation of the backbones and improve the inter-chain π–π overlaps.[12-15] In this studies, alkylthienyl-substituted benzo[1,2-*b*:4,5-*b*']dithiophene (BDT) and bisthiazole (BBTz) were incorporated as the core into this D^1–A–D^2–core– D^2–A–D^1 system, forming BDT-X and BBTz-X, respectively (Figure A.2). Different film processing methods and detailed in-situ film-forming sequences were conducted to examine how variation of the core segment influence the solid-state order.

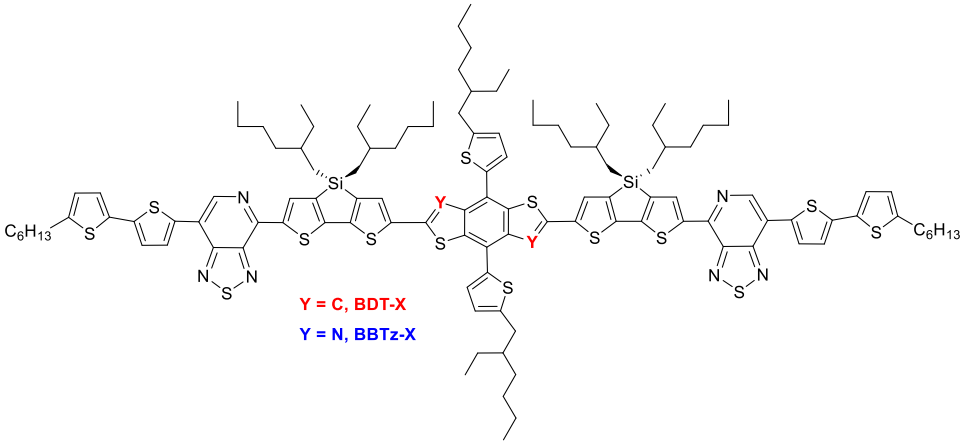

Figure A.2 Chemical structures of two molecules used in this study.

A.2 Characterization of BBTz-X and BDT-X

The two benzodithiophene and benzobisthiazole based oligomers were synthesized by Dr. Junxiang Zhang in Dr. Marder's group. Figure A.3 shows the general synthesis scheme for BDT and BBTz. Detailed synthesis procedures will be discussed

elsewhere.

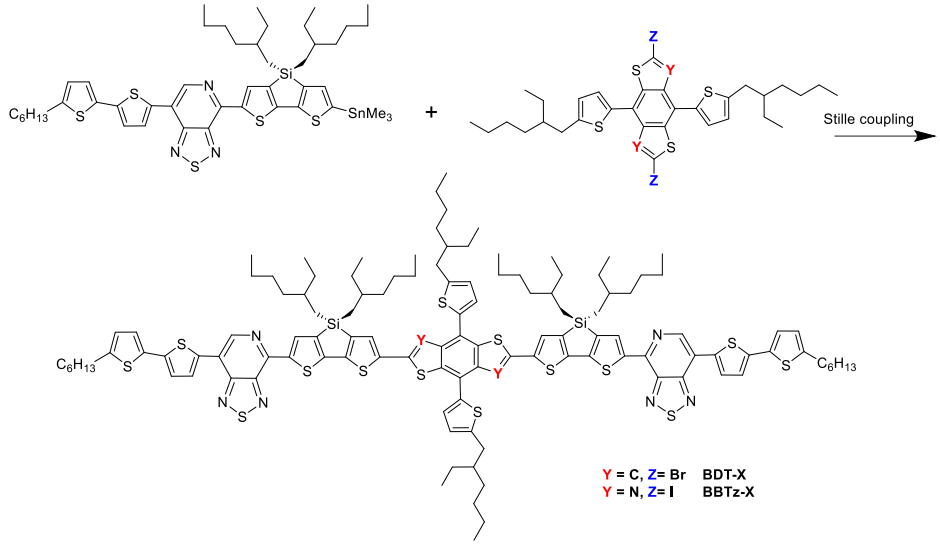

Figure A.3 General synthesis for BDT-X and BBTz-X.

DFT computation was performed by Dr. Junxiang Zhang. As shown in Figure A.4, the energy-minimized dihedral angle between planes of thienyl and BDT is ca. 30°, which is much larger than the calculated dihedral angle between planes of thienyl and BBTz group (ca. 10°). This may be due to the intermolecular (thienyl)S···N(thiazole) attractive interaction that stabilized the conformation, which does not exist between thienyl and BDT. This S···N interaction has been widely used to modulate the conformational preference of a molecule in drug design and organic synthesis.[16-19] This flat configuration in BBTz allows the HOMO to slightly spread over to the two pendant thiophenes. Frontier orbital energies in BBTz containing compound are lower than those of BDT counterpart, due to the presence of more electronegative N atoms in BBTz.

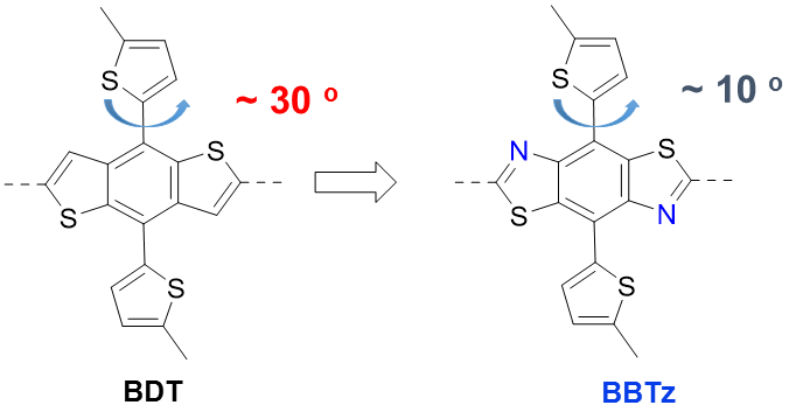

Figure A.4 Calculated dihedral angle for BDT and BBTz moieties (B3LYP/6-31G*).

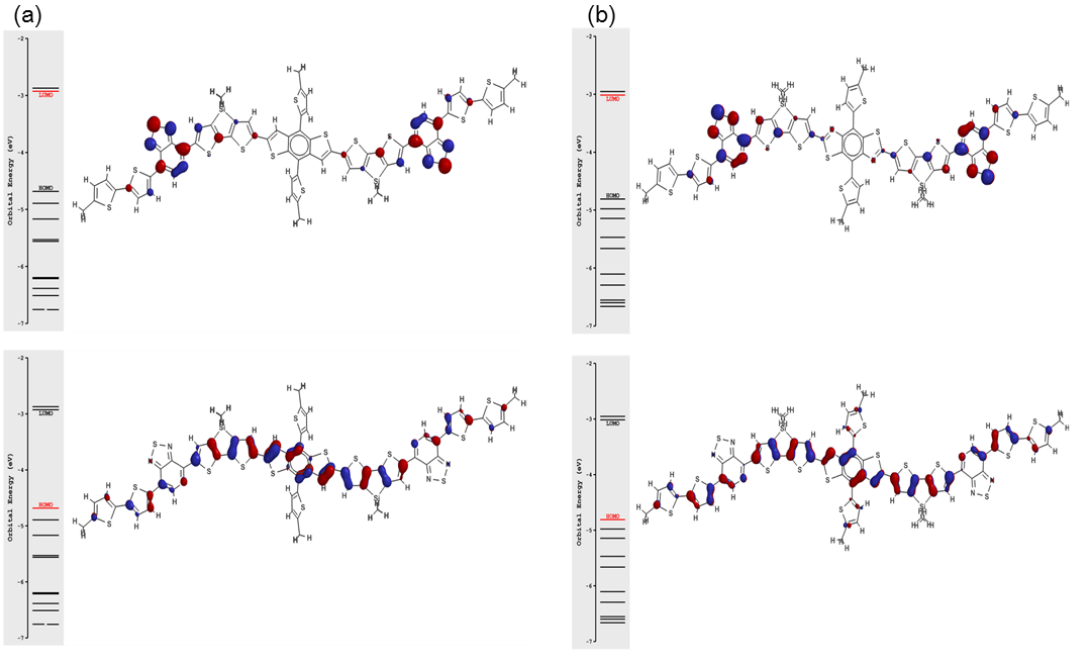

Figure A.5 Calculated optimized geometries and HOMOs and LUMOs of (a) BDT-X and (b) BBTz-X (B3LYP/6-311G*).

Organic field-effect transistor (OFET) and space charge-limited current (SCLC) measurements were used to investigate the film mobility parallel and perpendicular to the substrate plane, respectively. OFETs used a bottom-contact-bottom-gate device architecture. Solution of compounds in chloroform (5 mg/mL) were spin-coated onto OFET substrates, which consist of 300 nm SiO_2 dielectric grown on heavily n-doped

Si. The channel between gold source and drain electrodes is 2 mm wide and 50 μm long. The transfer curves for devices fabricated are shown in Figure A.6 (Figure A.7 for the thermal stability test), and the resulting motilities calculated from the saturation regime are listed in Table A.1. Both molecules show moderate hole-mobility on the order of 10^{-3} cm^2 V^{-1} s^{-1}, while BDT-X presents slightly higher mobility (on the order of 10^{-2} cm^2 V^{-1} s^{-1}) than BBTz-X (on the order of 10^{-3} cm^2 V^{-1} s^{-1}). Upon solvent vapor annealing (SVA) and thermal annealing (TA), the mobility increases ca. 3× for both the molecules, but start to drop after annealing at 200 °C. It should be noted that the OFET devices were not intensively optimized. The primary purpose of OFET experiments was to show their potentials as semiconductors, and compare the effects of TA and SVA on charge transport abilities. SCLC measurements were used to quantify the charge mobility perpendicular to the substrate plane in bulk-heterojunction blend film. For hole-only devices, the blend films yield 6.2×10^{-4} cm^2 V^{-1} s^{-1} and 2.8×10^{-4} cm^2 V^{-1} s^{-1} for BDT-X and BBTz-X, respectively. These values are comparable to those reported high efficiency small molecules bulk heterojunction films.[2,11,20] Electron mobilities (μ_e) measured by the electron-only devices are on the same order of μ_h. This balanced μ_e and μ_h are important for the high filled factors.[2,20]

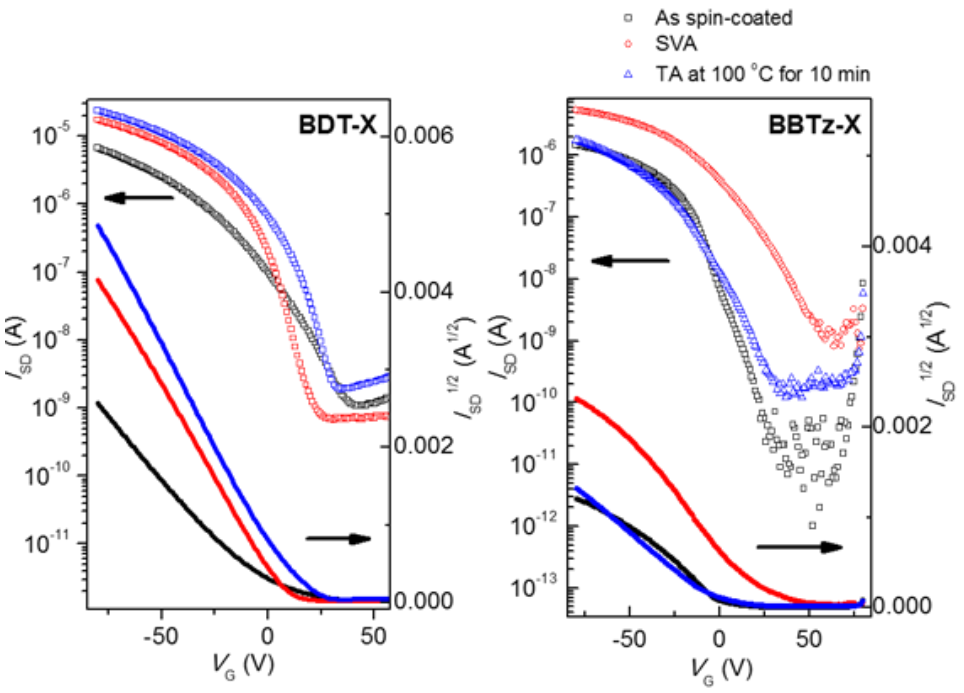

Figure A.6 OFET transfer curves for BDT-X and BBTz-X after spin-coating, thermal annealing (TA) and solvent vapor annealing (SVA).

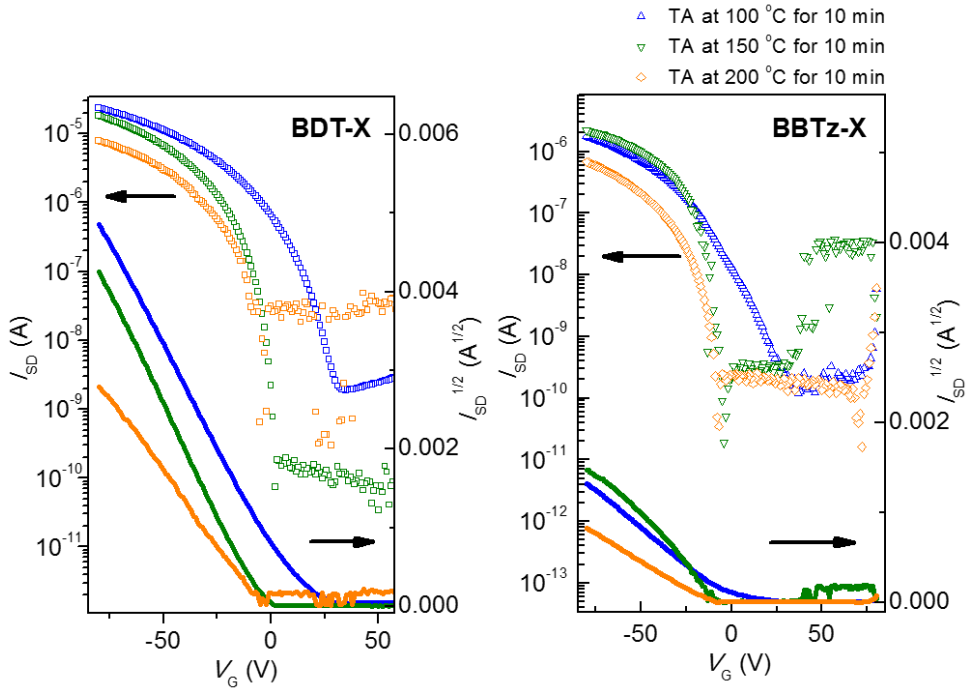

Figure A.7 OFET transfer curves for annealed BDT-X and BBTz-X films.

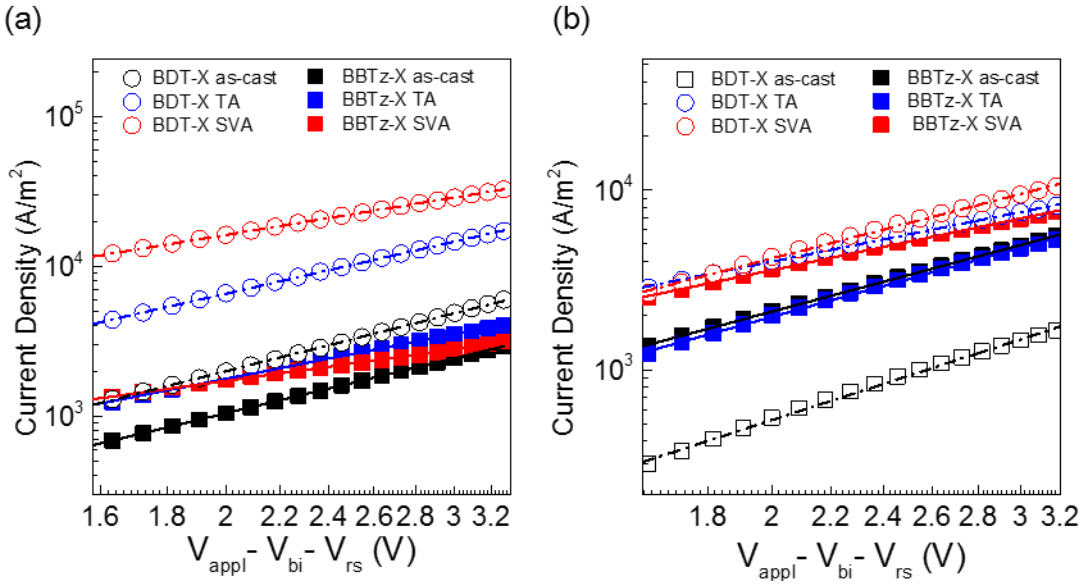

Figure A.8 *J-V* characteristics under dark for (a) hole-only and (b) hole-only devices. The bias (V) is corrected as (V_{appl}-V_{bi}-V_{rs}). The solid lines represent the fitting curves.

Table A.1 Hole-transport properties of BDT-X and BBTz-X based OFET and SCLC devices.

Samples		OFET			SCLC (BHJ)	
		Hole mobility ($cm^2V^{-1}s^{-1}$)	**$I_{ON/OFF}$**	**$V_{TH,avg}$ / V**	**Hole mobility ($cm^2V^{-1}s^{-1}$)**	**Electron mobility ($cm^2V^{-1}s^{-1}$)**
BDT-X	As-cast	4.7×10^{-3}	10^4-10^5	2.9	5.6×10^{-5}	2.1×10^{-5}
	SVA	1.3×10^{-2}	10^5-10^6	8.6	6.2×10^{-4}	6.0×10^{-4}
	TA (100 °C)[b]	1.1×10^{-2}	10^5-10^6	18.2	3.0×10^{-4}	5.2×10^{-4}
	TA (150 °C)	1.1×10^{-2}	10^5-10^6	~0	N/A	N/A
	TA (200 °C)	7.4×10^{-3}	10^3-10^4	~0	N/A	N/A
BBTz-X	As-cast	1.7×10^{-3}	10^5-10^6	~0	1.6×10^{-4}	1.0×10^{-4}
	SVA	3.5×10^{-3}	10^4-10^5	30.2	2.8×10^{-4}	4.6×10^{-4}
	TA (100 °C)	4.7×10^{-3}	10^4-10^5	~0	3.3×10^{-4}	1.2×10^{-4}
	TA (150 °C)	2.5×10^{-3}	10^4-10^5	-10	N/A	N/A
	TA (200 °C)	6.6×10^{-4}	10^3-10^4	-10	N/A	N/A

The photovoltaic properties of new compounds were investigated with conventional architectures, indium tin oxide (ITO)/MoOx/ BDT-X or BBTz-X: [6,6]-phenyl-C_{60}-butyric acid methyl ester ($PC_{60}BM$)/Ca/Al. The MoO_x hole extraction layer

was vacuum-deposited, and the active layer were spin-coated from $CHCl_3$ solution with a total concentration of 20 mg/mL. Different active-layer compositions (donor:$PC_{60}BM$ ratios), film thickness, additive, and post-treatment conditions were investigated systematically (shown in Table A.2 and A.3). Photovoltaic parameters were obtained under AM 1.5G at 100 mA/cm^2 are summarized in Table A.4. An optimal weight ratio of 50:50 was observed. For BDT-X, upon thermal annealing (TA), and solvent vapor annealing (SVA), the efficiency for devices with optimized thickness increased from ~3 % to ~5% and ~8%, respectively. SVA blend film showed the best device performance, which mainly contributed from the high J_{sc} (14.00 mA/cm^2) and high *FF* (74.10 %), but with slightly lower V_{oc} (0.78 V). Device assembly was reproducible with around 50 SVA-treated OPV devices having an average PCE of 7.74 ± 0.31%. This enhanced FF and J_{sc}, but lower V_{oc} are consistent with reported observations of the effects of SVA treatment,[21-23] where the solvent vapor can penetrate into the film and allow the molecules to re-organize and form a more ordered packing structure. It was shown that, SVA can also improve the hole-mobility,[22] which is consistent with what is observed here. However, the post-treatment effects are not as obvious in BBTz-X blend films: both the as spin-coated film and film after TA treatment give around ~6%, and only increase to ~7% after SVA treatment. The difference between BDT-X and BBTz-X may be caused by the different dihedral angle between the planes of the side-chain and backbone, where BBTz-X has smaller dihedral angle and torsion, thus packed better than BDT-X after spin-coating, and re-organize to less extent during the post-treatment. Similar trends were observed for the mobility measurements.

Table A.2 Summary of photovoltaic parameters for BDT-X, BBTz-X fabricated with $PC_{60}BM$ at different ratio and film thickness. No post-treatments, such as TA or SVA are applied.

Acceptor	D/A ratio	Spin-speed (rpm)	J_{sc} (mA/cm^2)	V_{oc} (V)	FF (%)	η (%)	best η (%)
BDT-X &$PC_{60}BM$	60:40	1600	7.63 ± 0.07	0.80 ± 0.01	39.6 ± 0.8	2.41 ± 0.31	2.82
	60:40	1900	7.45 ± 0.15	0.80 ± 0.01	40.0 ± 0.8	2.38 ± 0.25	2.54
	60:40	2200	7.48 ± 0.18	0.78 ± 0.00	39.8 ± 0.7	2.32 ± 0.16	2.56
	50:50	1600	8.81 ± 0.71	0.80 ±0.01	58.13 ± 0.53	4.10 ± 0.10	4.34
	50:50	1900	7.58 ± 0.49	0.80 ± 0.01	59.01 ± 1.54	3.58 ± 0.16	3.71
	50:50	2200	9.64 ± 0.17	0.80 ± 0.01	54.01± 1.17	4.17 ± 0.22	4.41
	40:60	1900	8.50 ± 0.16	0.81 ± 0.00	40.64 ± 3.50	2.80 ± 0.68	3.03
	40:60	2200	8.89 ± 0.59	0.83 ± 0.01	45.15 ± 1.66	3.33 ± 0.28	3.64
BBTz-X &$PC_{60}BM$	70:30	1600	5.85 ± 0.43	0.85 ± 0.02	44.7 ± 2.6	2.24 ± 0.17	2.43
	70:30	1900	4.10 ± 0.34	0.87 ± 0.01	45.3 ± 1.7	1.61 ± 0.11	1.77
	70:30	2200	3.58 ± 0.150	0.86 ± 0.00	44.6 ± 0.4	1.37 ± 0.06	1.43
	60:40	1600	6.66 ± 0.21	0.87 ± 0.01	48.1 ± 2.5	2.78 ± 0.17	3.04
	60:40	1900	8.38 ± 1.39	0.87 ± 0.01	45.9 ± 3.9	3.32 ± 0.40	4.00
	60:40	2200	6.93 ± 0.92	0.87 ± 0.01	39.3 ± 3.4	2.35 ± 0.26	2.80
	50:50	1600	9.95 ± 1.58	0.85 ± 0.01	55.2 ± 5.0	4.52 ± 0.55	5.09
	50:50	1900	9.12 ± 0.98	0.85 ± 0.01	53.1 ± 5.5	4.12 ± 0.45	4.71
	50:50	2200	8.51 ± 0.06	0.86 ± 0.00	43.8 ± 0.3	3.21 ± 0.02	3.34
	40:60	1900	10.3 ± 1.7	0.86 ± 0.01	49.8 ± 3.3	4.37 ± 0.55	4.77
	40:60	2200	10.1 ± 1.2	0.86 ± 0.00	49.0 ± 2.8	4.29 ± 0.70	4.69

Table A.3 Summary of photovoltaic parameters for BDT-X fabricated with $PC_{60}BM$ with different ratio 1,8-diiodooctane (DIO) of additive .

Acceptor	DIO ratio (%)	Spin-speed (rpm)	J_{sc} (mA/cm^2)	V_{oc} (V)	FF (%)	η (%)	best η (%)
BDT-X &$PC_{60}BM$	1	1600	5.81 ± 0.47	0.84 ± 0.01	31.26 ± 0.41	1.53 ± 0.24	1.82
	1	1900	5.97 ± 0.35	0.84 ± 0.01	31.46 ± 1.24	1.59 ± 0.10	1.91
	1.5	1600	6.03 ± 0.22	0.84 ± 0.00	39.8 ± 0.62	2.02 ± 0.24	2.56
	1.5	1900	6.05 ± 0.43	0.84 ±0.01	40.13 ± 0.73	2.06 ± 0.51	2.34
	3	1600	5.98 ± 0.29	0.83 ± 0.01	31.01 ± 0.64	1.54 ± 0.33	1.71
	3	1900	5.88 ± 0.17	0.83 ± 0.01	34.05 ± 0.13	1.64 ± 0.41	1.91

Table A.4 Summary of photovoltaic parameters for BDT-X, BBTz-X and X2 fabricated under the same condition.

Acceptor	Film treat	J_{sc} (mA/cm^2)	V_{oc} (V)	FF (%)	η (%)	best η (%)
BDT-X &$PC_{60}BM$	as-cast	10.18 ± 0.20	0.86 ± 0.01	38.20 ± 0.62	3.34 ± 0.10	3.47
	TA	11.85 ± 0.17	0.81 ± 0.01	58.48 ± 0.72	5.51 ± 0.24	5.66
	SVA	13.71 ± 0.21	0.78 ± 0.01	73.04 ± 0.91	7.74 ± 0.31	8.10
BBTz-X &$PC_{60}BM$	as-cast	11.14 ± 0.25	0.87 ± 0.01	60.04 ± 1.25	6.02 ± 0.23	6.20
	TA	11.53 ± 0.21	0.86 ± 0.01	62.78 ± 0.37	6.09 ± 0.19	6.26
	SVA	12.27 ± 0.31	0.84 ± 0.01	69.50 ± 0.44	7.20 ± 0.30	7.39
X2 & $PC_{60}BM$	as-cast	15.15 ± 0.47	0.69 ± 0.06	65.21 ± 6.3	6.76 ± 0.17	6.98
	TA	15.50 ± 0.48	0.68 ± 0.01	59.87 ± 2.26	6.31 ± 0.10	6.39
	SVA	15.41 ± 0.19	0.66 ± 0.01	69.00 ± 1.62	7.01 ± 0.12	7.19

J_{sc} is lower than previous reported molecule X2, which was fabricated under the optimized condition (the values are comparable to the literature[2]), presumably due to the suboptimal bandgaps (ca. 1.5 eV versus ca. 1.4 eV). Higher efficiency is largely ascribable to higher V_{oc} and fill factors. The V_{oc} of BBTz-X is ca. 50 mV greater than BDT-X, which is in agreement with the HOMO order.

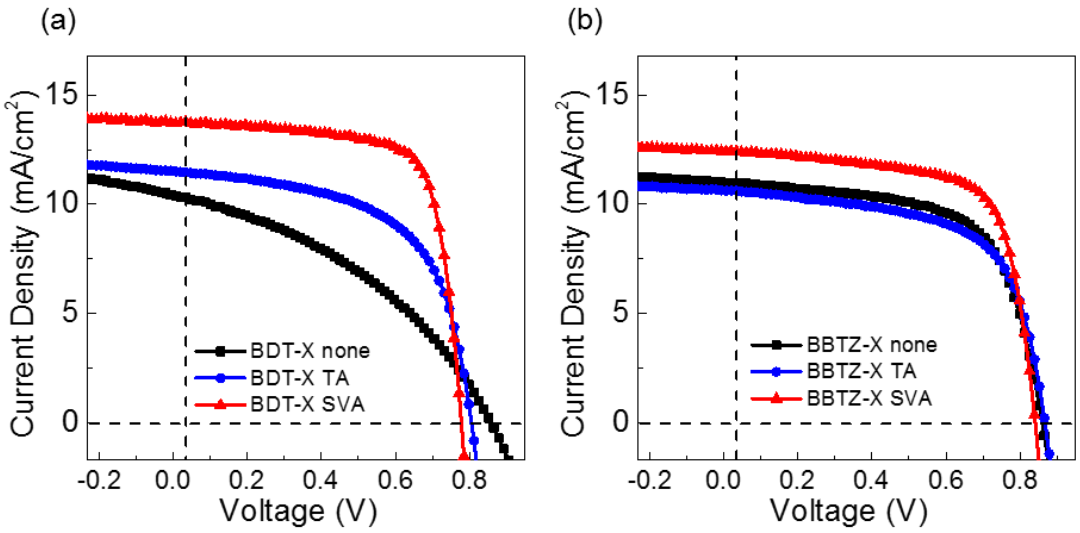

Figure A.9 (a) Current−voltage characteristics of molecule:$PC_{61}BM$ BHJ solar cell devices for BDT-X. (b) BBTz-X fabricated under the same condition.

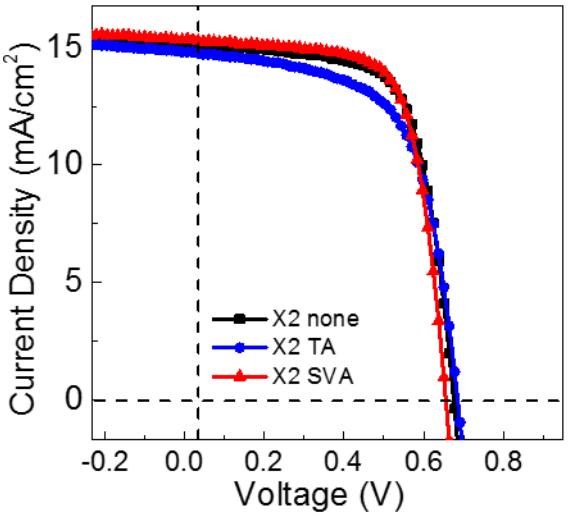

Figure A.10 Current−voltage characteristics of X2:$PC_{61}BM$ BHJ solar cell devices.

The dependence of *J*–*V* characteristics on light intensity can also provide useful information on the recombination loss of devices, and it has been widely used to distinguish between the monomolecular and/or bimolecular recombination.[24,25] Under the short-circuit condition, the generated excitons will be swept out prior to recombination, thus bimolecular recombination can be considered negligible, and a linear dependence of J_{sc} on light intensity (both on log scale) with slope close to 1 should be observed. As shown in Figure A.12, for both molecules, the fitted slopes of J_{sc} versus light intensity for SVA blend films are higher than as-cast and TA films, which suggests reduced bimolecular recombination in BHJs. Moreover, the slope of V_{oc} versus light intensity will be equal to kT/q if bimolecular recombination is dominant. In the case of trap-assisted SRH recombination, a stronger dependence of V_{oc} on the light intensity will occur (have a slope of $2kT/q$).[25]. For all the BHJ films, V_{oc} dependence on light intensity has slope close to $1kT/q$, which represent the absence of the trap-assist

recombination.

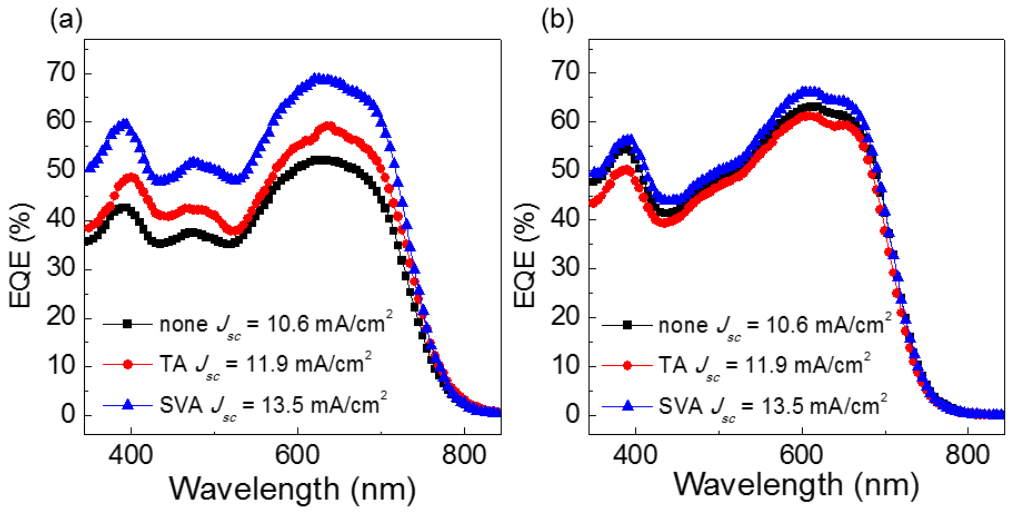

Figure A.11 (a) EQE curves of the corresponding devices from (a) and (b) respectively.

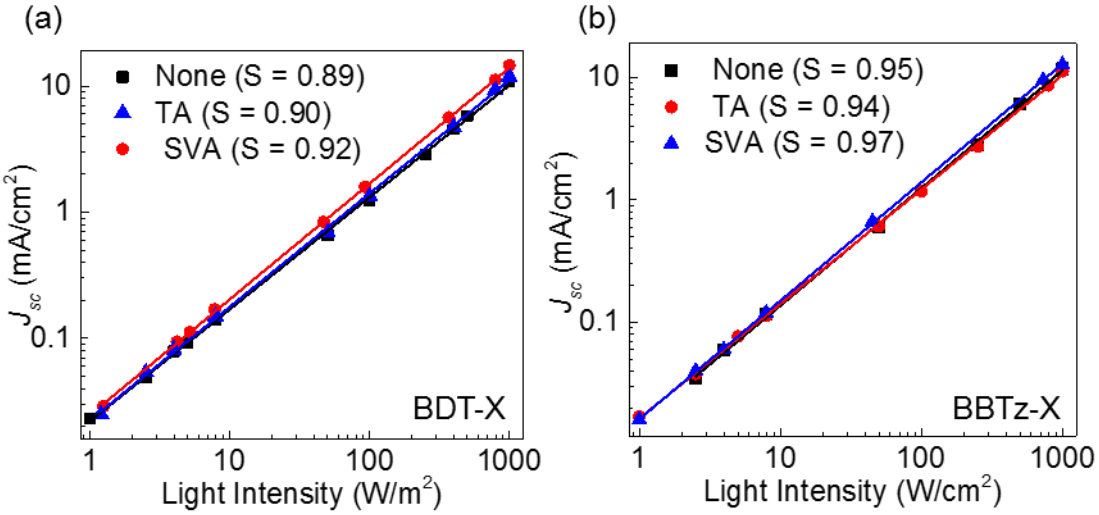

Figure A.12 Light-intensity dependence of J_{sc} for molecule:$PC_{61}BM$ BHJ solar cell devices for BDT-X (a) and BBTz-X (b)

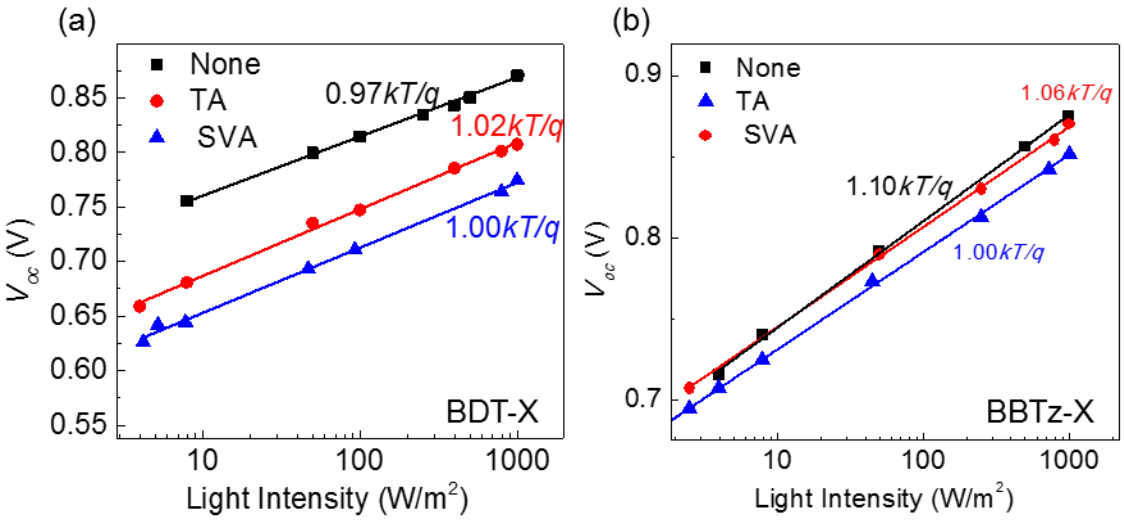

Figure A.13 Light-intensity dependence of V_{oc} for molecule:$PC_{61}BM$ BHJ solar cell devices for BDT-X (a) and BBTz-X (b).

The solid-state structure of neat and blend films was examined by grazing incidence wide-angle X-ray scattering (GIWAXS). Figure A.14 and Figure A.15 show the GIWAXS images, and their corresponding out-of-plane and in-plane linecuts. Both as-cast films for BDT-X and BBTz-X show strong reflection along the in-plane at q values of 0.31 Å^{-1}, which is assumed to be contributed from the alkyl spacing direction. Thus, the calculated "lamellar" spacing is 20.3 Å. The peak attributed to π-π stacking at q = 1.73 Å^{-1} is only observed in the out-of-plane, suggesting strong preference for the face-on π-π stacking. These implies that different conjugated main-chain has little influence on the molecular packing of the neat film. Further TA and SVA treatment lead to a slightly decrease of d spacing for BDT-X: q value increase to 0.32 (TA) and 0.33 Å^{-1} (SVA), while that of BBTz-X is maintained at 0.31 Å^{-1} (d = 20.3 Å). Compared with the neat film, the preferred face-on π-π stacking is disrupted. The as-cast films exhibit (100) lamellar packing reflections along all polar angles, π-π stacking only start to show

after post-treatment. An isotropic ring feature at q = 1.36 Å^{-1}, (d = 4.62 Å) is observed, corresponding to Bragg diffraction from crystalline PCBM. The π-π stacking peak was observed at the SVA and TA treatment.

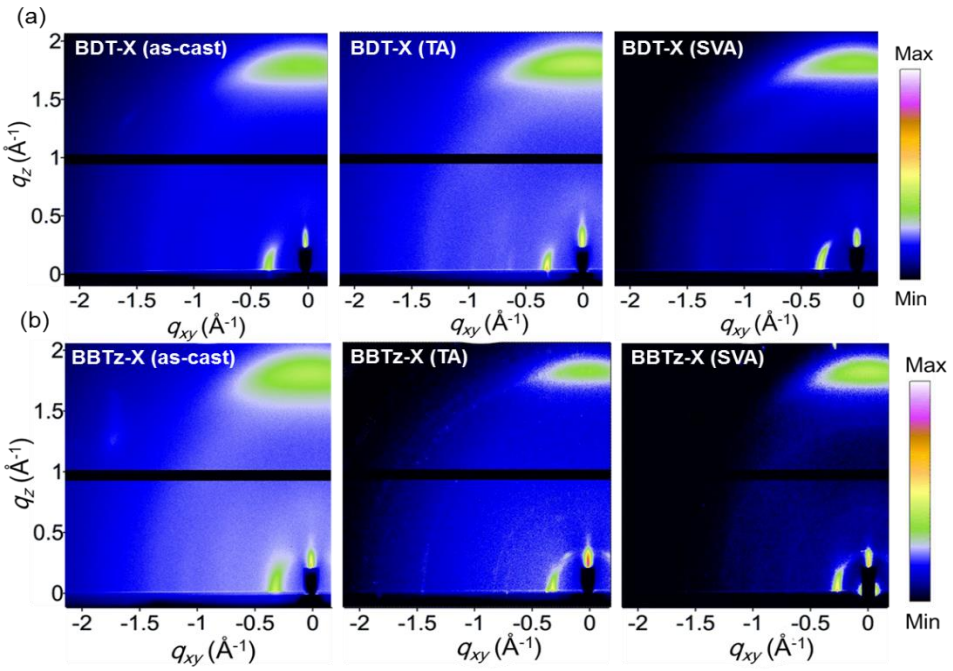

Figure A.14 GIWAXS of the BDT-X and BBTz-X neat films on silicon wafer under different treatments: as-cast, thermal annealing and solvent vapor annealing (from left to right).

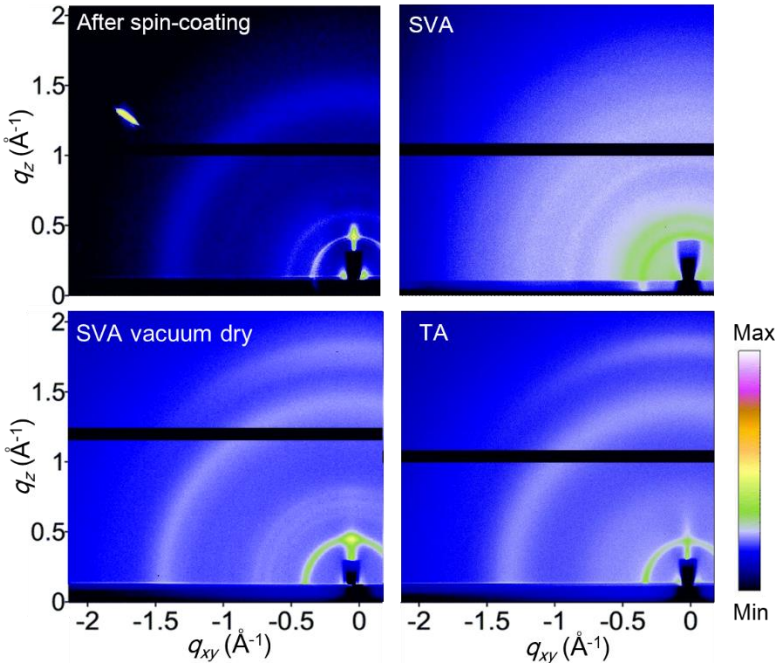

Figure A.15 GIWAXS data for BHJ blend films for BDT-X. a) Two-dimensional (2D) GIWAXS image of BDT-X blend film with PCBM under different conditions, as noted on the graph. b) Out-of-plane linecuts of 2D GIWAXS of films. c) In-plane linecuts of 2D GIWAXS of films.

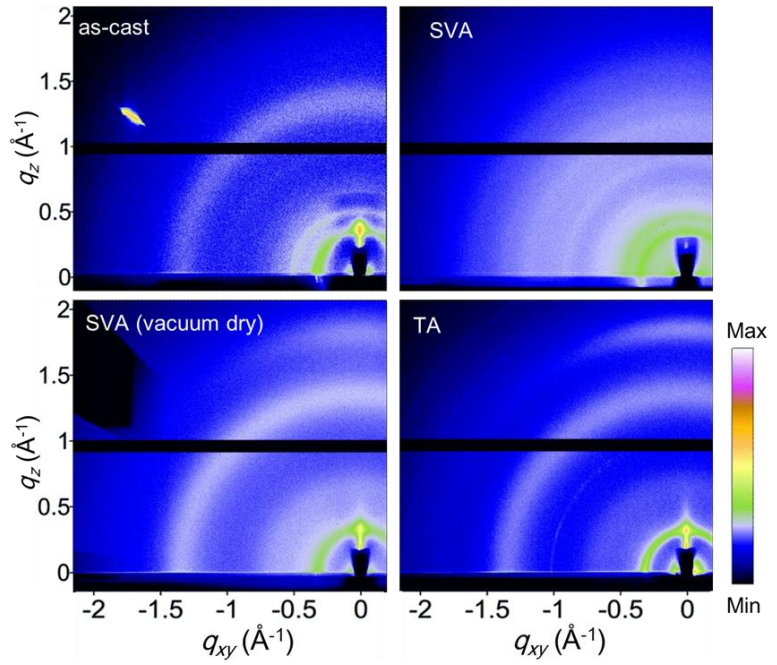

Figure A.16 GIWAXS data for BHJ blend films for BBTz-X. a) Two-dimensional (2D) GIWAXS image of BDT-X blend film with PCBM under different conditions, as noted on the graph. b) Out-of-plane linecuts of 2D GIWAXS of films. c) In-plane linecuts of 2D GIWAXS of films.

Atomic force microscopy (AFM) measurements were performed to investigate the topography and phase separation. Both of the molecules are highly soluble in chloroform and form smooth films with an root-mean-square (r.m.s.) roughnesses of 0.4 nm (BDT-X) and 0.6 nm (BBTz-X) when spin-coated atop indium tin oxide (ITO)-coated glass substrates with a 9-nm layer of vacuum deposited MoO_x (Figure A.17 and Figure A.18). The topographic and phase images of the as-cast film for BDT-X are featureless with small domain size. On the contrary, the as-cast film for BBTz-X exhibits a more ordered structure, with fiber-like small domain. This is consistent with the small dihedral angle between the planes of conjugated thienyl-side chain and the backbone. After annealing at 100 °C for 10 min in nitrogen, surface roughness increase to ~0.8 nm, similar changes in the BBTz-X film but with less increase of the roughness (~0.7 nm). Figure A.17 and Figure A.18 also show the corresponding phase images of donor:PCBM blend films. Two distinct domains represented as blue and red in figure are observed. There is a clear change of the phase separation under different treatments. In both molecules, the size for fiber-like domains order TA > SVA> as-cast films, which also reflect the surface roughness. The optimized domain size should be that which is large enough for an effective continuous interpenetrating D−A charge transport pathway and small enough for efficient exciton separation matching the short effective exciton diffusion length. It is possible that the slightly increased domain size with SVA treatment matches this criteria, thus generating an improved FF and PCE.

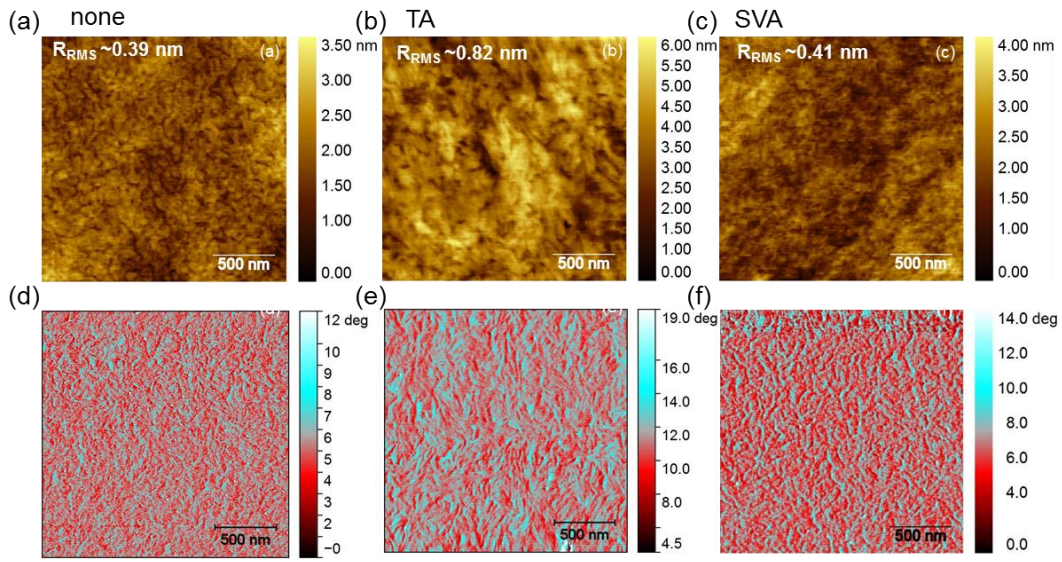

Figure A.17 AFM images of BDT-X:PCBM films spin-coated on ITO/MoO_x substrates. a-c) Height image of as-cast film (a), film after anneal at 100 °C (b) and film after solvent vapor annealing (c). d-f) Phase image of as-cast film (a), film after anneal at 100 °C (b) and film after solvent vapor annealing (c). The scan size for all images is 2 µm × 2 µm.

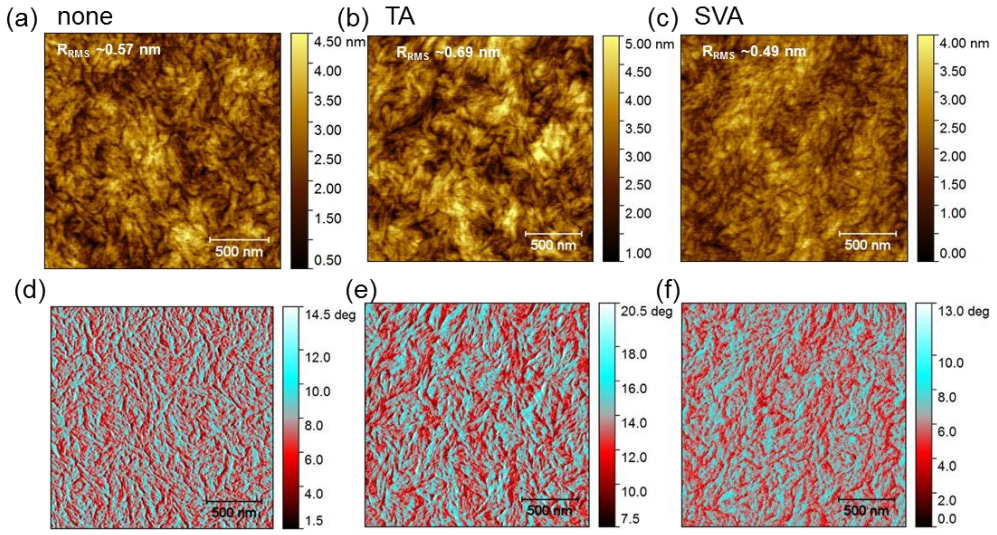

Figure A.18 AFM images of BBTz-X:PCBM films spin-coated on ITO/MoO_x substrates. a-c) Height image of as-cast film (a), film after anneal at 100 °C (b) and film after solvent vapor annealing (c). d-f) Phase image of as-cast film (a), film after anneal at 100 °C (b) and film after solvent vapor annealing (c). The scan size for all images is 2 µm × 2 µm.

In all, two oligomers with different core, BDT-X and BBTz-X, were synthesized and characterized. The results indicated that, for the as-prepared film, the variation of the core from BDT to BBTz has minimal effects on molecular packing, device morphology and charge transport properties for both the pristine donor film or blend film with the acceptor ($PC_{61}BM$), however, the difference became larger after the post treatment, which presumably caused by the rearrangement of the oligomer during SVA and TA treatment. From BDT-X to BBTz-X, the V_{oc} increased from 0.78 eV to 0.84 eV, while the J_{sc} and *FF* decreased slightly. Higher efficiency was demonstrated with BDT-X (avg. 7.74%) than BBTz-X (7.2%).

A.3 References

(1) Chang, Y.-T.; Hsu, S.-L.; Chen, G.-Y.; Su, M.-H.; Singh, T. A.; Diau, E. W.-G.; Wei, K.-H. *Adv. Funct. Mater.* **2008**, *18*, 2356.

(2) Liu, X.; Sun, Y.; Hsu, B. B. Y.; Lorbach, A.; Qi, L.; Heeger, A. J.; Bazan, G. C. *J. Am. Chem. Soc.* **2014**, *136*, 5697.

(3) Oktem, G.; Balan, A.; Baran, D.; Toppare, L. *Chem. Commun.* **2011**, *47*, 3933.

(4) Wang, M.; Hu, X.; Liu, P.; Li, W.; Gong, X.; Huang, F.; Cao, Y. *J. Am. Chem. Soc.* **2011**, *133*, 9638.

(5) Zhao, J.; Li, Y.; Yang, G.; Jiang, K.; Lin, H.; Ade, H.; Ma, W.; Yan, H. *Nat. Energy* **2016**, *1*, 15027.

(6) Zhang, Q.; Kan, B.; Liu, F.; Long, G.; Wan, X.; Chen, X.; Zuo, Y.; Ni, W.; Zhang, H.; Li, M.; Hu, Z.; Huang, F.; Cao, Y.; Liang, Z.; Zhang, M.; Russell, T. P.; Chen, Y. *Nat. Photon.* **2015**, *9*, 35.

(7) Deng, D.; Zhang, Y.; Yuan, L.; He, C.; Lu, K.; Wei, Z. *Adv. Energy Mater.* **2014**, *4*, n/a.

(8) Walker, B.; Kim, C.; Nguyen, T.-Q. *Chem. Mater.* **2011**, *23*, 470.

(9) Welch, G. C.; Perez, L. A.; Hoven, C. V.; Zhang, Y.; Dang, X.-D.; Sharenko, A.; Toney, M. F.; Kramer, E. J.; Nguyen, T.-Q.; Bazan, G. C. *J. Mater. Chem.* **2011**, *21*, 12700.

(10) Sun, Y.; Welch, G. C.; Leong, W. L.; Takacs, C. J.; Bazan, G. C.; Heeger, A. J. *Nat. Mater.* **2012**, *11*, 44.

(11) Zhou, J.; Zuo, Y.; Wan, X.; Long, G.; Zhang, Q.; Ni, W.; Liu, Y.; Li, Z.; He, G.; Li, C.; Kan, B.; Li, M.; Chen, Y. *J. Am. Chem. Soc.* **2013**, *135*, 8484.

(12) Ye, L.; Zhang, S.; Huo, L.; Zhang, M.; Hou, J. *Acc. Chem. Res.* **2014**, *47*, 1595.

(13) Huo, L.; Zhang, S.; Guo, X.; Xu, F.; Li, Y.; Hou, J. *Angew. Chem. Int. Ed.* **2011**, *50*, 9697.

(14) Huang, F.; Chen, K.-S.; Yip, H.-L.; Hau, S. K.; Acton, O.; Zhang, Y.; Luo, J.;

Jen, A. K. Y. *J. Am. Chem. Soc.* **2009**, *131*, 13886.

(15) Dou, L.; Gao, J.; Richard, E.; You, J.; Chen, C.-C.; Cha, K. C.; He, Y.; Li, G.; Yang, Y. *J. Am. Chem. Soc.* **2012**, *134*, 10071.

(16) Beno, B. R.; Yeung, K.-S.; Bartberger, M. D.; Pennington, L. D.; Meanwell, N. A. *J. Med. Chem.* **2015**, *58*, 4383.

(17) Hayashi, K.; Ogawa, S.; Sano, S.; Shiro, M.; Yamaguchi, K.; Sei, Y.; Nagao, Y. *Chem. Pharm. Bull.* **2008**, *56*, 802.

(18) Fukumoto, S.; Nakashima, T.; Kawai, T. *Angew. Chem., Int. Ed.* **2011**, *50*, 1565.

(19) Lin, S.; Wrobleski, S. T.; Hynes Jr, J.; Pitt, S.; Zhang, R.; Fan, Y.; Doweyko, A. M.; Kish, K. F.; Sack, J. S.; Malley, M. F.; Kiefer, S. E.; Newitt, J. A.; McKinnon, M.; Trzaskos, J.; Barrish, J. C.; Dodd, J. H.; Schieven, G. L.; Leftheris, K. *Bioorg. Med. Chem. Lett.* **2010**, *20*, 5864.

(20) Liu, X.; Sun, Y.; Perez, L. A.; Wen, W.; Toney, M. F.; Heeger, A. J.; Bazan, G. C. *J. Am. Chem. Soc.* **2012**, *134*, 20609.

(21) Sun, K.; Xiao, Z.; Lu, S.; Zajaczkowski, W.; Pisula, W.; Hanssen, E.; White, J. M.; Williamson, R. M.; Subbiah, J.; Ouyang, J.; Holmes, A. B.; Wong, W. W. H.; Jones, D. J. *Nat. Commun.* **2015**, *6*.

(22) Sun, K.; Xiao, Z.; Hanssen, E.; Klein, M. F.; Dam, H. H.; Pfaff, M.; Gerthsen, D.; Wong, W. W.; Jones, D. J. *J. Mater. Chem. A* **2014**, *2*, 9048.

(23) He, Z.; Zhong, C.; Huang, X.; Wong, W. Y.; Wu, H.; Chen, L.; Su, S.; Cao, Y. *Adv. Mater.* **2011**, *23*, 4636.

(24) Koster, L. J. A.; Kemerink, M.; Wienk, M. M.; Maturová, K.; Janssen, R. A. J. *Adv. Mater.* **2011**, *23*, 1670.

(25) Cowan, S. R.; Roy, A.; Heeger, A. J. *Phys. Rev. B* **2010**, *82*, 245207.